

# Frontiers in Disaster Risk Reduction for Sustainable Development

Lead Guest Editor: Fadzli Mohamed Nazri

Guest Editors: Baki Ozturk and Moustafa Moufid Kassem





---

# **Frontiers in Disaster Risk Reduction for Sustainable Development**

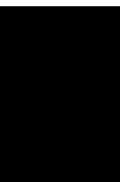
Advances in Civil Engineering

---

## **Frontiers in Disaster Risk Reduction for Sustainable Development**

Lead Guest Editor: Fadzli Mohamed Nazri

Guest Editors: Baki Ozturk and Moustafa Moufid Kassem



---

Copyright © 2023 Hindawi Limited. All rights reserved.

This is a special issue published in "Advances in Civil Engineering." All articles are open access articles distributed under the Creative Commons Attribution License, which permits unrestricted use, distribution, and reproduction in any medium, provided the original work is properly cited.



# Chief Editor

Cumaraswamy Vipulanandan, USA









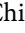

## Associate Editors

Chiara Bedon , Italy  
Constantin Chalioris , Greece  
Ghassan Chehab , Lebanon  
Ottavia Corbi, Italy  
Mohamed ElGawady , USA  
Husnain Haider , Saudi Arabia  
Jian Ji , China  
Jiang Jin , China  
Shazim A. Memon , Kazakhstan  
Hossein Moayedi , Vietnam  
Sanjay Nimbalkar, Australia  
Giuseppe Oliveto , Italy  
Alessandro Palmeri , United Kingdom  
Arnaud Perrot , France  
Hugo Rodrigues , Portugal  
Victor Yepes , Spain  
Xianbo Zhao , Australia

## Academic Editors

José A.F.O. Correia, Portugal  
Glenda Abate, Italy  
Khalid Abdel-Rahman , Germany  
Ali Mardani Aghabaglou, Turkey  
José Aguiar , Portugal  
Afaq Ahmad , Pakistan  
Muhammad Riaz Ahmad , Hong Kong  
Hashim M.N. Al-Madani , Bahrain  
Luigi Aldieri , Italy  
Angelo Aloisio , Italy  
Maria Cruz Alonso, Spain  
Filipe Amarante dos Santos , Portugal  
Serji N. Amirkhania, USA  
Eleftherios K. Anastasiou , Greece  
Panagiotis Ch. Anastasopoulos , USA  
Mohamed Moafak Arbili , Iraq  
Farhad Aslani , Australia  
Siva Avudaiappan , Chile  
Ozgur BASKAN , Turkey  
Adewumi Babafemi, Nigeria  
Morteza Bagherpour, Turkey  
Qingsheng Bai , Germany  
Nicola Baldo , Italy  
Daniele Baraldi , Italy

Eva Barreira , Portugal  
Emilio Bastidas-Arteaga , France  
Rita Bento, Portugal  
Rafael Bergillos , Spain  
Han-bing Bian , China  
Xia Bian , China  
Huseyin Bilgin , Albania  
Giovanni Biondi , Italy  
Hugo C. Biscaia , Portugal  
Rahul Biswas , India  
Edén Bojórquez , Mexico  
Giosuè Boscato , Italy  
Melina Bosco , Italy  
Jorge Branco , Portugal  
Bruno Briseghella , China  
Brian M. Broderick, Ireland  
Emanuele Brunesi , Italy  
Quoc-Bao Bui , Vietnam  
Tan-Trung Bui , France  
Nicola Buratti, Italy  
Gaochuang Cai, France  
Gladis Camarini , Brazil  
Alberto Campisano , Italy  
Qi Cao, China  
Qixin Cao, China  
Iacopo Carnacina , Italy  
Alessio Cascardi, Italy  
Paolo Castaldo , Italy  
Nicola Cavalagli , Italy  
Liborio Cavaleri , Italy  
Anush Chandrappa , United Kingdom  
Wen-Shao Chang , United Kingdom  
Muhammad Tariq Amin Chaudhary, Kuwait  
Po-Han Chen , Taiwan  
Qian Chen , China  
Wei Tong Chen , Taiwan  
Qixiu Cheng, Hong Kong  
Zhanbo Cheng, United Kingdom  
Nicholas Chileshe, Australia  
Prinya Chindaprasirt , Thailand  
Corrado Chisari , United Kingdom  
Se Jin Choi , Republic of Korea  
Heap-Yih Chong , Australia  
S.H. Chu , USA  
Ting-Xiang Chu , China

Zhaofei Chu , China  
Wonseok Chung , Republic of Korea  
Donato Ciampa , Italy  
Gian Paolo Cimellaro, Italy  
Francesco Colangelo, Italy  
Romulus Costache , Romania  
Liviu-Adrian Cotfas , Romania  
Antonio Maria D'Altri, Italy  
Bruno Dal Lago , Italy  
Amos Darko , Hong Kong  
Arka Jyoti Das , India  
Dario De Domenico , Italy  
Gianmarco De Felice , Italy  
Stefano De Miranda , Italy  
Maria T. De Risi , Italy  
Tayfun Dede, Turkey  
Sadik O. Degertekin , Turkey  
Camelia Delcea , Romania  
Cristoforo Demartino, China  
Giuseppe Di Filippo , Italy  
Luigi Di Sarno, Italy  
Fabio Di Trapani , Italy  
Aboelkasim Diab , Egypt  
Thi My Dung Do, Vietnam  
Giulio Dondi , Italy  
Jiangfeng Dong , China  
Chao Dou , China  
Mario D'Aniello , Italy  
Jingtao Du , China  
Ahmed Elghazouli, United Kingdom  
Francesco Fabbrocino , Italy  
Flora Faleschini , Italy  
Dingqiang Fan, Hong Kong  
Xueping Fan, China  
Qian Fang , China  
Salar Farahmand-Tabar , Iran  
Ilenia Farina, Italy  
Roberto Fedele, Italy  
Guang-Liang Feng , China  
Luigi Fenu , Italy  
Tiago Ferreira , Portugal  
Marco Filippo Ferrotto, Italy  
Antonio Formisano , Italy  
Guoyang Fu, Australia  
Stefano Galassi , Italy

Junfeng Gao , China  
Meng Gao , China  
Giovanni Garcea , Italy  
Enrique García-Macías, Spain  
Emilio García-Taengua , United Kingdom  
DongDong Ge , USA  
Khaled Ghaedi, Malaysia  
Khaled Ghaedi , Malaysia  
Gian Felice Giaccu, Italy  
Agathoklis Giaralis , United Kingdom  
Ravindran Gobinath, India  
Rodrigo Gonçalves, Portugal  
Peilin Gong , China  
Belén González-Fonteboa , Spain  
Salvatore Grasso , Italy  
Fan Gu, USA  
Erhan Güneyisi , Turkey  
Esra Mete Güneyisi, Turkey  
Pingye Guo , China  
Ankit Gupta , India  
Federico Gusella , Italy  
Kemal Hacıfendioglu, Turkey  
Jianyong Han , China  
Song Han , China  
Asad Hanif , Macau  
Hadi Hasanzadehshooiili , Canada  
Mostafa Fahmi Hassanein, Egypt  
Amir Ahmad Hedayat , Iran  
Khandaker Hossain , Canada  
Zahid Hossain , USA  
Chao Hou, China  
Biao Hu, China  
Jiang Hu , China  
Xiaodong Hu, China  
Lei Huang , China  
Cun Hui , China  
Bon-Gang Hwang, Singapore  
Jijo James , India  
Abbas Fadhil Jasim , Iraq  
Ahad Javanmardi , China  
Krishnan Prabhakan Jaya, India  
Dong-Sheng Jeng , Australia  
Han-Yong Jeon, Republic of Korea  
Pengjiao Jia, China  
Shaohua Jiang , China

MOUSTAFA KASSEM , Malaysia  
Mosbeh Kaloop , Egypt  
Shankar Karuppanan , Ethiopia  
John Kechagias , Greece  
Mohammad Khajehzadeh , Iran  
Afzal Husain Khan , Saudi Arabia  
Mehran Khan , Hong Kong  
Manoj Khandelwal, Australia  
Jin Kook Kim , Republic of Korea  
Woosuk Kim , Republic of Korea  
Vaclav Koci , Czech Republic  
Loke Kok Foong, Vietnam  
Hailing Kong , China  
Leonidas Alexandros Kouris , Greece  
Kyriakos Kourousis , Ireland  
Moacir Kripka , Brazil  
Anupam Kumar, The Netherlands  
Emma La Malfa Ribolla, Czech Republic  
Ali Lakirouhani , Iran  
Angus C. C. Lam, China  
Thanh Quang Khai Lam , Vietnam  
Luciano Lamberti, Italy  
Andreas Lampropoulos , United Kingdom  
Raffaele Landolfo, Italy  
Massimo Latour , Italy  
Bang Yeon Lee , Republic of Korea  
Eul-Bum Lee , Republic of Korea  
Zhen Lei , Canada  
Leonardo Leonetti , Italy  
Chun-Qing Li , Australia  
Dongsheng Li , China  
Gen Li, China  
Jiale Li , China  
Minghui Li, China  
Qingchao Li , China  
Shuang Yang Li , China  
Sunwei Li , Hong Kong  
Yajun Li , China  
Shun Liang , China  
Francesco Liguori , Italy  
Jae-Han Lim , Republic of Korea  
Jia-Rui Lin , China  
Kun Lin , China  
Shibin Lin, China

Tzu-Kang Lin , Taiwan  
Yu-Cheng Lin , Taiwan  
Hexu Liu, USA  
Jian Lin Liu , China  
Xiaoli Liu , China  
Xuemei Liu , Australia  
Zaobao Liu , China  
Zhuang-Zhuang Liu, China  
Diego Lopez-Garcia , Chile  
Cristiano Loss , Canada  
Lyan-Ywan Lu , Taiwan  
Jin Luo , USA  
Yanbin Luo , China  
Jianjun Ma , China  
Junwei Ma , China  
Tian-Shou Ma, China  
Zhongguo John Ma , USA  
Maria Macchiaroli, Italy  
Domenico Magisano, Italy  
Reza Mahinroosta, Australia  
Yann Malecot , France  
Prabhat Kumar Mandal , India  
John Mander, USA  
Iman Mansouri, Iran  
André Dias Martins, Portugal  
Domagoj Matesan , Croatia  
Jose Matos, Portugal  
Vasant Matsagar , India  
Claudio Mazzotti , Italy  
Ahmed Mebarki , France  
Gang Mei , China  
Kasim Mermerdas, Turkey  
Giovanni Minafò , Italy  
Masoomah Mirrashid , Iran  
Abbas Mohajerani , Australia  
Fadzli Mohamed Nazri , Malaysia  
Fabrizio Mollaioli , Italy  
Rosario Montuori , Italy  
H. Naderpour , Iran  
Hassan Nasir , Pakistan  
Hossein Nassiraei , Iran  
Satheeskumar Navaratnam , Australia  
Ignacio J. Navarro , Spain  
Ashish Kumar Nayak , India  
Behzad Nematollahi , Australia

Chayut Ngamkhanong , Thailand  
Trung Ngo, Australia  
Tengfei Nian, China  
Mehdi Nikoo , Canada  
Youjun Ning , China  
Olugbenga Timo Oladinrin , United Kingdom  
Oladimeji Benedict Olalusi, South Africa  
Timothy O. Olawumi , Hong Kong  
Alejandro Orfila , Spain  
Maurizio Orlando , Italy  
Siti Aminah Osman, Malaysia  
Walid Oueslati , Tunisia  
SUVASH PAUL , Bangladesh  
John-Paris Pantouvakis , Greece  
Fabrizio Paolacci , Italy  
Giuseppina Pappalardo , Italy  
Fulvio Parisi , Italy  
Dimitrios G. Pavlou , Norway  
Daniele Pellegrini , Italy  
Gatheeshgar Perampalam , United Kingdom  
Daniele Perrone , Italy  
Giuseppe Piccardo , Italy  
Vagelis Plevris , Qatar  
Andrea Pranno , Italy  
Adolfo Preciado , Mexico  
Chongchong Qi , China  
Yu Qian, USA  
Ying Qin , China  
Giuseppe Quaranta , Italy  
Krishanu ROY , New Zealand  
Vlastimir Radonjanin, Serbia  
Carlo Rainieri , Italy  
Rahul V. Ralegaonkar, India  
Raizal Saifulnaz Muhammad Rashid, Malaysia  
Alessandro Rasulo , Italy  
Chonghong Ren , China  
Qing-Xin Ren, China  
Dimitris Rizos , USA  
Geoffrey W. Rodgers , New Zealand  
Pier Paolo Rossi, Italy  
Nicola Ruggieri , Italy  
JUNLONG SHANG, Singapore

Nikhil Saboo, India  
Anna Saetta, Italy  
Juan Sagaseta , United Kingdom  
Timo Saksala, Finland  
Mostafa Salari, Canada  
Ginevra Salerno , Italy  
Evangelos J. Sapountzakis , Greece  
Vassilis Sarhosis , United Kingdom  
Navaratnarajah Sathiparan , Sri Lanka  
Fabrizio Scozzese , Italy  
Halil Sezen , USA  
Payam Shafigh , Malaysia  
M. Shahria Alam, Canada  
Yi Shan, China  
Hussein Sharaf, Iraq  
Mostafa Sharifzadeh, Australia  
Sanjay Kumar Shukla, Australia  
Amir Si Larbi , France  
Okan Sirin , Qatar  
Piotr Smarzewski , Poland  
Francesca Sollecito , Italy  
Rui Song , China  
Tian-Yi Song, Australia  
Flavio Stochino , Italy  
Mayank Sukhija , USA  
Piti Sukontasukkul , Thailand  
Jianping Sun, Singapore  
Xiao Sun , China  
T. Tafsirojjan , Australia  
Fujiao Tang , China  
Patrick W.C. Tang , Australia  
Zhi Cheng Tang , China  
Weerachart Tangchirapat , Thailand  
Xiixin Tao, China  
Piergiorgio Tataranni , Italy  
Elisabete Teixeira , Portugal  
Jorge Iván Tobón , Colombia  
Jing-Zhong Tong, China  
Francesco Trentadue , Italy  
Antonello Troncone, Italy  
Majbah Uddin , USA  
Tariq Umar , United Kingdom  
Muahmmad Usman, United Kingdom  
Muhammad Usman , Pakistan  
Mucteba Uysal , Turkey









Ilaria Venanzi , Italy  
Castorina S. Vieira , Portugal  
Valeria Vignali , Italy  
Claudia Vitone , Italy  
Liwei WEN , China  
Chunfeng Wan , China  
Hua-Ping Wan, China  
Roman Wan-Wendner , Austria  
Chaohui Wang , China  
Hao Wang , USA  
Shiming Wang , China  
Wayne Yu Wang , United Kingdom  
Wen-Da Wang, China  
Xing Wang , China  
Xiuling Wang , China  
Zhenjun Wang , China  
Xin-Jiang Wei , China  
Tao Wen , China  
Weiping Wen , China  
Lei Weng , China  
Chao Wu , United Kingdom  
Jiangyu Wu, China  
Wangjie Wu , China  
Wenbing Wu , China  
Zhixing Xiao, China  
Gang Xu, China  
Jian Xu , China  
Panpan , China  
Rongchao Xu , China  
HE YONGLIANG, China  
Michael Yam, Hong Kong  
Hailu Yang , China  
Xu-Xu Yang , China  
Hui Yao , China  
Xinyu Ye , China  
Zhoujing Ye, China  
Gürol Yildirim , Turkey  
Dawei Yin , China  
Doo-Yeol Yoo , Republic of Korea  
Zhanping You , USA  
Afshar A. Yousefi , Iran  
Xinbao Yu , USA  
Dongdong Yuan , China  
Geun Y. Yun , Republic of Korea





Hyun-Do Yun , Republic of Korea  
Cemal YİĞİT , Turkey  
Paolo Zampieri, Italy  
Giulio Zani , Italy  
Mariano Angelo Zanini , Italy  
Zhixiong Zeng , Hong Kong  
Mustafa Zeybek, Turkey  
Henglong Zhang , China  
Jiupeng Zhang, China  
Tingting Zhang , China  
Zengping Zhang, China  
Zetian Zhang , China  
Zhigang Zhang , China  
Zhipeng Zhao , Japan  
Jun Zhao , China  
Annan Zhou , Australia  
Jia-wen Zhou , China  
Hai-Tao Zhu , China  
Peng Zhu , China  
QuanJie Zhu , China  
Wenjun Zhu , China  
Marco Zucca, Italy  
Haoran Zuo, Australia  
Junqing Zuo , China  
Robert Černý , Czech Republic  
Süleyman İpek , Turkey







# Contents

**Retracted: Integrating Intrinsic and Eccentric Seismic Vulnerability Indices to Prioritize Road Network Accessibility**  
Advances in Civil Engineering  
Retraction (1 page), Article ID 9897306, Volume 2023 (2023)


**A Method for Rapidly Determining the Seismic Performance of Buildings Based on Remote-Sensing Imagery and Its Application**  
Sihan Yu, Xiaofeng Xie , Peng Du, Xiaoqing Wang, Shun Yang , and Chao Liu   
Research Article (15 pages), Article ID 5760913, Volume 2022 (2022)


**Effects of Glacier and Geomorphology on the Mechanism Difference of Glacier-Related Debris Flow on the South and North Banks of Parlung Zangbo River, Southeastern Tibetan Plateau**  
Jiajia Zhang , Jiankang Liu , Yuanling Li, Junchao Wang, Long Chen , and Bo Gao  
Research Article (11 pages), Article ID 3510944, Volume 2022 (2022)



**Mitigating Risks in the Disaster Management Cycle**  
Huay Ling Tay , Ruth Banomyong , Paitoon Varadejsatitwong , and Puthipong Julagasigorn   
Research Article (14 pages), Article ID 7454760, Volume 2022 (2022)

**Reduction of Seepage Risks by Investigation into Different Lengths and Positions for Cutoff Wall and Horizontal Drainage (Case Study: Sattarkhan Dam)**  
Widodo Brontowiyono , Ali T. Hammid , Yasir M. Jebur , Ahmed Q. A. S. Al-Sudani , Dhameer A. Mutlak , and Masoud Parvan   
Research Article (10 pages), Article ID 6441646, Volume 2022 (2022)

**Scaling Method Application for Seismic Design along the Central Anatolian Fault Zone**  
Erhan Gumus , Baki Ozturk , and Fadzli Mohamed Nazri   
Research Article (19 pages), Article ID 1963553, Volume 2022 (2022)

**[Retracted] Integrating Intrinsic and Eccentric Seismic Vulnerability Indices to Prioritize Road Network Accessibility**  
Ahmad Mohamad El Maissi, Sotirios A. Argyroudis, Moustafa Moufid Kassem, Lee Vien Leong, and Fadzli Mohamed Nazri   
Research Article (20 pages), Article ID 5888020, Volume 2022 (2022)

**Understanding the Slow Motion of the Wangjiashan Landslide in the Baihetan Reservoir Area (China) from Space-Borne Radar Observations**  
Mingtang Wu, Xiaoyu Yi , Jiawei Dun, Jianyuan Yang, Wei Cai, and Guoqiang Zhang  
Research Article (14 pages), Article ID 1766038, Volume 2022 (2022)

**Comprehensive Review of Community Seismic Resilience: Concept, Frameworks, and Case Studies**  
H'ng Chee Yin, Moustafa Moufid Kassem , and Fadzli Mohamed Nazri   
Review Article (19 pages), Article ID 7668214, Volume 2022 (2022)

## *Retraction*

# **Retracted: Integrating Intrinsic and Eccentric Seismic Vulnerability Indices to Prioritize Road Network Accessibility**

### **Advances in Civil Engineering**

Received 15 August 2023; Accepted 15 August 2023; Published 16 August 2023

Copyright © 2023 Advances in Civil Engineering. This is an open access article distributed under the Creative Commons Attribution License, which permits unrestricted use, distribution, and reproduction in any medium, provided the original work is properly cited.

This article has been retracted by Hindawi following an investigation undertaken by the publisher [1]. This investigation has uncovered evidence of one or more of the following indicators of systematic manipulation of the publication process:

- (1) Discrepancies in scope
- (2) Discrepancies in the description of the research reported
- (3) Discrepancies between the availability of data and the research described
- (4) Inappropriate citations
- (5) Incoherent, meaningless and/or irrelevant content included in the article
- (6) Peer-review manipulation

The presence of these indicators undermines our confidence in the integrity of the article's content and we cannot, therefore, vouch for its reliability. Please note that this notice is intended solely to alert readers that the content of this article is unreliable. We have not investigated whether authors were aware of or involved in the systematic manipulation of the publication process.

Wiley and Hindawi regrets that the usual quality checks did not identify these issues before publication and have since put additional measures in place to safeguard research integrity.

We wish to credit our own Research Integrity and Research Publishing teams and anonymous and named external researchers and research integrity experts for contributing to this investigation.

The corresponding author, as the representative of all authors, has been given the opportunity to register their agreement or disagreement to this retraction. We have kept a record of any response received.

### **References**

- [1] A. M. El Maissi, S. A. Argyroudis, M. M. Kassem, L. V. Leong, and F. Mohamed Nazri, "Integrating Intrinsic and Eccentric Seismic Vulnerability Indices to Prioritize Road Network Accessibility," *Advances in Civil Engineering*, vol. 2022, Article ID 5888020, 20 pages, 2022.

## Research Article

# A Method for Rapidly Determining the Seismic Performance of Buildings Based on Remote-Sensing Imagery and Its Application

Sihan Yu,<sup>1</sup> Xiaofeng Xie ,<sup>1</sup> Peng Du,<sup>1</sup> Xiaoqing Wang,<sup>2</sup> Shun Yang ,<sup>1</sup> and Chao Liu <sup>1</sup>

<sup>1</sup>Earthquake Agency of Ningxia Hui Autonomous Region, Yinchuan 750001, China

<sup>2</sup>Institute of Earthquake Science, China Earthquake Administration, Beijing 100036, China

Correspondence should be addressed to Xiaofeng Xie; feashange@126.com

Received 14 May 2022; Revised 11 August 2022; Accepted 17 September 2022; Published 3 October 2022

Academic Editor: Fadzli Mohamed Nazri

Copyright © 2022 Sihan Yu et al. This is an open access article distributed under the Creative Commons Attribution License, which permits unrestricted use, distribution, and reproduction in any medium, provided the original work is properly cited.

Remote-sensing images are visually interpreted in this study to obtain information on buildings in the urban and rural areas of Ningxia, China. Overall, area estimates yielded by the proposed equations followed a normal distribution. Correlation and error analyses indicated that the coefficients are reasonable and reliable and that the building area estimates have an accuracy of 90% and are also reliable. These results were used in conjunction with drone aerial images, Baidu street view images, and paper maps to determine the seismic performance (SP) of the buildings in the study area. On this basis, the buildings were classified into three groups, namely, those with the required SP, suspected substandard SP, and substandard SP. Examination based on the field survey data collected from at least one sample site in each village and township in all 22 county-level divisions (CLDs) of Ningxia showed an average SP accuracy of 76% for all 22 CLDs and an SP accuracy exceeding 70% for 20 (91%) of the 22 CLDs. Based on this approach and the results obtained, the ArcGIS spatial analysis method was employed to determine the percentages and distribution patterns of the buildings in the three SP groups in the 22 CLDs. The results revealed the following features. Buildings with the required SP were clustered in the urban areas of each CLD, with a few in the village and township government seats. Buildings with suspected substandard SP were distributed predominantly in the rural-urban fringe (RUF) areas and the village and township government seats. Buildings with substandard SP were found primarily in urban villages, RUF areas, and urban areas. The soundness of the spatial analysis results was corroborated by the field survey data, lending credence to the feasibility of the proposed calculation method. This method can satisfy the real-world need for rapidly assessing the SP and distribution of buildings in a region before an earthquake occurs and provide a reliable reference for disaster prevention, mitigation, and relief efforts.

## 1. Introduction

Earthquakes are unpredictable and highly destructive natural disasters that gravely threaten social and economic development, the safety of lifeline facilities, and people's lives and property [1]. Rapid economic progress and accelerated urbanisation have broadened and deepened the impact of destructive earthquakes on urban development in China.

Aboveground structures often suffer damage and even collapse during destructive earthquakes, constituting the principal cause of casualties and property losses. Massive volumes of building data considerably affect the timeliness and accuracy of rapid damage assessments after strong earthquakes. Generally, postdisaster building damage can be assessed through either a detailed field investigation of the

damage sustained by individual buildings or the determination of the damage sustained by buildings over a large area using an efficient analysis method [2]. Findings from available studies suggest that the number of buildings within an assessment zone increases exponentially as the earthquake magnitude increases [3]. Field investigations are time- and labour-intensive and thus unsuitable for assessing damage over a large area after a strong earthquake [4]. Hence, the focus of research examining earthquake damage has gradually shifted from postearthquake investigations to preearthquake disaster mitigation preparations. Well-prepared emergency management strategies can alleviate the losses from earthquakes [5].

Because of its ability to provide timely, multipurpose, multiangle image-based services, remote-sensing (RS)

technology has become a convenient tool for obtaining information before and after an earthquake and facilitating postearthquake emergency response and recovery efforts. The earliest use of RS technology to acquire earthquake damage information dates back to 1906 when G. R. Lawrence photographed San Francisco in the United States after a magnitude-8.3 earthquake using kites. Technological advances have enabled substantial progress in RS technology in recent decades. With higher resolutions and update rates, satellite images can now better facilitate assessment of the damage caused by historical earthquakes and the acquisition of earthquake damage information. A growing number of researchers have retrieved information on the damage sustained by buildings over large areas during earthquakes from RS imagery [4, 6–17]. Satellite RS technology has become a convenient and efficient tool for obtaining and disseminating information before and after earthquakes, facilitating a more effective emergency response to earthquakes and minimising their impact. Swiftly understanding the seismic performance (SP) of buildings in an earthquake-prone area before the occurrence of an earthquake plays a crucial role in urban disaster mitigation and emergency rescue efforts.

In this study, using the Seismic Ground Motion Parameter Zonation Map of China (GB18306-2015) [18] and the Code for Seismic Design of Buildings (GB50011-2016) [19] as guidelines, urban and rural buildings in Ningxia, China, were preliminarily classified based on their SP through visual interpretation of high-resolution RS imagery into three groups (termed SP groups), namely, those with the required SP, suspected substandard SP, and substandard SP. The reliability of the results obtained based on visual interpretation is comprehensively examined using drone aerial images, Baidu street view images, and paper maps. However, visual interpretation of RS imagery can only yield the number of buildings and cannot give the area of the buildings in each SP group. Therefore, a method must be established to determine the total area of the buildings in each of the three SP groups and its percentage in a region, with the goal of effectively mitigating earthquake damage. Rural and urban buildings are separately classified in this study. Separate equations are established to calculate the areas of rural and urban buildings. Error analysis revealed a high level of consistency between the building areas determined based on field survey data and rapidly yielded by the models. Within a permissible error range, the calculation models can be used to quickly estimate building areas in a region. On this basis, together with the SP estimates, the proportions of buildings with different SP levels and the distribution pattern of SP in a region can be determined. This method can provide powerful support for obtaining building information for an earthquake-prone region and estimating potential economic losses before an earthquake.

## 2. Study Area and Image Interpretation

**2.1. Study Area.** In terms of the geological structure, Ningxia is situated on the northeastern margin of the Tibetan Plateau, where active faults are densely distributed.

According to historical records, this region has experienced multiple strong earthquakes, including two earthquakes with a magnitude of 8 and above: the magnitude-8 earthquake that occurred in Pingluo, Yinchuan, in 1739 and the magnitude-8.5 earthquake that occurred in Haiyuan in 1920. Modern instrumental records also show that Ningxia is prone to earthquakes. Figure 1 shows the study area.

**2.2. Image Interpretation.** Gaofen-2 imagery is used for analysis in this study. Its high spatial resolution (>1 m) meets the requirement for visual interpretation and allows aboveground structures to be quickly classified based on their SP. Considering its offsets, the geographical information system method is employed to correct the position coordinates in the Gaofen-2 imagery in the ArcGIS platform prior to visual interpretation [20].

The Seismic Ground Motion Parameter Zonation Map of China (GB18306-2015) and the Standard for Classification of Seismic Protection of Building Constructions (GB50223-2008) [21] are used in this study as a basis for determining building SPs. To relatively accurately distinguish building SPs, urban and rural buildings are processed separately during visual interpretation. The outlines of urban buildings are extracted individually based on their image texture. In other words, one polygon corresponds to one building. In contrast, the outlines of rural buildings are extracted based on the outlines of the blocks where they are located. In other words, one polygon can contain one or multiple buildings. Figure 2 illustrates the overall process used to determine building SPs and validate the results based on field survey data. Figure 3 shows separate standard maps of building outline information for urban and rural areas.

The Code for Seismic Design of Buildings (GB50011-2016) stipulates three fortification levels, that is, “no damage under minor earthquake,” “repairable damage under moderate earthquake,” and “no collapse under major earthquake.” The degree of damage to buildings is qualitatively classified in the Classification of Earthquake Damage to Buildings and Special Structures (GB/T 24335-2009) [22]. According to the Seismic Ground Motion Parameter Zonation Map of China (GB18306-2015), Ningxia is mainly located in seismic fortification area VIII. In this study, the buildings in Ningxia are divided into three categories, namely, buildings with the required SP, suspected substandard SP, and substandard SP, according to the seismic standard for seismic fortification area VIII and with reference to the above two specifications.

Visually interpreting images of urban buildings is relatively easy. A building is considered to meet the SP standard if its polygon has a well-defined texture boundary. Buildings whose polygons have an indistinct or dark grey texture boundary are mostly structures consisting of 3–5 storeys and are suspected to be below the SP standard. Buildings lacking the above features and whose polygons are appreciably smaller than those of the buildings in the above two groups are mostly structures in urban villages and are considered to be below the SP standard. Using Baidu street view images

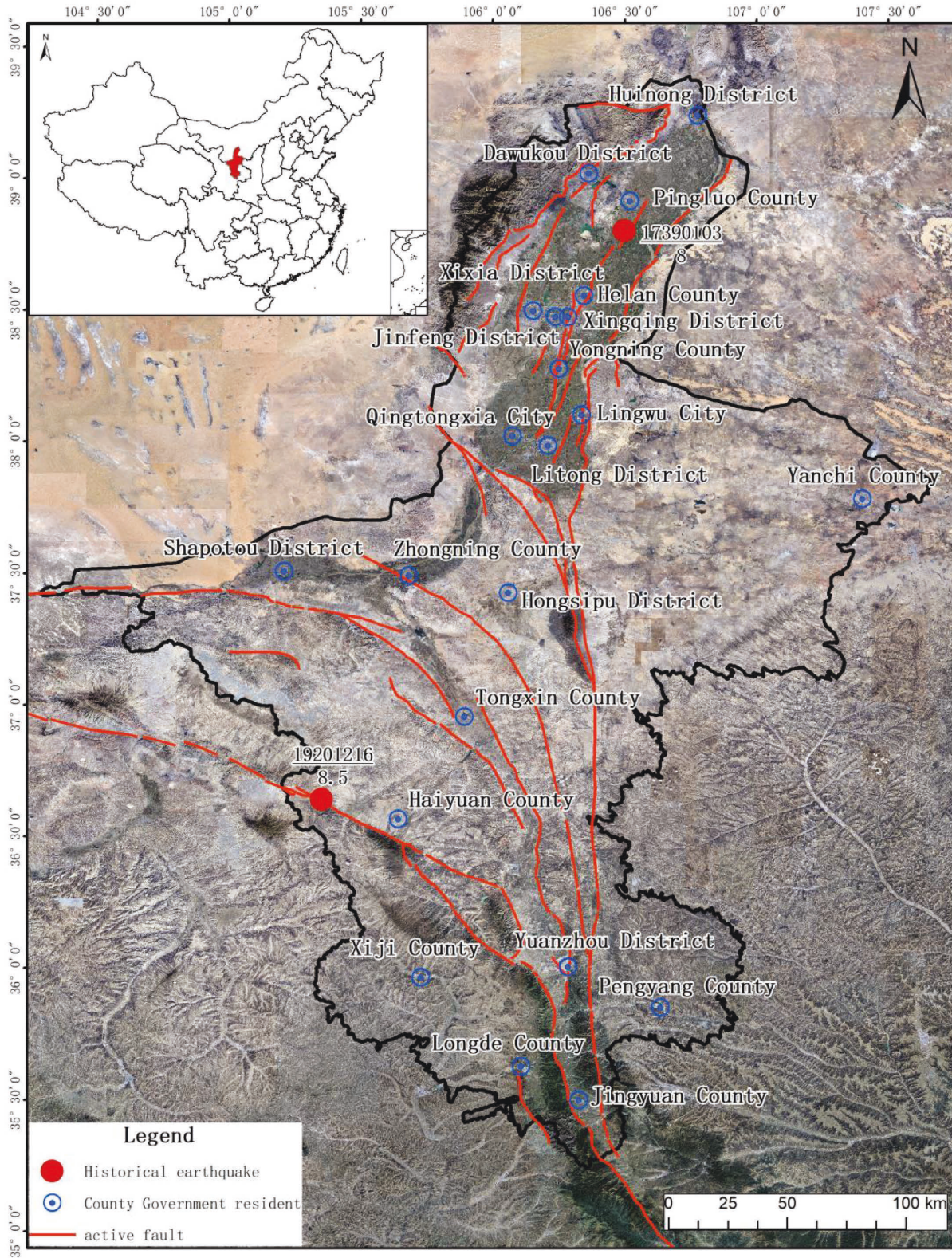


FIGURE 1: Study area.

can help determine the SP of individual buildings that appear to be ambiguous based on the information extracted from the RS images.

Rural and rural-urban fringe (RUF) areas are home to buildings of complex and varied structures and types. Therefore, a uniform standard for determining the SP of

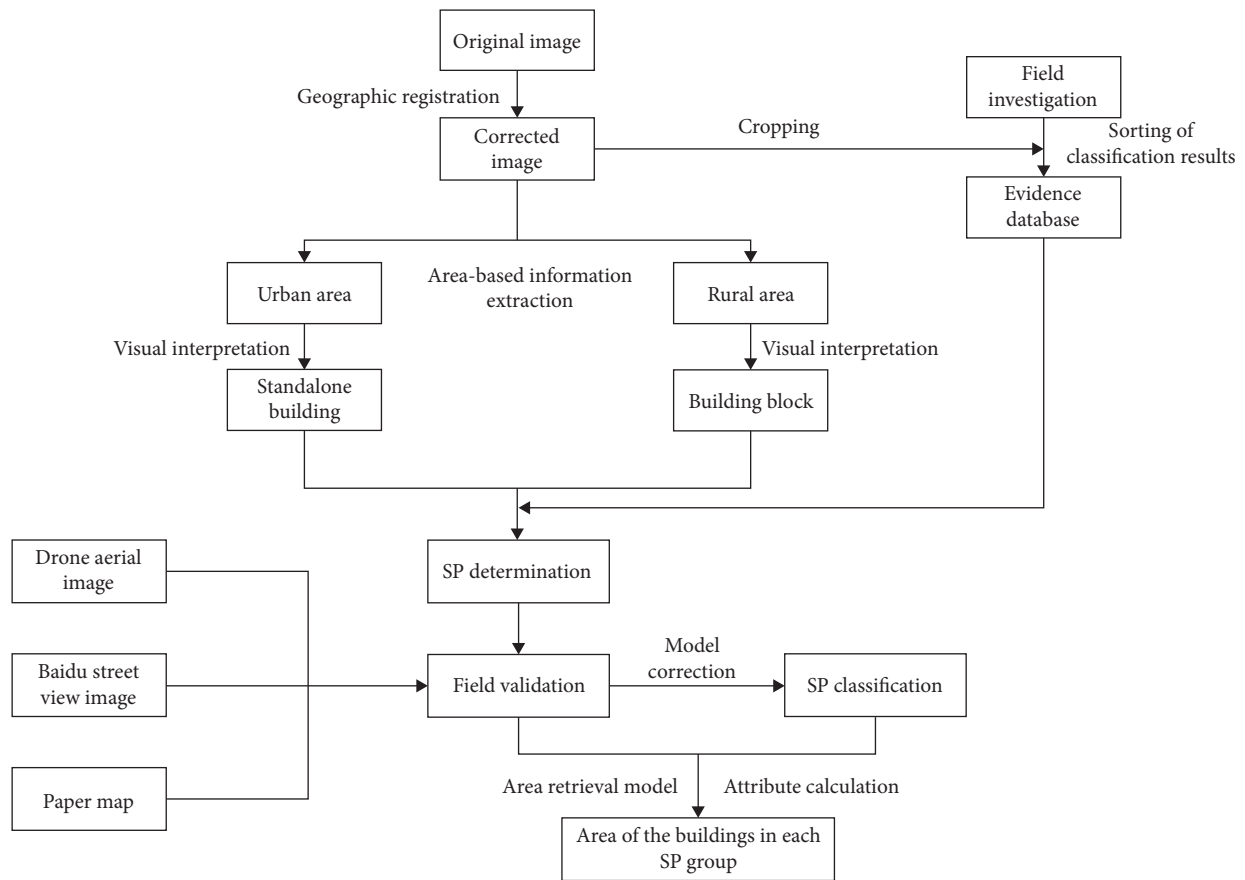


FIGURE 2: Flowchart of the method for visually interpreting the RS imagery and SP correction.



FIGURE 3: Standard maps of extracted building information for (a) an urban area and (b) a rural area.

buildings needs to be established to facilitate laboratory visual interpretation. Prior to visual interpretation, field surveys were conducted to determine the typical features of the buildings in representative areas identified in the RS images. It is difficult to visually interpret RS images for buildings in rural and RUF areas and to extract their information (e.g., geometries and roof and shadow features) from RS images. Considering these factors in conjunction with field sample survey data, buildings in rural and RUF

areas are classified based on their SP into three groups. The classification criteria, as shown in Figure 4, are described as follows:

- (1) Buildings designed and constructed in rural areas by their owners themselves lack a uniform plan and layout and display various texture patterns and colours in the RS images. These buildings are classified as self-constructed (SC) buildings in rural areas. Field surveys



FIGURE 4: Typical buildings in rural and RUF areas.

show that most SC buildings are not seismically fortified and do not meet the SP standard. In the RS images, these buildings feature blurry texture boundaries and are mostly dark grey. During field surveys, extremely few SC buildings were found to possess seismic structures, such as structural columns and ring beams. These buildings do not fully meet the SP standard and are suspected to be below the SP standard. Their texture boundaries appear relatively distinct in the RS images.

- (2) A relatively uniform plan and layout can be observed for the streets within the blocks in the RS images. Buildings showing similar texture patterns and colours in a polygon are uniformly classified as government-subsidised (GS) buildings. These buildings are constructed by the government according to the Standard for Seismic Fortification of Buildings and are therefore considered to meet the SP standard.
- (3) RUF areas are home to alternating seismically fortified and unfortified buildings of various forms. As seen in the RS images, of the buildings in RUF areas,

those neighbouring thoroughfares are mostly multistorey structures, while those distant from thoroughfares are generally densely and irregularly distributed low-rise structures. These buildings are classified as RUF buildings. Field surveys show that the SP standard is met by multistorey RUF buildings adjacent to thoroughfares but not by densely and irregularly distributed low-rise RUF buildings.

Typical buildings were photographed during field surveys. Information obtained from the photographs was subsequently statistically summarised to establish a database on the ArcGIS platform as a standard for determining building SPs in these areas.

### 3. Methods for Calculating Building Areas

From the principles of statistics, a sample is representative of and reflects the population, and population attributes can be estimated and inferred by analysing the sample drawn. Under the condition that the sample sites were evenly



distributed in space and among administrative divisions, this paper proposes a relatively simple formula to calculate building area. The main considered factors in the formula are as follows: the building area can be quickly calculated after visually interpreting the RS imagery, a more accurate building area can be obtained, and others can obtain relatively accurate results using this formula in visual interpretation of RS imagery research. Based on these considerations, this paper proposes two equations to calculate urban, RUF, and rural building areas.

**3.1. Method for Calculating Urban Building Areas.** During visual interpretation, standards of different scales are used to extract building polygons from urban and rural areas. Considering factors such as the structural type, seismic fortification standard, and lateral stiffness of buildings [23, 24], urban buildings are classified into three types: low-rise buildings (i.e., buildings with 1–3 storeys), multistorey buildings (i.e., buildings with 4–6 storeys), and high-rise buildings (i.e., buildings with 7 storeys or more). Each building is treated as a zoning unit for extraction. The building area model is given as follows:

$$M_C = \lambda_i \times M, \quad (i = 1, 2, 3), \quad (1)$$

where  $M_C$  is the building area of an urban building,  $M$  is the polygon area obtained from the RS image, and  $\lambda_1$ ,  $\lambda_2$ , and  $\lambda_3$  are the sample survey coefficients for low-rise, multistorey, and high-rise buildings, respectively. The areas of low-rise, multistorey, and high-rise buildings in urban areas are calculated separately using this equation with the help of the ArcGIS Field Calculator.

To accurately obtain a reasonable sample survey coefficient  $\lambda_i$  that can be used to calculate urban building areas across the study area, field sample surveys were conducted to collect data for low-rise, multistorey, and high-rise buildings. The numbers of storeys determined during the surveys were subsequently fitted to yield the corresponding value of  $\lambda_i$ .

Here, multistorey buildings are used as an example. Multistorey buildings at 88 sites were surveyed to determine their numbers of storeys, which were subsequently fitted to yield  $\lambda_2$  (5.32). Table 1 summarises the polygon areas, actual numbers of storeys, areas determined based on survey data (treated as the actual areas), and estimated areas at the survey sites. The polygon area referred to here is the area of a polygon obtained during visual interpretation, that is, the area of a building interpreted from remote-sensing images. The field-surveyed area was calculated by multiplying the number of storeys obtained in the field survey by the area of the corresponding polygon, and the estimated building area was calculated by multiplying the fitted multistorey building coefficient by the corresponding polygon area. Then, a linear correlation analysis was performed on the actual and estimated building areas. The reliability of the fitting coefficient was examined through correlation analysis. Figure 5 shows the correlation analysis results for the actual and estimated areas of the multistorey buildings at the survey sites. In the figure, the small blue dots represent the linear trendline, and

the large blue dots represent the estimated building areas. An analysis of Figure 5 reveals a correlation coefficient of 0.92 between the areas of the multistorey buildings determined based on survey data and those estimated with  $\lambda_2$ . This finding suggests that building areas estimated with  $\lambda_i$  are strongly correlated with those determined based on the actual numbers of storeys and that  $\lambda_i$  can be used to calculate urban building areas across the study area.

**3.2. Methods for Calculating Areas of Buildings at Rural and RUF Sites.** Most buildings in rural and RUF areas appear to be sheet-like structures in the RS images and are thus difficult to extract as individual polygons. In this study, buildings in rural and RUF areas are extracted based on block outlines. In other words, the outline of one block is extracted as one polygon, the area of which is denoted by  $M$ .

$$M_S = \beta_i \cdot M + \sigma, \quad (2)$$

where  $M_S$  is the building area in a block in a rural or RUF area,  $\beta_i$  is the regression coefficient (i.e., the ratio of the building area in the block determined based on survey data to the block area determined through visual interpretation;  $i = 1, 2$ , and 3 for SC, GS, and RUF buildings, resp.), and  $\sigma$  is the error compensation coefficient for the areas of stand-alone buildings (e.g., the building polygon areas indicated by B in Figure 6). The areas of SC, GS, and RUF buildings are calculated separately using this equation with the help of the ArcGIS Field Calculator. The polygon area here refers to the area obtained by visual interpretation. That is, the area is one block interpreted on the RS image. The definition of the survey point in the RUF area is consistent with the sample point in this area.

Here, the method used to calculate the regression coefficient for uniform GS buildings,  $\beta_2$ , is described.  $\beta_2$  is the average ratio of the GS building areas determined based on field survey data to the corresponding polygon areas, that is, the proportion of the area of a GS building block that is occupied by all the buildings within the block (see Figure 6). To ensure accuracy, the obtained value of  $\beta_2$  is validated based on survey data obtained at 88 sites (see Table 2). Figure 7 shows the results of the statistical error analysis. In the figure, the blue dots indicate the percentages of building area, and the short, vertical lines are error bars, each with a standard deviation of 1. The two horizontal lines above and below the error bars correspond to 40% and 20% of the total building area, respectively. The standard deviation statistical analysis indicates that the  $\beta_2$  value is within a reasonable range. The same method is used to calculate  $\beta_1$  and  $\beta_3$ , and thus the process is not described again.

## 4. Result Analysis

**4.1. Estimated Area Correction.** Normal statistical analysis was conducted to estimate the frequency distribution with a known mean and standard deviation. To verify whether the accuracy of the building areas calculated by equations (1) and (2) met the requirements, another 88 sample sites were selected from 22 districts and counties across the entire

TABLE 1: Numbers of storeys and areas of multistorey buildings in urban areas.

No.	Polygon area (m <sup>2</sup> )	Actual number of storeys	Actual building area (m <sup>2</sup> )	Estimated building area (m <sup>2</sup> )	No.	Polygon area (m <sup>2</sup> )	Actual number of storeys	Actual building area (m <sup>2</sup> )	Estimated building area (m <sup>2</sup> )
1	851.7	6	5110.5	4531.3	45	1243.6	4	4974.3	6615.8
2	1415.8	6	8494.9	7532.1	46	552.9	4	2211.6	2941.5
3	1604.8	6	9628.8	8537.5	47	1038.7	5	5193.6	5526.0
4	1449.5	5	7247.5	7711.3	48	1069.5	6	6417.0	5689.7
5	1471.9	4	5887.5	7830.3	49	1302.3	6	7813.6	6928.1
6	1146.7	5	5733.6	6100.6	50	759.9	6	4559.5	4042.8
7	997.2	6	5983.0	5304.9	51	750.2	4	3000.8	3991.1
8	774.5	5	3872.5	4120.3	52	1475.1	5	7375.4	7847.4
9	618.4	5	3092.0	3289.9	53	1395.9	5	6979.5	7426.2
10	1467.2	6	8803.4	7805.7	54	1009.8	6	6058.9	5372.2
11	1112.0	4	4447.9	5915.8	55	744.9	4	2979.4	3962.6
12	784.2	4	3136.8	4171.9	56	2668.9	5	13344.4	14198.4
13	1431.2	6	8587.0	7613.8	57	917.3	5	4586.6	4880.2
14	797.4	6	4784.4	4242.1	58	1243.4	6	7460.4	6614.9
15	1257.3	6	7543.8	6688.8	59	868.9	6	5213.7	4622.8
16	1025.4	5	5126.8	5454.9	60	517.5	6	3104.7	2752.9
17	1261.5	5	6307.5	6711.2	61	2663.7	5	13318.7	14171.1
18	1061.1	4	4244.5	5645.2	62	1406.2	5	7031.0	7480.9
19	513.5	5	2567.7	2732.1	63	722.5	4	2889.8	3843.5
20	834.2	6	5005.1	4437.8	64	966.2	6	5797.4	5140.3
21	695.8	6	4174.8	3701.6	65	981.9	4	3927.5	5223.6
22	775.5	6	4652.7	4125.4	66	1445.9	6	8675.7	7692.4
23	1012.3	5	5061.7	5385.7	67	1488.3	6	8930.1	7918.0
24	1857.0	5	9285.0	9879.3	68	1219.5	6	7316.9	6487.7
25	1068.5	6	6411.2	5684.6	69	861.7	5	4308.3	4584.0
26	1285.5	4	5142.0	6838.9	70	1051.4	6	6308.5	5593.5
27	947.7	6	5686.3	5041.8	71	1350.6	6	8103.6	7185.2
28	629.5	6	3777.1	3349.0	72	1233.0	4	4932.2	6559.8
29	1022.9	5	5114.4	5441.7	73	1004.5	4	4018.1	5344.0
30	1149.0	6	6894.1	6112.8	74	1033.0	5	5165.2	5495.8
31	1266.0	5	6330.0	6735.1	75	1347.3	6	8084.0	7167.8
32	1032.4	5	5161.8	5492.1	76	727.3	6	4364.0	3869.4
33	1258.8	6	7552.9	6696.9	77	1218.4	4	4873.7	6482.1
34	1254.2	6	7525.1	6672.2	78	1224.9	6	7349.4	6516.5
35	779.4	6	4676.1	4146.2	79	926.9	6	5561.4	4931.1
36	1038.1	4	4152.3	5522.6	80	1019.9	5	5099.5	5425.8
37	616.4	4	2465.7	3279.3	81	1248.8	5	6244.1	6643.8
38	616.9	6	3701.2	3281.8	82	860.7	6	5164.3	4579.1
39	1363.8	5	6819.1	7255.5	83	1038.3	6	6229.5	5523.5
40	1090.8	6	6544.7	5803.0	84	784.1	4	3136.3	4171.3
41	670.8	5	3353.8	3568.4	85	935.0	6	5610.1	4974.3
42	1036.8	6	6220.8	5515.8	86	610.8	6	3664.7	3249.4
43	1258.9	6	7553.6	6697.5	87	1094.1	6	6564.3	5820.4
44	1051.0	6	6305.8	5591.2	88	1910.9	5	9554.5	10166.0

Ningxia area for field surveys to verify the reliability and accuracy of the calculated building areas. The results indicated that the calculated building areas had an accuracy of 90%. The results of normal statistical analysis are shown in Figure 8.

The main influencing factors limiting the accuracy are as follows. First, the accuracy of visual interpretation varies among people. Second, some of the RS images are satellite images captured in the second or third quarter, which makes building boundaries difficult to interpret because of the occlusion of trees, thus resulting in an inaccurate acquisition of polygon boundaries.

*4.2. SP Estimates.* The building SPs in all the CLDs of Ningxia were preliminarily determined by visually interpreting the RS imagery. Subsequently, at least one sample site was surveyed in each village and township in all 22 CLDs of Ningxia. During field surveys, the building SPs at the survey sites were determined based mainly on three factors: (1) the SP data for the survey sites obtained from the local construction authorities, (2) the external appearance and structural features of the buildings (i.e., whether the buildings were equipped with seismic structures such as structural columns and ring beams), and (3) feedback from the occupants with respect to whether seismic measures

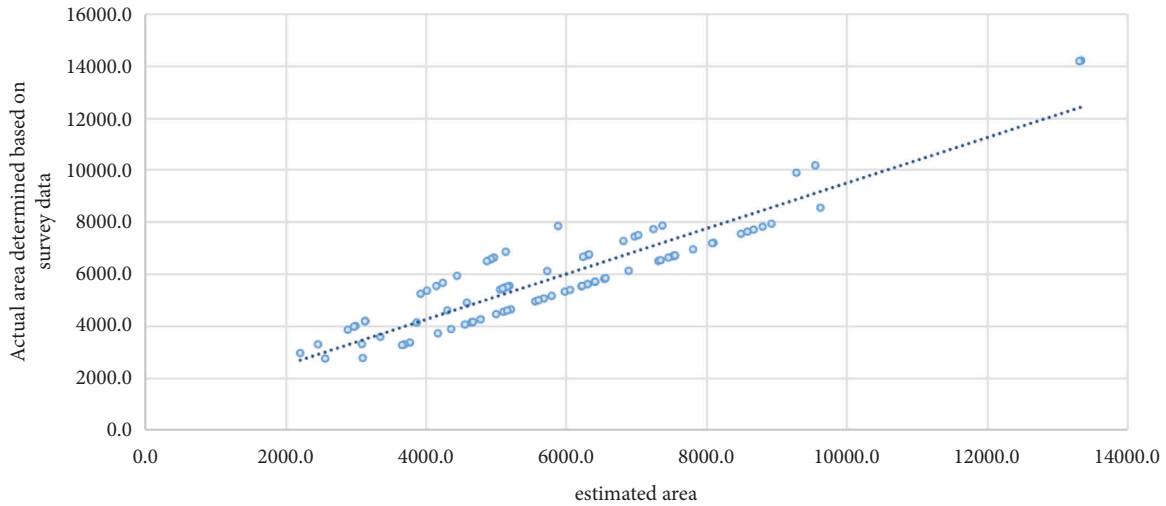


FIGURE 5: Correlation analysis of actual and estimated building areas.

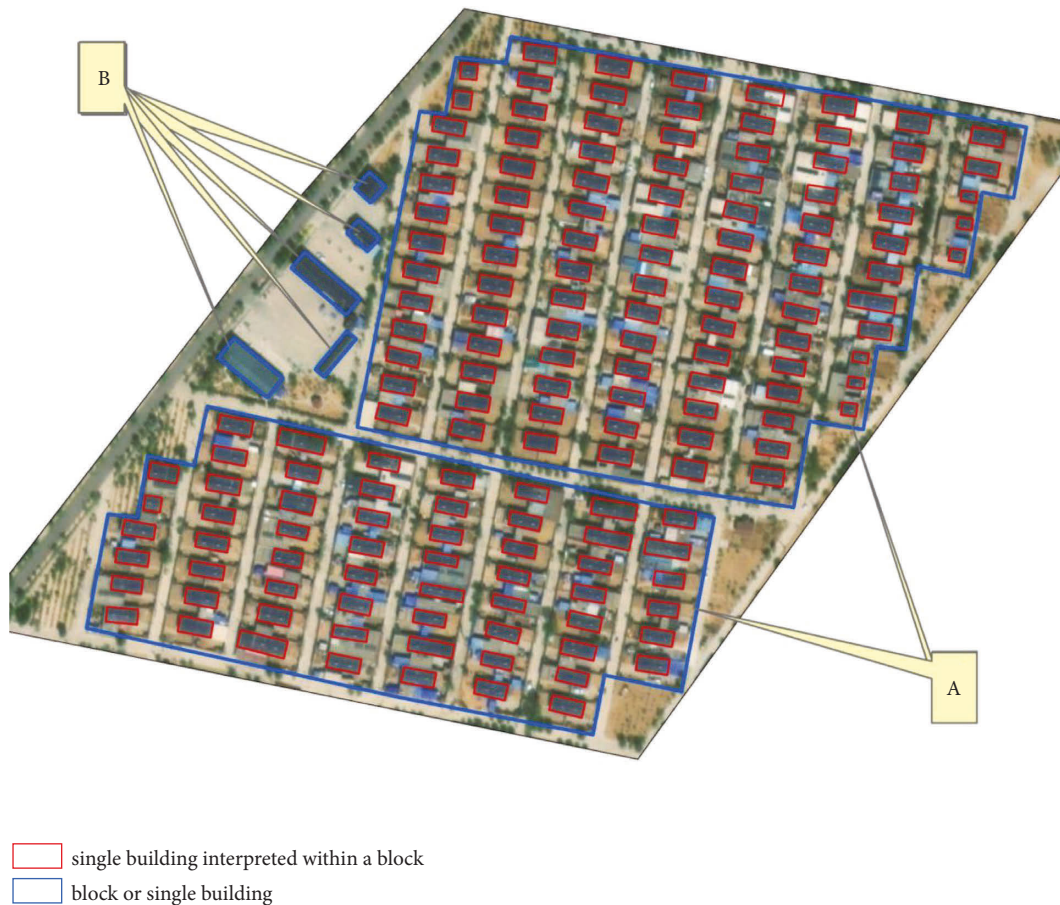


FIGURE 6: Visually interpreted GS building block and standalone building polygons.

were implemented during construction. The error correction of the original SP results was carried out based on the field survey results. The SP accuracy in Table 3 refers to the percentage of the sample sites in which the SP based on visual interpretation and the SP based on field survey data at the sample site are consistent. Here, the sample site is a

zoning unit displayed by a building in the urban area or a block in the rural or RUF areas on a remote-sensing image. The results contain the following information. The SP accuracy is greater than 80% for Yuanzhou District, Xiji County, Delong County, Jingyuan County, Pengyang County, Haiyuan County, Hongsibu District, Tongxin

TABLE 2: Proportions of the areas of GS buildings determined based on field survey data.

No.	Polygon area (m <sup>2</sup> )	Actual building area (m <sup>2</sup> )	Proportion of the building area (%)	No.	Polygon area (m <sup>2</sup> )	Actual building area (m <sup>2</sup> )	Proportion of the building area (%)
1	29603	7844	26.5	45	17196	5346	31
2	38537	13600	35.2	46	5674	2040	36
3	21714	10304	47.6	47	30500	9216	30.3
4	20643	5632	27.2	48	11571	3025	26.1
5	3820	987	25.9	49	17083	6109	35.8
6	7872	2538	32.1	50	11470	3552	31.1
7	2372	905	38.2	51	18869	4508	24
8	7998	2576	32.1	52	33812	10452	30.8
9	2257	846	37.5	53	8395	1168	13.9
10	2047	820	40	54	118826	24750	20.8
11	43994	13776	31.3	55	11587	3380	29.1
12	18170	6960	38.3	56	3805	882	23.1
13	4428	1008	22.8	57	4872	1755	36.1
14	7855	2565	32.6	58	9829	2700	27.6
15	6904	1980	28.6	59	21014	6975	33.2
16	5561	1755	31.5	60	1853	715	38.6
17	13685	4925	35.9	61	106230	34182	32.1
18	5070	1708	33.8	62	12199	3300	27
19	13971	4416	31.7	63	3053	1170	38.4
20	858	354	41.3	64	59944	15860	26.5
21	15366	2808	18.2	65	231045	45770	19.8
22	66359	17157	25.8	66	7012	1854	26.4
23	33167	6270	18.9	67	21612	8228	38.1
24	51630	8580	16.6	68	4299	1096	25.4
25	24665	5278	21.4	69	23105	4255	18.4
26	4147	1331	32.2	70	1093	532	48.5
27	7186	2560	35.6	71	66524	8316	12.5
28	4214	1716	40.6	72	35280	8142	23.1
29	6124	1785	29.2	73	34830	5940	17.1
30	24279	7875	32.5	74	38649	7200	18.6
31	11680	2768	23.8	75	27292	7458	27.3
32	28288	4284	15.2	76	23203	6528	28.1
33	54917	20790	37.8	77	30596	7920	25.9
34	16505	2575	15.5	78	18319	4004	21.9
35	24317	8556	35.2	79	48775	15750	32.3
36	145650	33060	22.7	80	23021	6555	28.5
37	41683	14896	35.6	81	42684	15228	35.8
38	17948	6407	35.8	82	6920	1764	25.5
39	3193	1000	31.2	83	14928	4826	32.4
40	2459	852	34.8	84	19870	8370	42.3
41	39456	11808	30	85	28199	8140	28.9
42	14554	4321	29.7	86	8947	2976	33.2
43	5660	2028	35.9	87	10307	2728	26.5
44	10147	2662	26.2	88	5129	1800	35.2

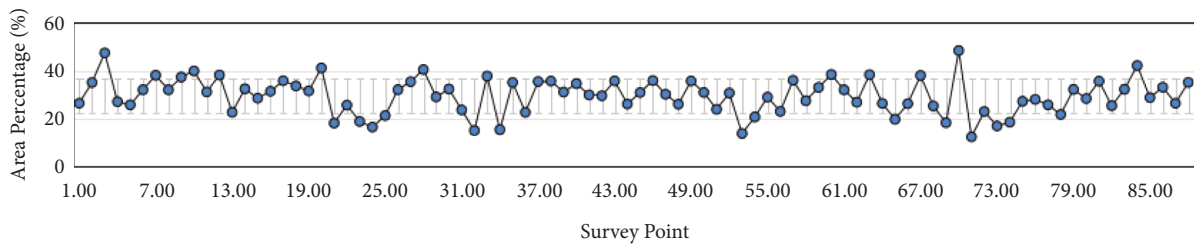


FIGURE 7: Proportions (in percentage) of the building areas at the survey sites to the corresponding polygon areas.

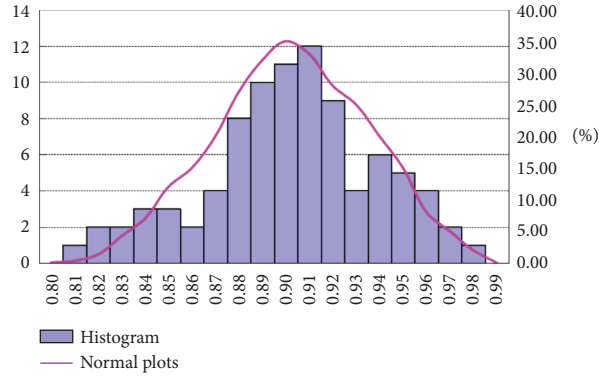


FIGURE 8: Normal distribution of the accuracy of the area estimates.

TABLE 3: Sample verification of building SPs.

No.	Name	Number of sample points	SP accuracy (%)
1	Xingqing District	16	70.7
2	Jinfeng District	7	71.4
3	Xixia District	8	75
4	Helan County	9	67.7
5	Yongning County	13	77
6	Lingwu City	13	84.6
7	Dawukou District	11	72.7
8	Huinong District	13	69.2
9	Pingluo County	26	76.9
10	Litong District	15	80
11	Hongsibu District	10	90
12	Yanchi County	12	75
13	Tongxin County	25	88
14	Qingtongxia City	20	80
15	Yuanzhou District	42	90.5
16	Xiji County	27	85.2
17	Longde County	15	86.7
18	Jingyuan County	10	90
19	Pengyang County	23	82.6
20	Shapotou District	23	74
21	Zhongning County	8	75
22	Haiyuan County	10	80
	Average	16	76

County, Qingtongxia City, Litong District, and Lingwu city (50% of all the CLDs). The SP accuracy is greater than 70% for 20 (91%) of the 22 CLDs. The SP accuracy is considerably higher for the CLDs in southern Ningxia than for Xingqing, Jinfeng, and Xixia Districts and Yongning and Helan Counties under the jurisdiction of Yinchuan City and Pingluo County and Huinong and Dawukou Districts under the jurisdiction of Shizuishan City. Based on the field survey results, this significant difference can be mainly ascribed to the following factors. First, buildings in the CLDs of northern Ningxia are complex and varied. Here, seismically fortified buildings alternate with unfortified buildings. As a result, interpreting the corresponding RS images is difficult and prone to errors. Figure 9 shows the distribution of SP accuracy for the buildings across the study area. Second, the RS images do not have a high spatial resolution; thus, some building SPs are difficult to accurately determine. Third, for

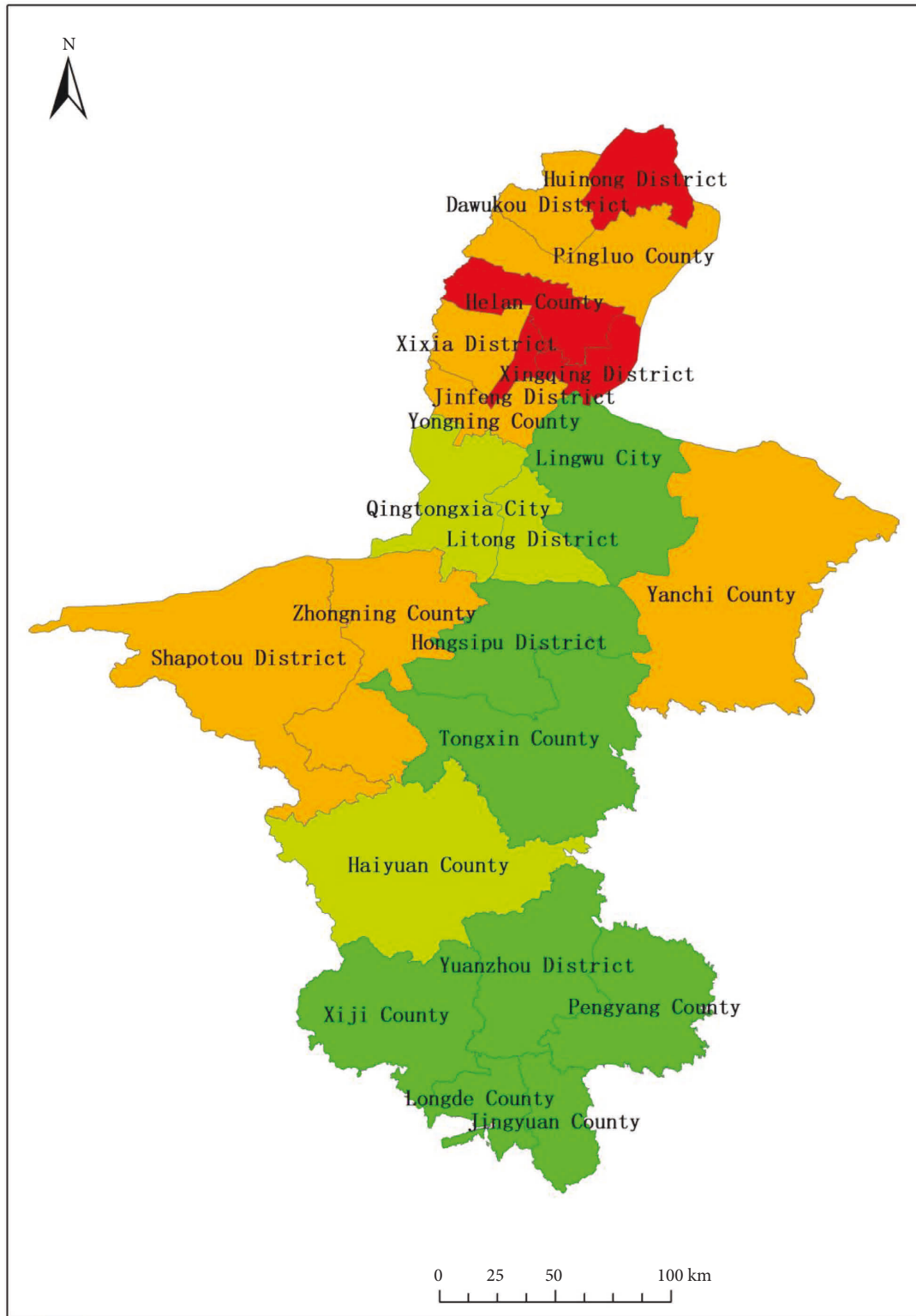
the RUF buildings, using block-based acquisition in SP determination tends to ignore buildings with a certain SP that account for a relatively small proportion within a block.

**4.3. Distribution Pattern of Building SPs.** Based on the area and SP estimates, ArcGIS spatial analysis was used in this study to analyse the correlations between spatial location and SP attributes of buildings throughout the Ningxia region. The basic process of ArcGIS spatial analysis is as follows.

Spatial join analysis is a method that joins attributes from one feature to another based on the spatial relationship. Target features and the joined attributes from the join features are written to the output feature class. We used “many-to-one” to associate the join features with the target features. The join features were buildings, and the target features were CLDs (consisting of districts, county-level cities, and counties). The Match Option of different buildings in one CLD was set to the CLD.

Overall, the proportion of buildings with the required SP in each CLD is higher in northern Ningxia than in southern Ningxia, while the proportion of the buildings with substandard SP in each CLD is appreciably higher in southern Ningxia than in northern Ningxia, as shown in Figure 10. An analysis of the field survey results identifies two factors primarily responsible for the high proportion of buildings with substandard SP in southern Ningxia: (1) The efforts of nearly four decades of resettlement and nearly a decade of targeted poverty alleviation have improved the living environment and rural buildings in southern Ningxia. However, earlier government poverty alleviation efforts were mainly dedicated to substantially ameliorating rural buildings in terms of safety and comfort and failed to consider their SP. Most rural buildings with the required SP have been constructed in the last decade. (2) New and old buildings generally coexist in rural areas, presenting a certain challenge to the determination of building SPs and, therefore, the classification of buildings based on their SP.

Figure 11 shows the overall distribution of the buildings with the required SP, suspected substandard SP, and substandard SP, as obtained using the ArcGIS spatial analysis method; the figure reveals the following features. Buildings with the required SP are predominantly clustered in urban



Accuracy rate of seismic performance

67.0 - 72.0  
72.1 - 77.0

77.1 - 82.0  
82.1 - 90.5

FIGURE 9: Distribution of the SP accuracy for the buildings across the study area.

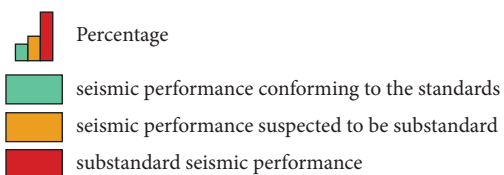
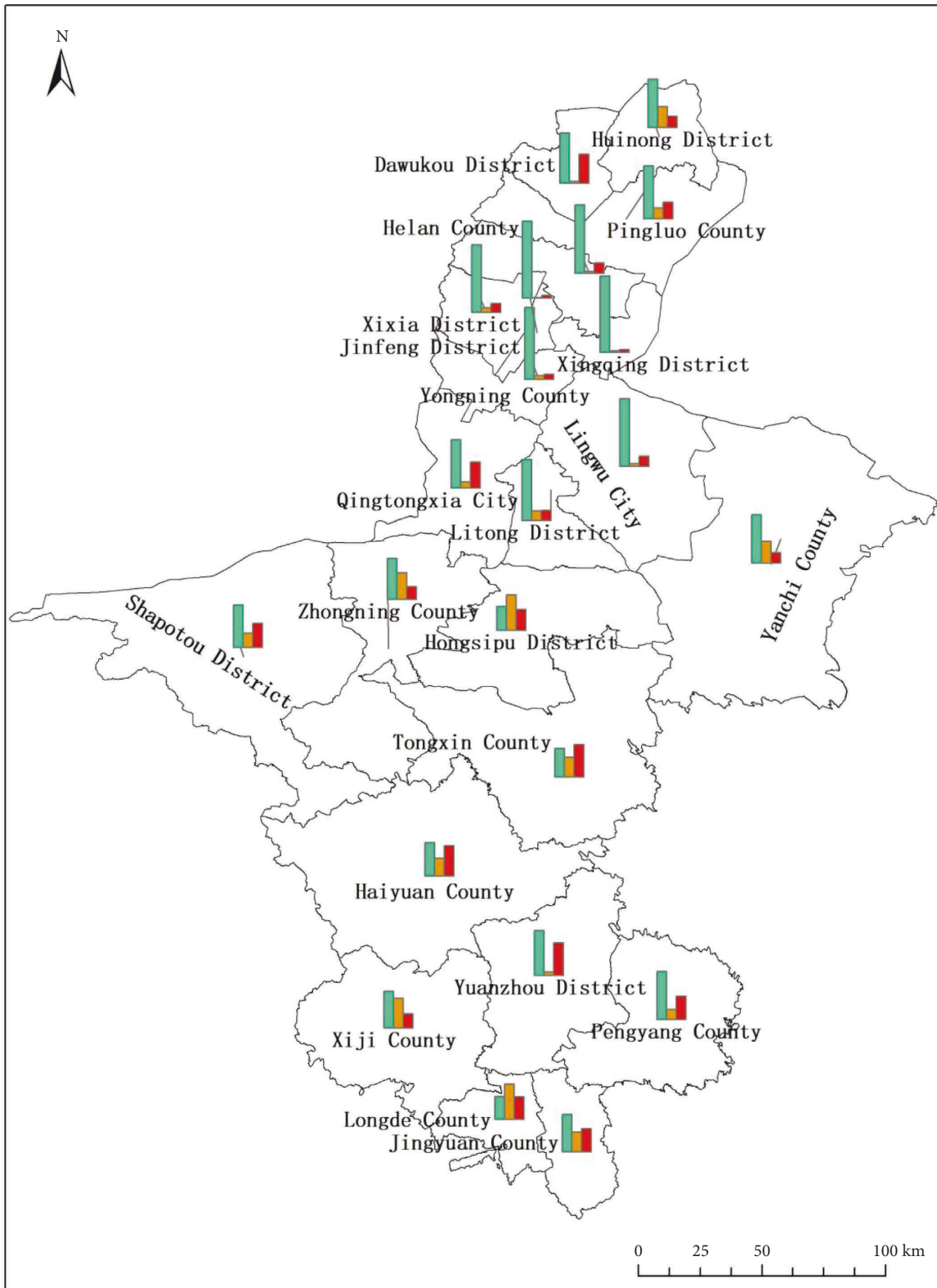
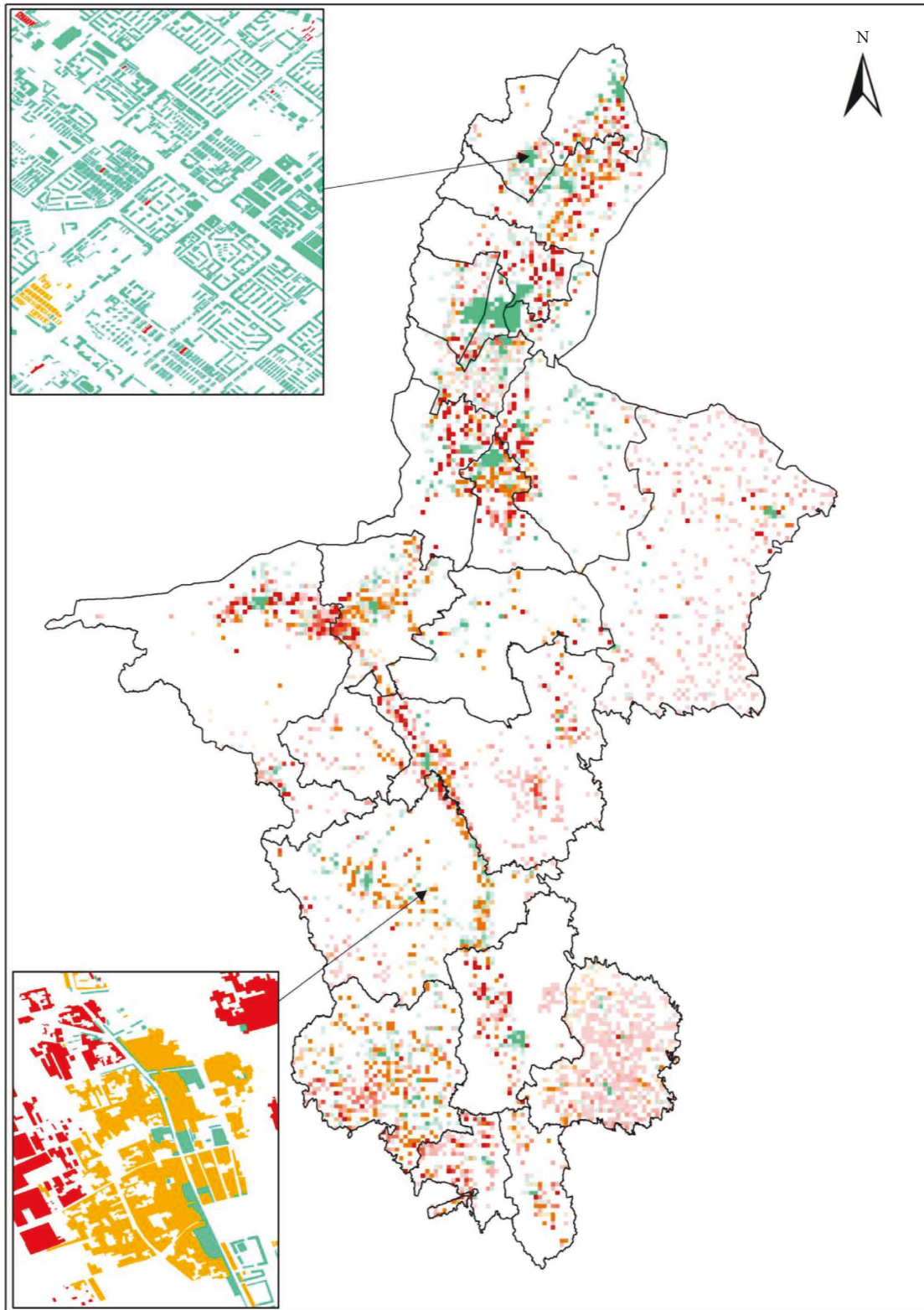


FIGURE 10: Proportions of the buildings in the three SP groups.



- seismic performance conforming to the standards
- seismic performance suspected to be substandard
- seismic performance substandard

FIGURE 11: Distribution of the SP of the buildings among the three SP groups.



areas, with only a few distributed in villages and townships. Buildings with a suspected substandard SP and substandard SP are distributed mainly on the outskirts of urban areas and in the residential areas of villages and townships. This finding conforms to the field survey results. An analysis of the building SPs across Ningxia determined based on visual interpretation reveals generally high levels of SP in urban buildings and relatively low levels of SP in rural buildings.

## 5. Conclusion and Discussion

RS technology can be used to examine the SP and seismic vulnerability of building groups. Assessing the SP of buildings before earthquakes can save time and labour and produce timely data. This study presents a set method for extracting building area attributes and determining the SP of buildings that involves identifying building features in high-resolution RS images and statistical analysis of field sample survey results. The conclusions of this study are summarised as follows:

- (1) Urban buildings are first classified based on the number of storeys into three types: low-rise buildings (i.e., buildings with 1–3 storeys), multistorey buildings (i.e., buildings with 4–6 storeys), and high-rise buildings (i.e., buildings with 7 storeys or more). Each building is treated as a zoning unit for polygon identification. The values of the fitting coefficients  $\lambda_1$ ,  $\lambda_2$ , and  $\lambda_3$  are determined based on sample survey data. Subsequently, the areas of low-rise, multistorey, and high-rise buildings are calculated by directly multiplying their polygon areas by  $\lambda_1$ ,  $\lambda_2$ , and  $\lambda_3$ , respectively. Correlation analysis reveals a strong correlation between the areas estimated using this method and determined based on sample survey data, suggesting that this method can be used to calculate urban building areas.
- (2) For rural and RUF areas, the outline of a block is treated as a zoning unit for visual interpretation. An equation is established to estimate building areas. Building areas estimated with  $\beta_1$  and subsequently checked and corrected based on field sample survey results follow a normal distribution.
- (3) The SP estimates are validated based on data collected at one or more sample sites in each village and township in all 22 CLDs of Ningxia. The results show an SP accuracy greater than 80% for 50% of the CLDs and an SP accuracy greater than 70% for 20 CLDs, suggesting that the SP estimates are satisfactory.
- (4) Based on the SP estimates, the ArcGIS spatial analysis method was used to determine the distribution of the buildings in the three SP groups across Ningxia. The results reveal the following features. Buildings with the required SP are clustered in the urban areas of each CLD, with a few distributed at the seats of the village and township governments. Buildings with a suspected substandard SP are distributed predominately in RUF areas and at the

seats of the village and township governments. Buildings with a substandard SP are clustered in urban villages and RUF and rural areas. The field survey results lend concrete credence to the correctness and reliability of this analysis.

To summarise, the methods for determining building SP and calculating building area proposed in this study provide new ideas and approaches to solving the problem of identifying building SPs on a large scale. Ningxia is an earthquake-prone region that has experienced numerous destructive earthquakes, all of which caused many casualties and much damage. The available findings of seismic activity tectonic studies indicate that the region faces a high seismic risk. The results of this study play a guiding role in the seismic strengthening of buildings in the region by screening buildings with substandard SP.

In addition, despite the extensive research on applying RS technology in a postearthquake disaster assessment, few studies have applied RS images to evaluate preearthquake building SP on a large scale. This study has the advantages of high output efficiency, low input cost, and the ability to carry out a large-scale evaluation of building SPs. The research findings enrich the applied research on RS technology in the prevention and control of preearthquake risks and provide new ideas and new means for evaluating building SPs.

RS images are the basis for this analysis. To produce reliable results, RS images obtained during the same period that have sufficiently high resolution and are representative of the current situation should be used for the same region. The ages of buildings in a region can also be approximated based on their polygon features, positions, and spatial combinations in high-resolution RS images in conjunction with the regional characteristics to improve the accuracy of SP estimates. An overlay of the temporal and spatial distribution patterns of the population and buildings in a region can be used to quickly assess the impact of earthquakes of different magnitudes, such as potential economic losses and the number and distribution of casualties. All these areas warrant in-depth discussion and investigation.

## Data Availability

The data of the remote-sensing images used in this study are from GF-2 satellite.

## Conflicts of Interest

The authors declare that they have no conflicts of interest.

## Acknowledgments


This study was supported by the (1) National key R&D Program of China (no. 2017YFB0504104) and (2) the First National Survey on Natural Disaster Risk (the Project on Seismic Risk Investigation and Elimination of Major Hidden Dangers of Ningxia).

## References

- [1] L. L. Xie and J. F. Zhang, "Application of satellite remote sensing technology in earthquake disaster reduction," *Journal of Natural Disasters*, vol. 9, no. 4, pp. 1–8, 2000.
- [2] H. Wu, Z. P. Cheng, W. Z. Shi, Z. L. Miao, and C. C. Xu, "An object-based image analysis for building seismic vulnerability assessment using high-resolution remote sensing imagery," *Natural Hazards*, vol. 71, no. 1, pp. 151–174, 2014.
- [3] P. Gueguen, C. Michel, and L. LeCorre, "A simplified approach for vulnerability assessment in moderate-to-low seismic hazard regions: application to Grenoble (France)," *Bulletin of Earthquake Engineering*, vol. 5, no. 3, pp. 467–490, 2007.
- [4] M. Mueller, K. Segl, U. Heiden, and H. Kaufmann, "Potential of high-resolution satellite data in the context of vulnerability of buildings," *Natural Hazards*, vol. 38, no. 1–2, pp. 247–258, 2006.
- [5] H. S. B. Duzgun, M. S. Yucemen, H. S. Kalaycioglu et al., "An integrated earthquake vulnerability assessment framework for urban areas," *Natural Hazards*, vol. 59, no. 2, pp. 917–947, 2011.
- [6] S. Valero, J. Chanussot, and P. Gueguen, "Classification of basic roof types based on VHR optical data and digital elevation model," in *Proceedings of the IEEE International Geoscience and Remote Sensing Symposium*, Boston, MA, USA, July 2008.
- [7] H. Wu, L. Zhou, X. Chi, Y. Li, and Y. R. Sun, "Quantifying and analyzing neighborhood configuration characteristics to cellular automata for land use simulation considering data source error," *Earth Science Informatics*, vol. 5, no. 2, pp. 77–86, 2012.
- [8] H. Wu, Y. Sun, W. Shi, X. Chen, and D. Fu, "Examining the satellite-detected urban land use spatial patterns using multidimensional fractal dimension indices," *Remote Sensing*, vol. 5, no. 10, pp. 5152–5172, 2013.
- [9] C. Gei and H. Taubenbock, "Remote sensing contributing to assess earthquake risk: from a literature review towards a roadmap," *Natural Hazards*, vol. 68, no. 1, pp. 7–48, 2013.
- [10] M. Pittore and M. Wieland, "Toward a rapid probabilistic seismic vulnerability assessment using satellite and ground-based remote sensing," *Natural Hazards*, vol. 68, no. 1, pp. 115–145, 2013.
- [11] D. Ehrlich, T. Kemper, X. Blaes, and P. Soille, "Extracting building stock information from optical satellite imagery for mapping earthquake exposure and its vulnerability," *Natural Hazards*, vol. 68, no. 1, pp. 79–95, 2013.
- [12] Y. W. Zhao, C. Y. Hu, H. L. Shen, D. F. Ma, X. Li, and Y. G. Huang, "A hierarchical organization approach of multi-dimensional remote sensing data for lightweight Web Map Services," *Earth Science Informatics*, vol. 5, no. 1, pp. 61–75, 2012.
- [13] X. Q. Wang, A. X. Dou, and L. Wang, "RS-based assessment of seismic intensity of the 2013 Lushan, Sichuan, China MS7.0 earthquake," *Chinese Journal of Geophysics*, vol. 48, no. 1, pp. 163–171, 2015.
- [14] X. Fu, Q. Zhu, C. Liu et al., "Estimation of landslides and road capacity after August 8, 2017, MS7.0 Jiuzhaigou earthquake using high-resolution remote sensing images," *Advances in Civil Engineering*, vol. 2020, pp. 1–11, Article ID 8828385, 2020.
- [15] J. X. Guo, X. Y. Zhang, and J. Z. Ji, "A preliminary study on the method of seismic intensity assessment based on residential building data and high resolution remote sensing images," *Seismology and Geology*, vol. 42, no. 4, pp. 968–980, 2020.
- [16] L. Wang, X. Q. Wang, and X. Ding, "Study on loss assessment of construction earthquake damage based on remote sensing and GIS," *Earthquake*, vol. 27, no. 4, pp. 77–83, 2007.
- [17] F. J. Zhao, S. Cai, and X. Chen, "Application of rapid seismic damage assessment based on remote sensing to Wenchuan earthquake," *Journal of Natural Disasters*, vol. 19, no. 1, pp. 1–7, 2010.
- [18] "State Administration for Market Regulation & Standardization Administration of China," in *Seismic Ground Motion Parameters Zonation Map of China: GB18306-2015*, pp. 229–230, Standards Press of China, Beijing, 2015.
- [19] *Ministry of Housing and Urban-Rural Development of the People's Republic of China & State Administration for Market Regulation, Code for Seismic Design of Building: GB50011-2010 (2016 Edition)*, vol. 6, no. 214, pp. 1–3, China Construction Industry Press, Beijing, 2010, in Chinese.
- [20] C. Qiao, Y. Ding, X. Yongsun, Y. Yao, and H. Wang, "Image registration method based on geo-location information and precision analysis," *Acta Optica Sinica*, vol. 37, no. 8, Article ID 08280, 2017.
- [21] *Ministry of Housing and Urban-Rural Development of the People's Republic of China & State Administration for Market Regulation, Standard for Classification of Seismic Protection of Building Constructions: GB50223-2008*, pp. 1–2, China Construction Industry Press, Beijing, China, 2008, in Chinese.
- [22] "State Administration for Market Regulation & Standardization Administration of China," *The Classification of Earthquake Damage to Buildings and Special Structures: GB/T 24335-2009*, pp. 1–12, Standards Press of China, Beijing, China, 2009, in Chinese.
- [23] J. F. Wang, *Research and Application of Extracting Building Anti-seismic Factors Based on Remote Sensing Technology*, Institute of Engineering Mechanics, CEA, 2021.
- [24] S. H. Yu, Q. Y. Lei, and Y. Wang, "Study on high-precision static population spatial distribution in Xixia district, Yinchuan," *Technology for Earthquake Disaster Prevention*, vol. 15, no. 4, pp. 757–766, 2020.

## Research Article

# Effects of Glacier and Geomorphology on the Mechanism Difference of Glacier-Related Debris Flow on the South and North Banks of Parlung Zangbo River, Southeastern Tibetan Plateau

Jiajia Zhang <sup>1,2,3</sup>, Jiankang Liu <sup>4</sup>, Yuanling Li,<sup>1,3</sup> Junchao Wang,<sup>1,3</sup>  
Long Chen <sup>1,3</sup> and Bo Gao<sup>1,3</sup>

<sup>1</sup>Institute of Exploration Technology, Chinese Academy of Geological Sciences, Chengdu 611734, China

<sup>2</sup>School of Earth Science, Chengdu University of Technology, Chengdu 610059, China

<sup>3</sup>Technology Innovation Center for Risk Prevention and Mitigation of Geohazard, Ministry of Natural Resources, Chengdu 611734, China

<sup>4</sup>School of Emergency Science, Xihua University, Chengdu 610039, China

Correspondence should be addressed to Jiajia Zhang; jimjia2008@163.com

Received 16 July 2022; Revised 1 September 2022; Accepted 9 September 2022; Published 30 September 2022

Academic Editor: Fadzli Mohamed Nazri

Copyright © 2022 Jiajia Zhang et al. This is an open access article distributed under the Creative Commons Attribution License, which permits unrestricted use, distribution, and reproduction in any medium, provided the original work is properly cited.

Alpine glaciers are vulnerable to climate changes, and their recession due to warming has already induced a large number of geohazards closely related to the glacial motion, such as debris flow. Strong coupling of the geology, geomorphology, climate, and glacial action controls the type, size, development, and frequency of debris flow along the Parlung Zangbo River, Southeastern (SE) Tibetan Plateau. Field investigation in recent years indicates that the north bank is prone to much more frequenter debris flows than the south bank. The sharp contrast between the two river banks is due to the different formation conditions of debris flows, especially glaciers and geomorphology. The present paper examines the differences in the glacier and geomorphology conditions for glacier-related debris flows to occur, through a combination of field investigation, interviews with local residents, and geomorphological parameter, and glacier distribution analysis in the ArcGIS platform. The result indicates that, compared to the south bank of the Parlung River, the north bank has more favorable conditions in the glacier and geomorphology south, which is more conducive to the occurrence of debris flow. In conclusion, three kinds of mechanisms due to different formation conditions, especially glacier and geomorphology, are analyzed. The glacier-related debris flows on the south and north banks occur through different mechanisms due to different formation conditions. The debris flows on the north bank primarily occur in modes I and III, while the south bank is dominated by modes II and III debris flows. Based on the result, effective measures are proposed for mitigating damage to roads and railways within this area.

## 1. Introduction

Glacier-related debris flow is a natural geological phenomenon closely related to the glacial motion, usually triggered by glacial meltwater or intense rainfall. Large glacier-related debris flows could also be caused by icefalls, avalanches, or failure of dams across gullies [1–6]. Glacier-related debris flows are sudden, violent, and difficult to forecast, and tend to travel long distances at high speed. This kind of geohazard, which typically occurs in alpine regions, can cause severe damage to villages, towns,

factories, mines, roads, and railways along gullies or at their mouths and thereby terrible loss of life and property [1, 7–10].

Running across the Tibetan Plateau, the Parlung Zangbo River (hereafter “Parlung River”) is among the world’s rivers with the highest elevation drops and greatest erosive forces. Due to this as well as the frequent earthquakes and abundant precipitation there, this river is located in one of the regions subjected to the largest-scale, most violent, and most hazardous debris flows in the world [11–13]. The Parlung River is home to the largest temperate glaciers in China [14, 15].

The river basin has undergone active endogenic and exogenic geological processes and has an extremely complex tectonic setting and strong neotectonic activity [16]. This, combined with the alpine-gorge terrain, high precipitation, and modern glacial activity, contributes to landslides, debris flow, and other major geohazards, among which glacial debris flow is the most destructive [13, 16, 17].

Many large debris flows have taken place along the Parlung River throughout history. The Sichuan–Tibet Highway, a section of China National Highway 318 (G318) on the north bank of the Parlung River, has been blocked by many debris flows since it was built in the 1950s. For this reason, researchers have conducted a systematic regional survey. Glacier-related debris flows in this area were intensively studied during the comprehensive scientific investigation of the Tibetan Plateau in the 1970s [16, 18]. Recent studies have looked at deglaciation resulting from global warming in detail. Existing research has provided plenty of valuable data and insights into the characteristics of geohazards along the Sichuan–Tibet Highway and the conditions and mechanisms for their occurrence and also proposed preventive measures [17, 19, 20].

Large glacier-related debris flows are considered a serious obstacle to regional economic development and a threat to major construction projects, such as the Sichuan–Tibet Railway (from Chengdu to Lhasa, Figure 1), which is planned to span the Parlung River region. In order to ensure normal traffic along the Sichuan–Tibet Highway and the successful implementation of China’s Western Development Program, there is currently an urgent need to address glacier-related debris flows and ensuing environmental problems in the study area in glacier cover and geomorphological settings.

The present paper examines the differences in the Glacier and geomorphology conditions for glacier-related debris flows to occur between the south and north banks of the Parlung River, analyzes the primary mechanisms due to different formation conditions, through a combination of field investigation, and interviews with local residents, geomorphology parameters analysis and glacier distribution analysis in ArcGIS platform. Based on the result, effective measures are proposed for mitigating damages to roads and railways in the study area.

Geohazard history and size scale are from field investigation, interviews with local residents, and previous research. Geomorphology parameters like catchment morphological index, HI which are extracted from ArcGIS software, and high-resolution DEM which is from unmanned aerial vehicle mapping, describe the feature of gullies on both banks. Glacier data from the Second Glacier Inventory Dataset of China [15] are used to analyze the glacier distribution in every gully in GIS.

## 2. Materials and Methods

**2.1. Geological Conditions, Climate, and Precipitation.** The Parlung River is located in the northeastern part of the Eastern Himalayan Syntaxis, at the eastern end of the

Gangdise–Nyainqentangla fault-fold belt. The area is mainly composed of gneiss of the Nyainqentanglha group and the Gangdise granite and metamorphic Paleozoic rocks (Figure 1; [21, 23–25]). Neotectonics is characterized by fast regional crustal uplift with multiple fault activities. The Tongmai–Zhongkxing fault (TZF) and the Tongmai–Jingzhou (TJF) are two important active faults with an average dextral strike-slip rate of 4 mm/a (Figure 1; [26, 27]). The syntaxis region is highly seismic with 100 earthquakes of M 5.0 or greater from 1950 to 2018, including the Ms 8.6 Assam–Tibet earthquake in 1950 [28].

Located in the southeastern Tibetan Plateau, the Parlung River is more sensitive to climate change than any other parts of Western China. It has a subtropical alpine climate affected by the Indian monsoon. The Indian monsoon carries moisture to the Tibetan Plateau, primarily along the valley of the Yarlung Zangbo River (hereafter “Yarlung River”) west of the Parlung River and the Dandong and Chayu Rivers to the south, which all flow southward (Figure 1). This leads to high precipitation on the plateau. For example, the average annual precipitation is as high as 1100–1400 mm/a in Tongmai and Bomi (Figure 1). Due to the humid air and high elevations, the Parlung River has the largest expanses of temperate glaciers in China. A total of 1320 modern temperate glaciers are distributed in the Kangri Karpo Mountains on the river’s south bank, covering an area of 2655 km<sup>2</sup> [29–31]. The high precipitation and temperature attributed to the warm moist air from the Bay of Bengal, plus global warming, keep the surface temperatures of the temperate glaciers in this area at around 0°C. Therefore, the glaciers undergo faster ablation than an accumulation of ice and move actively. As a result, deglaciation occurs extensively and provides a lot of materials and water needed for the formation of debris flows.

**2.2. Geomorphology.** The Parlung River extends to the northeast of the Eastern Himalayan Syntaxis. It is characterized by alpine gorges and deep-incised river valleys with extremely high erosion rates of >5 mm/a [24], and its elevation tends to decrease from east to west. The river flows through wide valleys in its upper reaches and through narrow gorges in its lower reaches. It is bounded to the north by the southeastern branch of the Nyainqentangla Mountains and to the south by the Kangri Karpo Mountains (Figure 2). The extensive development of glaciers and intense tectonic processes has created a wide variety of geomorphic features, such as glacial landforms, alpine gorges, and fluvial depositional landforms (Figure 2).

In the paper, Ke and HI parameters are used to describe the geomorphology features of each gully on the two banks of the Parlung River, Ke is the plane shape index of the catchment, and HI is the hypsometric integral. The parameters are calculated in ArcGIS software based on the digital elevation model (DEM), whose resolution is 8 m. The larger the Ke value is, the closer the plane shape of the catchment is to the circle, and the better the catchment capacity is [32]. Ke can be obtained by using equation (1) [33].

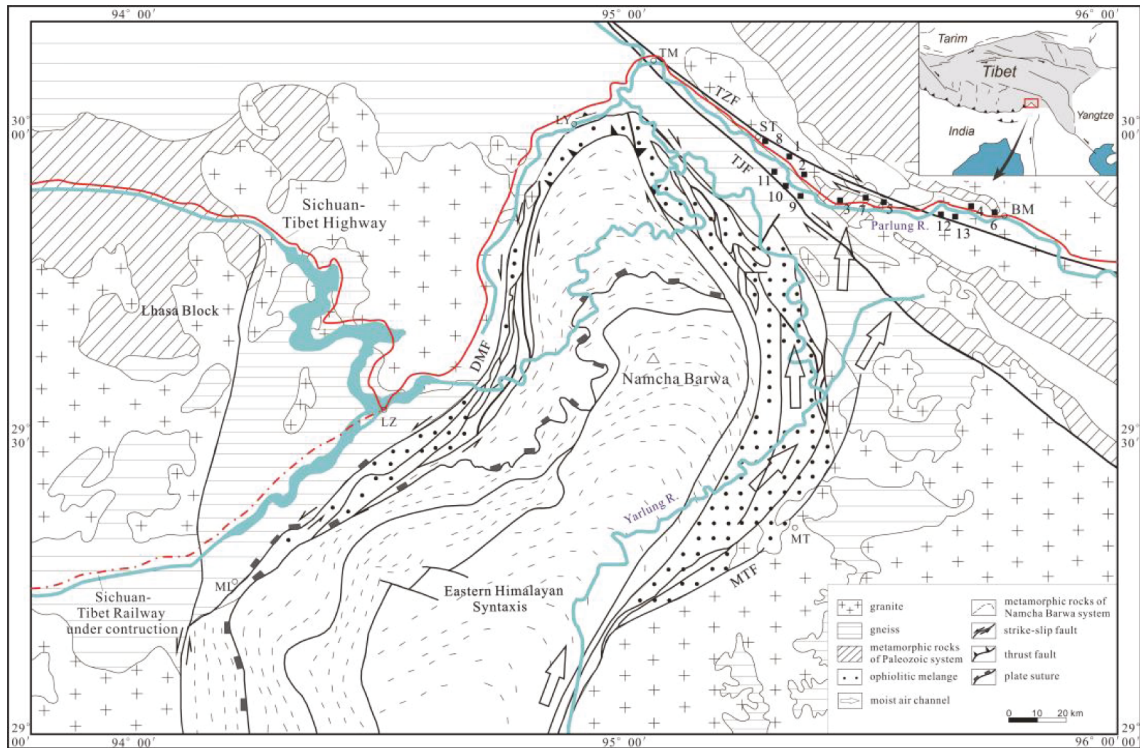


FIGURE 1: Geological sketch map of the eastern Himalayan syntaxis (after [21, 22]); (Abbrs.: towns, BM-Bomi, ST-Suotong, TM-Tongmai, LY-Layue, LZ-Linzi, ML-Milin, MT-Motuo. Faults, TZF-Tongmai-Zhongkang fault; TJF-Tongmai-Jinzhula fault; DMF-Dongjiu-Milin fault; MTF-Motuo fault. Numbers: 1-bitong debris flow; 2-dada rock avalanche-debris flow; 3-jiaolong debris flow; 4-cangguo debris flow; 5-zhataduo debris flow; 6-naha debris flow; 7-guxiang rock avalanche-debris flow; 8-suotong debris flow; 9-qiuzhu debris flow; 10-chidan debris flow; 11-songrao debris flow; 12-michong debris flow; 13-danka debris flow).

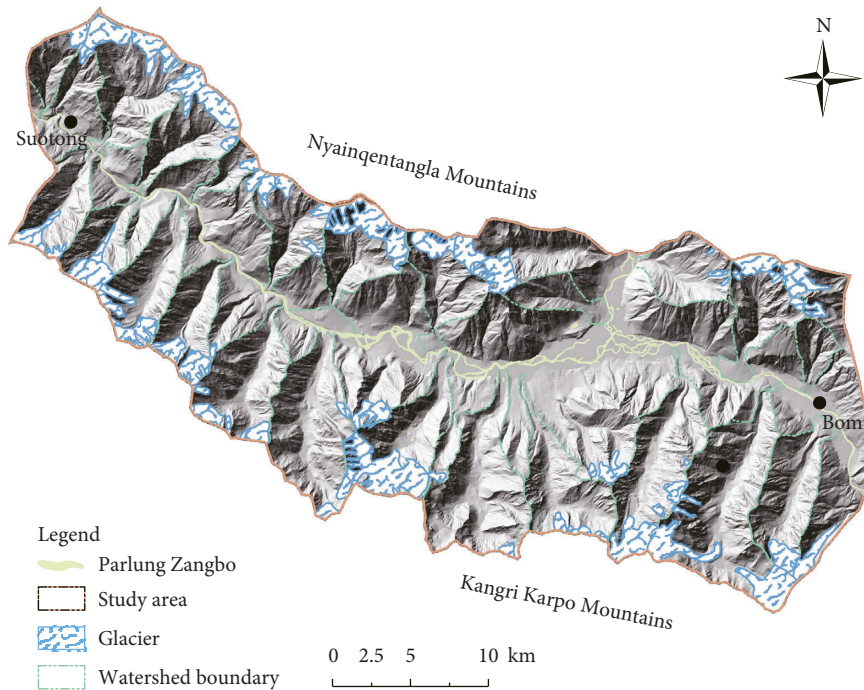


FIGURE 2: Glacier distribution and overall form of gullies along two banks between Bomi and Suotong in Figure 1 (glacier data are from [15]).

$$Ke = \frac{W}{L}. \quad (1)$$

where  $W$  is the largest width of the catchment and  $L$  is the length of the valley.

HI is widely used to quantitatively determine the evolution stage of landforms. The smaller the value is, the more mature the landform is, and the higher the erosion degree is. HI can be obtained by equation (2) [34].

$$E = \frac{H_{\text{mean}} - H_{\text{min}}}{H_{\text{max}} - H_{\text{min}}} = HI. \quad (2)$$

$H_{\text{mean}}$ ,  $H_{\text{max}}$ , and  $H_{\text{min}}$  are mean value, maximum value, and minimum value of elevation in one catchment.

**2.3. Geohazard History.** Strong coupling of the above geology, climate, geomorphology, and glacial actions control the type, size, development, and frequency of debris flows in the Parlung River region. Since the 1950s, the study area has been frequently hit by debris flows of different sizes, resulting in huge loss of life and properties (e.g. 1–13 in Figure 1; [16]) and has a tendency for concentrated outbreaks (Figure 3). In particular, some debris flows were extremely disastrous, such as that occurring in the Gu Xiang area on September 29, 1953 [14].

According to the size classification, which is based on the total volume, peak discharge, and flooded area in the field, the size classes of the debris flows are given in Table 1, coinciding with the debris flow frequency based on interviews with locals and previous studies. The result shows that in the region between Bomi and Suotong (Figure 2), the south and north banks of the Parlung River differ greatly in terms of the occurrence of debris flows. Compared to the north bank, the south bank shows much smaller sizes and a lower frequency of debris flows (Table 1).

### 3. Analysis of the Glacier and Geomorphology Conditions of Debris Flow

Due to its unique geographic location and climate, debris flows along the Parlung River are closely associated with moisture distribution and glacial movement. Zheng et al., [35] found that they are a direct consequence of glacier's recession.

**3.1. Comparison of Hydrology and Glacier Distribution between the Two River Banks.** The data from field investigation and the Second Glacier Inventory Dataset of China [15] suggest significant differences in glacier distribution between the north and south banks of the Parlung River. In terms of the glacier type, valley glaciers are distributed only along the south bank, while the north bank is covered primarily by cirque glaciers and hanging glaciers. The snow line is generally higher in the east than in the west (Table 2).

In the region between Bomi and Suotong, the north bank of the river has 28 glaciers, which account for 32.56% of the region's total number of glaciers, 34.56% of glacier coverage, and 35.62% of ice reserves. The south bank has 58 glaciers,

which make up 67.44% of the region's total number of glaciers, 65.44% of glacier coverage, and 64.39% of ice reserves (Table 2). It is clear that the south bank has more glaciers than the north bank.

It is clear that glaciers are more developed along the south bank of the Parlung River than along its north bank. The north bank shows a snow line higher than that along the south bank and has no valley glacier, indicating that snow and ice along the north bank are more lacking. Numerous large glaciers have formed on the Kangri Karpo Mountains because the mountains just stand in the way of the warm moist air brought by the southwest monsoon blowing from the great bend of the Yarlung River (Figure 1) and thus become the wettest part of the Tibetan Plateau. After the moist air climbs over the Kangri Karpo Mountains and passes the Parlung River, it decreases in moisture content and thus supplies less moisture to the river's north bank (the Nyainqentangla Mountains). Therefore, the north bank is dominated by cirques and hanging glaciers.

Moreover, glaciers along the south bank (ubac) melt at slow rates as they have lower surface temperatures due to low solar irradiation received. After a certain amount of snow has accumulated on a glacier, the glacier tends to move down the valley under gravity or pressure. This contributes to the higher probability of the formation of valley glaciers along this bank. In contrast, glaciers along the north bank (adret) show higher surface temperatures due to greater solar irradiation and thus melt faster. For this reason, glaciers are unlikely to fill valleys, and the dominant glacier types are cirque glaciers and hanging glaciers. Due to their differences in moisture supply and solar insolation, the north bank has a snow line higher than that of the south bank. The more active glacial motions and faster rate of melting along the north bank are regarded as preconditions for the formation of glacial debris flow. Glacier melting provides enough water and glacier transforms into solid matter in the glacial debris flow.

**3.2. Differences in Geomorphology between North and South Banks.** Ke and HI values of every valley are obtained to analyze the difference of geomorphology between north and south banks. Figure 4 just shows that Ke and HI values of valleys along the north bank are both larger than valleys along the south bank, especially the Ke index, which means closer the plane shape of catchment is to the circle, and higher the erosion degree is.

Therefore, under the effect of long-term structural erosion and glacier erosion, valleys along the two banks of Parlung Zangbo reflect sharply different geomorphological features (Figure 4), see Table S1 in the Supplementary Material for comprehensive analysis. As shown in Figure 5, a generalized model is used to describe the geomorphological differences of the valleys between the two banks. The overall form of the valley along the north bank is prone to taking the shape of a funnel and the cross section takes V-shape. While for most valleys along the south bank, its overall form is prone to take the shape of oak leaf and cross section takes U-shape. The probable reason may be that due to intense sun



FIGURE 3: Debris flow events from investigation in the field. (a) Bitong debris flow in 2016; (b) Dada debris flow in 2017. (c) Guxiang debris flow in 2020. (d) Jiaolong debris flow in 2016; (e) Chidan debris flow in 2016. (f) Songrao debris flow in 2018).

TABLE 1: Typical debris flows along the Parlung River from Bomi to Suotong (e.g. 1–13 in Figure 1).

No.	Name	Date	Size class	Data source	Location
1	Bitong gully	5 Sep. 2007	Middle	Interviews with local residents	North bank
		5 Sep. 2016	Large	Field investigation	
2	Dada gully	4 Aug. 2013	Small	Interviews with local residents	
		20 Jul. 2017	Middle	Field investigation	
3	Jiaolong gully	Sep. 1988	Middle	[14]	
		15 Aug. 1989	Large	[14]	
4	Canguo gully	5 Sep. 2016	Middle	Field investigation	
		1975	Large	[14]	
5	Zhataduo gully	1996	Large	[14]	
		Jul. 1987	Large	[14]	
6	Naha gully	1968	Super-large	Interviews with local residents	
		1978	Large	[14]	
7	Guxiang gully	Sep. 2018	Middle	Field investigation	
		29 Sep. 1953	Super-large	[28]	
8	Suotong gully	1954	Large	[14]	
		1963	Large	[14]	
8	Suotong gully	30 Jul. 2005	Large	Interviews with local residents	
		Jul. 2020	Large	Field investigation	
8	Suotong gully	26 Jul. 1991	Middle	[14]	

TABLE 1: Continued.

No.	Name	Date	Size class	Data source	Location
9	Qiuzhu gully	2014 28 Aug. 2016	Middle	Interviews with local residents	South bank
10	Chidan gully	5 Sep. 2016	Middle	Field investigation	
11	Songrao gully	4 Sep. 2007 25 Jul. 2010 11 Jul. 2018	Large	[32]	
12	Michong gully	Aug. 2015	Small	Field investigation	
13	Danka gully	Aug. 2015	Small	Interviews with local residents	
				Interviews with local residents	

TABLE 2: Glaciers along the Parlung river from Bomi to Suotong.

Location	Types of glacier	Number of glaciers and percentage		Area of glaciers (km <sup>2</sup> ) and percentage		Volume of glaciers (10 <sup>6</sup> × m <sup>3</sup> ) and percentage		Average snow line (m)
North bank	Hanging glacier	18	20.93%	41.12	30.84%	2867.45	33.93	4040
	Cirque glacier	10	11.63%	4.96	3.72%	142.57	1.69%	
	Valley glacier	0	0%	0	0%	0	0%	
South bank	Hanging glacier	23	26.74%	31.18	23.38%	2058.01	24.35%	3429
	Cirque glacier	15	17.44%	5.82	4.36%	194.73	2.30%	
	Valley glacier	20	23.26%	50.27	37.70%	3188.54	37.73%	
Sum total	—	86	100%	133.35	100%	8451.3	100%	—

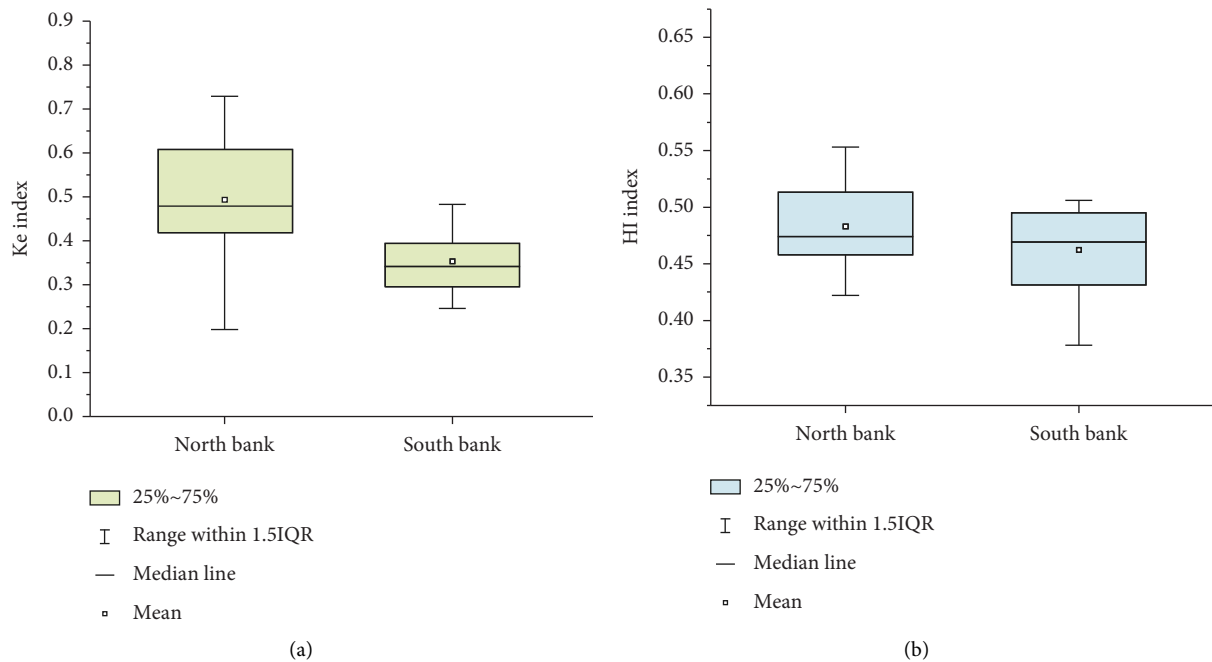


FIGURE 4: Comparison of Ke index and HI between valleys along two banks ((a) Ke index; (b) HI index).

exposure, it is hard to form a large-scale glacier running through the whole valley along the north bank, and the glacier remains mostly at the edge of the valley at high altitude. Under the effect of freeze-thaw weathering and glacier erosion over the years, only mountains at high altitudes suffer repeated erosion, thus forming wide tops and narrow bottoms. Its overall form takes the shape of a funnel, and its cross section takes the shape of “v” at the lower part, which is favorable for debris flow events (Figure 5).

#### 4. Formation Mechanism of Debris Flow along the Parlung River

The occurrence of landslides, debris flows, and other geohazards depends on a combination of internal and external conditions, including active tectonics, topography, climate, and hydrology. Field investigation and the abovementioned analysis show that glacier-related debris flows vary between the south and north banks despite their overall wide



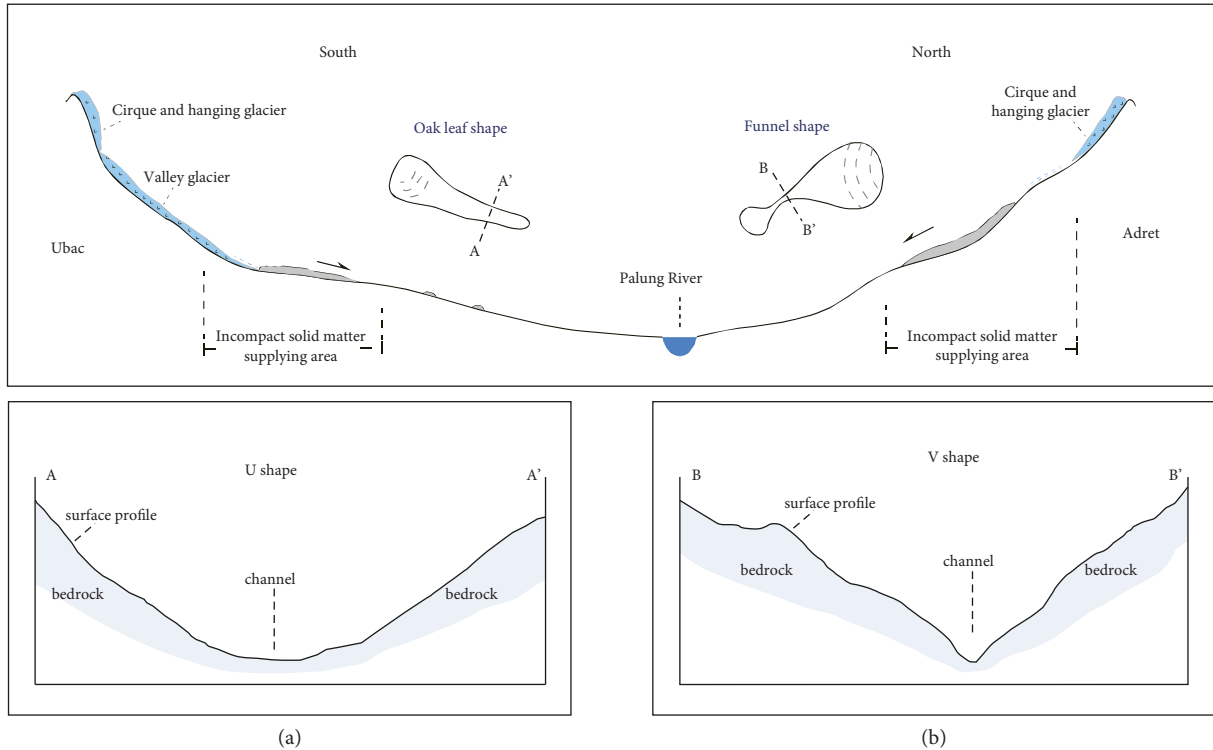


FIGURE 5: The generalized model to describe the comparison of gully geography along the two banks ((a) cross section of most gullies in the south bank; (b) cross section of most gullies in the north bank).

distribution across the region. According to field investigation and previous research [14, 16, 22, 36], the formation of debris flows on the south and north banks of the Parlung River can be explained by three modes:

Mode I: During movement, a glacier tends to fracture during intense melt at its snout. The glacial meltwater then moves into the glacial body along the resulting fractures and accumulates into runoff at the glacier base. Cavities form at the glacier snout due to erosion by runoff. As the fractures continue to grow the glacial till deposited by the glacier tends to collapse, motivating the slow-moving glacier to move downward faster. During fall and breakage, ice will melt and the huge amounts of energy contained in meltwater runoff will destabilize the loose gully deposits, which then develop into a debris flow (Figure 6(a)).

Mode II: In the early stage, the small quantities of glacial meltwater and surface runoff generated by rainfall also provide solid materials for the formation of a debris flow. When the ablation of a glacier accelerates or heavy rainfall occurs, the resulting water forms runoff, which will erode the glacial till and debris from landslides previously deposited in the gully and entrain the underlying sediments. The sediments will then be fluidized and move, forming a debris flow (Figure 6(b)).

In mode III, upstream rainfall and glacial meltwater will be blocked by the dam formed by a landslide in the narrow part and moraine in the gully. After the dam breaks the water will be discharged rapidly. The discharged water then entrains the underlying sediments, resulting in a glacial debris flow (Figure 6(c)).

### 5. Discussion

As mentioned above, the north bank has more favorable conditions in glacier and geomorphology than the south bank, which is more conducive to the occurrence of debris flows and this is consistent with the present situation of debris flow events. The dominance of cirque and hanging glaciers on the upper part of gullies in the north bank indicates greater potential energy carried by icefalls and avalanches. As the north bank is the adret, the glaciers there are more active and melt more intensely, increasing the probability of icefalls, avalanches, and rockfalls. Therefore, the mode of debris flow changes to mode I. The Guxiang debris flow on September 29, 1953, is the typical event [14]. Active glaciers will produce more meltwater and modern glacial till. The unique funnel shape of gullies not only facilitates the confluence of water from different sources but also increases the likelihood of blockage and dam breakage at the narrow part of a gully. Then, mode III debris flow will occur. The Bitong debris flow in 2016 (Figure 3(a)) and Dada debris flow in 2017 (Figure 3(b)) are the typical events on the north bank. On the south bank (ubac), the gullies are oak leaf-shaped and typically covered with valley glaciers. As the speeds of glacier motion and water catchment are slow, it will take a longer time for the materials produced by repeated freezing and thawing in the early stages and from a gully to develop into a debris flow. In this situation, a mode II debris flow is more likely to occur. In fact, as the statistics in Table 1, most of the debris flows along the south bank are Mode II. However, in extreme conditions, there is also the possibility

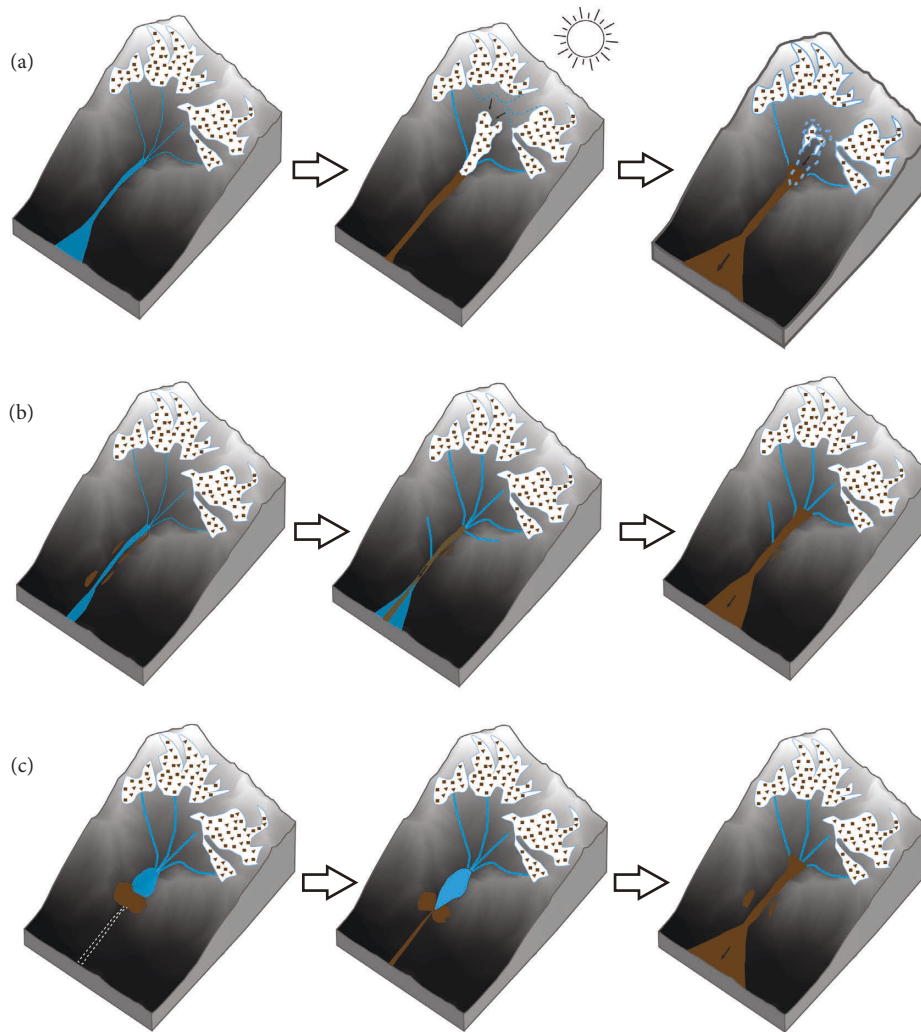


FIGURE 6: Formation mechanisms of debris flow along the Parlung River. (a) Mode I, (b) mode II, and (c) mode III.

of a model I or III debris flow. The debris flow event in 2018 in Songrao gully is just the typical one which outbreak for the reason of rockfall/moraine-initiating (Figure 3(f)) and dam-breaking debris flow in 2010, respectively [22, 36]. For the reason that the initiating course is hard to observe, the formation mechanisms of several debris flows could not be obtained; however, according to the field investigation in recent years, the result is clear that the debris flows on the north banks primarily occur in modes I and III, while the south banks are dominated by mode II debris flows (Table 3).

The Parlung glacier is the controlling dynamic factor of debris flow in the Parlung River. Warming is the main cause of glacial recession. Mass meteorological data show that climate warming has been significant in the Parlung River since the 1970s, the warming rate in Bomi is  $0.23^{\circ}\text{C}/10$  years [36, 37]. It is speculated that the melting rate of glaciers will accelerate in the future, and that the north bank will be more

affected than the south bank, for smaller glaciers are more sensitive than larger ones and are easier to lose material.

The disappearance and recession of glaciers brings enough water and impact solid matter for glacier-related debris flows. No doubt, debris flows in the region will increase gradually in the future [16, 17, 22, 38, 39]. Strong earthquakes are bound to be the center of the centralized breaking out of glacier-related debris flows. In addition, the melting of the glacier will form moraine lakes, which pose a hidden danger from the subsequent debris flows caused by glacial-lake outburst floods.

The paper suggests that the major transport projects to be built on the Parlung River, such as the Sichuan–Tibet Expressway and the Sichuan–Tibet Railway, should be located on its southern bank, in order to mitigate the influence of debris flows. To spare gullies prone to debris flows, bridges and tunnels are proper solutions.



## 6. Conclusion

The present paper indicates that compared to the south bank of the Parlung River, the north bank shows much larger and higher frequency debris flows in recent years. In fact, the north bank has more favorable conditions in glacier and geomorphology than the south bank, which is more conducive to the occurrence of debris flow. There are more active and distributed glaciers on the north bank of the Parlung River than on the south bank, which means enough water and material for the debris flow. The Ke index and HI show that valleys along the north bank reflect higher circle and erosion degree, the overall shape of gullies in the north bank is mainly funnel shaped and the cross section shows the shape of “v” at the lower part, which is favorable for debris flow formation. Relevant results provide a way to study the relationship between environmental conditions and the glacier-related debris flow, not just in SE Tibet Plateau but also in the marine alpine area.

Three formation mechanisms are concluded: mode I: icefalls, avalanches, and rockfalls mix with water in a gully and transform into a debris flow; mode II: gully bed deposits are destabilized by surface runoff and then develop into a debris flow; and mode III: the break of a debris dam suddenly causes a debris flow. The glacier-related debris flows on the south and north banks occur through different mechanisms due to different formation conditions, the debris flows on the north banks primarily occur in modes I and III, while the south banks are dominated by modes II debris flows. The understanding of the regional debris flow could be promoted in the initiation mechanism.

The disappearance and recession of glaciers bring enough water and impact solid matter for glacier debris flows, no doubt debris flow in the region will increase gradually in the future, and the north bank is more prone than the south bank. This paper suggests that the major transport projects to be built on the Parlung River should be located on its south bank, in order to mitigate the influence of debris flows. To spare gullies prone to debris flows, bridges and tunnels are proper solutions.

## Data Availability

The glacier dataset used in this study were provided by the National Cryosphere Desert Data Center (<https://www.ncdc.ac.cn>).

## Disclosure

This study has previously been presented at a conference [40].

## Conflicts of Interest

The authors declare that they have no conflicts of interest.

## Acknowledgments

The work was supported by the Second Tibetan Plateau Scientific Expedition and Research (STEP) Program (Grant no. 2019QZKK0902), “Geo-Hazard Survey and Risk

Management in Southeast Margin and Transition Zone of the Tibetan Plateau (DD20221741)” which was funded by the China Geological Survey and Key laboratory of Deep-Earth Dynamics of Ministry of Natural Resources Open Project (no. J1901). The authors convey their sincere thanks to Dr. Dongxu Yang and Eng. Dong Yang for providing valuable discussions in the field.

## Supplementary Materials

Table S1 shows that the mean and max Ke index of the north bank is 0.49 and 0.73, much larger than the south bank. For HI index, there is not much large difference between the north and south banks, while the north bank is generally larger than the south bank. (*Supplementary Materials*)

## References

- [1] O. Korup and J. J. Clague, “Natural hazards, extreme events, and mountain topography,” *Quaternary Science Reviews*, vol. 28, no. 11-12, pp. 977–990, 2009.
- [2] S. T. McColl, “Paraglacial rock-slope stability,” *Geomorphology*, vol. 153, pp. 1–16, 2012.
- [3] L. Fischer, R. S. Purves, C. Huggel, J. Noetzli, and W. Haeberli, “On the influence of topographic, geological and cryospheric factors on rock avalanches and rockfalls in high-mountain areas,” *Natural Hazards and Earth System Sciences*, vol. 12, no. 1, pp. 241–254, 2012.
- [4] J. Gao, T. Yao, V. Masson-Delmotte, H. C. Steen-Larsen, and W. Wang, “Collapsing glaciers threaten Asia’s water supplies,” *Nature*, vol. 565, no. 7737, pp. 19–21, 2019.
- [5] A. Kääh, M. Jacquemart, A. Gilbert et al., “Sudden large-volume detachments of low-angle mountain glaciers - more frequent than thought,” *The Cryosphere*, vol. 15, pp. 1751–1785, 2021.
- [6] B. An, W. Wang, W. Yang et al., “Process, mechanisms, and early warning of glacier collapse-induced river blocking disasters in the Yarlung Tsangpo Grand Canyon, southeastern Tibetan Plateau,” *Science of the Total Environment*, vol. 816, Article ID 151652, 2022 Apr 10.
- [7] T. Takahashi, *Debris Flow Mechanics, Prediction and Countermeasures*, pp. 103–168, Taylor & Francis, London, 2014.
- [8] N. Chen, Q. Zou, F. Su, P. Cui, and Y. Zhang, “Risk assessment and disaster reduction strategies for mountainous and meteorological hazards in Tibetan Plateau,” *Chinese Science Bulletin*, vol. 60, no. 32, pp. 3067–3077, 2015.
- [9] A. Kääh, S. Leinss, A. Gilbert et al., “Massive collapse of two glaciers in western Tibet in 2016 after surge-like instability,” *Nature Geoscience*, vol. 11, no. 2, pp. 114–120, 2018.
- [10] S. Luo, J. Xiong, S. Liu et al., “New insights into ice avalanche-induced debris flows in southeastern Tibet using SAR technology,” *Remote Sensing*, vol. 14, no. 11, p. 2603, 2022.
- [11] Y. J. Shang, Z. Yang, L. Li, D. Liu, Q. Liao, and Y. Wang, “A super-large landslide in Tibet in 2000: background, occurrence, disaster, and origin,” *Geomorphology*, vol. 54, no. 3-4, pp. 225–243, 2003.
- [12] Y. G. Ge, P. Cui, Fh Su, Jq Zhang, and Xz Chen, “Case history of the disastrous debris flows of Tianmo watershed in Bomi County, Tibet, China: some mitigation suggestions,” *Journal of Mountain Science*, vol. 11, no. 5, pp. 1253–1265, 2014.
- [13] W. Tang, Ht. Ding, Ns. Chen et al., “Artificial neural network-based prediction of glacial debris flows in the Parlung Zangbo

- basin, southeastern Tibetan plateau, China,” *Journal of Mountain Science*, vol. 18, no. 1, pp. 51–67, 2021.
- [14] Y. F. Shi and S. Yang, “The glacial debris flow in Guxiang, Tibet,” *Chinese Science Bulletin*, vol. 6, pp. 542–544, 1964.
- [15] S. Y. Liu, W. Q. Guo, J. L. Xu et al., “The Second Glacier inventory dataset of China (version 1.0),” *Cold and Arid Regions Science Data Center at Lanzhou*, vol. 61, 2013.
- [16] I. T. S. Imhe, “A study of typical mountain hazards along sichuan-tibet Highway,” in *The Chinese Academy of Sciences and Water Conservancy Ministry of China and ITS (Institute of the Traffic Science, the Tibet Autonomous Region)*, pp. 158–184, IMHE (Institute of Mountain Hazards and Environment), Chengdu, 1999.
- [17] Y. J. Shang, H. D. Park, Z. Yang, and J. Yang, “Distribution of landslides adjacent to the northern side of the yarlu tsangpo grand canyon in Tibet, China,” *Environmental Geology*, vol. 48, no. 6, pp. 721–741, 2005.
- [18] R. Du, H. Li, L. Wang, Y. L. Wang, and Z. L. Qian, “Formation and development of glacial debris flow in the Guxiang gully, Xizang,” in *Proceedings of the Lanzhou Institute of Glacier and Permafrost, CAS, Special Issue on China Debris Flow*. Science Press, p. 1, Beijing, 1985.
- [19] Q. L. Zeng, *Formation of Huge-Thick Loose Accumulations in Southeast Tibet with Associated Hazards Modes and Mitigations: A Case Study in Ranwu to Lulang Section of Sichuan-Tibet Highway*, pp. 87–95, Thesis of University of Chinese Academy of Science, 2007.
- [20] J. J. Zhang, J. K. Liu, B. Gao et al., “Characteristics of material sources of Galongqu glacial debris flow and the influence to Zhamo Road,” *Journal of Geomechanics*, vol. 24, no. 1, pp. 106–114, 2018a.
- [21] Z. Q. Xu, Z. H. Cai, Z. M. Zhang, L. Huaqi, C. Fangyuan, and T. Zhemin, “Tectonic and fabric kinematics of the namche barwa terrane, eastern himalayan syntaxis,” *Acta Petrologica Sinica*, vol. 24, no. 7, pp. 1463–1476, 2008.
- [22] R. Q. Wei, Q. L. Zeng, T. Davies et al., “Geohazard cascade and mechanism of large debris flows in Tianmo gully, SE Tibetan Plateau and implications to hazard monitoring,” *Engineering Geology*, vol. 233, pp. 172–182, 2018.
- [23] L. Ding and Zhong, “Fission track evidence for the Neocene rapid uplifting of the eastern Himalayan syntaxis,” *Chinese Science Bulletin*, vol. 40, no. 16, pp. 1497–1500, 1995.
- [24] P. K. Zeitler, A. S. Meltzer, L. Brown, W. S. Kidd, C. Lim, and E. Enkelmann, “Tectonics and topographic evolution of namche barwa and the easternmost Lhasa block, Tibet,” *GSA Bull. Spec.*, vol. 507, pp. 23–58, 2014.
- [25] J. J. Zhang, J. C. Wang, and L. Chen, “Distribution of the Quaternary accumulation along Zhamu-Suotong section of the Sichuan-Tibet high way and their occurrence characteristics,” *Science Technology and Engineering*, vol. 17, no. 32, pp. 37–43, 2016.
- [26] R. Jinwei, S. Jun, C. Zhongquan, and W. Yipeng, “Quaternary faulting of Jiali fault, southeastern Tibetan plateau,” *Seismology and Geology*, vol. 22, no. 4, p. 344, 2000.
- [27] F. . t. Tang, J. Song, Z. Q. Cao et al., “The movement Characters of main faults around Eastern Himalayan Syntaxis revealed by the latest GPS data,” *Chinese Journal of Geophysics*, vol. 53, no. 9, pp. 2119–2128, 2010.
- [28] Ceic, “Earthquake Catalogue from China Earthquake Network Center,” 2018, <http://www.csndmc.ac.cn/newweb/data.htm>.
- [29] J. J. Li and Zheng, *Tibet Glacier. 1-36*, pp. 217–228, Science Press, Beijing, 1986.
- [30] D. S. Mi and Xie, *Glacier Inventory of China, XI, the Ganga Drainage Basin*, pp. 9–437, Xi'an Cartographic Press, Xi'an, 2002.
- [31] W. Yang, T. Yao, B. Xu, G. Wu, L. Ma, and X. Xin, “Quick ice mass loss and abrupt retreat of the maritime glaciers in the Kangri Karpo mountains, southeast Tibetan Plateau,” *Science Bulletin*, vol. 53, no. 16, pp. 2547–2551, 2008.
- [32] A. Faghih, B. Samani, T. Kusky, S. Khabazi, and R. Roshanak, “Geomorphologic assessment of relative tectonic activity in the m lake basin, zagros mountains of Iran,” *Geological Journal*, vol. 47, no. 1, pp. 30–40, 2012.
- [33] M. T. Ramirez-Herrera, “Geomorphologic assessment of active tectonics in the Acambay graben, Mexican Volcanic Belt,” *Earth Surface Processes and Landforms*, vol. 23, no. 4, pp. 317–332, 1998.
- [34] R. J. Pike and S. E. Wilson, “Elevation-relief ratio, hypsometric i and geomorphic area-altitude analysis,” *The Geological Society of America Bulletin*, vol. 82, no. 4, pp. 1079–1084, 1971.
- [35] B. X. Zheng and Q. H. Ma, “Relationship between the glacier variation and the debris flow development of the holocene in the GongGa mountainous region,” *Lanzhou institute of Gliacolgy and Geocryolog, Chinese Academy of Sciences*, vol. 12, no. 1, pp. 1–8, 1994.
- [36] M. F. Deng, N. Chen, and M. Liu, “Meteorological factors driving glacial till variation and the associated periglacial debris flows in Tianmo valley, south-eastern Tibetan Plateau,” *Natural Hazards and Earth System Sciences*, vol. 17, no. 3, pp. 345–356, 2017.
- [37] W. Yang, T. Yao, B. Xu, L. Ma, Z. Wang, and M. Wan, “Characteristics of recent temperate glacier fluctuations in the Parlung Zangbo River basin, southeast Tibetan Plateau,” *Chinese Science Bulletin*, vol. 55, no. 20, pp. 2097–2102, 2010.
- [38] C. U. Peng, C. H. Rong, X. Lingzhi, and S. Fenghuan, “Risk analysis of mountain hazards in Tibetan Plateau under global warming,” *Progressus Inquisitiones de Mutatione Climatis*, vol. 10, no. 2, pp. 103–109, 2014.
- [39] S. L. Gariano and F. Guzzetti, “Landslides in a changing climate,” *Earth-Science Reviews*, vol. 162, pp. 227–252, 2016.
- [40] J. J. Zhang, J. K. Liu, Y. L. Li, J. C. Wang, L. Chen, and B. Gao, “Conditions and mechanism for formation of glacial debris flows in Parlung Zangbo, SE Tibetan Plateau,” in *Proceedings of the 5th International Conference Debris Flows: Disasters, Risk, forecast, protection*, p. 671p, Tbilisi, Georgia, 2018b.

## Research Article

# Mitigating Risks in the Disaster Management Cycle

Huay Ling Tay <sup>1</sup>, Ruth Banomyong <sup>2</sup>, Paitoon Varadejsatitwong <sup>2</sup>,  
and Puthipong Julagasigorn <sup>2</sup>

<sup>1</sup>School of Business, Singapore University of Social Sciences, Singapore

<sup>2</sup>Thammasat Business School, Thammasat University, Bangkok 10200, Thailand

Correspondence should be addressed to Huay Ling Tay; [hltay@suss.edu.sg](mailto:hltay@suss.edu.sg)

Received 20 July 2022; Accepted 16 August 2022; Published 30 September 2022

Academic Editor: Fadzli Mohamed Nazri

Copyright © 2022 Huay Ling Tay et al. This is an open access article distributed under the Creative Commons Attribution License, which permits unrestricted use, distribution, and reproduction in any medium, provided the original work is properly cited.

*Purpose.* The disaster management cycle (DMC) is often considered part of the essential efforts to handle disaster risk and consists of four key phases, namely preparedness, response, recovery, and mitigation. The purpose of this conceptual article is two-fold. The first is to identify dominant risks, and the second is to propose risk mitigation strategies for these four phases in the DMC. *Design/Methodology/Approach.* The study uses primary and secondary data to identify the dominant risks in each DMC phase. The primary data sources include responses from an online questionnaire and transcripts from three semi-structured interviews with stakeholders in the humanitarian supply chain. The secondary data sources include practitioner reports and archival data triangulation. *Findings.* The findings reveal five dominant risk factors in the DMC and classify them within the DMC phases, which are (1) demand risk, (2) supply risk, (3) operational risk, (4) infrastructure risk, and (5) disruption risk. The severity and frequency of each risk vary in each DMC phase. We found that several supply chain strategies (SCSs), such as raising risk awareness and horizontal and vertical collaboration and coordination among the key stakeholders in the DMC, can be essential risk mitigation strategies that apply across the four DMC phases. *Research Limitations/Implications.* The study highlighted dominant risks and the appropriate SCSs for mitigating the risk factors within each DMC phase. These findings are encapsulated in a conceptual framework for guiding risk prioritisation, decision-making, and policy-making. Our study has several limitations. First, although we followed a systematic process in computing the risk scores based on the likelihood of occurrences and impacts, the scores are nonetheless considered subjective perceptions of the respondents. Second, the number of respondents was limited. Broader coverage of respondents across geographical regions will provide further insights into the perspectives on the relevant risk factors in the DMC phases. This leaves possibilities for future research, comparison with other risk computation methods, and evaluation. *Originality/Value.* This study is one of the few that collected multiple data to extend the knowledge of risk identification and mitigation within the DMC.

## 1. Introduction

Disasters bring about adverse economic, physical, and environmental impacts. They also threaten the sustainable development goals of the affected country [1]. While disaster risks can hardly be eliminated, it is possible to mitigate risks by minimising the adverse impacts they bring. Risks can be mitigated and managed to enhance the effectiveness of humanitarian operations while increasing the credibility of the humanitarian sector. These, in turn, will lead to increased fund-raising potential and support for humanitarian operations (Mizushima et al., 2008).

The disaster management cycle (DMC) is a recognised framework for managing disaster events and their impacts in pre-disaster, during, and post-disaster activities ([2]; Baird et al., 1975). Pre-disaster activities involve prevention, mitigation, and preparedness, whereas response activities usually include rescue and relief activities. Post-disaster activities include recovery and development [5]. All these activities collectively help to manage a disaster and reduce the risk of human and physical losses.

While there have been several risk categorisation frameworks (e.g., [6–11]), insights into the sources of risks and appropriate risk mitigation strategies in the DMC

phases seem to be lacking. Moreover, extant literature mostly explored the various risk categorisation approaches in the humanitarian contexts without providing insights into the risk categories present in the different phases of the DMC (e.g., [6–11]). In particular, [11] links humanitarian logistics (HL) and supply chain risk management (SCRM) to understand risk mitigation strategies that humanitarian organisations use or could use to improve their logistics preparedness. Based on systematic reviews of risk mitigation strategies (RMS) in supply chain risk management (SCRM) and supply chain strategies (SCSs) in the HL literature, [11] developed a framework that links SCSs in the HL literature. However, there seem to be limited discussions and empirical studies that attempt to adapt supply chain risk management and SCSs within the DMC. Our research attempts to fill this knowledge gap by addressing the following research questions using empirical data collected from humanitarian practitioners:

RQ 1: What are the dominant risks in each DMC phase?

RQ 2: How can SCSs be used to mitigate dominant risks in each DMC phase?

Our study contributes to the literature by integrating two bodies of literature—the disaster management cycle (DMC) and supply chain risk mitigation strategies (SCSs)—to develop a theoretical framework for the study. We collected empirical evidence from a web-based questionnaire and semi-structured interviews (online or face-to-face) with humanitarian operation practitioners and academics within this domain to identify the dominant sources of risks and appropriate SCSs for risk mitigation in the DMC.

The rest of the article is organised as follows: Section 2 discusses the literature related to the DMC, risk assessment, and mitigation strategies and provides the significance of the research. Section 3 explains the research method and proposes a conceptual framework for risk assessment and management in the DMC. Section 4 presents the findings and a modified DMC framework highlighting the dominant risks in the DMC phases and the appropriate risk mitigation strategies. Section 5 discusses research and managerial and policy implications. Section 6 concludes the article with the limitations of this research and opportunities for future research.

## 2. Literature Review

*2.1. Humanitarian Supply Chains and Disaster Management.* Humanitarian supply chains are characteristically involved in large-scale operations, addressing high magnitude risks to life and the need to coordinate speedy delivery of rescue and relief goods and services to disaster zones (Jabbour et al., 2017; [10, 11]). Humanitarian supply chains are often emergent, with short lives, responding to specific disasters, uncertainty, and mostly unforeseen situations [12]. Supply chain activities linked to disasters are classified into four key phases. Pre-disaster, the focus is on “mitigation” and “preparedness.” Post-disaster, the focus is on “response” and “recovery” [13]. The supply chain activities operate within

the DMC and focus on saving, preserving life, building, and maintaining standard life quality in disaster zones.

Kapucu [14] argued that disaster management is the organisation and management of resources and responsibilities for dealing with all humanitarian aspects of emergencies, particularly preparedness, response, and recovery, to lessen the impact of disasters [12]. The management of disasters is achieved in the form of disaster operations management and emergency planning [16].

Disaster operations represent activities performed before, during, and after a sudden, devastating incidence that seriously disturbs the functioning of a population and causes human, material, economic, or environmental damages beyond the coping capacity of the affected population using its resources [17].

*2.1.1. The Disaster Management Cycle (DMC).* According to Martinho and Reis [18], the United Nations’ perspective of disaster risk reduction aims at reducing vulnerabilities and disaster risks, preventing the loss of human lives as well as increasing communities’ resilience throughout society, public, and private. Martinho and Reis [18] further noted that disaster risk reduction requires managing risk beyond disaster responses to prevention and mitigation.

From the perspective of humanitarian supply chains, disaster risk reduction involves activities carried out before, during, and after disasters to reduce their impact, avoid losses, and save lives [11, 19]. With strategic process design, disaster management is key to successful disaster responses and relief efforts [20]. At an operational level, disaster management can be described as a process through several cyclical and overlapping stages [10]. However, in general, the literature concurs that disaster management has four phases, namely (1) preparedness, (2) response, (3) recovery, and (4) mitigation [10, 21, 22], which are described below.

*(1) Preparedness.* The preparation phase refers to activities taken before a disaster occurs to avoid possible consequences and prepare all relevant organisations and communities by learning from the past [10]. The literature suggests common preparedness activities, namely developing information and communication, developing collaboration and coordination between relevant organisations and people, training and practicing relief services with communities, designing physical networks, and stockpiling supplies and equipment [10, 11, 23].

*(2) Response.* The response phase refers to activities immediately implemented after a disaster [10]. Relief efforts are carried out to rescue and delivery basic supplies to the highest possible number of beneficiaries as well as to restore the essential services and infrastructures in the shortest time possible [10, 11]. In this phase, it is also important to assess the disaster situation and keep relevant people (e.g., beneficiaries and relief staff) updated on the disaster situation and the current relief efforts [23]. Therefore, coordination and collaboration among all organisations and actors involved is key to successful relief efforts [10, 24].

(3) *Recovery*. The recovery phase refers to activities involving reconstructions and rehabilitations operated in the aftermath of a disaster and carried out to recover the situation back to the default state [10, 23]. Therefore, activities are undertaken in this phase to address the problems from a long-term perspective [10].

(4) *Mitigation*. The mitigation phase refers to actions taken after and before a disaster to reduce the effects of disasters [25]. These actions often involve revising strategies, procedures, mechanisms, regulations, measures, and policies that aim to reduce social vulnerability [10, 23]. The key difference between mitigation and preparation is that mitigation is the application of measures that aim to prevent a disaster and reduce its impact, while preparation includes activities that prepare for an effective and efficient response [22, 25].

To summarise, DMC aims to determine the underlying risk factors and prepare for and initiate an immediate response to disasters to reduce and mitigate disaster risks. Accordingly, the DMC that incorporates risk management and performance outcomes into a single model as shown in Figure 1 was proposed by [10]. This study makes use of this adapted DMC model as the theoretical basis to examine the dominant risk factors and appropriate risk mitigation strategies in our empirical research design.

**2.2. Supply Chain Risks.** Supply chain risk (SCR) is defined as the “divergence in the distribution of potential outcomes of the supply chain, their probability, and their subjective values” [26]. Goh et al. [27] and Kull & Closs [37] defined SCR as the appearance of an accident with the disability of the influenced firms to deal with consequences. Furthermore, Jüttner et al. [38] described SCR as the potential and influence of a mismatch between supply and demand. It is also defined as anything that disrupts the information, materials, or product flow from original suppliers to end users [39].

SCR has been classified by scholars using various perspectives. One classification of supply chain risks is based on internal and external risks—external risks are such as natural disasters, and internal risks are such as quality problems of suppliers. Supply chain risks are also classified as strategic, tactical, and operational. Daultani et al. (2005) viewed disruption risks as those resulting from man-made or natural disasters and categorised supply chain risks as operational risks and disruption risks. Operational risks are further classified into supply, process, and demand risks. Supply risks are associated with the unforeseeable performance of upstream suppliers regarding quantity, quality, time, and cost. Process risks are usually caused by substandard processes in manufacturing systems, and this will lead to inconsistent quality, target yield, and production time. Demand risk is associated with sales fluctuations resulting from forecast errors, leading to negative consequences like shortage or excessive inventory. This form of risk categorisation (i.e., supply risk, process risk, demand risk, and disruption risk) was reflected in Samvedi et al. [37],

except that Samvedi et al. [37] classify disruption risk as an environmental risk.

Tang and Musa [38] offered an alternative supply chain risk categorisation based on three types of flows, namely material flow, financial flow, and information flow. Risks at the source stage are related to purchasing and sourcing physical goods and services. Risks in the make stage may occur during product development, while risks in the delivery stage are those influenced by forecasting challenges. Financial flow risk is associated with “the inability to settle payment and improper investments” [38]. These may include credit terms and payment schedules. Information risk is associated with information flows like inventory status, product and process design changes, and capacity status [38]. Information flow binds supply chain elements and is typically used to link material flow and financial flow. A comprehensive classification of supply chain risks and the main characteristics of supply chain risks closely related to the organisations’ objectives in the supply chain can be found in [39].

### 2.3. Risk Mitigation Strategies

**2.3.1. Application of Supply Chain Strategies (SCSs) in Disaster Management.** Supply chain risk management is the application of strategies to manage daily and extraordinary risks in the supply chain. Relative to commercial supply chains, supply chain risk management is crucial in the humanitarian context. Supply chain disruptions can add to the challenges in relief and recovery efforts, leading to worsened conditions during humanitarian crises (McLachin et al., 2009). In the humanitarian context, the risk is “the combined susceptibility and vulnerability of the community to potential damage caused by a particular hazard within a specified future time period” [1], p.7).

Supply chain strategies (SCSs) are often used in commercial supply chains and are based on continued risk estimation, aiming to minimise vulnerability and guarantee continuity [36]. Studies have attempted to adapt commercial supply chain risk management practices and risk mitigation strategies to address risks in the humanitarian supply chains (Jabbour et al., 2019).

In particular, Jahre [11] developed a humanitarian SCS framework that connects risk factors and supply chain risk mitigation strategies that could aid in counteracting risks in the humanitarian supply chain. The more common mitigation strategies were found to be strategic stock pre-positioning, postponement, collaboration, flexible transportation, and flexible supply base. However, there seems to be limited research on how SCSs can aid in managing specific risk factors in disaster management. Because of these, this paper seeks to extend the literature on disaster risk management and supply chain management strategies by building on the knowledge based on the humanitarian supply chain strategies framework by [11] and the DMC, to inform on the applicable mitigation strategies in phases and activities of the DMC.

Apart from traditional risk management strategies like risk assessment and continuity planning, resilience is



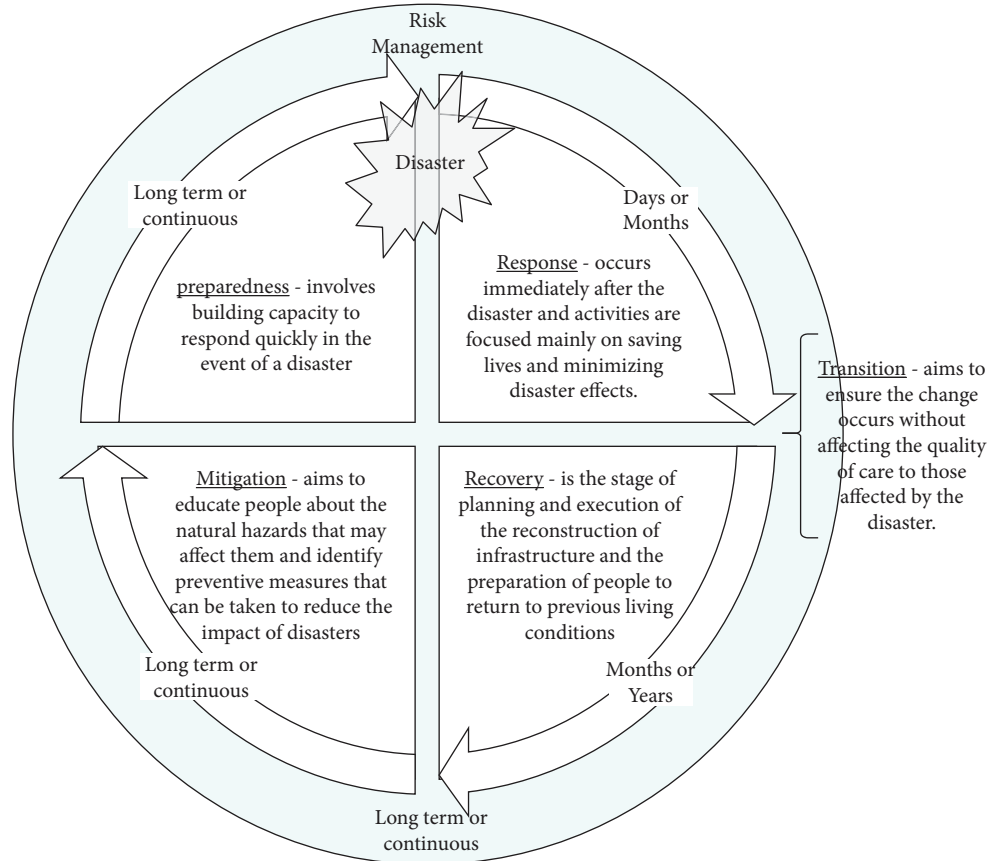


FIGURE 1: A model integrating risk management in the DMC used in this study (based on [10]).

another approach that can be adopted as “supply chain resilience can deal with unforeseeable disruptions and events” [22]. According to Scholten et al. [22], there are four elements of supply chain resilience, namely supply chain re-engineering, collaboration, agility, and risk awareness/knowledge management. In the humanitarian supply chain, where numerous stakeholders are involved, collaboration and cooperation among diverse stakeholders are core to ensure effective risk management and successful relief operations when disasters occur.

Based on our literature review, the common types of supply chain risks that resonate in extant literature can be summarised into five broad categories as listed in Table 1. These five key risk categories were deployed in this study.

Table 2 lists the SCSs (A to J) that were identified based on a review of prior research and literature in risk mitigation, such as Jahre [11] and Scholten et al. [22], as well as by practitioners and archival reports from international humanitarian organisations.

On the whole, while researchers have studied supply chain risks and mitigation strategies in humanitarian supply chains, studies that focus on understanding how the different sources of risk play out in the various phases of the DMC and the appropriate mitigation strategies that can aid in effective disaster management seem to be scarce. Moreover, most extant literature focused on an individual or a few

phases of the DMC [49, 43]. This article serves as an initial step to filling this gap.

We seek to integrate three main research streams and identify the dominant risks and the appropriate risk mitigation strategies in the different DMC phases to aid humanitarian organisations focusing on different disaster stages in prioritising risk and taking effective risk mitigation actions. Figure 2 presents our research approach that integrates the streams of literature adapted from the three main research streams, namely supply chain risk, disaster management cycle, and risk mitigation strategies. The empirical data collection instruments, including questionnaires and semi-structured interview protocols, were then developed for this research.

### 3. Methodology

**3.1. Research Design and Data Collection.** We took an exploratory approach in addressing the research questions and adopted a mixed method by collecting primary data through questionnaires and interviews. The primary data included responses from web-based questionnaires and semi-structured interviews with selected key informants involved in disaster management operations. Table 3 presents an overview of the empirical data sources, consisting of key stakeholders and practitioners involved in the DMC.

TABLE 1: Definitions and examples of the risk categories.

Risk categories	Definition	Source	Examples of risks
Demand risk	Demand risk refers to adverse events at the downstream partners of a firm	[37, 38]	(i) Shifting demand across time (ii) Shifting demand across markets (iii) Shifting demand across products
Supply risk	Supply risk refers to adverse events at the upstream partners of a firm	[37, 38]	(i) Uncertain supply yields (ii) Uncertain supply lead times (iii) Uncertain supply costs
Operational risk	Operational risk was conceived as the operational risk that affects HO's internal processes or operations that affect their ability to produce services, quality, and timeliness of their service provision to meet the needs of the beneficiaries effectively	(Wu et al.) [40]	Unanticipated changes in the volume requirements and mix of items needed, price increases, product unavailability, and product quality problems, lacking personnel, knowledge, and ability to manage new processes
Infrastructure risk (information, transport, finance)	To ensure the healthy functioning of a supply chain, information technology transportation and financial systems are also of critical importance. Any disruptions in these systems can also lead to serious problems in the supply chain. The risks relating to these three systems are classified as infrastructural risks	Information technology [39], transportation [40], and financial systems (Chopra et al. [39, 40])	Lockout or shutdown of transportation hubs such as docks, impacts of conflicts between employer management and labour groups, and the reaction of employers in the form of work slowdowns to changes such as the deployment of information technology. Incompatible IT system and financing mechanism
Disruption risk	Disruption or macro risks refer to adverse and relatively rare external events or situations that might have negative impacts on companies	Sodhi et al. [48];	Natural risks (e.g., earthquakes and weather-related disasters) and man-made risks (e.g., war and terrorism and political instability)

TABLE 2: Proposed supply chain strategies for mitigating risk in the DMC (adapted from [11]).

Proposed risk mitigation strategies	
A	Having a mobile logistics hub (assuming the chosen location is safe and accessible)
B	Having a centralised propositioned stock
C	Having a joint or bulk procurement system
D	Having a flexible supply base
E	Logistics outsourcing—use of a third-party logistics provider
F	Horizontal collaboration and coordination among players involved in the same phase of the DMC for joint planning and information sharing
G	Vertical collaboration and coordination among players involved in the different phases of the DMC for joint planning and information sharing
H	Pre-position vehicles and having a fleet management program
I	Having flexible transportation with an operational mix of vehicles and transport mode, depending on the location and accessibility of disaster site
J	Risk awareness

3.1.1. *Web-Based Questionnaires.* Web-based questionnaires are a convenient way to gather data relevant to the project, allowing respondents to answer the questionnaire at their own pace. The questionnaire was developed based on extant literature on DMC risks and supply chain risk mitigation strategies. The questionnaire consisted of closed-ended and open-ended questions designed to gather responses to the two research questions.

The research employed a purposive sampling approach [44] in the respondent selection and focused on recruiting participants from the key stakeholders and practitioners involved in the DMC. An essential inclusion criterion is that a respondent must assume a professional role in a

humanitarian organisation or carry out work in humanitarian operations. To recruit respondents, we posted calls for research participation on the LinkedIn sites of various humanitarian logistics groups and humanitarian logisticians networks. In total, 25 valid responses were gathered from the questionnaire.

(1) *Questionnaire Development.* The questionnaire comprises three sections of questions. The questions in the first section focused on the general information of the respondents, such as gender and designation. The questions in the second section relate to the risk factors that may be present. Respondents were asked to rate the importance of the risk

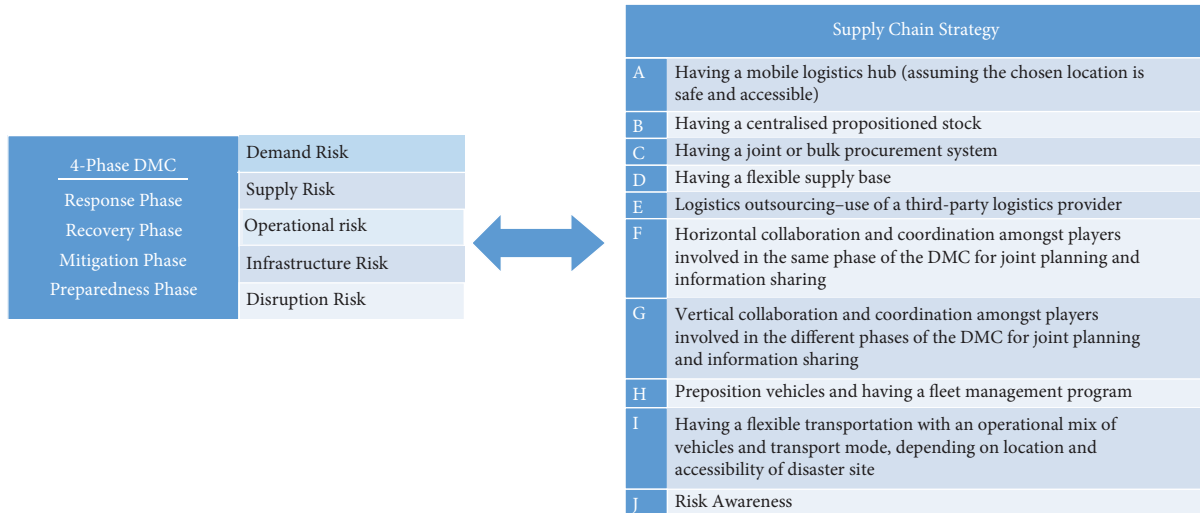


FIGURE 2: Research framework—integration of the literature relating to the source of risks, disaster management cycle, and supply chain risk mitigation strategies.

TABLE 3: Empirical data sources.

Primary sources		
Source	Brief description	Value to the study
Questionnaires	A total of 25 valid responses were gathered. Respondents are players of the DMC, including nongovernmental organisations (NGOs), aid agencies, and logistic companies	(i) Risk identification (ii) Risk analysis (iii) Strategies to manage risks
Interviews	3 semi-structured interviews were conducted	(i) Confirmation and validation of questionnaire results

factors (refer to Table 1). The third section covered the relevance of the SCSs in each DMC phase. Respondents were asked to select SCSs that they deemed relevant to mitigate the risks in each DMC phase.

The three sections in the questionnaire:

- (1) Professional profile and information about the involvement of the respondents in the DMC. These include years of experience in the humanitarian sector, affiliated organisations, and region.
- (2) Risk factors in each DMC phase. Respondents are to rate the risk factors on a Likert scale of 1–7.
- (3) Supply chain strategies (SCSs) for each DMC phase. Respondents are to select the relevant SCSs they deem relevant and helpful for mitigating risks in each DMC phase.

3.1.2. *Interviews.* Semi-structured interviews were also conducted with three key informants, and the informants were involved in the four phases of the DMC. The interviews were focused on issues identifying dominant risks in the DMC and how those risks can be managed by stakeholders involved in risk management decisions. On average, the interviews spanned 30 to 45 minutes and were all transcribed. The interviews provided qualitative insights relating to the experiences and knowledge of the key stakeholders. Table 4 shows the profile of the interviewees.

### 3.2. Data Analysis

3.2.1. *Questionnaire and Interview Data.* Qualitative and quantitative data collected from the questionnaires and interviews were examined. We analysed the responses relating to the risk rating using a Likert scale and conducted descriptive statistical analyses of the data using central tendency, and mean and mode were computed. The quantitative data will be analysed using graphical techniques whenever appropriate and relevant. Qualitative data from interviews and secondary data sources were analysed using a thematic approach where key themes were categorised and grouped accordingly.

3.2.2. *Risk Assessment and Impact Analysis.* A critical element of risk management is identifying and evaluating the impact of the relevant risk factors [37]. Several scholars have characterised risks based on the likelihood and impact (or consequences) of each risk factor (e.g., [45]; Tummala and Schoenherr, 2011). In this study, we use these two measures to evaluate the risk scores for each risk factor and their relative dominance in each DMC phase.

The risk scores were computed based on the combined ranking scores for each risk type based on a rating scale of 1 to 7 on the likelihood of occurrence and consequence for each risk. Specifically, the participants were asked to rate each of the five risk types (demand risk, supply risk,

TABLE 4: Profile of interviewees.

Informants	Roles and designations
Interviewee 1	A regional director of a nonprofit organisation. He oversaw the execution of operational activities and programmes in the Asia-Pacific region and was also responsible for engaging with his organisation's clients and/or partner organisation
Interviewee 2	A co-founder of a non-profit NGO. He oversees the activities and programmes his organisation provides in humanitarian assistance and disaster relief through new and innovative ways.
Interviewee 3	An independent researcher in humanitarian logistics and is active in Syrian relief operations since 2013

operational risk, infrastructure risk, and disruption risk) in terms of the likelihood of occurrence and consequences based on a rating scale of 1 to 7. Each risk factor is then weighted and averaged based on the ratings by the respondents for each DMC phase. The risk scores were standardised and rounded to 2 decimal places. The derived risk scores would enable stakeholders in the DMC to rank and better prioritise critical risks and plan effective measures to optimise humanitarian resources.

**3.2.3. Data Analysis on SCSs.** We used a two-step approach to analyse the data relating to SCSs to identify the relevant SCSs that could be useful for the phases and activities in the DMC.

*Step 1.* Computing average index and relative importance index

The relative importance index ( $R$ ) is a type of comparative importance analysis.  $R$  was used to determine the relative importance of the SCSs in each phase of the DMC based on the respondents' perspectives.

The average index is first computed as follows:

$$\text{Averageindex} = \frac{\sum a_i \times x_i}{\sum x_i}, \quad (1)$$

where  $a_i$  is the constant (weighing factor), and  $x_i$  are the variables representing the response frequency of respondents.

*Step 2.* Computing average frequency of SCSs selected in each DMC phase

The frequency analysis described the distribution and average frequency of the SCSs selected in each DMC phase. The average frequency is computed based on the selection and ranking of the respondents accordingly to determine the relative importance index for the SCSs. The SCSs with the higher relative importance index values are deemed more important for the DMC phase.

## 4. Findings

**4.1. Professional Profiles and Roles of Respondents.** There are many types of stakeholders in the DMC, and some organisations can play different roles in the DMC. Respondents could choose more than one option that best represents their organisation's role in the DMC. Figure 3 illustrates the roles played by respondents' organisations. "Others" refer to organisations that provide consultancy and advisory services to other players such as NGOs and governments. They are

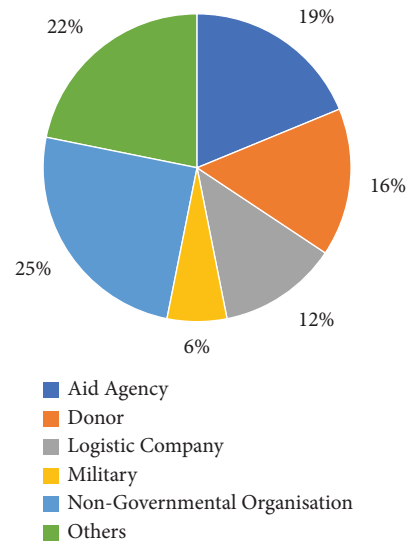


FIGURE 3: Professional profiles of respondents.

often in the education domain and coordinate with different players for fundraising and advocacy. Figure 4 shows the respondent's participation in the four phases of DMC by Viagi et al. (2016). As an organisation can be involved in more than one phase of the DMC, respondents can choose more than one option if it applies to them.

**4.2. Risks in the DMC.** The risk scores measure each risk's relative importance based on relative frequency and severity (e.g., [45] and Tummala, and Schoenherr, 2011). The risk scores for each risk factor (listed in Table 1) in the preparedness, response, recovery, and mitigation phases were computed based on their likelihood of occurrence and consequences.

Based on the risk scores, we can derive the risk ranking in each DMC phase. The top two dominant risks in each phase were identified to aid in risk prioritisation. Table 5 shows the risks ranking, and the highlighted cells show the dominant risks in the preparedness phase, response phase, recovery phase, and mitigation phase of the DMC.

Based on Table 5, demand risk is ranked the highest in the response phase. Further, operational risk is evident in the response phase but is not as apparent in the recovery phase. This finding is supported by the interviews, where interviewees unanimously agreed that the five risks apply to the DMC, though they are not consistent across all phases. As quoted by one interviewee: "there are higher levels of risks in some phases, and certain risks pose bigger risks as well."

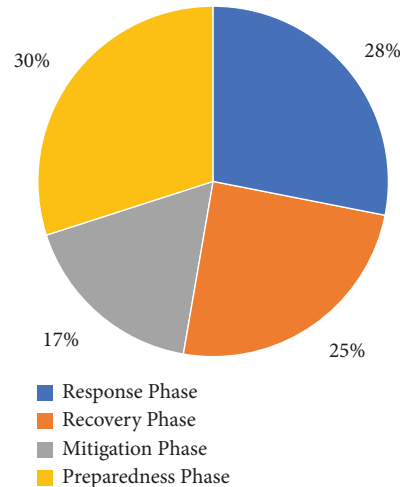


FIGURE 4: Participation of respondents in the DMC.

TABLE 5: Risk ranking in the DMC phases.

Risk ranking (based on risk likelihood and impact analysis)	Preparedness phase	Response phase	Recovery phase	Mitigation phase
Demand risk	5	1	2	2
Supply risk	3	5	1	1
Operational risk	2	4	5	3
Infrastructure risk	4	3	3	Not present
Disruption risk	1	2	4	4

Based on the distinctly higher risk score values, the top two dominant risks were then identified in each phase in the DMC. Table 6 shows a summary of the top two risks that must be prioritised for each phase.

**4.3. Risk Mitigation Strategies in the DMC.** The second phase of our data analysis seeks to identify the appropriate SCSs that can be deployed in the respective DMC phases. Respondents from both the web-based survey and interviews were asked to select the strategy or strategies listed in Table 2, which they deemed helpful in mitigating the dominant risks in each DMC phase, considering the strategy effectiveness and practicality of implementation in each DMC phase.

Table 7 shows the summary of the top strategies selected by respondents. Figure 5 presents a conceptual framework that encapsulates the findings presented above. It shows the dominant risks and supply chain risk mitigating strategies in each DMC phase.

The conceptual framework encapsulates the key findings that resonated with the verbatims of the three semi-structured interviews. In general, collaboration and coordination among players in the DMC, be it horizontal or vertical cooperation, and raising risk awareness are deemed essential in mitigating risks in the DMC.

**4.3.1. Risk Mitigation in Preparedness Phase.** The preparedness phase occurs in the pre-disaster stage. The preparedness phase aims to decide on operations to be carried out before a disaster strikes to support response operations effectively [48]. This phase is critical as information and

communications technology systems, physical network design, and bases for collaboration are developed in this phase [10]. From Table 5, the dominant risks in the preparedness phase are *operational risk* and *disruption risk*. The appropriate risk mitigation strategies deemed relevant in mitigating these two dominant risks are raising risk awareness and fostering *horizontal collaboration* and *coordination* among stakeholders in the DMC.

In building the resilience and capacity of the community to respond to potential disasters, the most fundamental step is to be conscious of probable disaster risks. Risk awareness can also come from the lessons learned from past disasters and how one can be better prepared for potential ones in the future. Awareness of these risks in the preparedness phase will allow organisations to be more mindful of the perils and hazards in disaster-prone areas and those associated with operational processes. In turn, they will understand how to better prepare for them. The community also needs to be aware of the risks and the negative impacts they bring. Risk awareness will significantly help implement operational plans or strategies as the community understands and recognises the significance of managing the risks.

Horizontal collaboration and coordination among stakeholders in the DMC are also instrumental in managing *disruption risk* and *operational risks*. Strategies developed in the mitigation phase may translate into actionable and operational plans in the preparedness phase. Thus, it is pivotal that stakeholders are aware of their respective roles and responsibilities so that relevant parties can respond effectively in the fastest possible time when disaster strikes. Horizontal collaboration and coordination are even more

TABLE 6: Summary of the top two dominant risks in each DMC phase.

Top risks	Preparedness phase	Response phase	Recovery phase	Mitigation phase
1	Disruption risk	Demand risk	Supply risk	Supply risk
2	Operational risk	Disruption risk	Demand risk	Demand risk

TABLE 7: Summary of top strategies for the dominant risks in each phase in the DMC.

Strategy	Preparedness phase		Response phase		Recovery phase		Mitigation phase	
	Disruption risk	Operational risk	Demand risk	Disruption risk	Supply risk	Demand risk	Supply risk	Demand risk
A Having a mobile logistics hub (assuming the chosen location is safe and accessible)				√				
B Having a centralised propositioned stock								
C Having a joint or bulk procurement system								
D Having a flexible supply base			√	√		√	√	
E Logistics outsourcing—use of a third-party logistics provider								
F Horizontal collaboration and coordination among players involved in the same phase of the DMC for joint planning and information sharing	√	√	√		√	√		√
G Vertical collaboration and coordination among players involved in the different phases of the DMC for joint planning and information sharing					√	√		√
H Pre-position vehicles and having a fleet management program								
I Having flexible transportation with an operational mix of vehicles and transport mode, depending on the location and accessibility of disaster site								
J Risk awareness	√	√		√	√	√	√	√

crucial since time is important after a disaster. Knowing one’s role well will also help one make more informed decisions, especially when the situation is highly critical, and there is little time for decision-making.

4.3.2. *Risk Mitigation in Response Phase.* The response phase occurs immediately after a disaster strikes. Activities focus on saving lives and minimising disaster impacts and suffering of the impacted community [10, 48]. Based on Table 7, it was found that the top risks in the response phase are *demand risk* and *disruption risk*.

*Demand risk* occurs when disruptions arise from demand volatility. There is a gap between forecasted demand and the actual demand required. The projected demand is insufficient to fulfil the needs of affected beneficiaries. As a result, beneficiaries may not receive the required aid in time.

The response phase is the most life-critical phase in the DMC and is time-bound as dire consequences may occur when food and medical supplies are not delivered promptly. In the first 72 hours of disaster response, operation relief teams must be deployed to the ground to ascertain the relief needs to effectively obtain and deliver the required supplies to the beneficiaries [10]. This view was echoed by the informants in the interviews, as seen in the following quote,

Hence, considering the aforementioned, demand risk is the top risk that is highly likely to occur and has severe repercussions if it is not managed well.

*Disruption risks* are typically caused by natural and man-made disasters such as floods, earthquakes, and terrorist attacks. In the response phase, humanitarian relief operations are carried out in areas where the disaster occurred, and there may be high casualty numbers, coupled with improper conditions and limited constraints. This is made

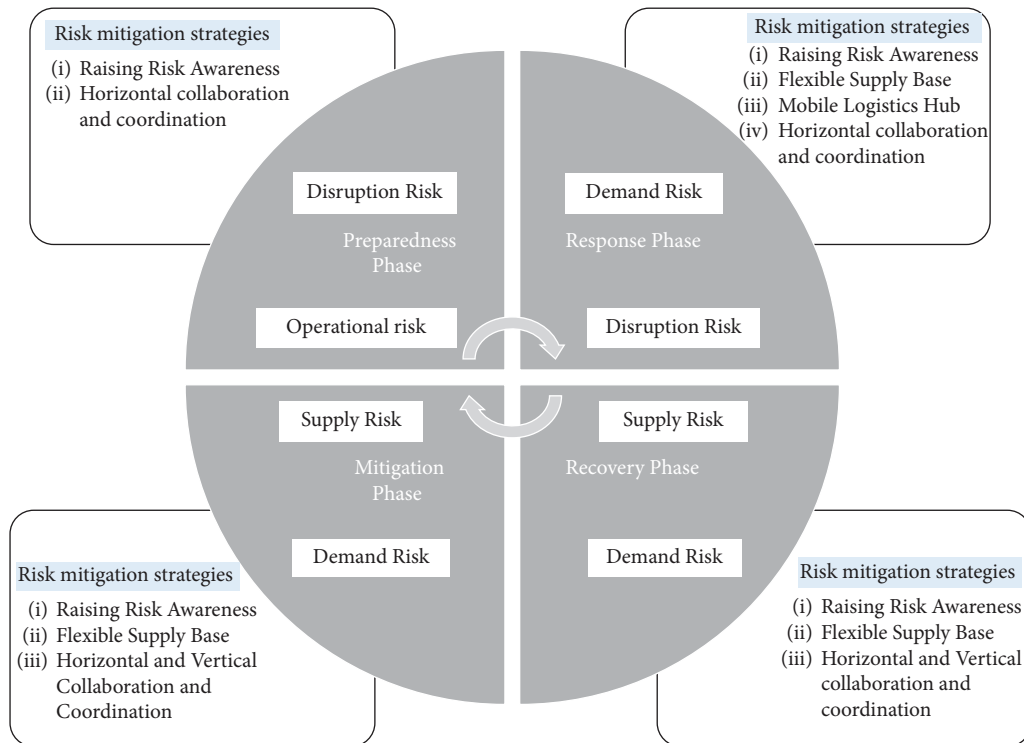


FIGURE 5: A conceptual framework identifying the dominant risks and supply chain risk mitigating strategies in the DMC phases.

worse when another disaster strikes after the initial one, such as aftershocks and landslides which are triggered by earthquakes and floods. Thus, it is inevitable that disruption risk is evident in the response phase and efforts need to be made to manage it well to reduce the repercussions.

To manage *demand risk*, organisations can adopt a flexible supply base. This includes having decentralised decision-making to allow for local adaptations. Decisions may be made on a smaller scale, possibly between smaller supply chain groups that manage their operations. Decisions can also be adapted to the local demand conditions of each area. This is unlike centralised decision-making, where decisions must account for the various operating structures and conditions different supply chain groups face. As organisations make decisions on a smaller scale, they may be better able to forecast the projected demand in different areas of a disaster-prone region and reduce demand volatility in the long term.

Other than having a flexible supply base, it is crucial to have horizontal collaboration and coordination among players in the response phase. Adopting horizontal collaboration capabilities enhances communication among the different stakeholders, which will help in the exchange of information sharing. This will facilitate information flow between the local communities and relevant stakeholders who deliver emergency supplies and enable effective disaster response management [6]. Even on occasions when projected demand is lower than the actual demand, the affected beneficiaries may still be able to receive aid in the fastest

possible time as there is proper communication and coordination among stakeholders. Hence, the two identified strategies will significantly manage demand fluctuations and risk in the response phase.

Three strategies are highly favoured to manage *disruption risk*. First, risk awareness should be advocated among stakeholders in the response phase. Relevant stakeholders must be aware of and understand disruption risk in the response phase. Stakeholders can only realise the urgency and need to collaborate to manage the disruption risk by first establishing awareness and understanding. The other strategy that can be adopted is locating mobile logistics hub (MLH) in affected regions. MLHs are “pre-designated for storing emergency logistics and telecommunication equipment” (see p.2 in [49]). One important consideration when locating an MLH is that the chosen location must be safe, yet still accessible and close to the disaster regions. The MLH serves as an operation centre where disaster relief supplies are managed and consolidated. If successfully implemented, the MLH can enhance the effectiveness and responsiveness of humanitarian supply chains, improving disaster response efforts.

Lastly, organisations can adopt a flexible supply base. It is a good practice that organisations have alternative sources. This view resonated with the interviewees in this study based on their rating of the appropriateness of the risk mitigation strategies. For instance, there can be various suppliers for an item, and organisations may consider different variations of the same item, as long as the item serves its intended

purpose. Such consideration will ensure that supplies can continue to reach vulnerable groups and affected communities in time of need, albeit from a different supplier or of a different variation.

*4.3.3. Risk Mitigation in Recovery Phase.* The recovery phase focuses on rehabilitation for the long term as the main objective is to restore the system as much as possible, reconstruct infrastructure, and rebuild the livelihoods of the impacted community [10, 24]. From Table 7, the top risks in the recovery phase are *supply risk* and *demand risk*.

*Supply risk* occurs due to the inconsistent performance from upstream supplies as a result of uncertainties associated with inbound supply, and this may, in turn, hinder product flow. Hence, this affects the number of supplies delivered to the impacted community and the corresponding time and cost required to transport the supplies. These supplies are crucial in helping the affected beneficiaries rebuild their houses and restore infrastructure in the community. More so, when another disaster hits during the rehabilitation period. The livelihoods of the impacted community are severely affected as they are constantly trapped in the cycle of rebuilding and rehabilitating infrastructure.

Supply and demand risk usually coexist. Thus, demand risk is also present in the recovery phase apart from supply risk. Delivering supplies and goods is paramount in the recovery phase, where the main objective is the rehabilitation of affected beneficiaries. Demand risks typically occur due to demand fluctuations that result from gaps between the actual and forecasted demand. These gaps exist due to the lack or breakdown of information sharing between the relevant stakeholders. As a result, information on required necessities and goods may not be communicated or relayed properly from affected beneficiaries to stakeholders like aid agencies, international NGOs, and donors. They all play an instrumental role in providing relief supplies in the recovery phase. Hence, this lack or breakdown of information flow will inevitably lead to the existence of demand risk in the recovery phase.

One important strategy in managing *supply risk* is risk awareness. Organisations that participate in the recovery phase have two main tasks on hand. They must ensure adequate support is given to the team for rehabilitative operations and proper resilience management [22]. However, these tasks can only be executed well if knowledge of the risk is present among stakeholders and they are aware of what to do during a product flow disruption.

Stakeholders would also be more prepared to provide the necessary support when they have adequate knowledge and awareness of the risk. Hence, this illustrates the importance of risk awareness in managing supply risk in the recovery phase. It is also essential to have horizontal collaboration and coordination among players in the recovery phase and vertical collaboration and coordination among other stakeholders in the DMC.

Such cooperation allows for joint planning among the stakeholders. This will significantly aid in integrating the

efforts and actions of the various players, especially when upstream product flow is disrupted. Apart from that, there would also be a deeper understanding of the community's vulnerabilities, which will go a long way in channelling the appropriate efforts in rebuilding and rehabilitation works.

One identified strategy to manage demand risk is to have flexible supply bases. Organisations can have separate co-operation agreements with various suppliers or service providers. This ensures that if high demand spikes and one supplier does not have sufficient supplies, alternative sources of relief goods are available from other supplies to fulfil the demand for necessities and other relief supplies.

Horizontal collaboration and coordination among players in the recovery phase and vertical collaboration and coordination among stakeholders in the DMC are also critical in managing demand risk. This will ensure accurate risk information sharing among all relevant stakeholders at different levels, aiding in effective recovery efforts. These collaboration and coordination capabilities will also allow stakeholders to have greater knowledge of each player's resources and skills. They may utilise resources and potential complementary skills most efficiently and effectively.

*4.3.4. Risk Mitigation in Mitigation Phase.* The objective of the mitigation phase is to deter potential hazards from becoming disasters and minimise any potential adverse disaster impacts through adopting preventive measures [10]. One important consideration when planning mitigation strategies is the demand and supply of goods and emergency supplies needed when disasters strike. Activities range from strategic-level decisions like policy determination to operational-level ones like discerning the most appropriate transportation route for hazardous materials [48]. Based on Table 6, it is found that *supply risk* and *demand risk* are the top risks in the mitigation phase. This requires considerable coordination and collaboration among stakeholders to ensure that disruptions from demand volatility and inbound flow of supplies are minimised. Thus, relevant stakeholders must consider supply and demand risks when planning mitigation strategies to reduce the community's vulnerability in disaster-prone regions and limit the damages caused by disasters.

Risk awareness is central to managing *supply risk* and *demand risk*. In the mitigation phase, various stakeholders like governments and local NGOs must develop a collective strategy to reduce negative disaster impacts. Such strategies are crucial in preventing disaster hazards. However, developing these strategies requires significant understanding and knowledge of the risks faced by the affected community. Thus, risk awareness is crucial so that appropriate mitigation strategies can be planned and developed to target critical risks.

A flexible supply base also helps in managing *supply risk*. In this regard, organisations can discern suppliers who pose the most significant risk or are likely to have operations disrupted and those whose operations are least likely to be interrupted. Thereafter, organisations can initiate cooperation agreements with the latter group and other suppliers



who can provide supplies to minimise the risk of operational disruptions. Organisations may also diversify the supplies of the various types of items to mitigate supply risk.

To manage *demand risk*, other than risk awareness, it is also necessary to have horizontal collaboration and coordination among players in the mitigation phase and vertical collaboration and coordination among stakeholders in the DMC. Apart from driving information sharing, establishing partnerships will also allow for programme activities to be integrated and carried out at different levels, such as the national and state levels. It would also help to ensure that there will not be any overlap of plans for the same group of beneficiaries, which will help save resources for other purposes.

## 5. Concluding remarks and Future Research

The findings from this study revealed specific risks in the DMC's preparedness, response, recovery, and mitigation phases and suggested appropriate risk mitigation strategies for each phase. Overall, we found several risk factors resonate strongly in each DMC phase. They are demand risk, supply risk, operational risk, infrastructure risk, and disruption risk, with only the infrastructure risk absent in the mitigation phase.

From the study, it appears that risk awareness and horizontal collaboration and coordination among players involved in the same phase of the DMC and vertical collaboration and coordination among players involved in different phases of the DMC are essential and fundamental for risk mitigation in the DMC. These strategies were found in separate frameworks in Jahre [11] and Scholten et al. [22]. Yet, the above discussion showed that there are overlapping themes in the frameworks which resonated with each other.

Risk awareness is crucial, and actionable plans such as close and strategic collaboration and coordination are essential components of risk mitigation. This study highlighted that all stakeholders must be wary of the five risks in the DMC. More importantly, there should be collaboration and coordination among stakeholders across levels and at different levels to better manage risks in the DMC, as reflected succinctly by the informants in the interviews:

*"... horizontal and vertical collaboration and coordination. They go hand-in-hand with each other and one cannot do without another"*

These cooperation capabilities will go a long way in enabling effective and efficient disaster responses and preparedness plans.

**5.1. Theoretical and Practical Implications.** In our research, we have focused on providing granularity to the knowledge in the DMC by integrating theories from conventional supply chain risk management and mitigation strategies. This article contributes in three ways. First, we provide a theoretical linking of supply chain risk management literature with the DMC by using two bodies of literature, the

DMC and supply chain risk mitigation strategies (SCSs), in developing a conceptual framework for the study. Second, we identified the dominant risk factors in the four phases of the DMC. Third, we add to the extant literature by developing a conceptual framework that links the risk factors, SCSs, and DMC that are expected to aid risk mitigation in humanitarian supply chain and disaster management. The conceptual framework presented in Figure 5 can be used to prioritise risks, guide decision-making, and develop risk mitigation policies in the DMC.

Overall, the findings from this study offer valuable insights and deepen the understanding of risk management strategies in the DMC. The findings could be extended to different types of humanitarian organisations and NGOs. Nonetheless, it is vital to accord attention to variant contextual needs in distinct humanitarian circumstances in each phase of the DMC so that optimal actions can be taken to meet the needs of the beneficiaries.

**5.2. Limitations and Future Research.** While the study addressed salient issues pertinent to risk management in the DMC, our research has several limitations that can be explored in future studies. First, though our research primarily targeted representative humanitarian operations and DMC stakeholders, we only managed to gather 25 valid questionnaire responses that were corroborated by three independent semi-structured interviews due to the limited data collection time frame. Although the computed risk scores are relative values based on the informants' perceptions, it nonetheless enables the identification of the dominant risks in each DMC phase. Further research can collect quantitative data to validate the conceptual framework. Longitudinal data over an extended period of disaster management could help generate deeper insights across a more extensive network of respondents in the DMC that is lacking in this study.

Second, this study focused on identifying the top risks in each disaster phase. Further studies can examine other risk factors to shed insights into areas that humanitarian practitioners may overlook. Lastly, the risk score values were averaged from the respondents' inputs, and the identified strategies were weighted based on the general responses from respondents. Future studies can explore other research approaches, such as case analyses of exemplary scenarios, to deepen the understanding of recurrent and common scenarios among the DMC phases. Overall, the findings from this article can be used as a basis for future studies to deepen the knowledge of supply chain risk management and resiliency in the HLSCM context.

## Data Availability

The questionnaire responses and interview transcripts used to support the findings of this study have not been made available to protect the interest and confidentiality of the research informants and organisational identities that were studied. Public archival data and the literature used to support the findings of this study are included within the article.

## Conflicts of Interest

The authors declare that they have no conflicts of interest.

## References

- [1] E. M. Guzman, *Towards Total Disaster Risk Management Approach*, A D R C, 2004.
- [2] M. A. Ülkü, K. M. Bell, and S. G. Wilson, "Modeling the impact of donor behavior on humanitarian aid operations," *Annals of Operations Research*, vol. 230, no. 1, pp. 153–168, 2015.
- [3] D. M. Neal, "Reconsidering the phases of disasters," *International Journal Of Mass Emergencies And Disasters*, vol. 15, no. 2, pp. 239–264, 1997.
- [4] A. O'Keefe Baird, K. Westgate, and B. Winsler, "Towards an explanation and reduction of disaster proneness, Occasional Papers, No. 11," *University of Bradford, Disaster Research Unit, Bradford*, 1975.
- [5] W. N. Carter, "Disaster management: a disaster manager's handbook," 2008, <http://hdl.handle.net/11540/5035.0%20License:%20CC%20BY%203.0%20IGO>.
- [6] J. Q. Zhang, N. Okada, and H. Tatano, "Integrated Natural Disaster Risk Management: Comprehensive and integrated model and Chinese strategy choice," *Journal of Natural Disasters*, vol. 15, no. 1, pp. 29–37, 2006.
- [7] A. Cozzolino, "Humanitarian logistics and supply chain management," in *Humanitarian Logistics. SpringerBriefs in Business*, Springer, Berlin, Heidelberg, 2012.
- [8] M. Jahre, "Humanitarian Supply Chain Strategies - a Review of How Actors Mitigate Supply chain risks," *Journal of Humanitarian Logistics and Supply Chain Management*, vol. 7, no. 2, pp. 82–101, 2017.
- [9] C. J. Chiappetta Jabbour, V. A. Sobreiro, A. B. Lopes de Sousa Jabbour, L. M. de Souza Campos, E. B. Mariano, and D. W. S. Renwick, "An analysis of the literature on humanitarian logistics and supply chain management: paving the way for future studies," *Annals of Operations Research*, vol. 283, no. 1, pp. 289–307, 2019.
- [10] B. Balcik, B. M. Beamon, C. C. Krejci, K. M. Muramatsu, and M. Ramirez, "Coordination in humanitarian relief chains: practices, challenges and opportunities," *International Journal of Production Economics*, vol. 126, no. 1, pp. 22–34, 2010.
- [11] G. Kovács and K. M. Spens, "Identifying challenges in humanitarian logistics," *International Journal of Physical Distribution & Logistics Management*, vol. 39, no. 6, pp. 506–528, 2009.
- [12] J. M. Day, S. A. Melnyk, P. D. Larson, E. W. Davis, and D. C. Whybark, "Humanitarian and disaster relief supply chains: a matter of life and death," *Journal of Supply Chain Management*, vol. 48, no. 2, pp. 21–36, 2012.
- [13] D. McLoughlin, "A framework for integrated emergency management," *Public administration review*, vol. 45, pp. 165–172, 1985.
- [14] N. Kapucu, "Disaster and emergency management systems in urban areas," *cities*, vol. 29, pp. S41–S49, 2012.
- [15] C. B. Field, Ed., *Managing the Risks of Extreme Events and Disasters to Advance Climate Change Adaptation: Special Report of the Intergovernmental Panel on Climate Change*, Cambridge University Press, Cambridge, UK, 2012.
- [16] M. C. Hoyos, R. S. Morales, and R. Akhavan-Tabatabaei, "Or models with stochastic components in disaster operations management: a literature survey," *Computers & Industrial Engineering*, vol. 82, pp. 183–197, 2015.
- [17] J. H. Powell, N. Mustafee, A. S. Chen, and M. Hammond, "System-focused risk identification and assessment for disaster preparedness: dynamic threat analysis," *European Journal of Operational Research*, vol. 254, no. 2, pp. 550–564, 2016.
- [18] B. Martinho and J. Reis, "United Nations (UN) disaster risk reduction framework: case study of the Portuguese army on UN challenges in the context of sustainable risk mitigation," *Sustainability*, vol. 14, no. 3, p. 1834, 2022.
- [19] M. Heazle, P. Tangney, P. Burton et al., "An analysis of the literature on humanitarian logistics and supply chain management: paving the way for future studies," *Annals of Operations Research*, vol. 283, pp. 1–19, 2017.
- [20] R. M. Tomasini and L. N. Van Wassenhove, "From preparedness to partnerships: case study research on humanitarian logistics," *International Transactions in Operational Research*, vol. 16, no. 5, pp. 549–559, 2009.
- [21] F. Maon, A. Lindgreen, and J. Vanhamme, "Developing supply chains in disaster relief operations through cross-sector socially oriented collaborations: a theoretical model," *Supply Chain Management: International Journal*, vol. 14, no. 2, pp. 149–164, 2009.
- [22] K. Scholten, P. Sharkey Scott, and B. Fynes, "Mitigation Processes - Antecedents for Building supply chain resilience," *Supply Chain Management: International Journal*, vol. 19, no. 2, pp. 211–228, 2014.
- [23] R. Banomyong, P. Julagasingorn, P. Varadejsatitwong, and P. Piboonrungraj, "The humanitarian supply chain assessment tool (HumSCAT)," *Journal of Humanitarian Logistics and Supply Chain Management*, vol. 9, no. 2, pp. 221–249, 2019.
- [24] L. N. Van Wassenhove, "Humanitarian aid logistics: supply chain management in high gear," *Journal of the Operational Research Society*, vol. 57, no. 5, pp. 475–489, 2006.
- [25] F. Sabouhi, A. Bozorgi-Amiri, M. Moshref-Javadi, and M. Heydari, "An integrated routing and scheduling model for evacuation and commodity distribution in large-scale disaster relief operations: a case study," *Annals of Operations Research*, vol. 283, no. 1–2, pp. 643–677, 2019.
- [26] J. G. March and Z. Shapira, "Managerial perspectives on risk and risk taking," *Management Science*, vol. 33, no. 11, pp. 1404–1418, 1987.
- [27] M. Goh, J. Y. Lim, and F. Meng, "A stochastic model for risk management in global supply chain networks," *European Journal Of Operational Research*, vol. 182, no. 1, pp. 164–173, 2007.
- [28] T. Kull and D. Closs, "The risk of second-tier supplier failures in serial supply chains: implications for order policies and distributor autonomy," *European Journal of Operational Research*, vol. 186, no. 3, pp. 1158–1174, 2008.
- [29] U. Jüttner, H. Peck, and M. Christopher, "Supply chain risk management: outlining an agenda for future research," *International Journal of Logistics Research and Applications*, vol. 6, no. 4, pp. 197–210, 2003.
- [30] H. Peck, "Reconciling supply chain vulnerability, risk and supply chain management," *International Journal of Logistics Research and Applications*, vol. 9, no. 2, pp. 127–142, 2006.
- [31] Y. Daultani, S. Kumar, O. S. Vaidya, and M. K. Tiwari, "A supply chain network equilibrium model for operational and opportunism risk mitigation," *International Journal of Production Research*, vol. 53, no. 18, pp. 5685–5715, 2015.
- [32] A. Samvedi, V. Jain, and F. T. Chan, "Quantifying Risks in a Supply Chain through Integration of fuzzy AHP and fuzzy

- TOPSIS,” *International Journal of Production Research*, vol. 51, no. 8, pp. 2433–2442, 2013.
- [33] O. Tang and N. Musa, “Identifying Risk Issues and Research Advancements in Supply chain Risk management,” *International Journal of Production Economics*, vol. 133, no. 1, pp. 25–34, 2011.
- [34] W. Ho, T. Zheng, H. Yildiz, and S. Talluri, “Supply chain risk management: a literature review,” *International Journal of Production Research*, vol. 53, no. 16, pp. 5031–5069, 2015.
- [35] R. McLachlin, P. D. Larson, and S. Khan, “Not-for-profit supply chains in interrupted environments: the case of a faith-based humanitarian relief organisation,” *Management Research News*, 2009.
- [36] G. L. Schlegel and R. J. Trent, *Supply Chain Risk Management: An Emerging Discipline*, CRC Press, Boca Raton, FL, USA, 2019.
- [37] G. A. Zsidisin, “A grounded definition of supply risk,” *Journal of Purchasing and Supply Management*, vol. 9, no. 5–6, pp. 217–224, 2003.
- [38] S. M. Wagner and C. Bode, “An empirical examination of supply chain performance along several dimensions of risk,” *Journal of Business Logistics*, vol. 29, no. 1, pp. 307–325, 2008.
- [39] S. Chopra and M. S. Sodhi, “Managing risk to avoid supply-chain breakdown,” *MIT Sloan Management Review*, vol. 46, pp. 53–62, 2004.
- [40] T. Wu, J. Blackhurst, and V. Chidambaram, “A model for inbound supply risk analysis,” *Computers in Industry*, vol. 57, no. 4, pp. 350–365, 2006.
- [41] M. S. Sodhi, B. G. Son, and C. S. Tang, “Researchers’ perspectives on supply chain risk management,” *Production and Operations Management*, vol. 21, pp. 1–13, 2012.
- [42] I. H. Sawalha, “A contemporary perspective on the disaster management cycle,” *Foresight*, vol. 22, no. 4, pp. 469–482, 2020.
- [43] J. P. Minas, N. C. Simpson, and Z. Y. Tacheva, “Modeling emergency response operations: a theory building survey,” *Computers & Operations Research*, vol. 119, Article ID 104921, 2020.
- [44] M. Saunders, P. Lewis, and A. Thornhill, *Research Methods*, Business Students 4th edition Pearson Education Limited, England, UK, 2007.
- [45] R. De Souza, M. Goh, and F. Meng, *A Risk Management Framework for Supply chain networks, networks*, pp. 1–19, TLI – Asia Pacific White Paper Series, 2007.
- [46] R. Tummala and T. Schoenherr, “Assessing and managing risks using the supply chain risk management process (SCRMP),” *Supply Chain Management: An International Journal*, vol. 16, no. 6, pp. 474–483, 2011.
- [47] A. Cozzolino, “Humanitarian logistics and supply chain management, Humanitarian Logistics,” *Springer Briefs in Business*, Springer, Berlin, Heidelberg, 2012.
- [48] M. Celik, O. Ergun, B. Johnson et al., “Humanitarian Logistics,” *INFORMS Topical Reviews in Operations Research*, pp. 18–49, 2012.
- [49] R. Maharjan, Y. Shrestha, B. Rakhal, and S. Suman, “Mobile Logistics Hubs (MLHs) pre-Positioning for emergency preparedness and response,” 2019, <https://docs.wfp.org/api/documents/WFP-0000105800/download/>.

## Research Article

# Reduction of Seepage Risks by Investigation into Different Lengths and Positions for Cutoff Wall and Horizontal Drainage (Case Study: Sattarkhan Dam)

Widodo Brontowiyono <sup>1</sup>, Ali T. Hammid <sup>2</sup>, Yasir M. Jebur <sup>3</sup>,  
Ahmed Q. A. S. Al-Sudani <sup>4</sup>, Dhameer A. Mutlak <sup>5</sup> and Masoud Parvan <sup>6</sup>

<sup>1</sup>Universitas Islam Infonesia, Yogyakarta, Indonesia

<sup>2</sup>Imam Ja'afar Al-Sadiq University, Baghdad, Iraq

<sup>3</sup>Al-Mustaqbal University College, Babylon, Iraq

<sup>4</sup>Al-Manara College, Misan, Iraq

<sup>5</sup>Al-Nisour University College, Baghdad, Iraq

<sup>6</sup>University of Tabriz, Tabriz, Iran

Correspondence should be addressed to Masoud Parvan; [masoud.parvan@yahoo.com](mailto:masoud.parvan@yahoo.com)

Received 21 April 2022; Revised 9 August 2022; Accepted 23 August 2022; Published 25 September 2022

Academic Editor: Baki Ozturk

Copyright © 2022 Widodo Brontowiyono et al. This is an open access article distributed under the Creative Commons Attribution License, which permits unrestricted use, distribution, and reproduction in any medium, provided the original work is properly cited.

Seepage from the earth dam's body reduces the amount of water in the dam's reservoir and threatens its stability. In this paper, the earth-type Sattarkhan Dam on the Aharchai River has been investigated. In this regard, the SEEP/W model from the GeoStudio 2018 software suite was used for modeling. This study examines the effects of various lengths and positions of cutoff wall and horizontal drainage on seepage, uplift pressure, and exit gradient. Increasing the length of the cutoff wall reduces seepage in both sections, with a more significant effect on Section 2; it also decreases the uplift pressure and the exit gradient. Changing the position of the cutoff wall has a significant effect on seepage fluctuations in Section 1 but has no effect on seepage in Section 2; in positions 2 to 7, the uplift pressure values are nearly identical, and the exit gradient is most significant at position 1 and least at position 2. Increasing the horizontal drainage's length increases seepage, reduces uplift pressure, and increases the exit gradient. The closer proximity of the horizontal drainage position to the dam's core increases seepage and decreases uplift pressure and exit gradient. Finally, it is concluded that the construction of a cutoff wall and horizontal drainage with appropriate lengths and positions reduces risk and improves the stability of earth dams.

## 1. Introduction

Engineers and geotechnical specialists are interested in constructing earthen dams [1]. Due to their high environmental compatibility and ability to be constructed on a softer bed, these types of dams have been widely used in Iran [2]. The dam's construction creates a significant hydraulic gradient upstream of the dam relative to downstream. This increases the likelihood that water will seep into the dam and move downstream [3]. Seepage control methods should reduce the amount of water seepage and minimize the risk of

damage from slope instability, washout, or scouring of refined grains [4].

The following are methods for reducing seepage in the body and foundation of an earth dam: (a) use of the core with very low permeability in the dam body; (b) use of the blanket on the upstream surface; (c) use of the cutoff wall in the dam foundation; (d) use of the grout curtain in the foundation; and (e) use of a layer with very low permeability at the bottom of the reservoir [5, 6]. Due to economic factors, cutoff walls are currently trendy. Water seepage downstream of dams can be observed in the form of increased humidity,

soil softening, and increased vegetation, as well as increased spring discharge and rising groundwater piezometric levels [7, 8].

For earth dams, using the cutoff wall is one way to seal the dam. Given that the construction of this cutoff wall affects the seepage and stability of the earth dam, its proper placement and length are among the most important factors to consider [9]. Using the SEEP/W model, the current study investigates the position and various lengths of the cutoff wall to improve the sealing of the earth dam. Different states of cutoff wall and horizontal drainage curtains in earth dams have been studied in order to increase the efficiency of dams and reduce the damage caused by seepage. Different states of cutoff wall and horizontal drainage and their effects on changes in uplift pressure and the piping phenomenon have been studied. As a result, the position and different lengths of cutoff wall and horizontal drainage for various situations have been determined.

First, the required data and information were obtained from the Regional Water Company of East Azerbaijan Province; then, modeling was conducted using the SEEP/W model in the GeoStudio software [10]. In the continuation of the study, the desired outputs from the model are extracted, and the outcomes are discussed. The first step in numerical simulation is selecting an appropriate numerical model for the subject. Due to the capabilities of the SEEP/W model in seepage simulation, this model has been utilized in the current study. The SEEP/W model is one of the GeoStudio software models that can simulate the flow in the soil environment under all possible conditions using the finite element method [11, 12].

Seepage paths in earth dam bodies, foundations, and abutments are affected by a variety of factors, including (a) embankment cracking caused by subsidence or displacement of foundations and abutments; (b) ineffective filters and drains; (c) improper connection of embankment to foundation or embankment to abutments; (d) permeable or soluble materials in the embankment; and (e) the presence of an alluvial layer or permeability in [36, 37].

Failure of dams and their foundations is caused by the problems and adverse effects of seepage; these effects include (A) high and uncontrolled exit gradient, (b) piping, (c) uplift or breaking of the slope due to seepage forces, (d) exit of large volumes of water, and (e) uplift force effects [15]. Excess and uncontrolled gradients will cause soil particles to float at the dam's base. Soil leaching may occur if the hydraulic gradient in the water seepage section increases downstream from the slope of the dam body [16]. Initially, the fine grains leach; as these particles leach, the soil's resistance to flow decreases, and the hydraulic gradient rises. As the hydraulic gradient increases, coarse grain particles are leached, and soil erosion accelerates, forming dam tunnels [17]. Due to seepage from the dam body, water may emerge from the downstream surface at high elevations, followed by dam failure. Due to seepage, a substantial amount of water may permeate downstream from the dam's body and foundation, rendering it economically unjustifiable [18]. The most critical design consideration is the influence of uplift force on the stability of a structure and its foundation. Dam

designers must have a realistic understanding of the flow conditions to detect the resulting forces [19].

Seepage analysis is required to determine the values of seepage flow, pore water pressure, uplift pressure, hydraulic gradient control, and scouring phenomena. Darcy initiated severe soil studies on seepage in 1856 [20, 21]. Darcy conducted sand-based experiments and presented the results as an empirical law. Darcy's law remains the foundation of seepage studies. Combining Darcy's law and the continuity equation yields (1) as the fundamental relation of steady-state flow seepage in a three-dimensional state [22, 23].

$$k_x \frac{\partial^2 h}{\partial x^2} + k_y \frac{\partial^2 h}{\partial y^2} + k_z \frac{\partial^2 h}{\partial z^2} = 0, \quad (1)$$

where  $h$  is the piezometric height,  $k_x$  is the permeability coefficient in the  $x$ -direction,  $k_y$  is the permeability coefficient in the  $y$ -direction, and  $k_z$  is the permeability coefficient in the  $z$ -direction.

Researchers have investigated seepage and its effects on earthen dams using various models and software. Mansuri et al. [24] investigated the effects of different locations and angles of the cutoff wall under a hypothetical dam on the uplift pressure. According to the findings, cutoff wall inclination reduces the uplift pressure. Mortazavi and Solaimani [25] by investigating the seepage from an earthen dam discovered that if the cutoff wall is positioned at the dam's base, it will be more effective at reducing seepage, and the exit hydraulic gradient will be approximately three-fourths of the critical hydraulic gradient. Nourani et al. [26] used a numerical model to find the optimal location of vertical drains in gravity dams. The result showed that the optimal location of vertical drains is not constant; as the distance between vertical drains increases and the diameter of the drain decreases, the optimal location of vertical drains moves downstream. Hekmatzadeh et al. [27] examined the impact of four cutoff walls on the stability and dependability of diversion dams against the boiling phenomenon. Increasing the shear resistance parameter of the surface between the soil and the barrier decreased the probability of dam failure, while increasing the horizontal coefficient of the earthquake significantly increased the likelihood of failure. Al-Mansori et al. [28], by investigating seepage in the earthen dam, concluded that the clay core significantly reduces the seepage and the existing gradient. Testing the effect of the anisotropy ratio on seepage revealed that an increase in the ( $k_x/k_y$ ) ratio increases the amount of seepage. Toumi and Remini [29], by evaluating the geology and hydrogeology of the water leakage in Hammam-Grouz Dam, concluded that sealing materials are the most appropriate technique. Having the same characteristics as waterproofing areas and adapting adequately to their geological formations, assigning sealing works to a highly qualified subcontractor is crucial to achieving satisfactory sealing results for the structure to function correctly. Hassan et al. [30] analyzed the transient seepage and slope stability of sandy and extremely silty sand soils. According to the numerical results, fine particles increase pore water pressure and decrease FOS. The design and maintenance of dikes are contingent on the

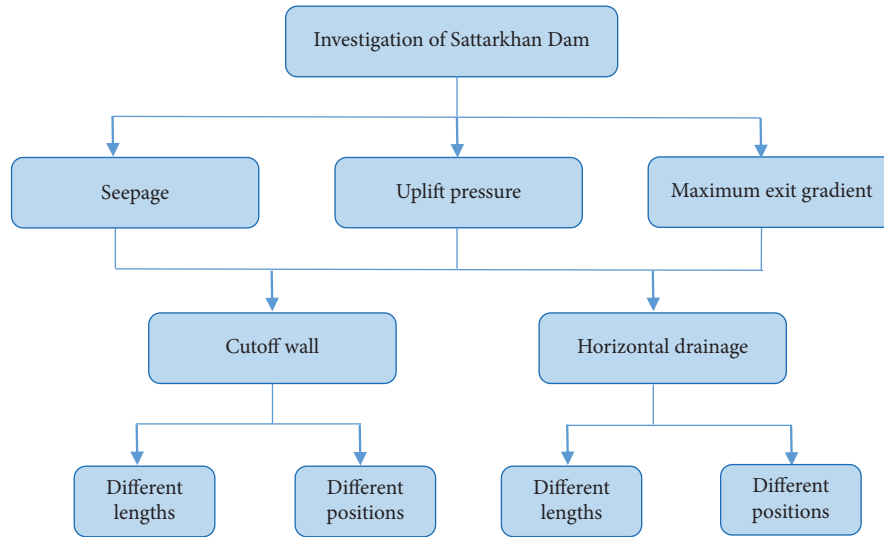


FIGURE 1: General structure of the study.

surrounding hydraulic conditions, dimensions, and soil types. Fine-particle, noncohesive materials were preferred. According to the literature review, various researchers have studied seepage in earthen dams. The main difference between this study and other research is the current study's comprehensive approach; different parameters, including seepage, uplift pressure, and maximum exit gradient, have been investigated.

The current study investigates the steady-state condition of an earth-fill dam (Sattarkhan Dam). The seepage values in two sections, the uplift pressure below the dam core and the maximum exit gradient at the dam claw, are extracted. Various states associated with varying lengths and positions of the cutoff wall and horizontal drainage have been evaluated to investigate these values. Detailed descriptions of the models under consideration are provided in the following sections. Figure 1 depicts the overall structure of this investigation. Analyzing the desired parameters can reduce the risks associated with earthen dams. These risks include the unintended reduction of water in the dam lake, the formation of cracks and dam failures, the dam's overturning, and the formation of piping phenomena within the dam.

Figure 2 shows the locations under review, including Sections 1 and 2 (to investigate seepage), under the dam core (to investigate uplift pressure) and the dam's claw (to exit gradient investigation). These parameters were selected to investigate the various causes of seepage and failure in earthen dams and to provide a comprehensive perspective to the readers of this article. In numerous studies, only one of the desired parameters was examined. All three parameters were examined simultaneously because the phenomena of uplift pressure and piping are closely related to percolation and percolation-influencing factors. In addition, each of the mentioned parameters generates a unique type of failure, necessitating a concurrent examination due to their close relationship. Due to the extensive use of cutoff walls and drains in Iran's earthen dams, the current study has investigated the cases mentioned.

It is necessary to reduce the dam's risk because of its high cost and fundamental role in meeting various needs. Therefore, maintaining the dam's stability and minimizing the water that escapes behind it are crucial. The present study's novelty resides in examining various associated parameters (including seepage, uplift pressure, and maximum exit gradient). The current study's objective is to examine the effect of various lengths and positions of the cutoff wall and horizontal drainage on the parameters mentioned above, thereby reducing seepage risks.

## 2. Materials and Methods

This section presents the studied dam's specifications first, followed by the numerical methods, software, and model. Finally, the dam's initial model is investigated.

**2.1. Case Study.** In the current study, the Sattarkhan Dam is considered a case study; the Aharchai River is situated within the dam. This river flows south of the city of Ahar before reaching the Aras River and, ultimately, the Khazar Sea. The geographic location of Sattarkhan Dam is shown in Figure 3. With the construction of the Sattarkhan Dam, while controlling and regulating the surface flows of the Aharchai River, a portion of the agricultural lands downstream of the dam was supplied with the necessary water, and the city of Ahar was supplied with potable water. The average annual flow of the Aharchai River at the dam site is 92 million cubic meters, with a catchment area of 950 square kilometers. Construction of the Sattarkhan Dam began in 1994 and was completed in 1997. The Sattarkhan Dam is made of Earth. Figure 4 shows the dam's various components. Also, to give an overview and more understanding of the physical characteristics of the dam, the general physical characteristics of Sattarkhan Dam are presented in Table 1.

The permeability of materials used in Sattarkhan Dam is shown in Table 2. Also, the values related to the

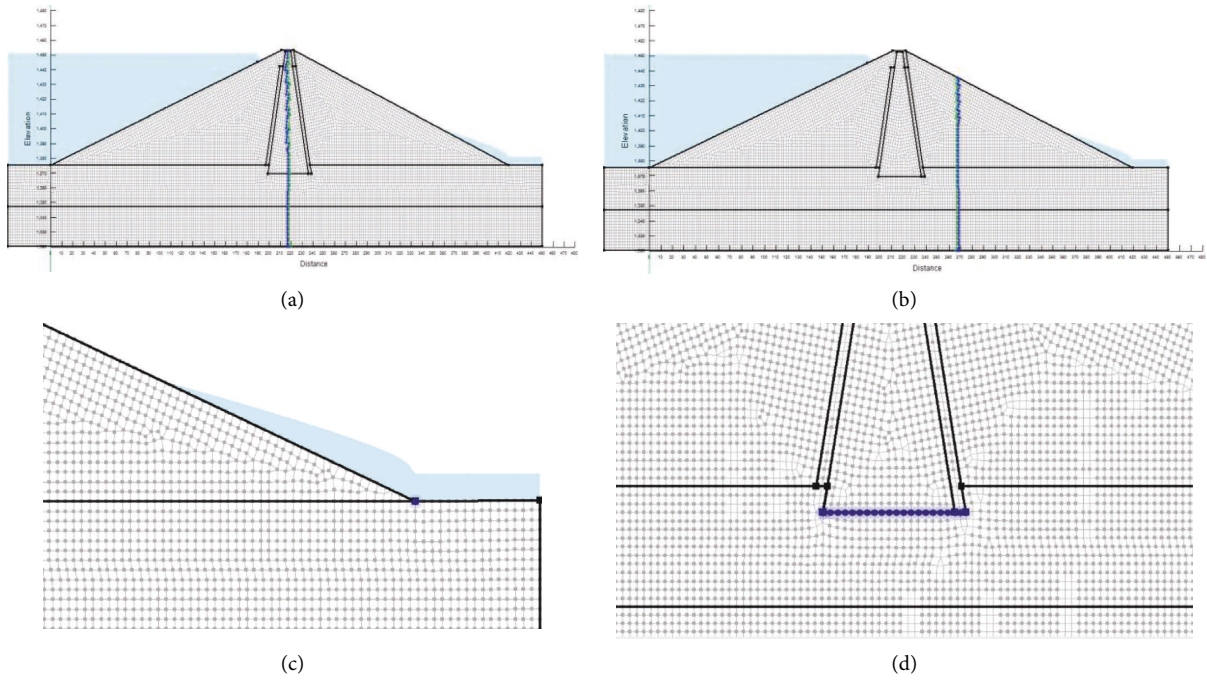


FIGURE 2: The studied locations. (a) Section 1. (b) Section 2. (c) Under the dam core. (d) Claw of the dam.

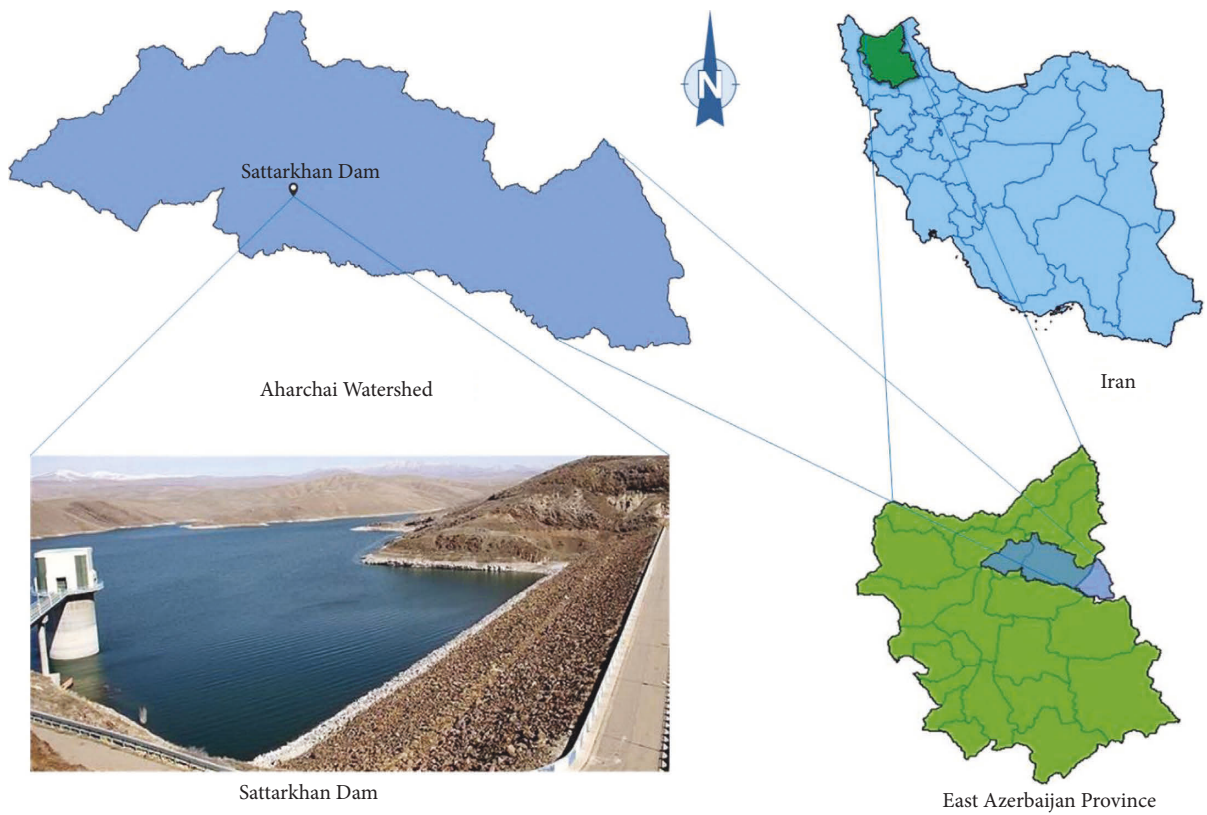


FIGURE 3: The geographic location of Sattarkhan Dam.

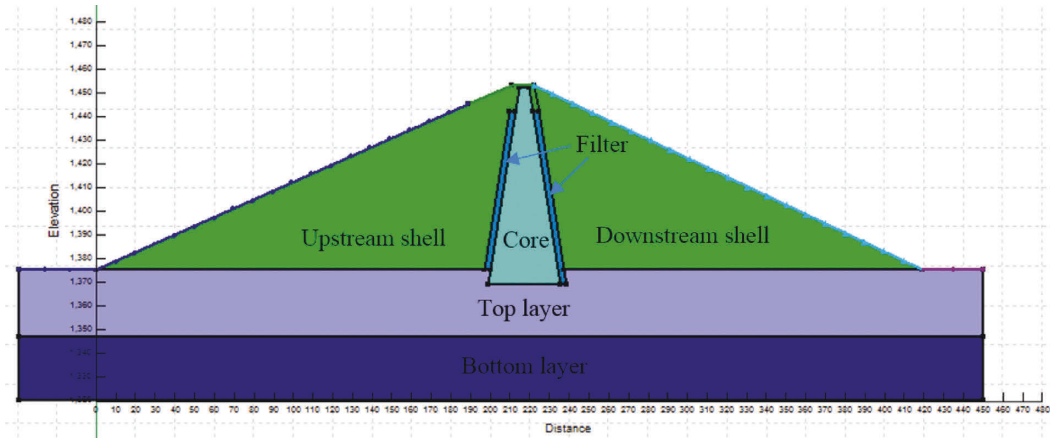


FIGURE 4: Different components of Sattarkhan Dam.

TABLE 1: General physical characteristics of Sattarkhan Dam.

Physical characteristics of the dam	Description
Dam type	Earth dam
Usage of dam	Providing water for a portion of the agricultural lands downstream of the dam and drinking water in Ahar city
Height of dam	1459 meters above sea level
Width of dam	350 meters
Maximum water level	1451 meters above sea level
Dam capacity	The reservoir's normal water level volume is 135 million cubic meters, and its useful volume is 120 million cubic meters
Type of spillway	Lateral free overflow with valve

TABLE 2: The permeability values of Sattarkhan Dam materials.

Type of the material	$K_x$ (m/s)	$K_x/k_y$
Core	$1 \times 10^{-8}$	0.1
Cutoff wall	$2 \times 10^{-7}$	1.0
Shell	$1 \times 10^{-5}$	0.1
Drainage	$3 \times 10^{-3}$	1.0
Filter	$1 \times 10^{-4}$	1.0
Top layer	$5 \times 10^{-6}$	1.0
Bottom layer	$1 \times 10^{-6}$	1.0

specifications of other dam components are presented in Table 3.  $K_x$  and  $k_y$  represent the permeability along axes 1 and 2, respectively;  $\rho$  is the density,  $E$  is the modulus of elasticity,  $C$  is the stickiness,  $\phi$  is the friction angle,  $\Psi$  is the expansion angle, and  $\nu$  is Poisson's ratio in Tables 2 and 3.

**2.2. Numerical Methods.** Because the differential equations of seepage cannot be solved analytically except in exceptional cases and with elementary boundary conditions, numerical methods for seepage analysis have become widespread in recent years and provide more precise results than other methods. Finite Element Methods, Finite Differences, and Boundary Element Methods are standard numerical methods for solving the flow equations [31, 32].

**2.2.1. Finite Element Method.** The Finite Element Method is a numerical instruction for solving differential equation-described physical problems. This method is distinguished from other numerical methods by two characteristics: (a) An integral formulation is used to generate a system of algebraic equations and (b) in this method, continuous smooth functions are employed to approximate unknown quantities [33, 34].

**2.2.2. SEEP/W Model.** SEEP/W is one of Geostudio's models based on the finite element method [35]. The model is a specific analytical technique that can model the flow in saturated and unsaturated states. This model's ability to simulate flow in an unsaturated environment has resulted in more realistic conditions than other models. In soils, the permeability coefficient of materials and the volume of water depend on the change in pore water pressure [36]. SEEP/W treats these relationships as continuous functions and computes them, whereas many other modeling systems cannot do so [37]. The general steps of modeling are presented in Figure 5.

Finally, we prepare the model for Finite Element analysis by dividing the plotted areas into more minor elements. The type of mesh can be selected from the Mesh menu. To achieve more precise results, a length of 2 m was considered for the elements in this study.



TABLE 3: Characteristic values of SattarKhan Dam materials.

Type of the material		$\rho$ (kg/m <sup>3</sup> )	$E$ (N/m <sup>2</sup> )	$C$ (KPa)	$\varphi$	$\Psi$	$\nu$
Core	CD	2030	$1 \times 10^7$	45	37	0	0.3
	CU	2030	$1 \times 10^7$	65	33	0	0.3
	UU	2030	$1 \times 10^7$	80	10	0	0.3
Shell		2100	$1 \times 10^8$	0	40	10	0.3
Drainage and filter		1560	$2.5 \times 10^7$	0	36	0	0.3
Top and bottom layers		2200	$1 \times 10^{10}$	750	50	8	0.3

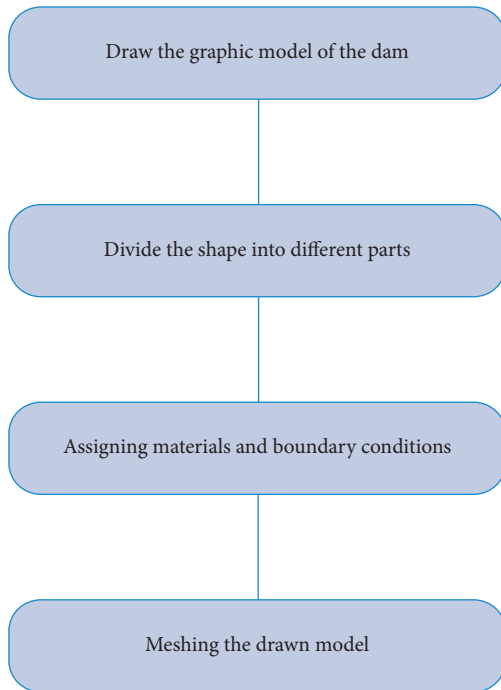


FIGURE 5: The general steps of modeling.

### 3. Results and Discussion

In this section, the software’s results are evaluated and discussed. Different lengths and positions of the horizontal drainage and cutoff wall are investigated for this purpose. Investigated are the seepage parameters that pass through the two desired body sections: the values related to the uplift pressure below the core and the exit gradient at the dam’s toe.

**3.1. The Effect of Different Lengths of Cutoff Wall.** This section investigates the effects of various cutoff wall lengths on various parameters. For this purpose, the location of the heel dam core has been considered, and different lengths of 0, 5, 10, 15, and 20 meters have been studied (the numbers used to check the length of the cutoff were chosen depending on the depth of the foundation’s upper layer). For each case, distinct seepage values in Sections 1 and 2 are extracted and compared. The values of the uplift pressure and the exit gradient are extracted and compared. Table 4 displays the

TABLE 4: The values of the parameters in the initial state.

Parameter	Value
Total seepage from Section 1 (m <sup>3</sup> /s/m <sup>2</sup> )	0.019899
Total seepage from Section 2 (m <sup>3</sup> /s/m <sup>2</sup> )	0.017735
Average uplift pressure (MPa)	502.35
Exit gradient	0.96888

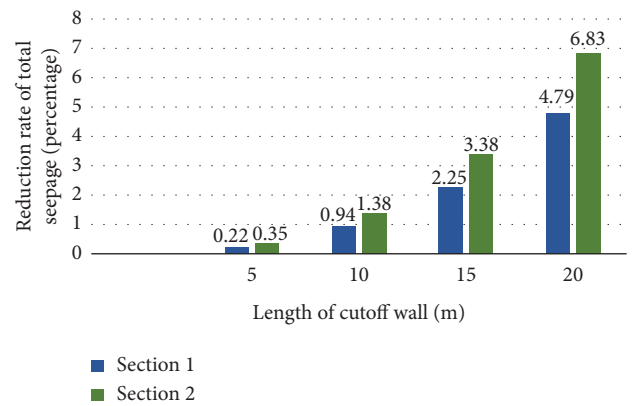


FIGURE 6: Percentage reduction of total seepage through Sections 1 and 2.

initial values of total seepage, average uplift pressure, and exit gradient (0 m).

Figure 6 shows the percentage of changes in the total seepage of various lengths of the cutoff wall compared to the state without the cutoff wall. According to Figure 6, it is evident that as the length of the cutoff wall increases, seepage decreases, and the amount of reduction in Section 2 relative to the state without the cutoff wall is greater than in Section 1.

As the cutoff wall length increases, the average uplift pressure decreases. Figure 7 shows the average changes in uplift pressure based on the percentage difference between the cutoff wall and no cutoff wall.

Increasing the length of the cutoff wall has reduced the exit gradient. Figure 8 also shows the changes in the exit gradient compared to the no cutoff wall.

**3.2. The Effect of Different Positions of the Cutoff Wall.** To investigate the effect of different positions of the cutoff wall, the width of the dam core is divided into 8 points with equal distances from each other, so that the first point is at the heel

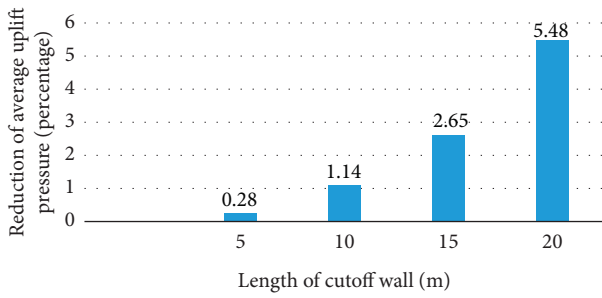


FIGURE 7: Percentage reduction of average uplift pressure.

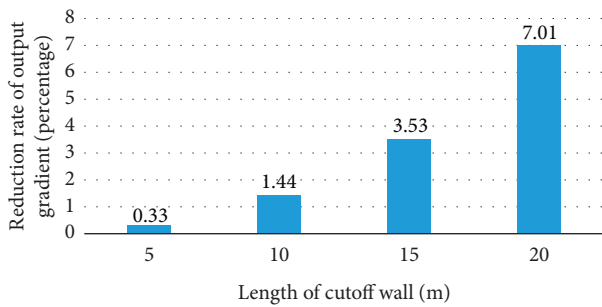


FIGURE 8: Percentage of exit gradient changes.

TABLE 5: The values of the parameters in point no 1.

Parameter	Value
Total seepage from Section 1 ( $m^3/s/m^2$ )	0.019689
Total seepage from Section 2 ( $m^3/s/m^2$ )	0.017499
Average uplift pressure (MPa)	560.13
Exit gradient	0.96423

of the core and the last point is at the toe of the core. Also, cutoff walls with a length of 10 meters have been considered and compared for all situations (a length of 10 meters was considered when attempting to select a typical size for cutoff walls). Table 5 presents the values of total seepage, average uplift pressure, and exit gradient at point No. 1. Also, the different positions considered for the cutoff wall are presented in Table 6.

Figure 9 shows the seepage changes in Sections 1 and 2. Position No. 5 in Section 1 has the most changes. Also, moving the position of the cutoff wall did not have much effect on the amount of seepage from Section 2.

Figure 10 shows the average change in uplift pressure relative to point 1. According to Figure 10, it is clear that the amount of uplift pressure has increased in all cases. Also, the increase in point No. 8 is more than in other points.

Figure 11 shows the reduction of the exit gradient in different positions of the cutoff wall. According to Figure 11, in position 2, the maximum decrease occurred, and in position 5, the lowest decrease in the exit gradient occurred.

3.3. The Effect of Different Lengths of Horizontal Drainage. This section investigates the effect of various horizontal drainage lengths on seepage parameters from Sections 1 and

TABLE 6: Different positions of the cutoff wall (considering the length of 10 meters of the cutoff wall).

Position no.	Distance from the heel of the core (m)
1	0
2	5
3	10
4	15
5	20
6	25
7	30
8	36

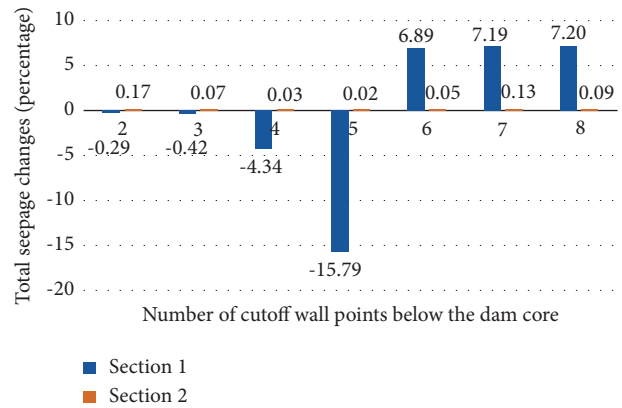


FIGURE 9: Percentage of changes in total seepage in Sections 1 and 2.

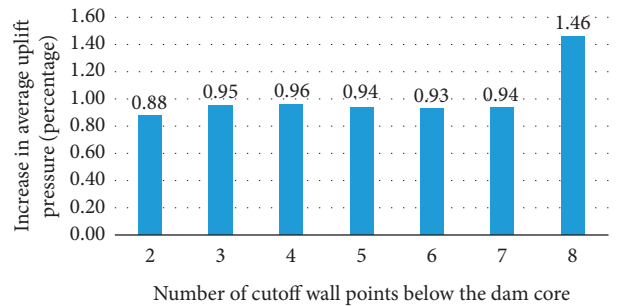


FIGURE 10: Percentage increase in average uplift pressure.

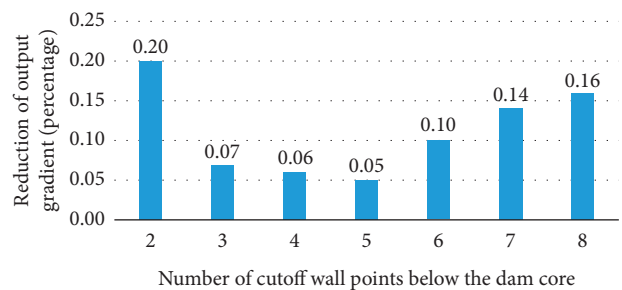


FIGURE 11: Percentage reduction of exit gradient in different positions of the cutoff wall.

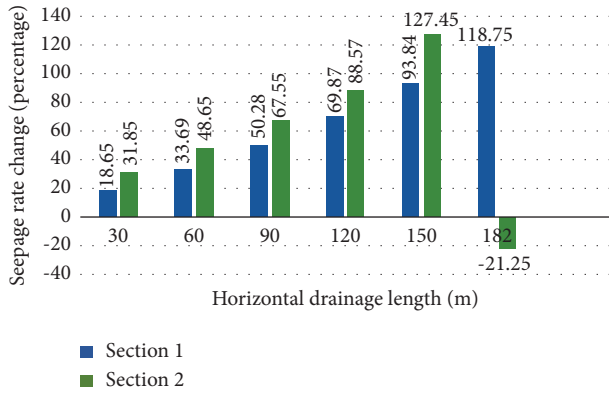


FIGURE 12: Percentage of seepage changes in Sections 1 and 2.

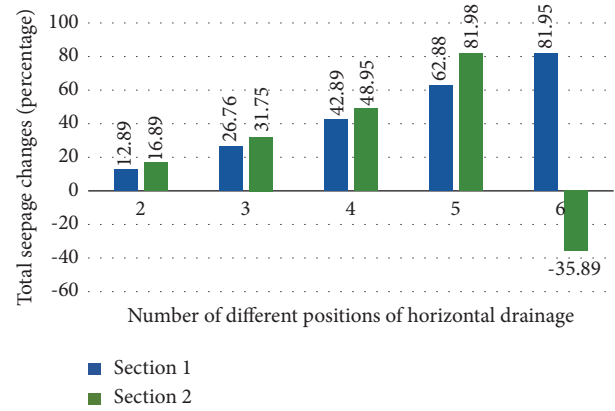


FIGURE 15: Percentage of changes in total seepage through Sections 1 and 2.

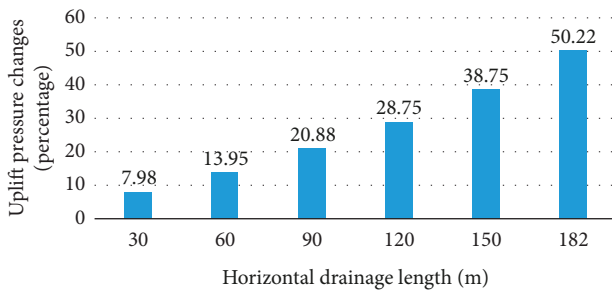


FIGURE 13: Percentage of changes in average uplift pressure.

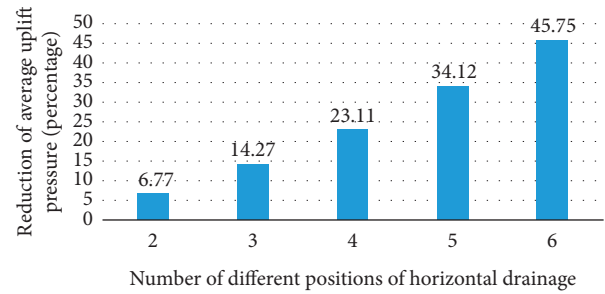


FIGURE 16: Percentage reduction of average uplift pressure in different positions of horizontal drainage.

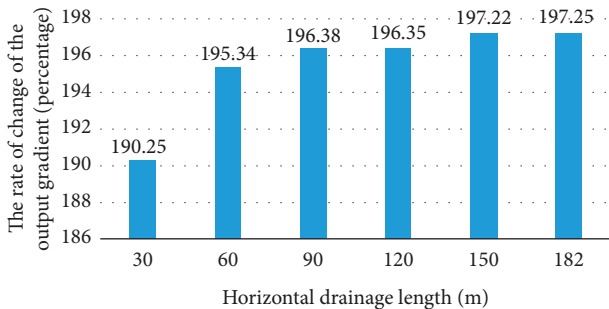


FIGURE 14: Percentage change of exit gradient in different cases of horizontal drainage length.

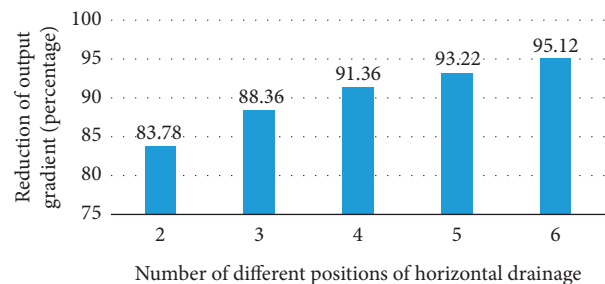


FIGURE 17: Percentage reduction of exit gradient in different positions of horizontal drainage.

TABLE 7: Different positions of horizontal drainage (with a length of 30 meters of horizontal drainage).

Position no.	Distance from the dam toe (m)
1	0
2	30
3	60
4	90
5	120
6	152

2, as well as uplift pressure and exit gradient. From the dam's toe, horizontal drainage lengths of 30, 60, 90, 120, 150, and 182 meters are considered for this purpose (the numbers used to determine the length of the drain were chosen according to the width of the dam's downstream shell).

Figures 12–14 show the results of the changes relative to the initial condition (Table 3). Figure 12 shows the variations in total seepage through Sections 1 and 2. As shown in Figure 12, the highest seepage of Section 1 occurred during 182 meters of drainage and the highest seepage of Section 2 occurred during 150 meters of drainage.

Figure 13 shows the average change in uplift pressure below the dam core. According to Figure 13, with increasing horizontal drainage length, the values of uplift pressure decrease.

Figure 14 shows the exit gradient changes in different horizontal drainage length cases. According to Figure 14, it is clear that the amount of exit gradient at the dam toe is much less than in other cases, in the case without drainage.

Also, the exit gradient values are almost the same in other cases.

**3.4. The Effect of Different Positions of Horizontal Drainage.** This section investigates the effect of different horizontal drainage positions on the seepage parameters of Sections 1 and 2, as well as the uplift pressure and exit gradient. The length of 30 meters of horizontal drainage at various distances from the dam (the drain was 30 meters long due to the width of the dam's shell downstream and the common length selection), including 0 meters, 30 meters, 60 meters, 90 meters, 120 meters, and 152 meters, must have been evaluated and compared for this purpose. Table 7 presents the different positions considered for horizontal drainage.

Figures 15–17 show the results of the changes compared to the initial state (Table 3). Figure 15 shows the changes in total seepage. According to Figure 15, the amount of total seepage has increased in all positions except position number 6 of Section 2.

Figure 16 shows the average uplift pressure reduction in different horizontal drainage positions. As the drainage position approaches the dam core, the amount of uplift pressure below the dam core decreases.

Figure 17 shows the exit gradient reduction in different horizontal drainage positions. According to Figure 17, the exit gradient in position 1 is much higher than in other positions due to the placement of the dam toe on the drain.

#### 4. Conclusion

Increasing the length of the cutoff wall decreased seepage in both sections, with a more significant effect on Section 2; it also decreased the uplift pressure and exit gradient. Changing the cutoff wall's position significantly affects seepage fluctuations in Section 1 but has no effect on seepage in Section 2. From positions 2 to 7, the uplift pressure values are nearly identical, and the exit gradient is most significant at position 1 and least at position 2. Except for the 182 meters of horizontal drainage in Section 2, increasing the length of horizontal drainage has increased seepage in both sections; it has also decreased the uplift pressure and increased the exit gradient. Closer placement of horizontal drainage to the dam core has increased seepage in both sections, except for position 6 in Section 2, and decreased uplift pressure and exit gradient.

#### Data Availability

The authors confirm that the data supporting the findings of this study are available upon request.

#### Conflicts of Interest

The authors declare that there are no conflicts of interest.

#### References

- [1] A. N. El-Hazek, N. B. Abdel-Mageed, and M. H. Hadid, "Numerical and experimental modelling of slope stability and seepage water of earthfill dam," *Journal of Water and Land Development*, vol. 44, no. 1-3, pp. 55–64, 2020.
- [2] M. I. Shongwe, T. Maseko, and B. R. T. Vilane, "Application of fuzzy cognitive mapping in the analysis of small earth dam failure," *Journal of Water and Land Development*, vol. 44, no. 1-3, pp. 136–142, 2020.
- [3] X. Zhao, S. Shang, Y. Yang, and M. Hu, "Three-Dimensional stochastic seepage field analysis of multimedia embankment," *Advances in Civil Engineering*, vol. 2021, pp. 1–7, Article ID 1936635, 2021.
- [4] M. Banan-Dallalian, M. Shokatian-Beiragh, A. Golshani, A. Mojtahedi, M. A. Lotfollahi-Yaghin, and S. Akib, "Study of the effect of an environmentally friendly flood risk reduction approach on the Oman coastlines during the Gonu tropical cyclone (Case study: the coastline of Sur)," *Engineering Times*, vol. 2, no. 2, pp. 141–155, 2021.
- [5] B. Yuan, Z. Cai, M. Lu, J. Lv, Z. Su, and Z. Zhao, "Seepage analysis on the surface layer of multistage filled slope with rainfall infiltration," *Advances in Civil Engineering*, pp. 1–13, Article ID 8879295, 2020.
- [6] J. W. Lee, J. Kim, and G. C. Kang, "Seepage behavior of earth dams considering rainfall effects," *Advances in Civil Engineering*, pp. 1–9, Article ID 8727126, 2018.
- [7] A. T. Siacara, G. F. Napa-García, A. T. Beck, and M. M. Futai, "Reliability analysis of earth dams using direct coupling," *Journal of Rock Mechanics and Geotechnical Engineering*, vol. 12, no. 2, pp. 366–380, 2020.
- [8] Y. Luo, Y. Liu, and J. Wang, "Isoparametric element analysis of two-dimensional unsaturated transient seepage," *Advances in Civil Engineering*, vol. 2021, pp. 1–8, Article ID 5571296, 2021.
- [9] M. Bayat, S. Eslamian, G. Shams, and A. Hajiannia, "The 3D analysis and estimation of transient seepage in earth dams through PLAXIS 3D software: neural network," *Environmental Earth Sciences*, vol. 78, no. 18, p. 571, Article ID 571, 2019.
- [10] S. Sica, L. Pagano, and F. Rotili, "Rapid drawdown on earth dam stability after a strong earthquake," *Computers and Geotechnics*, vol. 116, p. 103187, 2019.
- [11] A. Mouyeaux, C. Carvajal, P. Bressolette, L. Peyras, P. Breul, and C. Bacconnet, "Probabilistic stability analysis of an earth dam by Stochastic Finite Element method based on field data," *Computers and Geotechnics*, vol. 101, pp. 34–47, 2018.
- [12] X. Guo, D. Dias, C. Carvajal, L. Peyras, and P. Breul, "A comparative study of different reliability methods for high dimensional stochastic problems related to earth dam stability analyses," *Engineering Structures*, vol. 188, pp. 591–602, 2019.
- [13] X. Guo, Q. Sun, D. Dias, and E. Antoinet, "Probabilistic assessment of an earth dam stability design using the adaptive polynomial chaos expansion," *Bulletin of Engineering Geology and the Environment*, vol. 79, no. 9, pp. 4639–4655, 2020.
- [14] A. Zewdu, "Modeling the slope of embankment dam during static and dynamic stability analysis: a case study of Koga dam, Ethiopia," *Modeling Earth Systems and Environment*, vol. 6, no. 4, pp. 1963–1979, 2020.
- [15] A. R. Refaiy, N. M. AboulAtta, N. Y. Saad, and D. A. El-Molla, "Modeling the effect of downstream drain geometry on seepage through earth dams," *Ain Shams Engineering Journal*, vol. 12, no. 3, pp. 2511–2531, 2021.
- [16] X. Tan, X. Wang, S. Khoshnevisan, X. Hou, and F. Zha, "Seepage analysis of earth dams considering spatial variability of hydraulic parameters," *Engineering Geology*, vol. 228, no. 13, pp. 260–269, 2017.
- [17] T. Fukuchi, "New high-precision empirical methods for predicting the seepage discharges and free surface locations of

- earth dams validated by numerical analyses using the IFDM,” *Soils and Foundations*, vol. 58, no. 2, pp. 427–445, 2018.
- [18] A. Mouyeaux, C. Carvajal, P. Bressolette, L. Peyras, P. Breul, and C. Bacconnet, “Probabilistic analysis of pore water pressures of an earth dam using a random finite element approach based on field data,” *Engineering Geology*, vol. 259, p. 105190, 2019.
- [19] P. Rao, J. Wu, Q. Chen, and S. Nimbalkar, “Three-dimensional assessment of cracked slopes with pore water pressure using limit analysis,” *Environmental Earth Sciences*, vol. 80, no. 18, p. 645, Article ID 645.
- [20] M. Andreini, P. Gardoni, S. Pagliara, and M. Sassu, “Probabilistic models for the erosion rate in embankments and reliability analysis of earth dams,” *Reliability Engineering & System Safety*, vol. 181, pp. 142–155, 2019.
- [21] R. Pang, B. Xu, X. Kong, D. Zou, and Y. Zhou, “Seismic reliability assessment of earth-rockfill dam slopes considering strain-softening of rockfill based on generalized probability density evolution method,” *Soil Dynamics and Earthquake Engineering*, vol. 107, pp. 96–107, 2018.
- [22] Z. Jiang and J. He, “Detection model for seepage behavior of earth dams based on data mining,” *Mathematical Problems in Engineering*, pp. 1–11, Article ID 8191802, 2018.
- [23] W. Ye, F. Ma, J. Hu, and Z. Li, “Seepage Behavior of an Inclined wall Earth Dam under Fluctuating Drought and Flood Conditions,” *Geofluids*, vol. 2018, Article ID 4734138.
- [24] B. Mansuri, F. Salmasi, and B. Oghati, “Effect of location and angle of cutoff wall on uplift pressure in diversion dam,” *Geotechnical & Geological Engineering*, vol. 32, no. 5, pp. 1165–1173, 2014.
- [25] M. Mortazavi and S. Soleimani, “Leakage analysis of embankment dams using SEEP/W, SEEP/3D software,” *Journal of Applied Environmental and Biological Sciences*, vol. 5, pp. 122–128, 2015.
- [26] B. Nourani, F. Salmasi, A. Abbaspour, and B. Oghati Bakhshayesh, “Numerical investigation of the optimum location for vertical drains in gravity dams,” *Geotechnical & Geological Engineering*, vol. 35, no. 2, pp. 799–808, 2016.
- [27] A. Hekmatzadeh, F. Zarei, A. Johari, and A. Torabi Haghghi, “Effect of location and angle of cutoff wall on uplift pressure in diversion dam,” *Geotechnical & Geological Engineering*, vol. 32, pp. 1165–1173, 2018.
- [28] N. J. H. Al-Mansori, T. A. F. J. M. Al-Fatlawi, N. Y. Othman, and L. S. A. Al-Zubaidi, “Numerical analysis of seepage in earth-fill dams,” *Civil Engineering Journal*, vol. 6, no. 7, pp. 1336–1348, 2020.
- [29] A. Toumi and B. Remini, “Evaluation of geology and hydrogeology of the water leakage in hammam-grouz dam, Algeria,” *Journal of Human, Earth, and Future*, vol. 2, no. 3, pp. 269–295, 2021.
- [30] M. A. Hassan, M. A. M. Ismail, and H. H. Shaalan, “Numerical modeling for the effect of soil type on stability of embankment,” *Civil Engineering Journal*, vol. 7, pp. 41–57, 2022.
- [31] K. He, L. Pei, X. Lu, J. Chen, and Z. Wu, “Research and application of critical failure paths identification method for dam risk analysis,” *Mathematical Problems in Engineering*, vol. 2020, pp. 1–10, 2020.
- [32] L. Liu and Z. Wu, “Overtopping risk analysis of earth dams considering effects of failure duration of release structures,” *Complexity*, pp. 1–15, 2020.
- [33] X. Zhang, X. Chen, and J. Li, “Improving dam seepage prediction using back-propagation neural network and genetic algorithm,” *Mathematical Problems in Engineering*, pp. 1–8, 2020.
- [34] J. Amnyattalab and H. Rezaie, “Study of the effect of seepage through the body of earth dam on its stability by predicting the affecting hydraulic factors using models of Brooks–Corey and van Genuchten (Case study of Nazluchay and Shahrchay earth dams),” *International Journal of Environmental Science and Technology*, vol. 15, no. 12, pp. 2625–2636, 2018.
- [35] Y. X. Wu, S. L. Shen, H. M. Lyu, and A. Zhou, “Analyses of leakage effect of waterproof curtain during excavation dewatering,” *Journal of Hydrology*, vol. 583, p. 124582.
- [36] B. H. Maula and L. Zhang, “Assessment of embankment factor safety using two commercially available programs in slope stability analysis,” *Procedia Engineering*, vol. 14, pp. 559–566, 2011.
- [37] W. D. Fisher, T. K. Camp, and V. V. Krzhizhanovskaya, “Crack detection in earth dam and levee passive seismic data using support vector machines,” *Procedia Computer Science*, vol. 80, pp. 577–586, 2016.

## Research Article

# Scaling Method Application for Seismic Design along the Central Anatolian Fault Zone

Erhan Gumus <sup>1</sup>, Baki Ozturk <sup>2</sup> and Fadzli Mohamed Nazri <sup>3</sup>

<sup>1</sup>Department of Risky Structures, Directorate General for Infrastructure and Urban Transformation Services, Ministry of Environment, Urbanization and Climate Change, Ankara 06510, Turkey

<sup>2</sup>Department of Civil Engineering, Hacettepe University, Ankara 06800, Turkey

<sup>3</sup>School of Civil Engineering, Universiti Sains Malaysia, Engineering Campus, Nibong Tebal, Penang, Malaysia

Correspondence should be addressed to Baki Ozturk; bakiozturk@hacettepe.edu.tr

Received 18 April 2022; Accepted 27 July 2022; Published 27 August 2022

Academic Editor: Dawei Yin

Copyright © 2022 Erhan Gumus et al. This is an open access article distributed under the Creative Commons Attribution License, which permits unrestricted use, distribution, and reproduction in any medium, provided the original work is properly cited.

Cities located along the Central Anatolian Fault Zone (CAFZ), such as Kayseri and Mersin, have become metropolitan cities in Turkey since the 1950s and have been attracting big investments, such as the Akkuyu Nuclear Power Plant (Mersin), which is planned to be built close to the CAFZ. In this study, the ground motion records of earthquakes occurring along the CAFZ are scaled for single-degree-of-freedom (SDOF) systems conforming to the current design response spectra. This is a pioneering study on the analysis of seismic behavior using SDOF systems subjected to ground motions that were recorded in relation to earthquakes occurring on the CAFZ in Turkey. It defines the importance of selecting suitable records with certain features that can be used with the scaling method to ensure that real ground motion records match the design acceleration spectra defined in the earthquake codes and will provide a perspective on future destructive earthquakes that may occur on the CAFZ.

## 1. Introduction

Time domain analysis is frequently used to determine specifications involved in the design of structures regarding their earthquake performance. Acceleration records are required for such analyses if they are compatible with design spectra obtained from synthetic, simulated, or real earthquake records [1–3].

Real acceleration records obtained from earthquakes are more easily accessible nowadays, and thus, the use of real ground motion records is preferable for use in analysis. However, a large amount of different data pertaining to various parameters often exists, such as earthquake magnitude, scaled acceleration records, fault type, local ground conditions of stations, and distance from the earthquake source, and thus, it is difficult to obtain records specific to the actual situation in some cases [4]. Therefore, real earthquake records that fulfill conditions set out in earthquake codes are required, and these need to be scaled by adjusting with design response spectrum [5].

A large number of studies have been conducted [6] involving the selection and scaling of related codes using records obtained from real earthquakes, with the aim of using such information in structural design. These studies have analyzed methods used in the selection and scaling of records obtained from real earthquakes occurring in countries, such as the United States of America, China, European Union countries, New Zealand, and Taiwan, and reveal differences and similarities between the codes applied [5, 7–17]. In addition, studies have been conducted to select and scale earthquake records in the time domain.

Scholz [18] addressed the problem of how to predict strong ground motions for very large earthquakes from observations made of such motions produced by events of moderate size. McGarr [19] described how the state of stress as well as the focal depth clearly is an important factor to be considered in the prediction of seismic ground motion. Somerville [20] reviewed the magnitude scaling of near-fault ground motions. Kurama and Farrow [21] showed that scaling methods that work well for ground motions

representative of stiff soil and far-field conditions lose their effectiveness for soft soil and near-field conditions for a wide range of structural characteristics. Naeim et al. [22] presented a new approach to the selection and scaling of ground motion time histories for structural design using genetic algorithms. Watson-Lamprey and Abrahamson [23] proposed a procedure to select time series for use in nonlinear analyses that is intended to result in an average response of the nonlinear system that is not based simply on magnitude, distance, and spectral shape. Luco and Bazzurro [24] demonstrated that scaling can indeed introduce a bias that, for the most part, can be explained by differences between the elastic response spectra of the scaled and unscaled records. Kottke and Rathje [25] defined a semiautomated procedure for selecting and scaling recorded earthquake motions for dynamic analysis. Huang et al. [26] proposed a scaling method that explicitly considers spectral shape. Katsanos et al. [27] reviewed alternative selection procedures based on established methods for incorporating strong ground motion records within the framework of seismic design of structures. Jayaram et al. [28] defined a computationally efficient ground-motion selection algorithm for matching a target response spectrum mean and variance. Takewaki and Tsujimoto [29] defined the scaling of design earthquake ground motions for tall buildings based on drift and input energy demands. Ay and Akkar [30] presented a ground-motion selection and scaling methodology that preserves the basic seismological features of the scaled records with reduced scatter in the nonlinear structural response. Haselton et al. [31] provided guidance to design professionals on the selection and scaling of ground motions for the purpose of nonlinear response history analysis. Al Atik et al. [32] described a method for deriving kappa ( $\kappa$ ) scaling factors that can be applied to ground motion prediction equations (GMPEs) to account for site-specific  $\kappa$  estimates.

Historically, in 1717 [33] and 1835 [34], two major destructive earthquakes occurred at the Central Anatolian Fault Zone (CAFZ). In the 20th century, two subsequent destructive earthquakes occurred in 1940 along the CAFZ. In January, an earthquake of  $M_s = 5.0$  magnitude occurred, during which 58 people lost their lives, while in February, an earthquake of  $M_s = 6.7$  magnitude occurred, during which 37 people lost their lives [34].

Since the 1950s there has been significant urbanization in Turkey, accompanied by a rapid increase in the population of big cities. Cities located along the CAFZ, such as Kayseri and Mersin, have become metropolitan cities in Anatolia due to the high increase in population of Turkey during this era. Mersin (approximately 1.7 million people) and Kayseri (approximately 1.4 million people) are attracting big investments, such as the Akkuyu Nuclear Power Plant (Mersin), which is planned to be built close to the CAFZ.

However, to date, no study has been conducted on the scaling of records of real earthquakes that have occurred on the CAFZ in Middle Anatolia, Turkey, for use either in structural design or in the assessment of the earthquake performance of existing structures. This study is therefore the first to consider the ground motion records of

earthquakes occurring on the CAFZ in terms of the analysis of the seismic behavior of single-degree-of-freedom (SDOF) systems. In this respect, this study provides results that can be used in implementing earthquake engineering performance-based design principles within this seismic area.

In this study, general methods and criteria that are used to select earthquake records are discussed, and the records of earthquakes that occurred on the CAFZ are scaled to conform to the design response spectra of [35]. In addition, for SDOF linear systems with a 5% damping ratio and response spectra in the period from  $T_S = 0.01$  to  $T_F = 2.00$  s, spectral relative response, spectral velocity, and spectral displacement form are calculated. This research is being conducted between  $T_S = 0.01$  s and  $T_F = 2.00$  s since this period range covers the seismic design periods of almost all the building structures located along the CAFZ. It should be noted that this study will provide a perspective on future destructive earthquakes that may occur on the CAFZ that will affect the new metropolitan cities of Kayseri and Mersin.

## 2. Records of Earthquakes Occurring in the Central Anatolian Fault Zone, Turkey

The Central Anatolian Fault Zone (CAFZ) stretches over 700 km, beginning at a point to the west of the city of Mersin. It travels through the Gulek Strait, Pozanti, and Camardi (Nigde) to Erciyes (N20E), after which it changes direction (N50E) in the direction of Gemerek, Sarkisla, and Sivas. It eventually reaches the North Anatolian fault zone at Erzincan [36, 37], making it the second largest fault zone in Anatolia after the North Anatolian fault zone. A simplified map showing the neotectonic subdivision of Turkey and adjacent areas [38] is shown in Figure 1, while a simplified map showing major structural elements of east Central Anatolia [39] is provided in Figure 2.

The records of earthquakes occurring on the CAFZ are supplied by the Strong Ground Motion Database of Turkey. Figure 3 shows the 17 ground motion records selected for this study from earthquakes that occurred between 1976 and 2014 with a magnitude of  $M \geq 2.8$ . Further details of these earthquakes are supplied in Table 1, which shows the associated station location, ground conditions, distance, magnitude, acceleration values, and scaling factors related to these records.

## 3. Selection and Scaling of Real Earthquake Records in Line with the Design Response Spectra

The calculations of the seismic load on structures can be conducted using the “*Equivalent Static Earthquake Load Method*” and “*Mode Combination Method*.” Recent advances in technological developments have enabled the use of nonelastic calculation methods to be used in the design of structures when performing a structural analysis in the time domain. It is thus possible to conduct research on the selection of appropriate seismic records and associated scaling of such records using either a linear elastic or nonlinear inelastic analysis in the time domain.

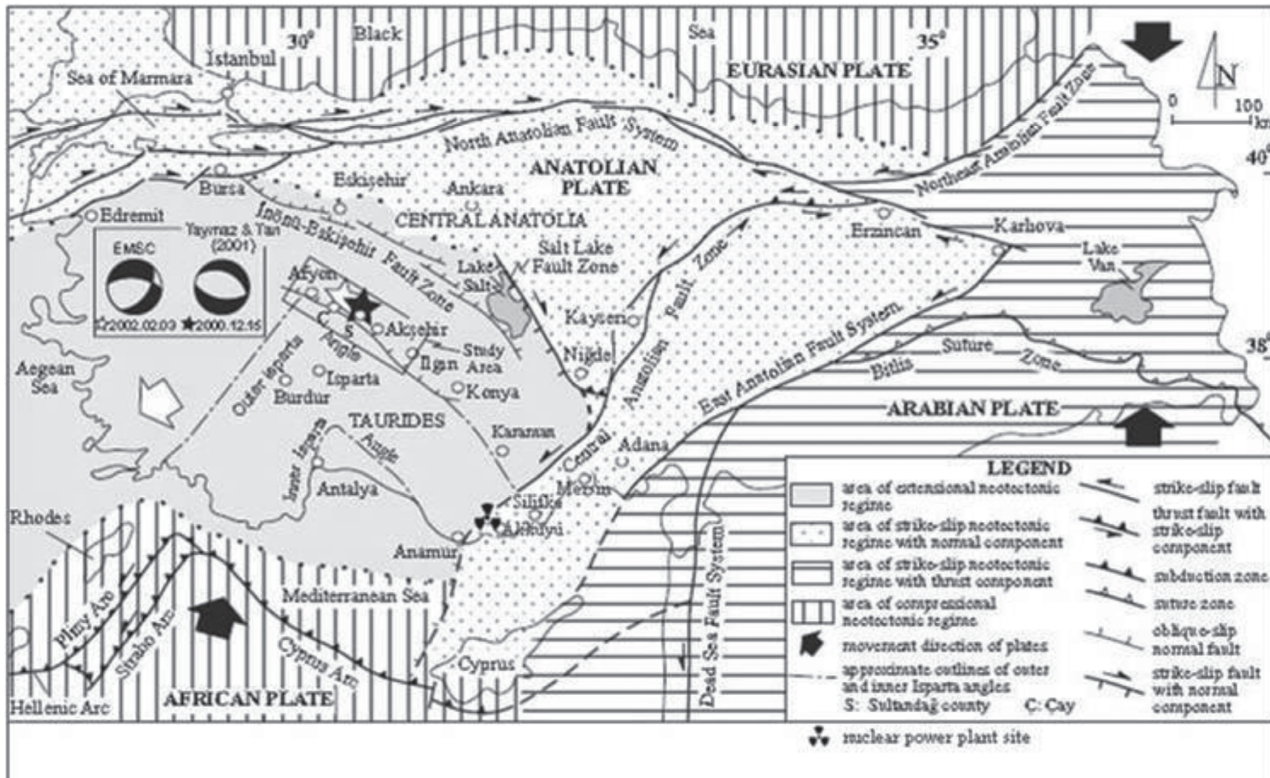


FIGURE 1: Simplified map showing the neotectonic subdivision of Turkey and adjacent areas [38] (location of the Akkuyu Nuclear Power Plant site is plotted on the map.).

**3.1. Earthquake Record Sources.** Accelerograms are used in earthquake calculations practiced in time-domain structural analysis and obtained from three different sources, which are described below [1–3].

**3.1.1. Earthquake Records Generated Synthetically.** Over a wide-ranging period, it is possible to generate synthetic records that are similar to those of an actual response spectrum. For example, the power spectral density function is calculated from simplified response spectra, and sinusoidal signals are generated by compounding this function with random phase angles; a synthetic record is thus obtained by collecting these sinusoidal functions. Moreover, an iterative method can be used to enhance matching with the design spectrum, wherein the scaling factor between the ordinates of a real response spectrum and a target design spectrum is calculated at a selected frequency. It is then possible to correct the record by adjusting the power spectral density function with the square of this scaling constant. As a result of these processes, new ground motion can be obtained.

**3.1.2. Simulated Earthquake Records.** Simulated earthquake records are obtained from seismological source models that consider the propagation medium and ground conditions. In that condition, the most different subject is the identification of suitable source, propagation medium, and ground conditions. In analyses used to obtain the physically

simulated records of source and wave propagation characteristics for the area to be examined, it is necessary to identify an earthquake scenario that depends on magnitude and distance. However, this information is usually unavailable, particularly, in cases where seismic design codes are used [4].

**3.1.3. Records Obtained from Real Earthquakes.** Real earthquake records include accurate information about certain characteristics and the nature of ground shaking (amplitude, duration, phase characteristics, and frequency content). They also reflect factors, such as the source influencing the records, propagation medium, and ground conditions. Therefore, with respect to the seismological parameters of an area, the selection of such records is more beneficial compared with other alternatives.

**3.2. Selection of Real Earthquake Records.** Real earthquake records are generally selected from locations where either the design spectrum is provided to represent the specified characteristics of ground motion or the earthquake scenario is given with minimum parameters, such as magnitude distance and soil class. Records selected for a specified region should be matched with the generated response spectrum because of seismic hazard analysis and should satisfy the geological and seismological conditions.

The magnitude of an earthquake strongly influences the frequency content and duration of ground motion, and thus,



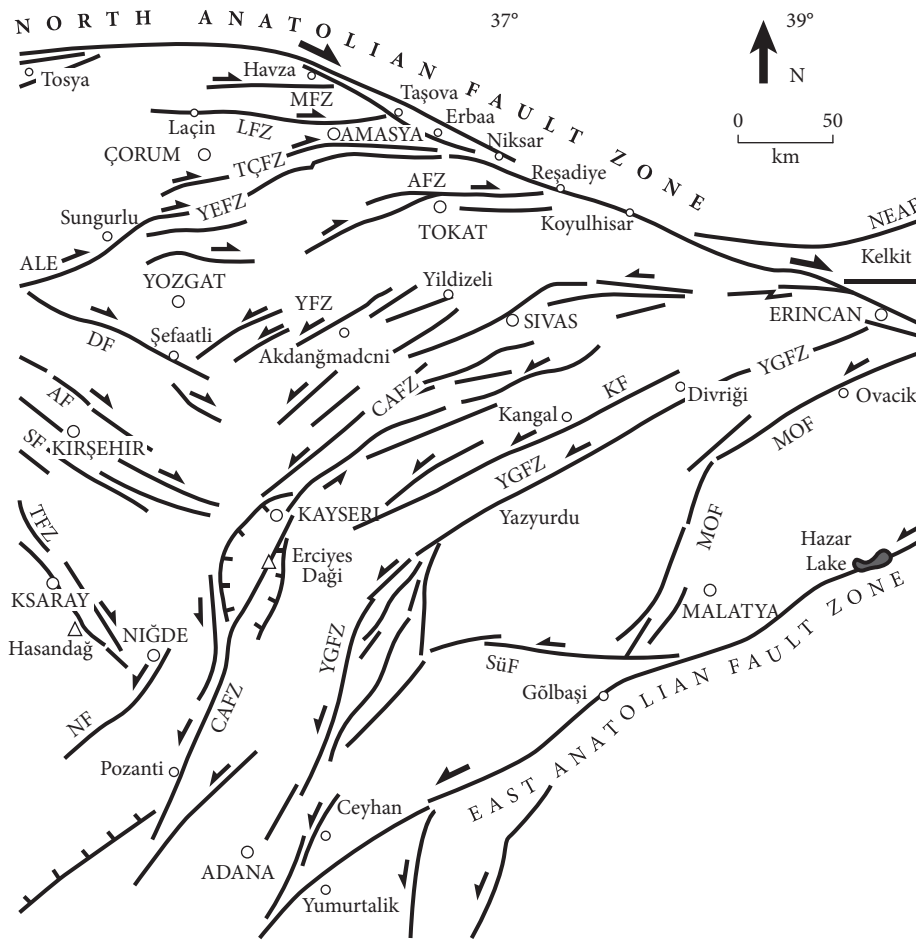


FIGURE 2: Simplified map showing major structural elements of east central Anatolia [39].

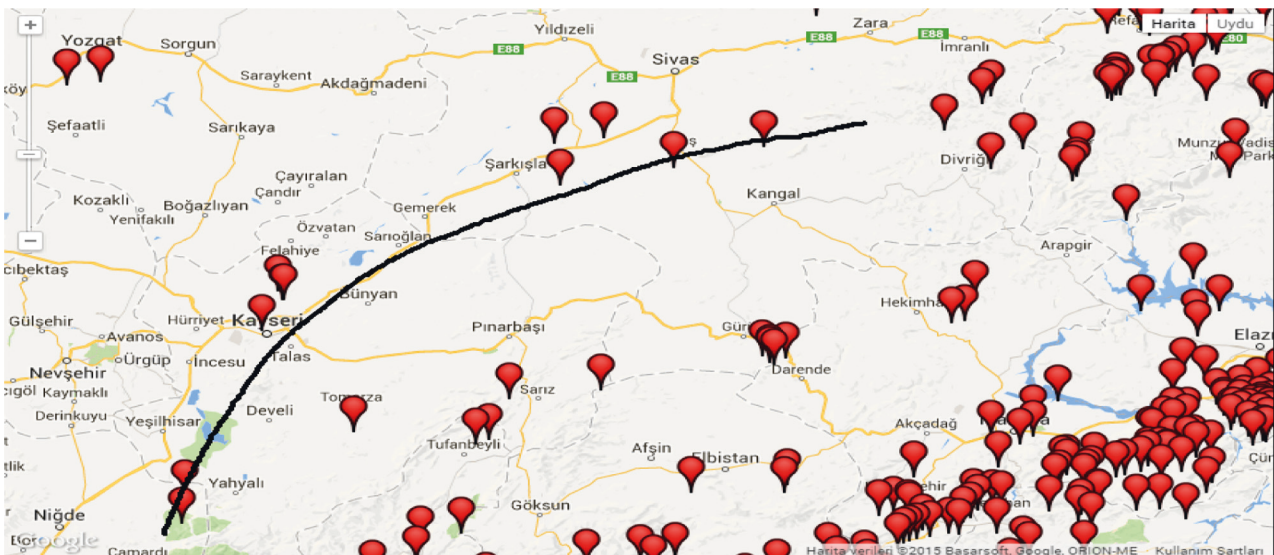


FIGURE 3: Earthquakes recorded on the Central Anatolian Fault Zone (CAFZ) by the strong ground motion database of Turkey [40].

it is important to select records of events with appropriate magnitudes. For example, the earthquake magnitude of selected records needs to be approximately  $\pm 0.25$  of the target magnitude [41].

3.3. *Ground Motion Scaling Methods.* Real earthquake records can be scaled in either the frequency or time domains using scaling methods. The scaling method used in the frequency domain alters the frequency content of the

TABLE 1: Details and calculated scaling constant ( $\alpha_{ST}$ ) of records of earthquakes that occurred throughout the Central Anatolian Fault Zone (CAFZ), Turkey.

Station		Date	Magnitude	Soil type	Earthquake zone	Recorded max. acceleration value (gal)			North-south (N-S)		East-west (E-W)	
Province	Country					N-S	E-W	U-D	Scaling constant ( $\alpha$ ST)	Fractional relative error (%)	Scaling constant ( $\alpha$ ST)	Fractional relative error (%)
Tokat	Centrum	11.06.1999	4.1	Z3	1	1.9	1.1	0.64	1.4	17.28	4.9	16.25
Tokat	Centrum	11.06.1999	4.5	Z3	1	4.11	1.4	1.1	1.1	18.2	1.1	17.81
Tokat	Centrum	14.04.2006	2.8	Z3	1	10.1	5.7	12.9	1.4	1.11	7.9	1.10
Kirikkkale	Centrum	12.08.2008	4.8	Z2	1	0.66	0.68	0.31	4.7	15.55	4.12	15.68
Ankara	Bala	12.08.2008	4.8	Z2	2	0.29	0.4	0.14	1.7	18.99	1.7	18.12
Ankara	S. kochisar	12.08.2008.	4.8	Z3	2	0.35	0.37	0.25	7.4	18.53	7.6	17.88
Aksaray	Centrum	12.08.2008	4.8	Z3	5	0.59	0.77	0.29	3.4	22.8	1.2	22.83
Kayseri	Centrum	13.11.2008	3.7	Z2	3	0.35	0.33	0.36	1.9	20.23	1.9	19.9
Kayseri	Centrum	19.11.2008	3.6	Z2	3	0.62	0.7	0.45	1.9	20.79	1.10	20.79
Kayseri	Centrum	15.01.2009	3.7-3.9	Z2	3	1.2	1.2	1.1	1.2	20.29	2.1	19.63
Nigde	Centrum	30.01.2009	4.3	Z2	4	1.3	1.2	1.8	1.1	22.9	1.1	22.46
Nevsehir	Centrum	30.09.2011	4.3	Z2	3	0.9	1.1	0.79	1.10	19.61	7.6	19.94
Sivas	Ulas	30.08.2013	3.3	Z2	4	0.34	1.01	0.47	26.13	22.29	—	—
Nigde	Camardi	01.11.2013	3.7	Z3	4	1.3	1.2	1.2	1.1	23.59	1.2	23.44
Sivas	Kangal	01.05.2014	4.2	Z2	4	0.6	0.61	0.47	1.6	23.48	1.5	23.13
Kayseri	Centrum	26.03.2015	3.8	Z2	3	0.52	0.46	0.38	8.4	20.78	1.10	20.3
Sivas	Gemerek	26./03/2015	3.8	Z2	3	0.66	0.62	0.27	12.2	19.27	1.9	20.1

accelerogram, whereas in the time domain, the amplitude of the record is changed.

### 3.3.1. Scaling of Ground Motion in Frequency Domain.

In this method, records are generated that are compatible with the design response spectrum recorded by accelerograms. This is a more effective method than other methods of earthquake record production, as the earthquake motion does not lose its physical characteristics during scaling in the frequency domain [42]. Using a scaling method in the frequency domain, attaining records that precisely match the design spectrum is possible. However, when these records are used in the nonlinear earthquake calculations of structures, it is necessary to determine whether an equal displacement rule in the sensitive area applies [43].

### 3.3.2. Ground Motion Scaling in Time Domain.

In this approach, the recorded ground motion is simply scaled up or down uniformly (multiplying by greater than one or less than one and by a constant) so that the results have the best match with the target spectrum within a period range of interest. When the use of more than one earthquake record is required, it is possible either to fit each record separately or to best fit the average of the produced spectra to the target spectrum.

Scaling in the time domain is based on minimizing the difference between the scaled behavior spectrum and the design response spectrum using the least-square method. The “difference” is scaled and defined as an integration of the square of differences among the target design spectrum amplitudes. It is calculated using the following equation:

TABLE 2: Spectrum characteristic periods,  $T_A$  and  $T_B$ .

Site class	$T_A$ (sec)	$T_B$ (sec)
Z1	0.10	0.30
Z2	0.15	0.40
Z3	0.15	0.60
Z4	0.20	0.90

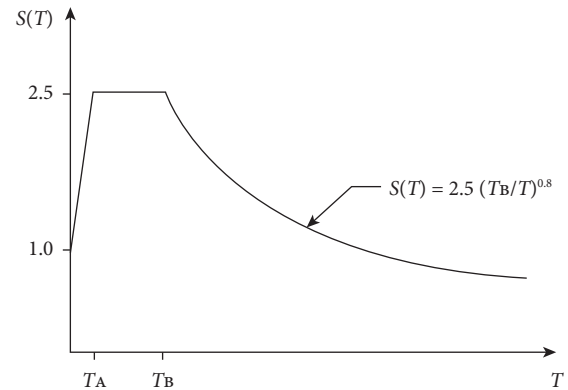


FIGURE 4: Spectrum function.

$$|Difference| = \int_{T_S}^{T_F} [\alpha S_a^{actual}(T) - S_a^{target}(T)]^2 dT, \quad (1)$$

where  $S_a^{target}$  is the target acceleration response spectrum,  $S_a^{actual}$  is the acceleration spectrum of the real earthquake record used,  $\alpha$  is the linear scaling factor,  $T$  is the period of the oscillator,  $T_S$  is the lower period range of scaling used, and  $T_F$  is the upper period range of scaling used.

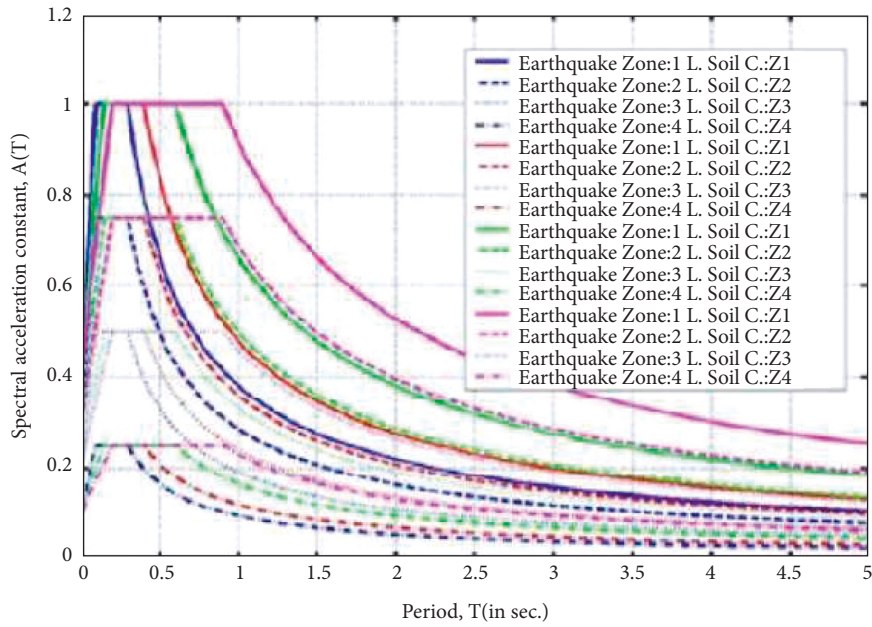


FIGURE 5: Elastic design acceleration spectra for four different earthquake zones and different local site classes [5].

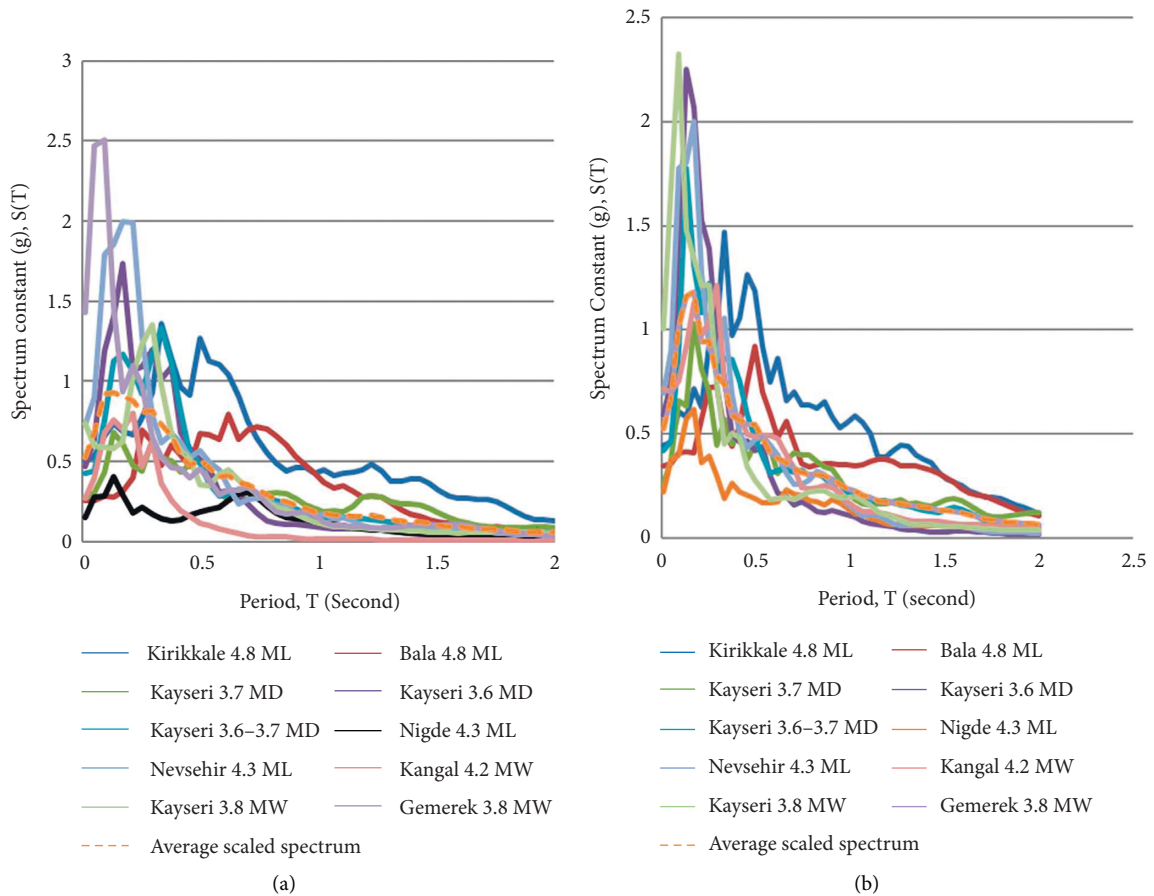


FIGURE 6: Response spectra of earthquake records scaled according to elastic design acceleration spectrum (with local site class Z2); (a) North-South (N-S) and (b) East-West (E-W) components.

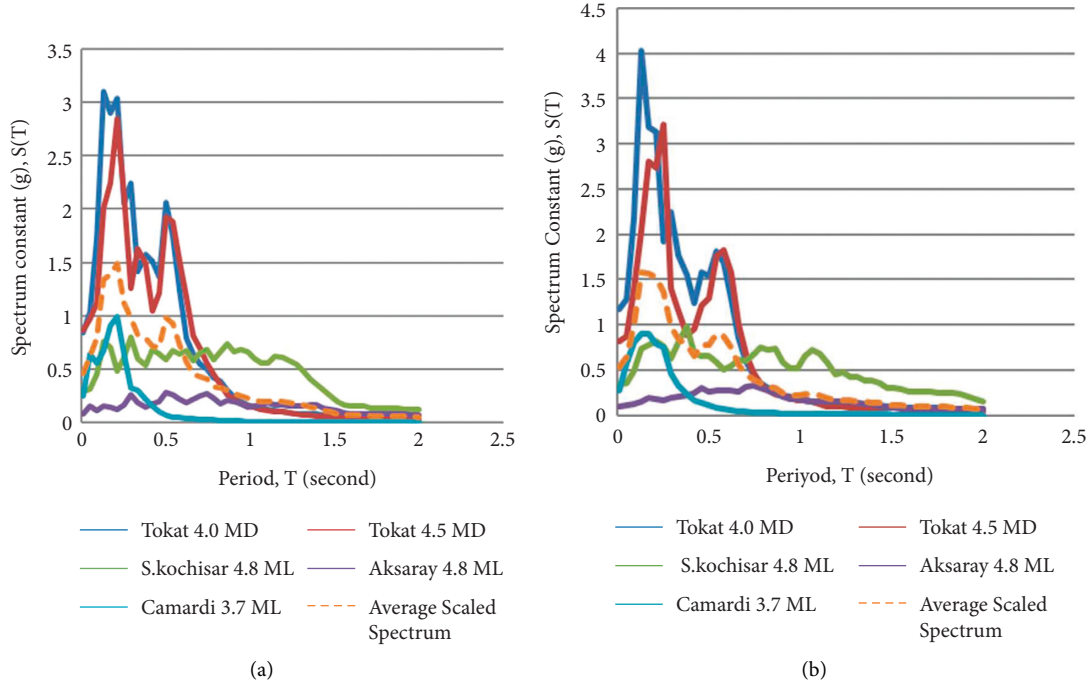


FIGURE 7: Response spectra of earthquake records scaled according to elastic design acceleration spectrum (with local site class Z3); (a) North-South (N-S) and (b) East-West (E-W) components.

To minimize the difference, the derivative of the “difference” function with respect to the scaling factor must be zero, as follows:

$$\min |\text{Difference}| \text{ occurs at } \frac{d|\text{Difference}|}{d\alpha} = 0, \quad (2)$$

where the “difference” function in Equation (1) is equated to zero by taking a derivative with respect to  $d\alpha$ . By changing the integrals in Equation (1) to discrete forms, a total form continuing to  $T_F$  with a  $\Delta T$  (step) increment from  $T_S$  is obtained, where  $\Delta T$  is the period step increment, as in the following equation.

$$\alpha = \frac{\sum_{T=T_A}^{T_B} (S_a^{\text{actual}}(T) * S_a^{\text{target}}(T))}{\sum_{T=T_A}^{T_B} (S_a^{\text{actual}}(T))^2}. \quad (3)$$

**3.4. Selection and Scaling of Real Records according to the Design Spectra.** In the earthquake codes, the design earthquake is accepted as being a ground motion that has a 10% probability of exceedance within a period of 50 years. To show this ground motion, a spectrum constant,  $S(T)$ , depending on local site classes with a 5% damping ratio, is identified. The differences of the local site classes on the design spectrum are reflected with the help of spectrum characteristic periods ( $T_A$  and  $T_B$ ); and [35] provides characteristic periods corresponding to four different site classes (Table 2).

The design spectrum function is given in Figure 4. The elastic spectral acceleration constant,  $A(T)$ , used in analysis is calculated by multiplying  $S(T)$ , which is equivalent to the

period of the structure; the effective ground acceleration constant,  $A_o$ , which shows the earthquake risk within the region; and the building importance constant,  $I$ , which varies according to the utilization type of the buildings, as follows.

$$A(T) = A_o I S(T). \quad (4)$$

The spectrum constant,  $S(T)$ , is evaluated according to the following equation.

$$\begin{aligned} S(T) &= 1 + 1.5 \frac{T}{T_A}, & (0 \leq T \leq T_A), \\ S(T) &= 2.5, & (T_A < T \leq T_B), \\ S(T) &= 2.5 \left( \frac{T_B}{T} \right)^{0.8}, & (T_B < T). \end{aligned} \quad (5)$$

Site classes provided are shown in Figure 5, together with the elastic spectral acceleration constants drawn for different earthquake zones.  $A_o$  is defined regarding the existing faults and records of prior earthquakes, and Turkey is separated into five earthquake zones.

**3.4.1. Definition of Scaling Constant for Elastic Spectral Acceleration.**  $A(T)$  is obtained by multiplying  $A_o I$ , and  $S(T)$ . In this study, records are selected and scaled only for  $S(T)$  using this feature; the scaling constant obtained from this process is named  $\alpha_{ST}$ . In addition,  $\alpha_{AT}$ , which is related to  $A(T)$  is obtained by multiplying  $\alpha_{ST}$  by  $A_o$  and  $I$  [5], as follows.

$$\alpha_{AT} = A_o I \alpha_{ST}. \quad (6)$$

**3.4.2. Limits of Scaling Factors.** Scaling performed on the amplitude of real earthquake records should not exceed specific limits. These limits are dependent on the type of problem for which the selection of ground motion is intended for use. In previously conducted studies [3, 19, 23, 44, 45], a scaling constant of 4 is accepted as the upper limit for the analyses of linear elastic structures. However, for the analyses of nonlinear inelastic structures,  $\alpha_{AT}$  should be in the range from 0.5 to 2, and for liquefaction,  $\alpha_{AT}$  should not be greater than 2.

**3.4.3. Criteria for the Selection of Records.** In the earthquake codes, it is permissible to use earthquake ground motion records that are artificially generated, previously recorded, or simulated for the linear and nonlinear seismic analysis of buildings and building-type structures within the time domain. However, the earthquake records used should have certain features. For example, the duration of the strong ground motion part of the earthquake record should be no shorter than five times the first natural vibration period of a building not longer than 15 s. In addition, the average of the spectral acceleration records, which is equivalent to the zero period, should be used for earthquake ground motion that is not less than  $A_{og}$ . Furthermore, in the earthquake direction considered, the average of the spectral acceleration records that conform to the acceleration record and are used for the 5% damping ratio should not be less than 90% of the elastic spectral acceleration records defined in [35], within a period range between  $0.2T_1$  and  $2T_1$  with respect to the first (dominant) period  $T_1$ . Finally, for linear and nonlinear calculations in the time domain, the maximum of the results, in which three ground motions are used, and the average of results, in which at least seven ground motions are used, is going to be the basis for design.

**3.4.4. Method for Selecting and Scaling Real Earthquake Records and Generating Response Spectra.** The following records and methods were used in time domain calculations in this study and are summarized as follows:

- (1) Data pertaining to the location, ground conditions, history, magnitude, and scaled acceleration value features of records of earthquakes occurring in the CAFZ, as found in the Turkish National Strong Ground Motion Database, are listed in Table 1.
- (2) For each N-S (north-south) and E-W (east-west) component, in the period range between  $T_S = 0.01$  s and  $T_F = 2.00$  s, for a 5% damping ratio, the response spectra were obtained using the Bispec-Earthquake Solutions Programme [46].
- (3) The scaling factors for each component of the earthquake records were calculated by matching the response spectra obtained for each earthquake record with the target response spectrum. In this study,

TABLE 3:  $S_a^{\text{actual}}(T)$  and  $S_a^{\text{target}}(T)$  values.

$T(s)$	$S_a^{\text{actual}}(T)$	$S_a^{\text{target}}(T)$
0.01	0.14	1.10
0.05	0.16	1.51
0.09	0.23	1.91
0.13	0.36	2.32
0.17	0.32	2.50
0.21	0.25	2.50
0.25	0.23	2.50
0.29	0.33	2.50
0.33	0.28	2.50
0.38	0.27	2.50
0.42	0.23	2.42
0.46	0.25	2.25
0.50	0.26	2.10
0.54	0.25	1.97
0.58	0.15	1.86
0.62	0.14	1.76
0.66	0.15	1.68
0.70	0.14	1.60
0.74	0.15	1.53
0.78	0.16	1.46
0.82	0.16	1.40
0.86	0.16	1.35
0.90	0.14	1.30
0.94	0.12	1.26
0.98	0.11	1.22
1.03	0.10	1.18
1.07	0.10	1.14
1.11	0.10	1.11
1.15	0.12	1.08
1.19	0.15	1.05
1.23	0.15	1.02
1.27	0.15	0.99
1.31	0.13	0.97
1.35	0.13	0.94
1.39	0.13	0.92
1.43	0.12	0.90
1.47	0.11	0.88
1.51	0.09	0.86
1.55	0.08	0.84
1.59	0.07	0.83
1.63	0.06	0.81
1.68	0.05	0.79
1.72	0.05	0.78
1.76	0.05	0.77
1.80	0.05	0.75
1.84	0.05	0.74
1.88	0.05	0.73
1.92	0.05	0.71
1.96	0.05	0.70
2.00	0.05	0.69

the following methods were applied, and they are listed in items 4–7, as follows.

- (4) Records with a scaling factor,  $\alpha_{ST}$ , greater than 20 and less than 1/20 were eliminated. For example, in Table 1, the scaling factor,  $\alpha_{ST}$ , of an earthquake with an epicenter at Sivas-Ulasli ( $M_L$ : 3.3) was eliminated for being greater than 20.

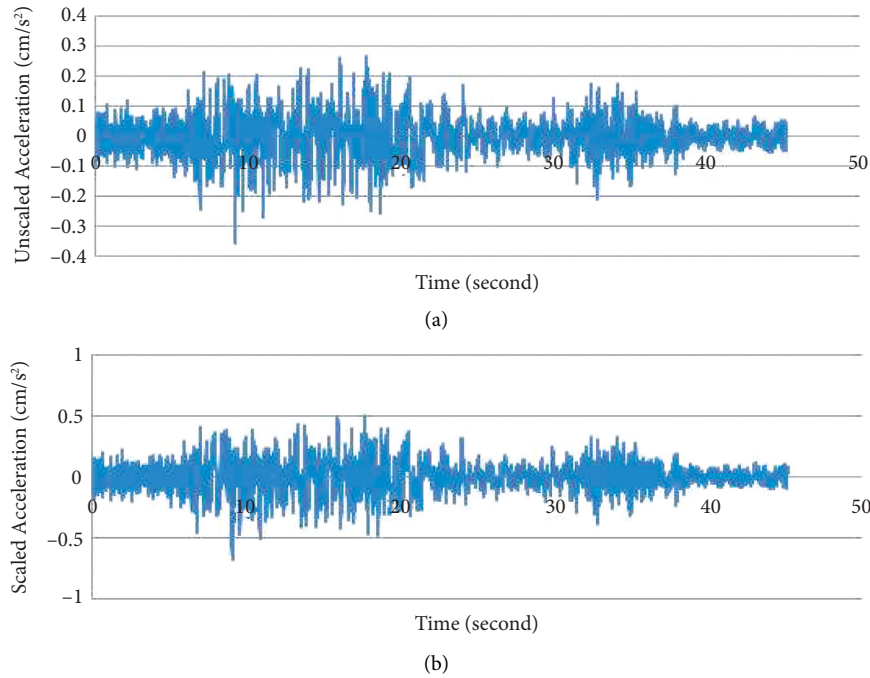


FIGURE 8: Earthquake with an epicenter at Kayseri-Kocasinan ( $M_L$ : 4.8). (a) Unscaled and (b) scaled acceleration record graph of this earthquake in the north-south (N-S) route.

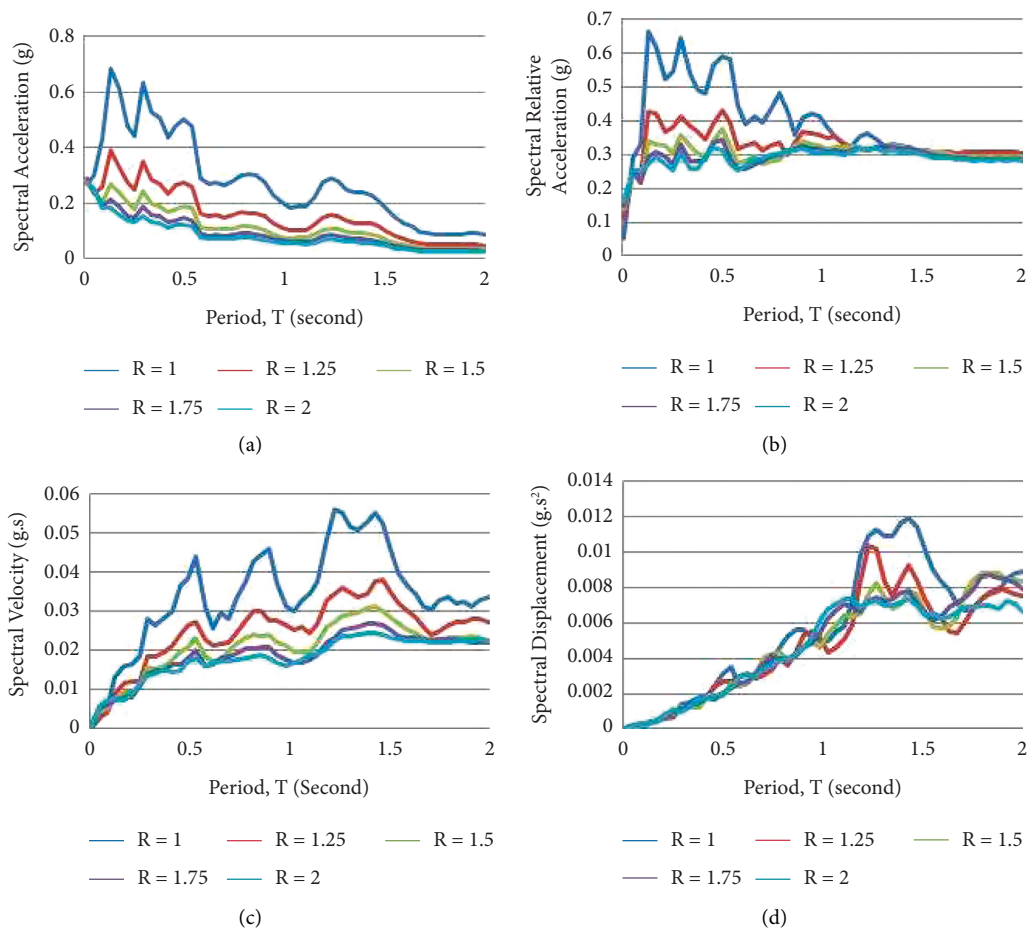


FIGURE 9: Earthquake with an epicenter at Kayseri-Kocasinan ( $M_D$ : 3.7) and the record of north-south (N-S) route. (a) Scaled spectral total acceleration, (b) spectral relative acceleration, (c) spectral velocity, and (d) spectral displacement spectrum graph.

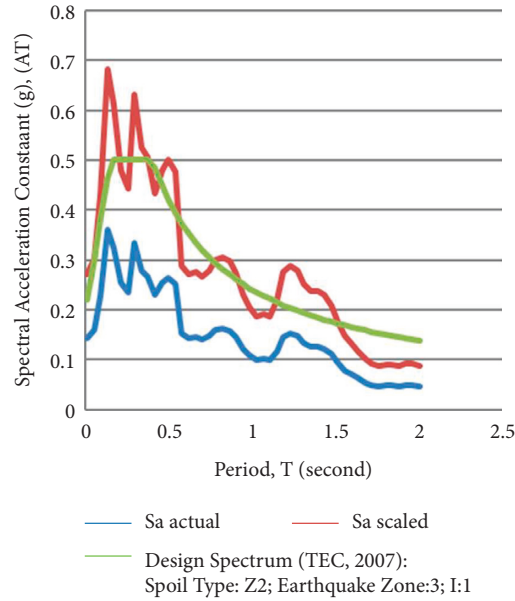


FIGURE 10: Earthquake with an epicenter at Kayseri-Kocasinan ( $M_D$ : 3.7) and response spectrum of north-south (N-S) route record scaled according to elastic design acceleration spectrum.

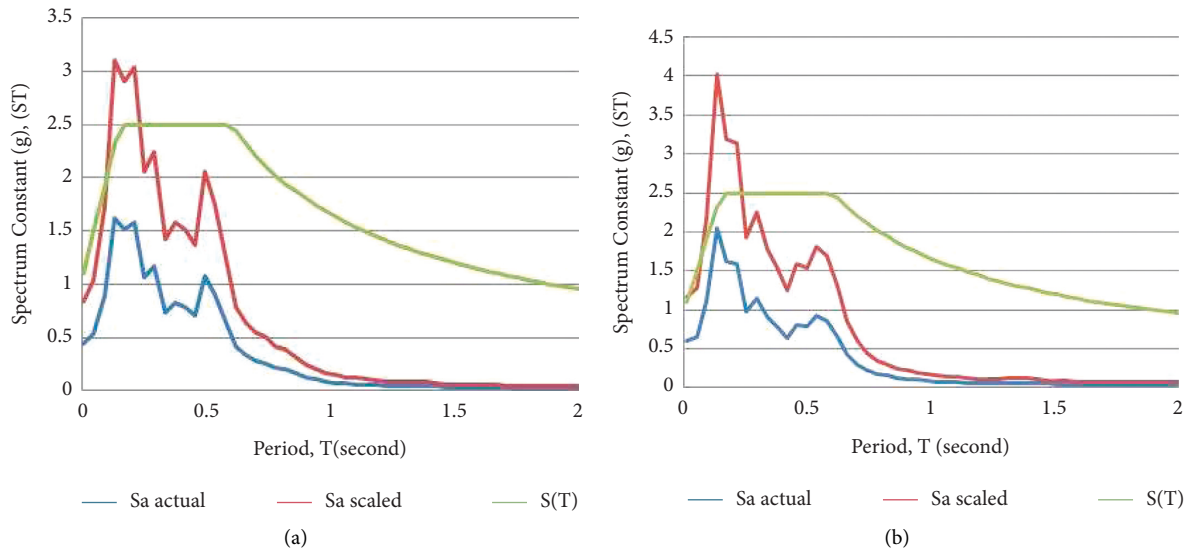


FIGURE 11: Evaluation of  $S(T)$  spectrum constants for (a) North-South (N-S) and (b) East-West (E-W) components of earthquake with epicenter at Sivas ( $M_D$ : 4.0).

- (5) Scaled response spectrum graphs were created by multiplying data related to real ground motion response spectrum graphs obtained using the Bispec-Earthquake Solutions Programme [46] with the scaling factor,  $\alpha_{ST}$ .
- (6) The differences between the design spectrum of each component for each record and the response spectrum amplitude of the scaled record, in the period range between  $T_S = 0.01$  s and  $T_F = 2.00$  s, were

computed using the “Sum Relative Errors” formula shown in the following equation.

$$|\text{Sum Relative Error}| = \sum_{TF}^{TS} \left[ \left| \frac{\alpha S_a^{\text{actual}}(T) - S_a^{\text{target}}(T)}{S_a^{\text{target}}(T)} \right| \right]. \quad (7)$$

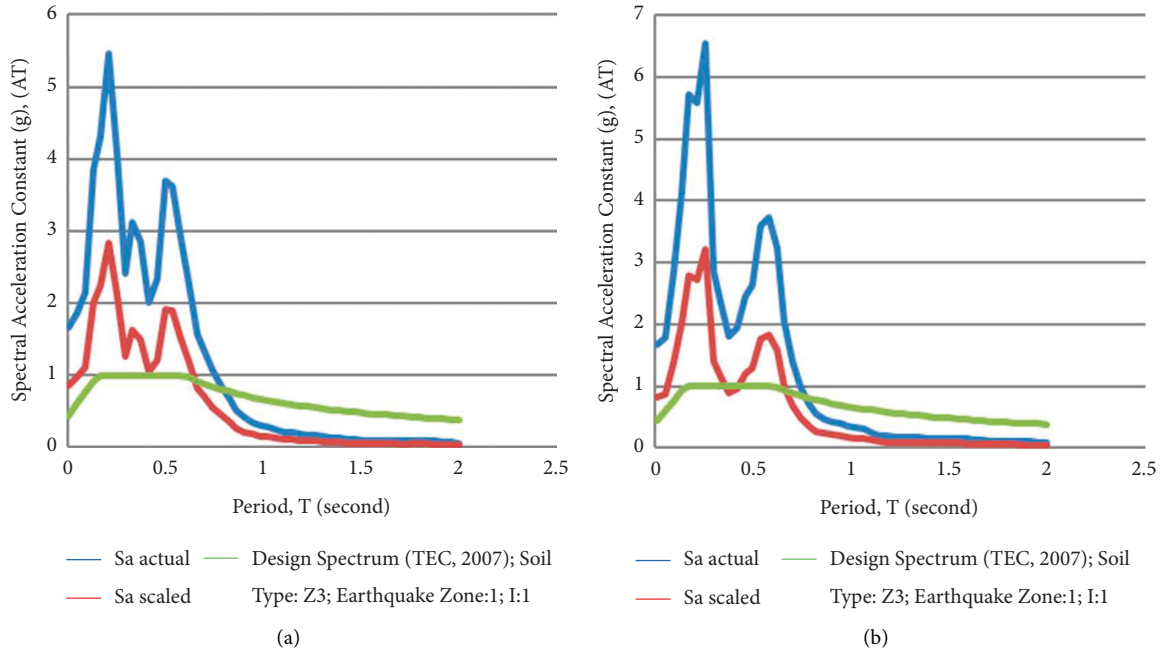


FIGURE 12: Evaluation of A(T) spectral acceleration constants for (a) North-South (N-S) and (b) East-West (E-W) components of earthquake with epicenter at Sivas ( $M_D$ : 4.5).

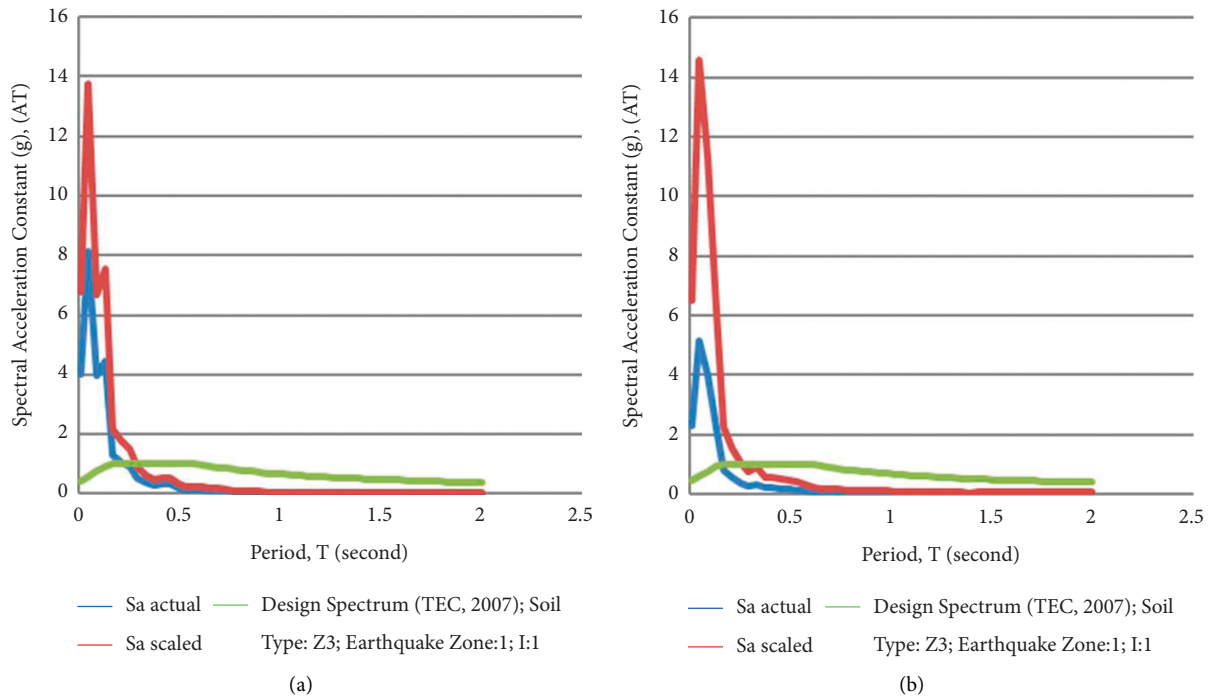


FIGURE 13: Evaluation of A(T) spectral acceleration constants for (a) North-South (N-S) and (b) East-West (E-W) components of earthquake with epicenter at Sivas ( $M_D$ : 2.8).

The error amount is calculated as a percentage by putting the “Sum Relative Error” obtained in the following equation.

$$|\text{Average Relative Error (\%)}| = \frac{1}{k} |\text{Sum Relative Error}| \times 100, \quad (8)$$

where  $k$  is the number of period steps ( $\Delta T$ ) used to generate the response spectrum of the record.

$$k = \frac{(T_F - T_S)}{\Delta T}. \quad (9)$$

(7) Each earthquake record was scaled for both the N-S (north-south) and E-W (east-west) components and



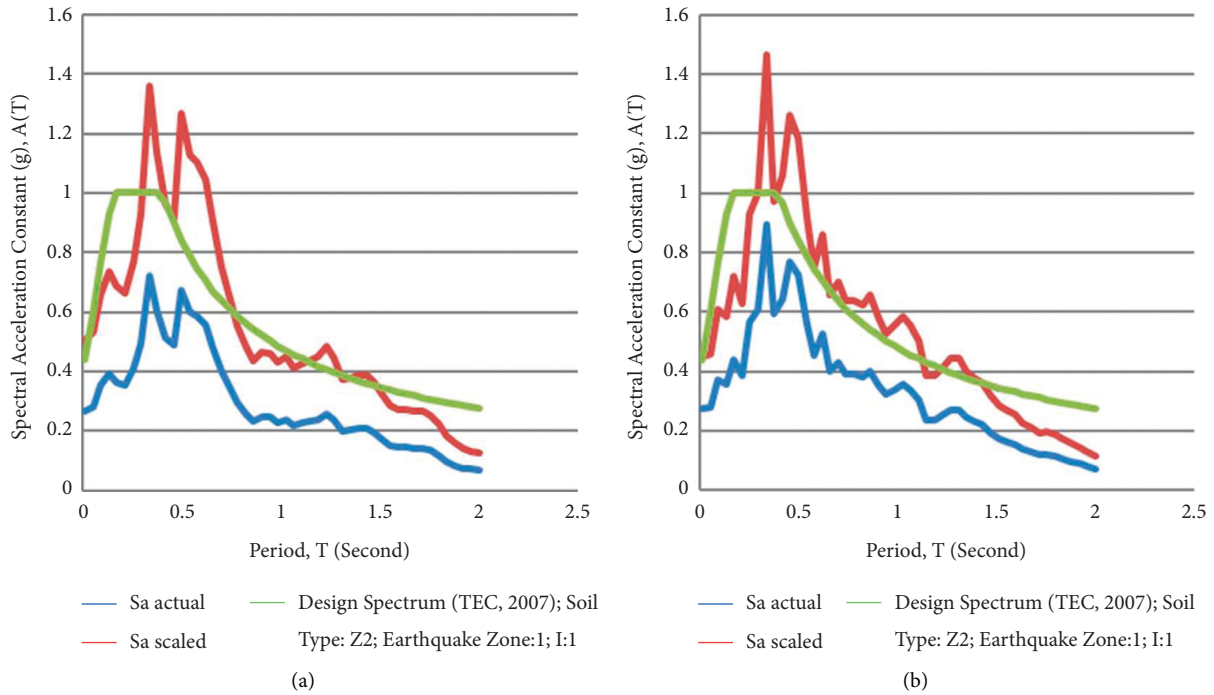


FIGURE 14: Evaluation of A(T) spectral acceleration constants for (a) North-South (N-S) and (b) East-West (E-W) components of earthquake with epicenter at Kayseri-Kocasinan ( $M_L$ : 4.8).

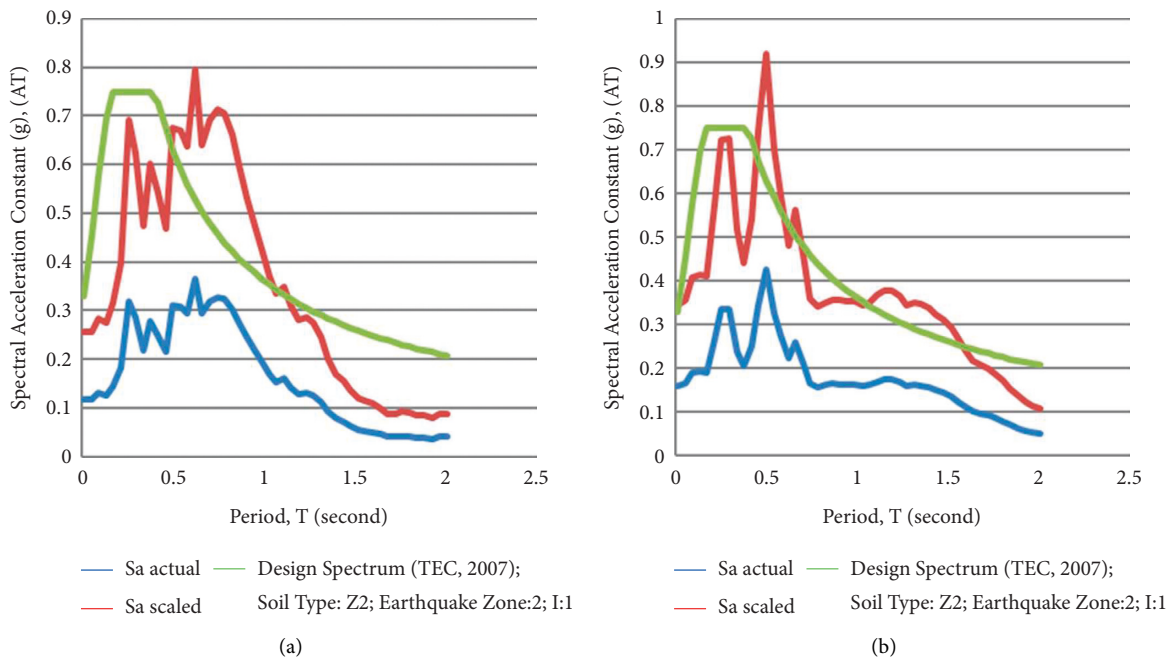


FIGURE 15: Evaluation of A(T) spectral acceleration constants at Bala station for (a) North-South (N-S) and (b) East-West (E-W) components of earthquake epicenter at Kayseri-Kocasinan ( $M_L$ : 4.8).

in the period range between  $T_S = 0.01$  s and  $T_F = 2.00$  s for the 5% damping ratio obtained. Scaled response spectrum graphs were created using the scaled acceleration record graphs, and the scaled or unscaled response spectrum graphs obtained were then compared to the design acceleration spectra.

Records of earthquakes occurring throughout the CAFZ were grouped as N-S (north-south) and E-W (east-west) according to the characteristics of local soil classes (Z2 and Z3 local site class) at stations where the earthquakes were scaled. The spectrum constant,  $S(T)$ , which was obtained by scaling to the design acceleration spectra defined, and the

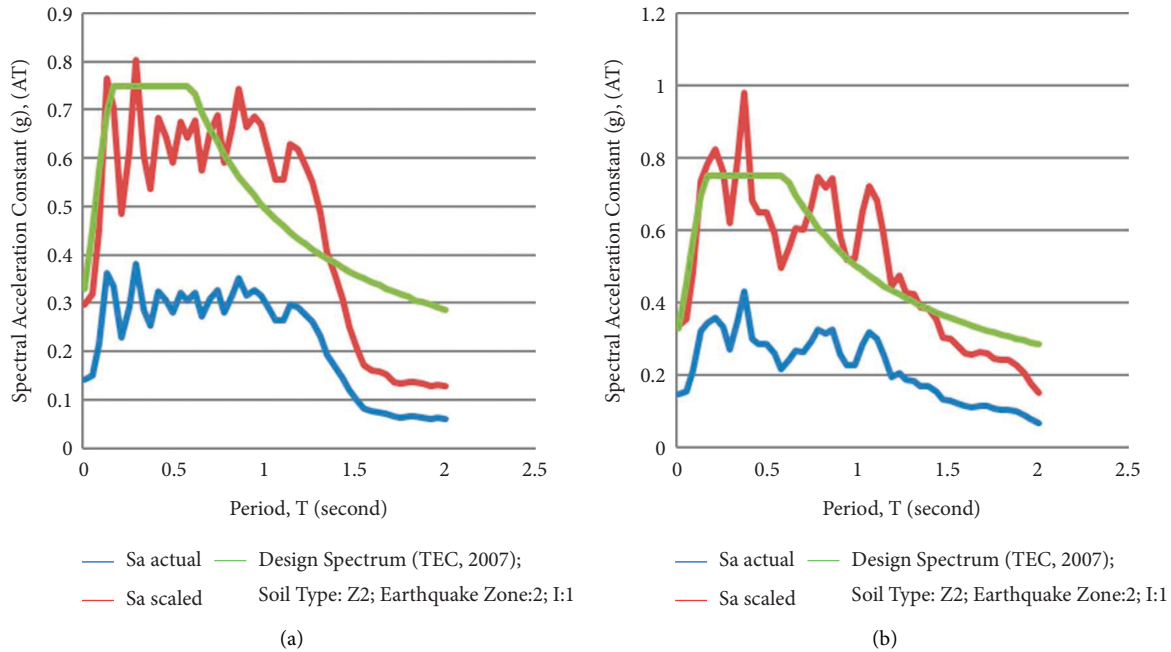


FIGURE 16: Evaluation of A(T) spectral acceleration constants at S. Kochisar station for (a) North-South (N-S) and (b) East-West (E-W) components of earthquake with epicenter at Kayseri-Kocasinan ( $M_L$ : 4.8).

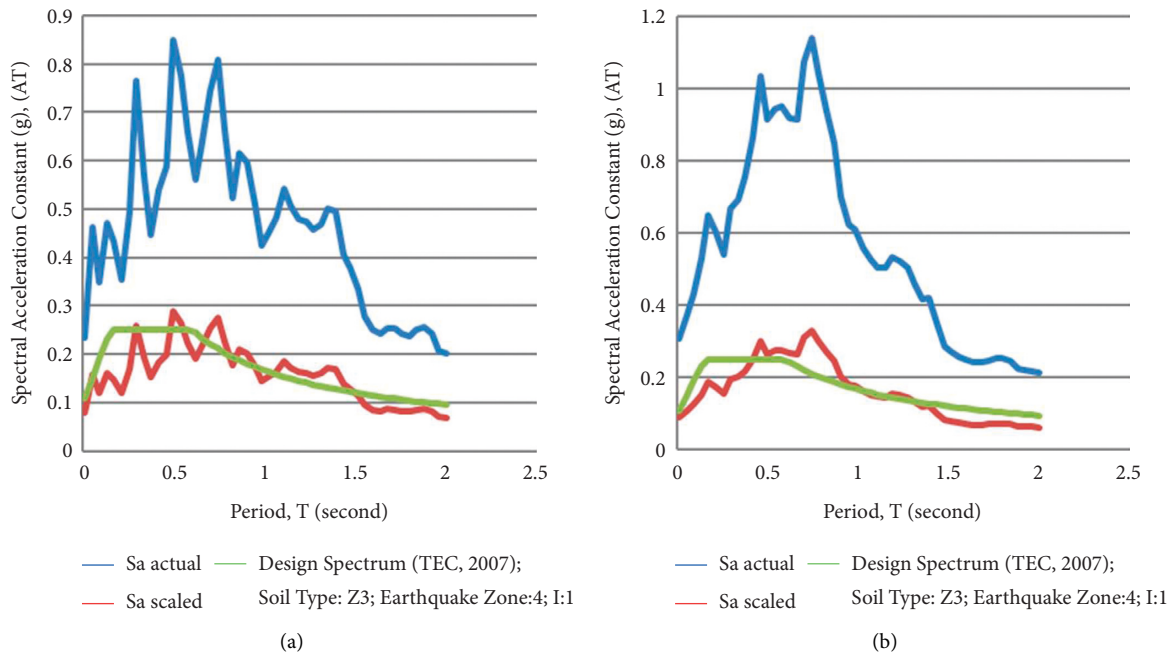


FIGURE 17: Evaluation of A(T) spectral acceleration constants at Aksaray station for (a) North-South (N-S) and (b) East-West (E-W) components of earthquake with epicenter at Kayseri-Kocasinan ( $M_L$ : 4.8).

average spectrum curve obtained using these records is shown in Figures 6 and 7.

**3.5. Implementation.** In this example, the earthquake record ( $M_D$ : 3.7) shown in Table 1 is selected. This event occurred in 2008 along the N-S route at Kayseri-Kocasinan on the CAFZ. The recording station at which the earthquake was

scaled is located on a Z2 local site class and in the 3rd degree earthquake zone ( $A_o = 0.2$ ); the building importance factor is selected as  $I = 1$ .

To enable this record to provide a match with the design acceleration spectrum identified for Z3 local site class, the  $\alpha_{ST}$  constant is found to be 8.79 using Equation (3).  $S_a^{actual}(T)$  and  $S_a^{target}(T)$  values used for calculation of  $\alpha_{ST}$  are given below in Table 3.

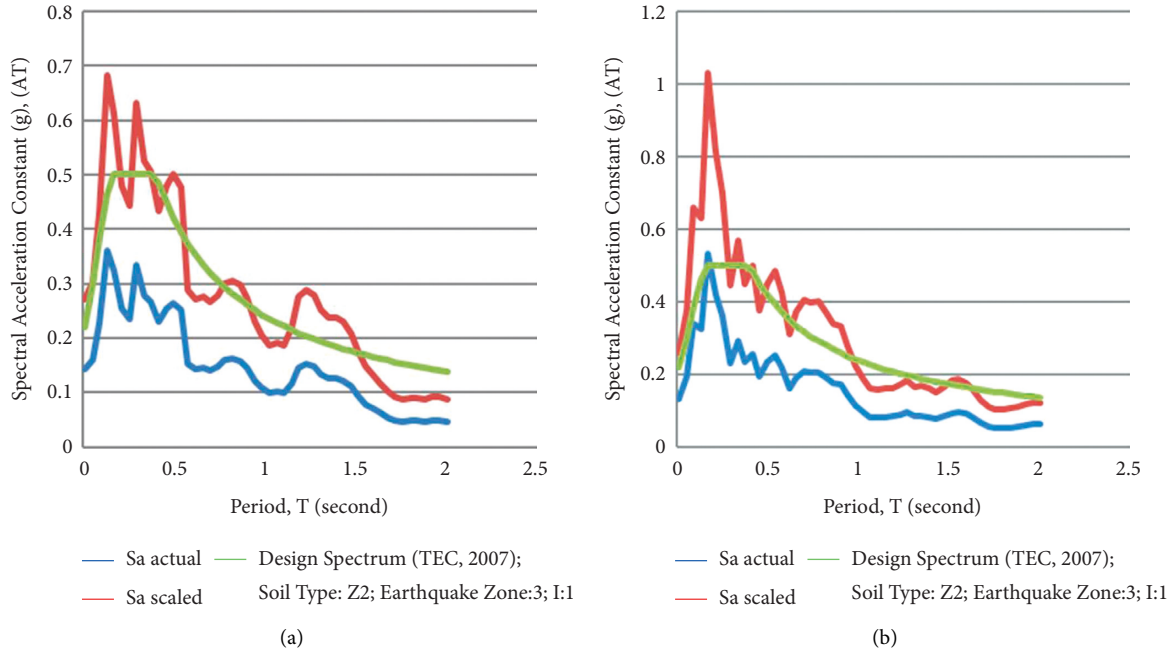


FIGURE 18: Evaluation of  $A(T)$  spectral acceleration constants for (a) North-South (N-S) and (b) East-West (E-W) components of earthquake with epicenter at Kayseri-Kocasinan ( $M_D: 3.7$ ).

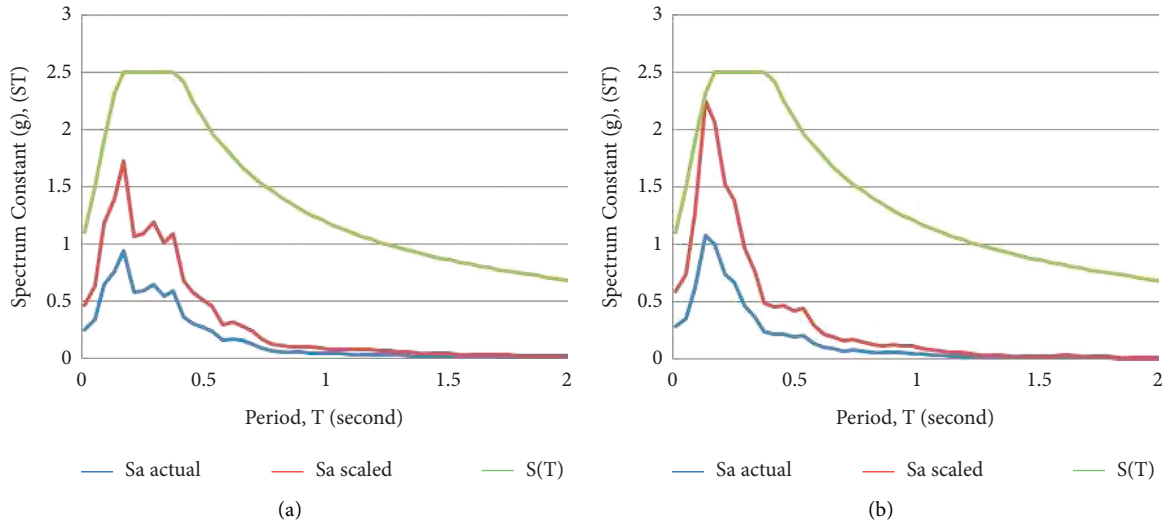


FIGURE 19: Evaluation of  $S(T)$  spectrum constants for (a) North-South (N-S) and (b) East-West (E-W) components of earthquake with epicenter at Kayseri-Kocasinan ( $M_D: 3.6$ ).

From Equation (3) and Table 3,  $\alpha_{ST} = 8.79$  is obtained. Then, Equation (6) is used to calculate the scaling factor as follows:

$$\alpha_{AT} = A_o I \alpha_{ST} = 0.2 \times 1 \times 8.79 = 1.758. \quad (10)$$

To obtain the scaled record, the amplitudes of earthquake records are thus linearly multiplied by  $\alpha_{AT}$ , the scaling constant. Figure 8 shows records that are both scaled and not scaled with  $\alpha_{AT}$ ; the acceleration response spectra of the scaled records have a period range of between  $T_S = 0.01$  s and

$T_F = 2$  s. The 5% damping ratio is shown in Figure 9 in the forms of spectral total acceleration, spectral relative acceleration, spectral velocity, and spectral displacement. Figure 10 shows acceleration response spectra with a 5% damping ratio for a SDOF linear system, and a design spectrum for a record scaled with  $\alpha_{AT}$  (with respect to this record).

While  $\alpha_{ST}$  linear scaling constant is being calculated, it should be considered that the response spectrum that is not scaled in the period range from  $T_S = 0.01$  s to  $T_F = 2$  s possesses a 5% damping ratio of  $S_a^{\text{target}}$  E-W (east-west)

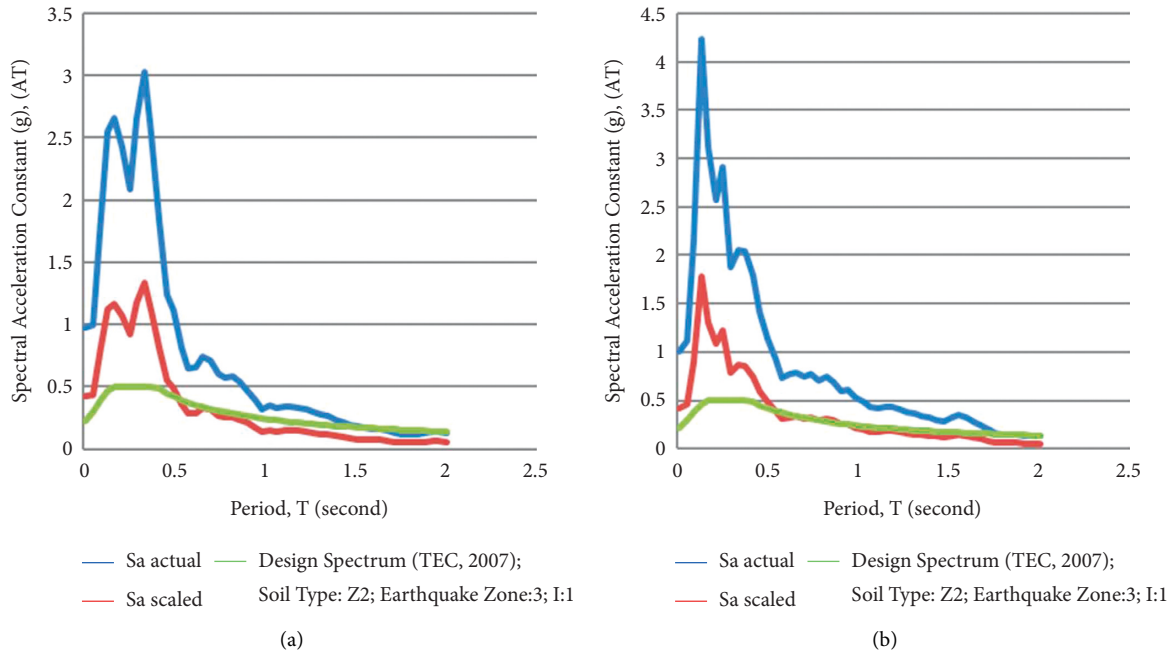


FIGURE 20: Evaluation of A(T) spectral acceleration constants for (a) North-South (N-S) and (b) East-West (E-W) components of earthquake with epicenter at Kayseri-Kocasinan ( $M_D$ : 3.7-  $M_L$ : 3.9).

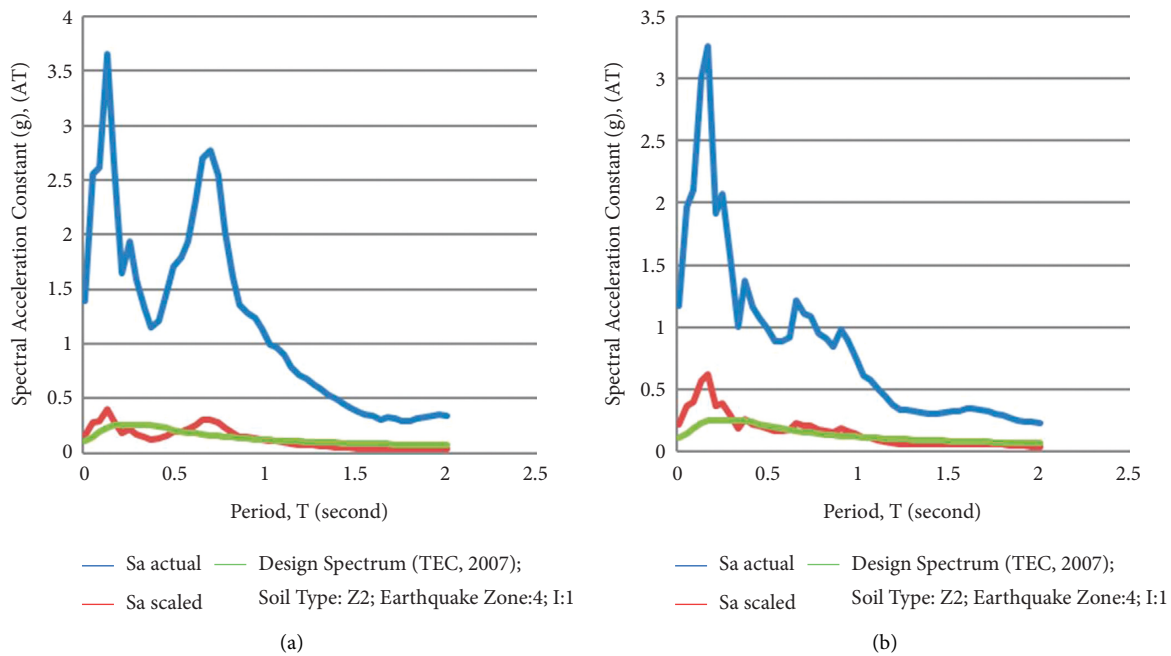


FIGURE 21: Evaluation of A(T) spectral acceleration constants at Nigde station for (a) North-South (N-S) and (b) East-West (E-W) components of earthquake with epicenter at Nigde-Camardi ( $M_L$ : 4.3).

earthquake route record, and for earthquake records measured in local site class Z3 and 3rd earthquake zone,  $S_a^{target}$  is the elastic design acceleration spectrum value in Figure 5.

3.6. Scaled Response Spectrum Graphs of Records. Scaled response spectrum graphs of records in the North-South (N-S) and East-West (E-W) earthquake routes that occurred on

the CAFZ, according to the elastic design acceleration spectra, are given below in Figures 11–26.

#### 4. Results and Discussion

This is a pioneering study on the analysis of seismic behavior using SDOF systems subjected to ground motions that were recorded in relation to earthquakes occurring on the CAFZ

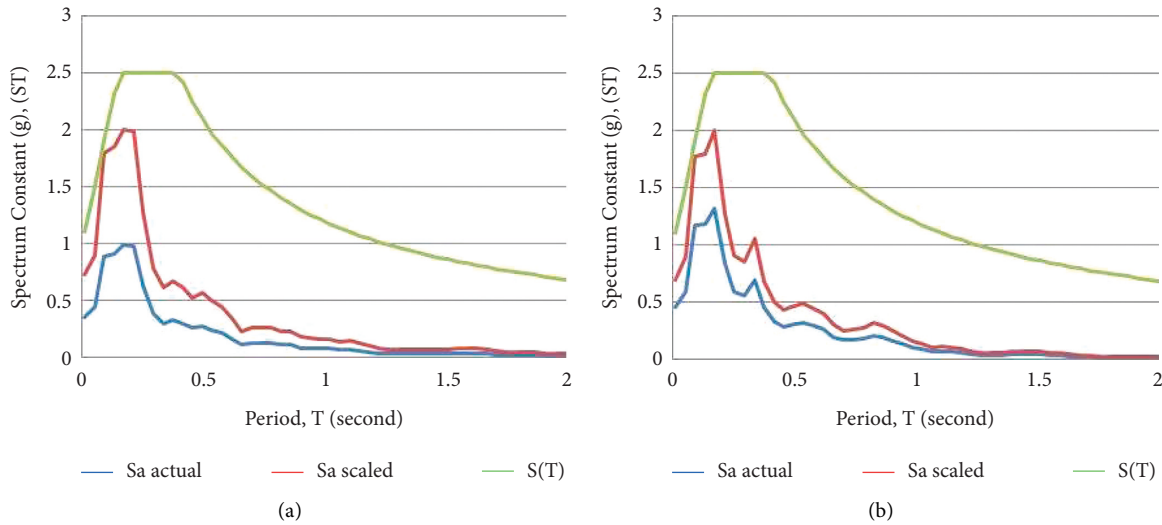


FIGURE 22: Evaluation of  $S(T)$  spectrum constants at Nevsehir station for (a) North-South (N-S) and (b) East-West (E-W) components of earthquake with epicenter at Nigde-Camardi ( $M_L$ : 4.3).

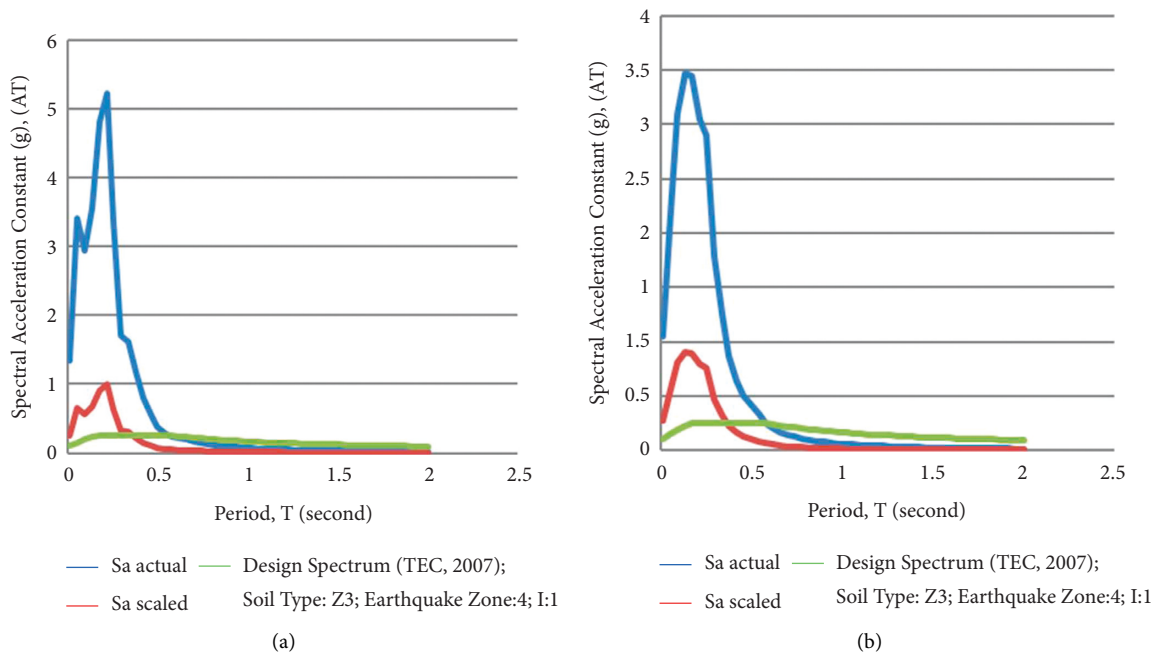


FIGURE 23: Evaluation of  $A(T)$  spectral acceleration constants for (a) North-South (N-S) and (b) East-West (E-W) components of earthquake with epicenter at Nigde-Camardi ( $M_L$ : 3.7).

in Turkey. It is considered that the study provides useful results for application in earthquake engineering performance-based design principles within the region.

It is essential that records have particular features for use and that scaling methods are selected to match real ground motion records and design acceleration spectra as defined in [35, 47]. Earthquake ground motion records occurring through this fault zone can then be scaled, thus conforming to the design acceleration spectrum defined.

This study uses the records of 17 ground motions recorded in the Turkish National Strong Ground Motion Database (2015) throughout the fault zone. Table 1 shows the

associated station location, ground conditions, distance, magnitude, acceleration values, and scaling factors related to these records. Acceleration record graphs that are both scaled and not scaled for each N-S (north-south) and E-W (east-west) component are shown; and the response spectrum graphs (spectral total acceleration, spectral relative acceleration, spectral velocity, and spectral displacement forms) with a 5% damping ratio of a SDOF linear system within the period range between  $T_S=0.01$  s and  $T_F=2$  s in the time domain are generated using the scaling method.

Compatible records are selected from the 17 ground motion records to fit scaling, with conditions provided in the

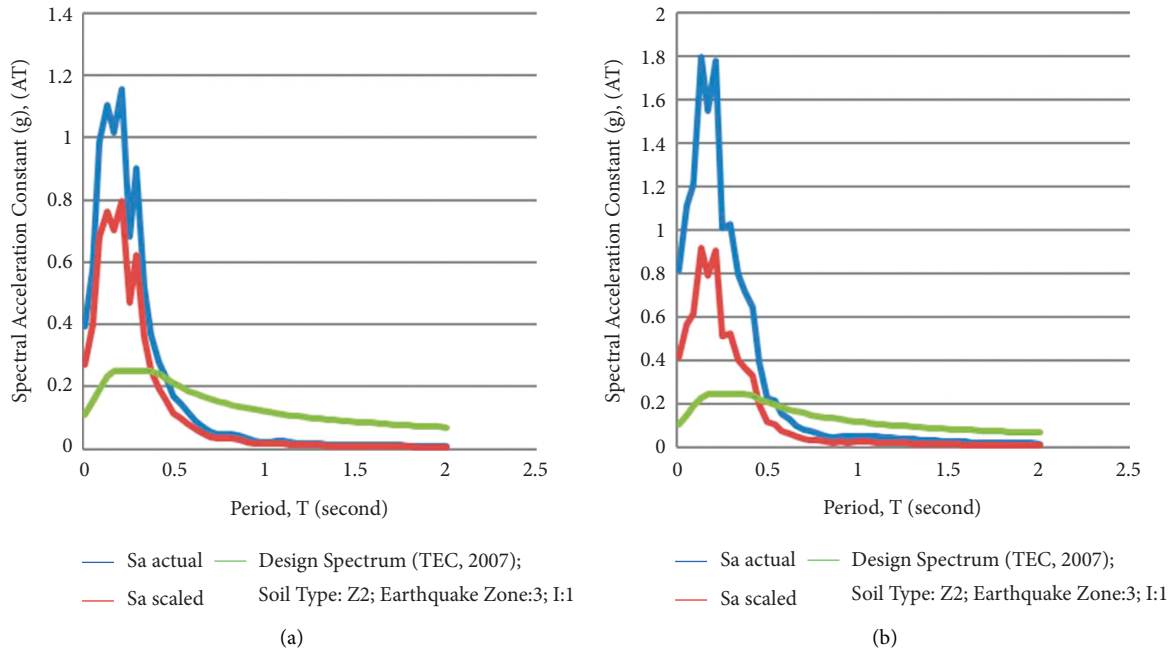


FIGURE 24: Evaluation of A(T) spectral acceleration constants for (a) North-South (N-S) and (b) East-West (E-W) components of earthquake with epicenter at Sivas-Kangal ( $M_W$ : 4.2).

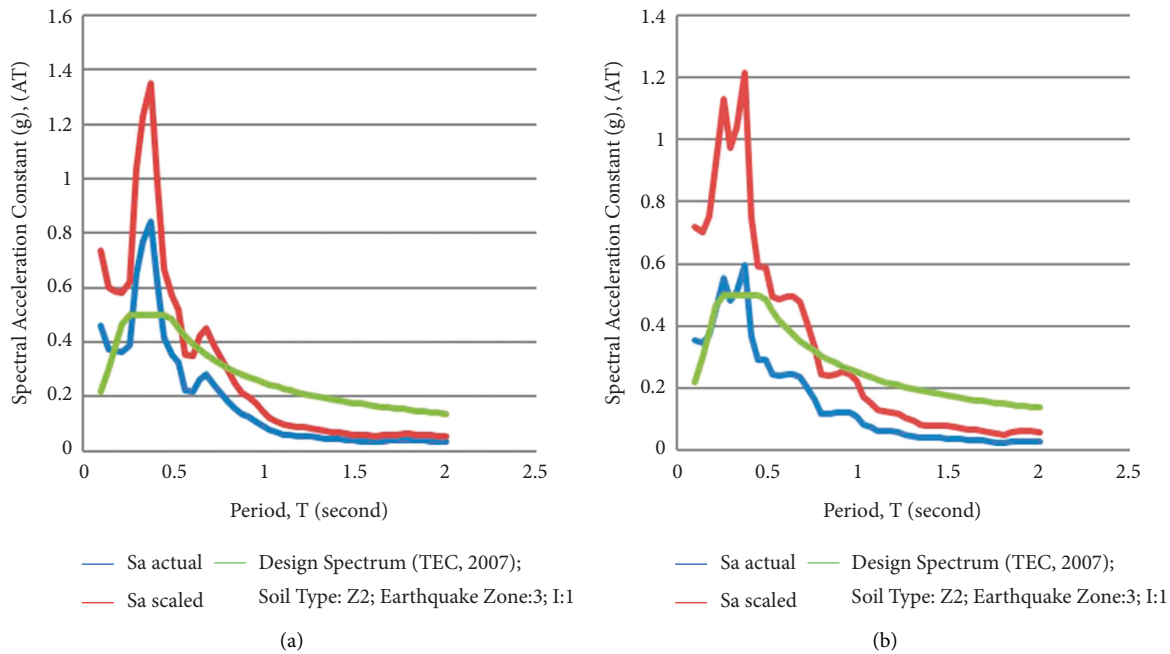


FIGURE 25: Evaluation of A(T) spectral acceleration constants for (a) North-South (N-S) and (b) East-West (E-W) components of earthquake with epicenter at Kayseri-Kocasinan ( $M_W$ : 3.8).

design acceleration spectrum defined. The study then shows the practice of record scaling in the period range between  $T_S=0.01$  s and  $T_F=2$  s with a proper SDOF linear system with a damping ratio of 5%.

The study mentions the importance of the compatible scaling of real earthquake records with the design response spectrum using conditions specified in the earthquake codes. When the earthquakes recorded throughout the CAFZ were

examined, some were found to be unsuitable for scaling. By examining response spectra formed by the scaled earthquake records, it was thus possible to understand which earthquake records were suitable or not for scaling in line with the design spectrum.

It should be noted that this is a study based on specific examples of building structures along the CAFZ. Meanwhile, this research method is applicable in other seismic regions of

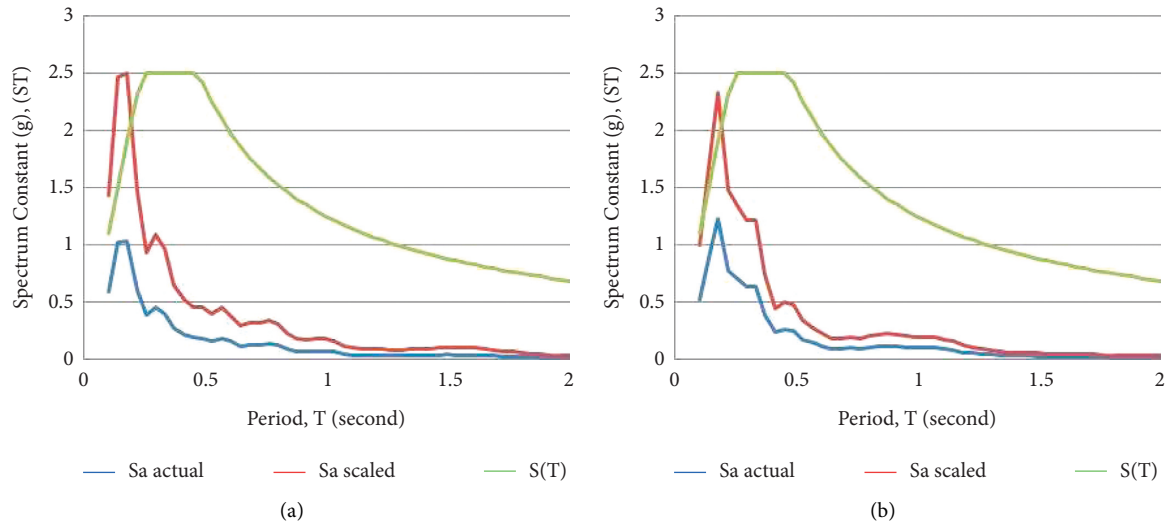


FIGURE 26: Evaluation of  $S(T)$  spectrum constants for (a) North-South (N-S) and (b) East-West (E-W) components of earthquake with epicenter at Sivas-Gemerek ( $M_w$ : 3.8).

the world because it is based on current scaling methods available in the literature. This study determines the importance of selecting suitable records with certain features that can be used with the scaling method to ensure that real ground motion records match the design acceleration spectrum defined in the earthquake codes.

### Data Availability

The data used to support the findings of the study can be obtained from the corresponding author upon request.

### Disclosure

This research was performed as part of the M. Sc. Thesis of Mr. Erhan Gumus at Nigde Omer Halisdemir University, Turkey.

### Conflicts of Interest

The authors declare that they have no conflicts of interest regarding the publication of this paper.

### References

- [1] N. A. Abrahamson, "Non-stationary spectral matching Program," RSPMATCH, User's Manual, 1993.
- [2] D. M. Boore, "Simulation of ground motion using the Stochastic method," *Pure and Applied Geophysics*, vol. 160, no. 3, pp. 635–676, 2003.
- [3] J. J. Bommer and A. B. Acevedo, "The Use of real earthquake accelerograms as input to dynamic analysis," *Journal of Earthquake Engineering*, vol. 8, no. sup001, pp. 43–91, 2004.
- [4] J. J. Bommer, A. B. Acevedo, and J. Douglas, "The selection and scaling of real earthquake accelerograms for Use in seismic design and assessment," *Proceedings of ACI International Conference on Seismic Bridge Design and Retrofit*, American Concrete Institute, 2003.
- [5] Y. M. Fahjan, "Selection and scaling of real earthquake accelerograms to fit the Turkish design spectra (DBYBHY, 2007)," *Chamber of Civil Engineers Technical Journal*, pp. 4423–4444, 2008.
- [6] M. M. Hachem, N. J. Mathias, Y. Y. Wang et al., "An International Comparison of ground motion selection criteria for seismic design," in *Proceedings of the Joint IABSE-fib Conference*, Dubrovnik, Croatia, May 2010.
- [7] A. Akinci, L. Malagnini, R. B. Herrmann, R. Gok, and M. B. Sørensen, "Ground motion scaling in the Marmara region, Turkey," *Geophysical Journal International*, vol. 166, no. 2, pp. 635–651, 2006.
- [8] P. Bodin, L. Malagnini, and A. Akinci, "Ground-motion scaling in the Kachchh basin, India, Deduced from After-shocks of the 2001 Mw 7.6 Bhuj earthquake," *Bulletin of the Seismological Society of America*, vol. 94, no. 5, pp. 1658–1669, 2004.
- [9] L. C. Haar, J. B. Fletcher, and C. S. Mueller, "The 1982 Enola, Arkansas, swarm and scaling of ground motion in the eastern United States," *Bulletin of the Seismological Society of America*, vol. 74, no. 6, pp. 2463–2482, 1984.
- [10] I. Iervolino, E. Cosenza, and C. Galasso, "Shedding some Light on seismic input selection in Eurocode 8," in *Proceedings of the Eurocode 8 Perspectives from the Italian Standpoint Workshop*, pp. 3–12, Doppiavoce, Naples, Italy, 2009.
- [11] A. H. Kayhan, "Obtaining the unscaled accelerogram setting compatible with Eurocode-8 by Armony research technic," in *Proceedings of the Turkish Earthquake Engineering and Seismology Conference*, METU, Ankara, Turkey, October 2011.
- [12] L. Malagnini, R. B. Herrmann, and K. Koch, "Regional ground-motion scaling in Central Europe," *Bulletin of the Seismological Society of America*, vol. 90, no. 4, pp. 1052–1061, 2000.
- [13] L. Malagnini, R. B. Herrmann, and M. Di Bona, "Ground-motion scaling in the Apennines (Italy)," *Bulletin of the Seismological Society of America*, vol. 90, no. 4, pp. 1062–1081, 2000.
- [14] P. Morasca, L. Malagnini, A. Akinci, D. Spallarossa, and R. B. Herrmann, "Ground-motion scaling in the western Alps," *Journal of Seismology*, vol. 10, no. 3, pp. 315–333, 2006.
- [15] A. Rovelli, O. Bonamassa, M. Cocco, M. Di Bona, and S. Mazza, "Scaling laws and spectral parameters of the ground motion in active extensional areas in Italy," *Bulletin of the*

- Seismological Society of America*, vol. 78, no. 2, pp. 530–560, 1988.
- [16] L. Scognamiglio, L. Malagnini, and A. Akinci, “Ground-motion scaling in eastern Sicily, Italy,” *Bulletin of the Seismological Society of America*, vol. 95, no. 2, pp. 568–578, 2005.
- [17] J. P. Stewart, S. Midorikawa, R. W. Graves et al., “Implications of the Mw9.0 Tohoku-Oki earthquake for ground motion scaling with source, Path, and site parameters,” *Earthquake Spectra*, vol. 29, no. 1\_suppl, pp. 1–21, 2013.
- [18] C. H. Scholz, “Scaling relations for strong ground motion in large earthquakes,” *Bulletin of the Seismological Society of America*, vol. 72, no. 6A, pp. 1903–1909, 1982.
- [19] A. McGarr, “Scaling of ground motion parameters, state of stress, and focal depth,” *Journal of Geophysical Research: Solid Earth*, vol. 89, no. B8, pp. 6969–6979, 1984.
- [20] P. G. Somerville, “Magnitude scaling of near fault ground motions,” *Earthquake Engineering and Engineering Seismology*, vol. 2, no. 2, pp. 15–24, 2000.
- [21] Y. C. Kurama and K. T. Farrow, “Ground motion scaling methods for different site conditions and structure characteristics,” *Earthquake Engineering & Structural Dynamics*, vol. 32, no. 15, pp. 2425–2450, 2003.
- [22] F. Naeim, A. Alimoradi, and S. Pezeshk, “Selection and scaling of ground motion time histories for structural design using genetic algorithms,” *Earthquake Spectra*, vol. 20, no. 2, pp. 413–426, 2004.
- [23] J. Watson-Lamprey and N. Abrahamson, “Selection of ground motion time series and limits on scaling,” *Soil Dynamics and Earthquake Engineering*, vol. 26, no. 5, pp. 477–482, 2006.
- [24] N. Luco and P. Bazzurro, “Does amplitude scaling of ground motion records result in biased nonlinear structural drift responses?” *Earthquake Engineering & Structural Dynamics*, vol. 36, no. 13, pp. 1813–1835, 2007.
- [25] A. Kottke and E. M. Rathje, “A semi-automated procedure for selecting and scaling recorded earthquake motions for dynamic analysis,” *Earthquake Spectra*, vol. 24, no. 4, pp. 911–932, 2008.
- [26] Y. N. Huang, A. S. Whittaker, N. Luco, and R. O. Hamburger, “Scaling earthquake ground motions for performance-based assessment of buildings,” *Journal of Structural Engineering*, vol. 137, no. 3, pp. 311–321, 2011.
- [27] E. I. Katsanos, A. G. Sextos, and G. D. Manolis, “Selection of earthquake ground motion records: a state-of-the-art review from a structural engineering perspective,” *Soil Dynamics and Earthquake Engineering*, vol. 30, no. 4, pp. 157–169, 2010.
- [28] N. Jayaram, T. Lin, and J. W. Baker, “A computationally efficient ground-motion selection algorithm for matching a target response spectrum mean and variance,” *Earthquake Spectra*, vol. 27, no. 3, pp. 797–815, 2011.
- [29] I. Takewaki and H. Tsujimoto, “Scaling of design earthquake ground motions for tall buildings based on drift and input energy demands,” *Earthquakes and Structures*, vol. 2, no. 2, pp. 171–187, 2011.
- [30] B. O. Ay and S. Akkar, “A procedure on ground motion selection and scaling for nonlinear response of simple structural systems,” *Earthquake Engineering & Structural Dynamics*, vol. 41, no. 12, pp. 1693–1707, 2012.
- [31] C. B. Haselton, A. S. Whittaker, A. Hortacsu, J. W. Baker, J. Bray, and D. N. Grant, “Selecting and scaling earthquake ground motions for performing response-history analyses,” in *Proceedings of the 15th World Conference on Earthquake Engineering*, Lisbon, Portugal, November 2012.
- [32] L. Al Atik, A. Kottke, N. Abrahamson, and J. Hollenback, “Kappa (K) scaling of ground motion prediction equations using an Inverse random vibration theory approach,” *Bulletin of the Seismological Society of America*, vol. 104, no. 1, pp. 336–346, 2014.
- [33] N. N. Ambraseys and C. Finkel, *The Seismicity of Turkey and adjacent areas*, p. 240, UNESCO, Istanbul, 1995.
- [34] N. Pinar and E. Lahn, *Turkish Earthquake Catalog with Descriptions*, Turkey Ministry of Public Works and Settlement, The General Directorate of Construction Affairs, Serial 6, Technical Report 36, p. 153, 1952.
- [35] Turkish Earthquake Code (Tec), *Specification for Buildings to Be Built in Seismic Zones*, Ministry of Public Works and Settlement, Government of the Republic of Turkey, Ankara, Turkey, 2007.
- [36] C. Yetis, *Geology Analysis of Near and Distant Region of Camardi (Nigde) and Characteristics of the Ecemis Fault Zone between Maden Strait and Kamisli*, PhD Thesis, p. 164, Istanbul University, Faculty of Sciences, Istanbul, Turkey, 1978.
- [37] C. Yetis, “Geology of the Camardi (Nigde) region and the characteristics of the Ecemis fault zone between maden Bogazi and Kamisli,” *Revue de la Faculte des Sciences*, vol. 43, pp. 41–61, 1978.
- [38] A. Kocyigit and A. A. Ozacar, “Extensional neotectonic Regime through the NE Edge of the outer Isparta angle, SW Turkey: new field and seismic data,” *Turkish Journal of Earth Sciences*, vol. 12, pp. 67–90, 2003.
- [39] E. Bozkurt, “Neotectonics of Turkey – a synthesis,” *Geodinamica Acta*, vol. 14, no. 1-3, pp. 3–30, 2001.
- [40] Kyhdata, “Strong ground motion Database of Turkey (SGMDT),” 2015, <http://kyhdata.deprem.gov.tr>.
- [41] J. P. Stewart, S. J. Chiou, J. D. Bray, R. W. Graves, P. G. Somerville, and N. A. Abrahamson, *Ground Motion Evaluation Procedures for Performance-Based Design*, PEER Report 2001/09, Pacific Earthquake Engineering Research Center, University of California, Berkeley, USA, 2001.
- [42] A. S. Nikolaou, *A GIS Platform for Earthquake Risk Analysis*, Ph.D. Dissertation, State University of New York at Buffalo, USA, 1998.
- [43] Z. Ozdemir and Y. M. Fahjan, “Comparison of scaling methods of real earthquake records conforming to design spectrum in time and frequency domain,” in *Proceedings of the 6th National Earthquake Engineering Conference*, Istanbul, Turkey, October 2007.
- [44] E. L. Krinitzsky and F. K. Chang, *Specifying Peak Motions for Design Earthquakes, State-Of The-Art for Assessing Earthquake Hazards in the United States*, Report 7, Miscellaneous Paper S-73-1, US Army Corps of Engineers, USA, 1977.
- [45] E. H. Vanmarcke, *State-of-the-Art for Assessing Earthquake Hazards in the United States: Representation of Earthquake Ground Motions – Scaled Accelerograms and Equivalent Response Spectra*, Miscellaneous Paper S-73-1, Report 14, Vicksburg, US Army Corps of Engineers Waterways Experiment Station, Mississippi, USA, 1979.
- [46] M. Hachem, “Bispec-earthquake Solutions Programme,” Bispec Version 2.20, 2015.
- [47] Turkish Building Earthquake Code (Tbec), *Specification for Buildings to Be Built in Seismic Zones, Disaster and Emergency Management Presidency*, Government of Republic of Turkey, Ankara, Turkey, 2018.



## *Retraction*

# **Retracted: Integrating Intrinsic and Eccentric Seismic Vulnerability Indices to Prioritize Road Network Accessibility**

### **Advances in Civil Engineering**

Received 15 August 2023; Accepted 15 August 2023; Published 16 August 2023

Copyright © 2023 Advances in Civil Engineering. This is an open access article distributed under the Creative Commons Attribution License, which permits unrestricted use, distribution, and reproduction in any medium, provided the original work is properly cited.

This article has been retracted by Hindawi following an investigation undertaken by the publisher [1]. This investigation has uncovered evidence of one or more of the following indicators of systematic manipulation of the publication process:

- (1) Discrepancies in scope
- (2) Discrepancies in the description of the research reported
- (3) Discrepancies between the availability of data and the research described
- (4) Inappropriate citations
- (5) Incoherent, meaningless and/or irrelevant content included in the article
- (6) Peer-review manipulation

The presence of these indicators undermines our confidence in the integrity of the article's content and we cannot, therefore, vouch for its reliability. Please note that this notice is intended solely to alert readers that the content of this article is unreliable. We have not investigated whether authors were aware of or involved in the systematic manipulation of the publication process.

Wiley and Hindawi regrets that the usual quality checks did not identify these issues before publication and have since put additional measures in place to safeguard research integrity.

We wish to credit our own Research Integrity and Research Publishing teams and anonymous and named external researchers and research integrity experts for contributing to this investigation.

The corresponding author, as the representative of all authors, has been given the opportunity to register their agreement or disagreement to this retraction. We have kept a record of any response received.

### **References**

- [1] A. M. El Maissi, S. A. Argyroudis, M. M. Kassem, L. V. Leong, and F. Mohamed Nazri, "Integrating Intrinsic and Eccentric Seismic Vulnerability Indices to Prioritize Road Network Accessibility," *Advances in Civil Engineering*, vol. 2022, Article ID 5888020, 20 pages, 2022.

## Research Article

# Integrating Intrinsic and Eccentric Seismic Vulnerability Indices to Prioritize Road Network Accessibility

Ahmad Mohamad El Maissi,<sup>1</sup> Sotirios A. Argyroudis,<sup>2</sup> Moustafa Moufid Kassem,<sup>1</sup> Lee Vien Leong,<sup>1</sup> and Fadzli Mohamed Nazri <sup>1</sup>

<sup>1</sup>School of Civil Engineering, Engineering Campus, Universiti Sains Malaysia, 14300 Nibong Tebal, Penang, Malaysia

<sup>2</sup>Department of Civil and Environmental Engineering, College of Engineering, Design and Physical Sciences, Brunel University, London UB8 3PH, UK

Correspondence should be addressed to Fadzli Mohamed Nazri; [cefmn@usm.my](mailto:cefmn@usm.my)

Received 4 June 2022; Accepted 5 July 2022; Published 10 August 2022

Academic Editor: Qian Chen

Copyright © 2022 Ahmad Mohamad El Maissi et al. This is an open access article distributed under the Creative Commons Attribution License, which permits unrestricted use, distribution, and reproduction in any medium, provided the original work is properly cited.

The main aim of this article is to shed light on the establishment of more resilient road networks, which can operate and interact regularly with the surrounding complex-built environment systems during various natural hazards such as earthquakes. This study is integrating engineering judgment and numerical methods to create a comprehensive evaluation for assessing the accessibility rates for road networks. Moreover, it is validating the significance of integrated seismic assessment on various critical sectors in society, such as improving emergency accessibility and adapting improved mitigation strategies for communities that live in disaster-prone districts. In this respect, this article investigates the seismic vulnerability assessment results, aiming at underpinning the understanding of road network risks by discussing the main results of the calculated probability of damage for various parameters of the roadway and its assets. A comparative study is performed to study the effect of spatially variable ground motions at different damage states for the main investigated four parameters. These extracted comparative results are used for weighting the main parameters to calculate the intrinsic seismic vulnerability index scores. Furthermore, the eccentric seismic vulnerability index is calculated, by following different steps such as assessing the calculated debris width resulting from the collapsed buildings and extracting the accessibility rates through concluding the effective width values. Subsequently, the variation between the accessibility rates is investigated and the integrated seismic risk assessment for a road system is developed with a focus on the integration between asset damage and functionality by generating integrated heat maps that take into consideration the correlation between all the developed vulnerability indices.

## 1. Introduction

The term “built environment” refers to a human-made ecosystem that gives the community identity and meaning in relation to its surroundings [1]. The built environment represents how a community interacts with the natural environment; for example, during earthquakes, it affects the number of deaths, injuries, and property damage. Consequently, it is necessary to analyze the built environments and reduce the amount of seismic damage [2, 3]. The concept of the “built environment” has more recently come to the attention of those conducting research on vulnerability;

nevertheless, it has been considered within the more generic domain of “physical vulnerability” [4, 5]. The vulnerability of a wide variety of urban structures with physical aspects, including buildings, municipal infrastructure, networks, and safety infrastructures, has been investigated on an individual basis. Indeed, it is essential to acknowledge that these elements do not exist in isolation from each other, and they interact systemically to produce the disaster effect in the face of a seismic event [6, 7].

Yet, in terms of disaster risk reduction, urban planning needs to be integrated into risk analysis tools [8]. Examining seismic response for complex-built environment systems is a

new study subject. Most of the previous studies concentrated on assessing the physical vulnerability of one parameter, such as the surrounding environment, road networks, transportation systems, or urban and emergency infrastructure services. However, it is crucial to integrate various parameters of the complex-built environment into the assessments. In addition, studies that consider more than one parameter are minimal and limited, compared to studies that analyze the seismic physical vulnerability of a specific or individual attribute in complex-built environment systems.

In previous studies, several frameworks used to evaluate the physical seismic vulnerability and resilience of critical infrastructures (CIs), and other subsystem of a community has been the subject of numerous studies. For example, Andrić and Lu [9] analyzed the seismic vulnerability and resiliency of a critical bridge that is situated in the state of California in the United States. The seismic hazard analysis, the bridge fragility analysis, and the seismic resilience evaluation are all components of the fuzzy framework that was utilized for this study. Another seismic vulnerability framework had been presented by C. Huang and S. Huang [10] for the reinforced concrete bridges that were at risk of being damaged by earthquakes. The physical vulnerability model, the restoration model, and the resilience analysis are the three components that are included in the framework. The physical vulnerability model was used to get the probability of damage to the bridge piers for given seismic intensities, while the restoration model was utilized to evaluate the functioning of the aging bridges. Sun et al. [11] used agent-based modelling to assess the seismic susceptibility of France's Luchon Valley road network. In the study, critical road network bridges were chosen to classify the earthquake resistance design for the investigated transportation systems. Shang et al. [12] have presented a quantitative framework that was created based on the Chinese seismic design code in order to evaluate the seismic resilience of the hospital systems in China (GB 20011–2010). The framework took into account the hospital's seven most important subsystems, which are the structural system, the electrical components, the mechanical structure, the water supply and sewage system, the healthcare system, and the evacuation system. The evacuation system of a road network is based on the emergency cars and how much they can be appropriate to be used in the emergency evacuation process during earthquakes. Moreover, Kassem [13] established a uniform seismic vulnerability index (SVI) framework for reinforced concrete building typology. This framework has been validated and investigated through the process of evaluating the seismic behaviour of hospital and school reinforced concrete buildings in Malaysia. During this process, the authors proposed a seismic vulnerability index by using nonlinear parametric analysis (NL-PA) in order to prioritize the damage to the buildings, in which this index was used to classify the severity of the damage to the buildings. These studies are used to determine the main typologies and the expected collapse ratios for the investigated buildings in this research [14, 15].

The approaches that investigate the physical vulnerability of road networks can be divided into two primary classifications. The first one is based on the Intrinsic Seismic Vulnerability Index (ISVI), which effectively addresses the evaluations of the components that are formulating the system itself such as pavement, embankments, and soil beneath roadway. The second one provides an evaluation of external influences that could disrupt the road system network through the Eccentric Seismic Vulnerability Index (ESVI). These factors or influences include the space that surrounds buildings, pylons, telecommunication towers, and others. The majority of the existing research on road networks focuses entirely on either the ISVI or the ESVI as their primary variable of interest.

As an example, Adafer and Bensaibi [16] studied the vulnerability of Algeria's road networks to seismic events using an ISVI model based on empirical data derived from seismic experts around the world and data extracted from previous earthquakes in Algeria, in order to use this method in weighting the road network's assets. The research team concentrated their attention in this study on the evaluation of the potential material damage that earthquakes could inflict upon roadways. On the other hand, several studies focused on the ESVI in order to investigate the influence of the natural setting of the surrounding environment on the susceptibility of roadways. Costa et al. [17] developed a probabilistic approach to evaluate the consequences of earthquakes on road traffic by analyzing the correlation between the physical damage to roadway systems and traffic flow of the urban road network of Messina, Italy. The spatial variance of seismically induced damage to buildings that can cause closure to roads was taken into consideration using a probabilistic approach. By comparing traffic behaviour on the road network in normal conditions and in the event of building debris, this study was able to determine the road network's functionality. Furthermore, Ertugay et al. [18] produced an accessibility model based on the probability of road closures in Thessaloniki, Greece, with maps depicting the impact of earthquake scenarios on the accessibility of specified shelter spots. Moreover, Argyroudis et al. [19] performed a risk assessment for road networks considering the interaction with the built environment in the surrounding area. This study's primary objective was to generate a probabilistic systemic risk analysis to evaluate the connectivity of the road network affected by debris caused by collapsed buildings along the roads.

Numerous studies have utilized the ESVI of road networks in order to evaluate the physical damage, accessibility to vital service centres, or interconnection of road networks (i.e., trip time and distance). These evaluations have been carried out for the purpose of determining whether or not the road networks are linked [20–26]. Nevertheless, several studies have also examined how buildings and roadways interact, with particular attention paid to traffic flow and reliability in an emergency [20, 27, 28]. In contrast, there are a few works that focus on street network punctual conditions and debris interactions, and only a few of them feature historical earthquake scenarios [29, 30].

Indeed, the research is still deemed to be quite restricted when it comes to the concept of an integrated seismic risk assessment approach that correlates the ISVI and ESVI to analyze the road network in a complex-built environment. Yet, the United Nations sustainable development goals (SDGs) such as SDG9 and SDG11 call for resilient, secure, and sustainable communities, and this will be achieved by reducing the risk of critical infrastructure to natural disasters such as earthquakes, and minimizing their consequences for the society and economy reducing deaths and injuries [13, 31, 32].

These studies highlight the need for an integrated seismic vulnerability assessment strategy for complex-built environments that considers the link between internal and extrinsic system properties. Regarding improving resilience and enhancing emergency access for certain urban built environment systems, this integrated approach is regarded as a critical first step. In this article, a comparative study is carried out to study the effect of different hazard scenarios that are considered with the spatial distribution of seismic intensities (VIII and IX) on each of the four main investigated parameters (P1: Embankment Height; P2: pavement strength; P3: soil type; and P4: number of lanes), which aims at improving the understanding of road network risks by addressing the determined probability of damage for the investigated parameters. These comparative results are utilized to weight the main parameters for the ISVI scores. In addition, the Eccentric Seismic Vulnerability Index (ESVI) is computed by first determining the calculated debris width ( $W_d$ ) as a consequence of the collapsed buildings and then determining the accessibility rates by drawing conclusions about the effective width values ( $W_{eff}$ ). Eventually, this aforementioned information is then used to develop an integrated seismic risk assessment for a road system, which considers the correlation between the various developed vulnerability indices and generates integrated heat maps that take into account the correlation between the various vulnerability indices.

This research is considered an original framework for building an analytical investigation approach and combining both Intrinsic and Eccentric Seismic Vulnerability Indices (ISVI and ESVI), in terms of internal and external factors of the roadway system to improve the established methods that have been done in past studies. The proposed approach for the ISVI is based on an analytical investigation that quantifies, for the first time in the literature, the impact caused by a parameter's physical performance on the road behaviour based on different earthquake scenarios and the probability of damage for each parameter of the roadway system that can be integrated uniformly into risk-based strategies. This step helps in prioritizing the parameters from the most to the least essential one, based on the results of the probability of damage for the roads. Moreover, the developed framework is considered significant due to the fact that it is building heat maps to find the correlations between the ISVI and the ESVI, where the past research focuses on assessing solely the internal or external factors, without investigating the effect of the integrated index on the accessibility rates.

## 2. Investigated Roads and the Main Surrounding Buildings

A small area is chosen in the southern-west part of Penang, Malaysia, as a case study. The road network under investigation contains 16 different roads and 29 intersecting nodes as shown in Figure 1. The investigated roads are classified as secondary and urban collector roads. Additionally, all roads are considered one-way roads because in case of earthquakes, the emergency vehicles may not follow the normal traffic regulations. The main parameters used in this study for each street include the width of road that is ranging between 3.8 m and 11 m with two main conditions building facing street from one side or from both sides of the road as shown in Table 1. The zoning of a sample street is shown also in Figure 1, where the street is divided into three main zones based on the buildings facing the road from two sides.

Figure 1 shows the roads surrounded by the classified buildings, where they are classified on the basis of buildings height that is ranging between 6.5 and 34 meters. Moreover, the building depth and volume values are specified for the calculation of the width of debris resulting from the collapsed buildings. The building depth range between 10.13 and 26.91 meters. The height and depth of the buildings are determined based on field investigation, while the ranges of building volume values are calculated based on the determined height, width, and depth of the building by taking into consideration the void volume inside the building. The volume of buildings ranges between 1025.78 m<sup>3</sup> and 5315.56 m<sup>3</sup>. The 37 buildings that are under investigation in this application are categorized into low-rise building (LRB), mid-rise building (MRB), and high-rise building (HRB) based on the determined heights as shown in Figure 1 and Table 2.

## 3. Assessment of Roadway System Resistance Based on the Intrinsic Seismic Vulnerability Index (ISVI) and Eccentric Seismic Vulnerability Index (ESVI) Approaches

To assess the resistance of roadway systems, two different approaches are developed. The first approach is developed based on the Intrinsic Seismic Vulnerability Index (ISVI) that takes into consideration four intrinsic main parameters (P1: embankment height, P2: pavement strength, P3: soil type, and P4: number of lanes) of the roadway system. These parameters are investigated with respect to the calculated probability of damage (POD) for varying ground motions at different damage states. The cumulative distribution function (CDF) assessment approach is used to calculate the POD values for different ground motions that are shown in Table 3 by using Equation (1), which was downloaded from the Consortium of Organizations for Strong-Motion Observation Systems (COSMOS) database and Pacific Earthquake Engineering Research (PEER) database. The POD values are extracted at two different fixed intensities for different  $S_a$  values VIII (0.5 g and 0.8 g) and IX (1.0 g and 1.3 g). After that, a comparative study is performed to compare the main values of POD for different parameters at different damage states (DSs) as shown in Table 4:

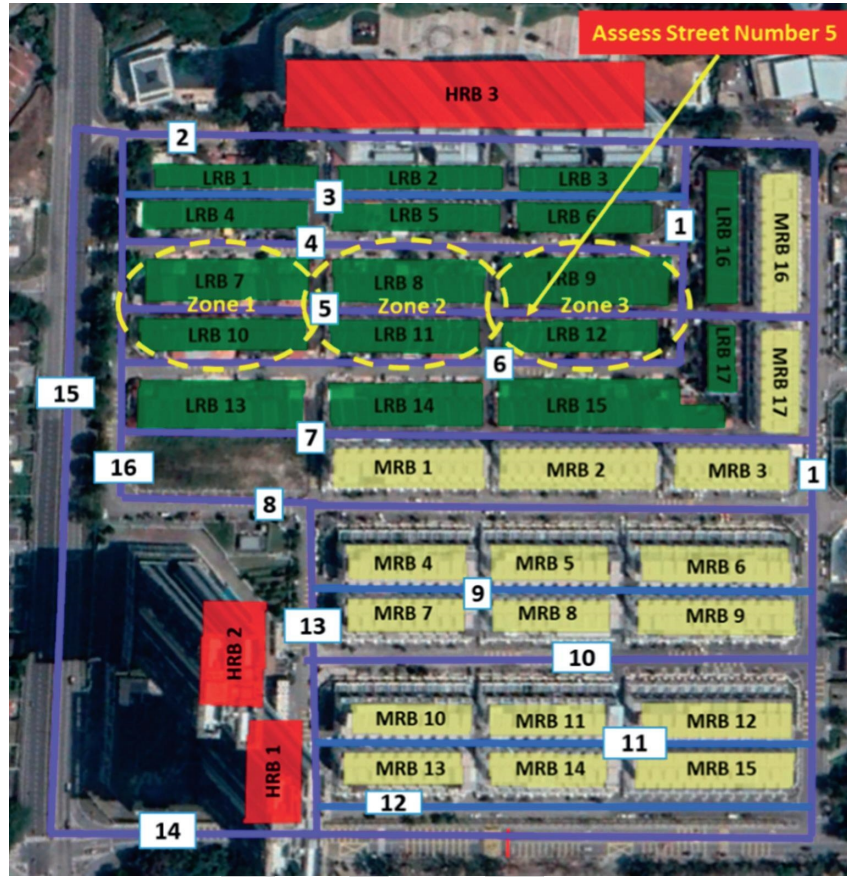


FIGURE 1: Map for categorized buildings and streets under investigation.

TABLE 1: Description of road network main parameters.

Street number	Street width (m)	Number of lanes	Buildings facing one side of road	Buildings facing two sides of road
1	8.80	2	x	—
2	12.31	4	—	x
3	3.28	1	—	x
4	7.00	2	—	x
5	5.00	1	—	x
6	7.81	2	—	x
7	3.15	1	—	x
8	6.30	2	—	x
9	7.64	2	—	x
10	3.76	1	—	x
11	4.38	1	—	x
12	7.5	2	x	—
13	9.04	2	—	x
14	13.00	4	—	—
15	11.79	4	—	—
16	7.50	2	x	—

$$P\left[\frac{\text{Damage} \geq \text{DS}}{\text{Sa}(T1)}\right] = \Phi\left(\frac{\ln[\text{Sa}(T1)] - \mu}{\sigma}\right), \quad (1)$$

where  $\text{Sa}(T1)$  is the spectral acceleration for a specific vibration period,  $\Phi$  is the standard normal distribution,  $\mu$  is the mean value for damage states, and  $\sigma$  is the standard deviation for each damage state [13].

The extracted result from the comparative analysis is used to determine the effectiveness of the investigated parameters where the results will show the prioritized parameters on the basis of their effectiveness on the roadway system during earthquakes. This is followed by weighting the parameters by using the analytical hierarchy process (AHP) method that is developed by Saaty [34] with respect to their

TABLE 2: Parameter values of main buildings.

Building ID	Building height, $H$ (m)	Building depth, $W$ (m)	Building volume, $V$ (m <sup>3</sup> )
LRB 1	7.00	11.13	1232.84
LRB 2	6.50	11.21	1143.35
LRB 3	7.00	10.13	1025.78
LRB 4	7.40	12.05	1403.19
LRB 5	6.50	12.00	1187.68
LRB 6	7.40	12.62	1124.65
LRB 7	8.60	20.38	1572.60
LRB 8	8.60	20.69	1528.57
LRB 9	8.60	21.55	1677.00
LRB 10	7.40	14.38	1338.51
LRB 11	7.40	15.06	1218.04
LRB 12	8.60	15.46	1445.83
LRB 13	10.00	20.79	1873.00
LRB 14	10.00	20.87	1775.40
LRB 15	8.60	21.12	1764.90
LRB 16	10.00	12.76	1564.80
LRB 17	10.00	12.22	845.20
MRB 1	12.90	18.85	2227.83
MRB 2	12.90	18.66	2339.28
MRB 3	12.90	18.58	1813.99
MRB 4	17.20	22.48	2621.97
MRB 5	17.20	22.40	2594.10
MRB 6	12.90	22.44	2303.94
MRB 7	15.00	15.86	2055.31
MRB 8	12.00	14.68	1636.80
MRB 9	12.00	15.68	2000.64
MRB 10	15.00	14.00	2007.00
MRB 11	14.40	13.88	1892.16
MRB 12	14.40	18.47	2552.25
MRB 13	17.20	16.48	2400.09
MRB 14	15.00	15.92	2039.40
MRB 15	17.20	16.19	3026.17
MRB 16	17.20	18.35	2772.65
MRB 17	17.20	18.88	2210.54
HRB 1	34.00	25.38	4806.92
HRB 2	34.00	26.91	5315.56
HRB 3	34.00	18.64	50254.72

TABLE 3: Selected sets of ground motion records.

No.	Earthquake	Year	Station	PGA (g)	Epical distance (km)	Magnitude (Mw)
1	Izmit-Kocaeli, Turkey	1999	Nuclear Research Center	0.181	101	7.4
2	Landers USA	1992	San Bernardino, CA	0.332	80	7.3
3	Superstition Hills, USA	1987	Calipatria, CA	0.252	27	6.5
4	Chi-Chi, Taiwan	1999	Taichung	0.527	39	7.6
5	Loma-Prieta, USA	1989	Emeryville, CA	0.490	68	7.0
6	Northridge, USA	1994	Santa Monica, CA	0.684	28	6.7
7	Ranau, Sabah, Malaysia	2015	KKM_HNE	0.125	65	6.1

TABLE 4: Damage States of Roadway and its Assets (Argyroudis and Kaynia [33]).

Serviceability	Damage states (DS)	Direct damages	Indirect damages
Fully or partially closed due to temporary maintenance and traffic for few weeks or few months.	Extensive	Major settlement or offset of the ground (>60 cm)	Considerable debris of collapsed structures
Fully closed due to temporary maintenance for few days. Partially closed to traffic due to permanent maintenance for few weeks.	Moderate	Moderate settlement or offset of the ground (30 to 60 cm)	Moderate amount of debris of collapsed structures
Open to traffic. Reduced speed during maintenance.	Minor	Slight settlement (<30 cm) or offset of the ground	Minor amount of debris of collapsed structures
Fully open.	None	—	No damage/Clean road

effectiveness rates as described in detail in Section 3.2. Subsequently, the ISVI scores are calculated from the extracted weights and the presented parameters for each road.

The ESVI is the second approach considered in this research to study the effect of extended debris from the collapsed surrounding buildings on the disruption of accessibility rates for the road network. The debris width  $W_d$  values are calculated using (2) and (3) based on two types of collapses that are represented in Figures 2(a) and 2(b) that is adopted from Argyroudis et al. [19]. The developed methods based on the integration between the ISVI and ESVI scores are considered more reliable when compared to previous studies that tackled the vulnerability assessment of road networks. This is due to the fact that the developed methods in this research are built on the basis of analytical investigations. On the other hand, empirical approaches have the limitation of information availability, while an empirical study requires large input data that might be impossible to collect in many developing countries [16]. Nevertheless, the main disadvantage that is related to the analytical approach is the high computational effort that is needed compared to empirical methods. Subsequently, due to the numerous variables, establishing an accurate integrated seismic risk assessment is a challenging approach. However, a model that incorporates intrinsic and eccentric parameters is necessary for a more accurate risk assessment of road networks:

$$W_d = \sqrt{\frac{2K_v \times W \times L}{\tan c}} - L, \quad (2)$$

$$W_d = \sqrt{W^2 + \frac{2K_v \times W \times H}{\tan c}} - W, \quad (3)$$

where  $W$  is the building width,  $K_v$  is the collapse ratio of the building,  $L$  is the building length,  $Y$  is the building height, and  $c$  is the collapse angle based on Argyroudis et al. [19].

Effective width  $W_{\text{eff}}$  that represents the accessible areas that are not obstructed by the debris of the collapsed buildings is calculated based on the resultant  $W_d$  values for the two types of collapses. The following equation is used to calculate the values of  $W_{\text{eff}}$ :

$$W_{\text{eff}} = W_r - W_d, \quad (4)$$

where  $W_{\text{eff}}$  represents the effective width of the road that vehicles can pass through,  $W_r$  is the width of road, and  $W_d$  is the width of debris resulting from building destruction.

Subsequently, the ESVI scores are calculated for two types of emergency vehicles: normal emergency vehicles (NEVs) and emergency service vehicles (ESVs) at a different intensity of (VIII) and for the intensity of (IX) with respect to the  $W_{\text{eff}}$  values as shown in using Equation (5). The NEV and ESV have a different manoeuvring limit, where the NEV is considered wider (3.5 m) when compared to the ESV (2.5 m):

$$\text{ESVI} = 100 - \frac{W_r - (W_{\text{eff}(L)} + W_{\text{eff}(R)})}{W_r}, \quad (5)$$

where  $W_r$  represents the road width,  $W_{\text{eff}(L)}$  effective width for the left side, and  $W_{\text{eff}(R)}$  effective width for the right side.

**3.1. Analysis of the Effect for Spatially Variable Ground Motions at Different Damage States.** For conducting the analysis of the effect of the spatially variable ground motions on the damage of road networks and their assets, different earthquake intensities and different average spectral acceleration ( $S_a$ ) are considered. For the intensity of VIII, the  $S_a$  is fixed at 0.5 g and 0.8 g. Meanwhile, for the intensity of IX, the  $S_a$  values are fixed at 1.0 g, and 1.3 g, respectively. The main specified intensities are selected based on their criticality and due to the fact that the values of these intensities are showing the variation gaps when compared to smaller intensity ranges and are reflecting the main aim of the seismic vulnerability analysis. After assessing the main investigated parameters for roadway and their assets at each specified earthquake intensity, the results of the probability of damage are extracted and distributed at each damage state. The variation in the probability of damage at each damage state for the assessed performance of each parameter at different seismic intensities is shown in Figures 2–5.

**3.1.1. (P1): Embankment Height.** The extracted results from the vulnerability assessment of embankment on the basis of the height difference show a high variation in the probability of damage at different damage states. It could be found that as the seismic intensity is increasing from 0.5 g to 1.3 g, the probability of damage is increasing gradually at all damage states as shown in Figure 3. For instance, the probability of damage values of embankments for all various heights at 0.5 g (VIII) and 0.8 g (VIII) that are demonstrated in Figures 3(a) and 3(b), the procedure of using an identical ground motion at the same earthquake intensities is overrating the occurrence of the probability of damage at minor state, and this is resulting in underestimating the occurrence of damage at moderate and extensive states. On the other hand, the probability of damage for the various embankment heights at 1.0 g (IX) and 1.3 g (IX) is given in Figures 3(c) and 3(d). The results are showing the same trend but for different damage states, where it is overrating the occurrence of the probability of damage at minor and moderate states, and this is resulting in underestimating the occurrence of damage at the extensive state. All that reveals that lower intensities give high ratings to the minor states compared with the moderate state, while higher intensities provide more ratings for minor and moderate states with less consideration for extensive damage. Mainly, Figures 3(a)–3(d) are reflecting the main results of the probability of damages through using cumulative distribution function (CDF) by showing that embankments with greater heights tend to have a high probability of damage in comparison with embankments with lower heights. Moreover, the results are showing high fluctuation rates between different classes that indicates the high effectiveness of this parameter on the roadway system.

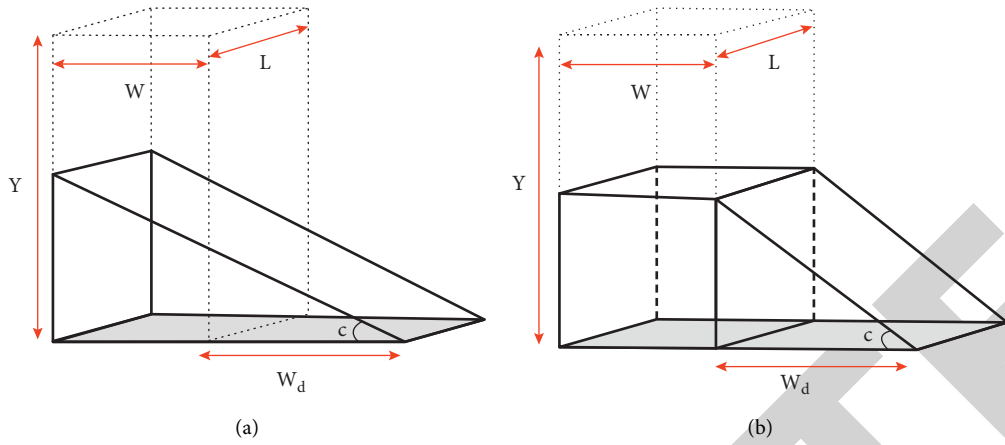


FIGURE 2: (a) Building collapse type 1. (b) Building collapse type 2 based on Argyroudis et al. [19].

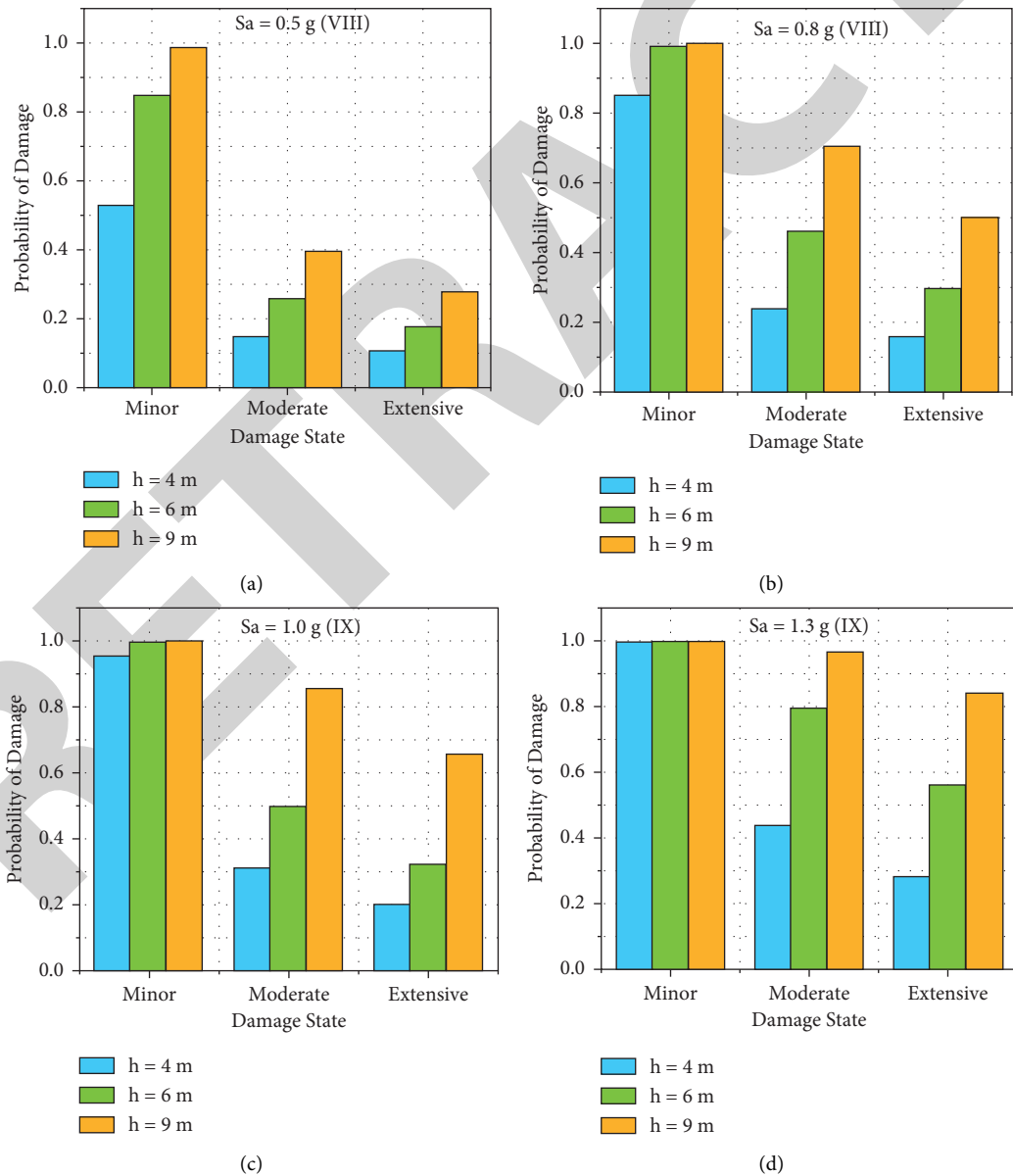


FIGURE 3: Damage probability for embankment with different heights (P1) for various damage states and seismic intensities.



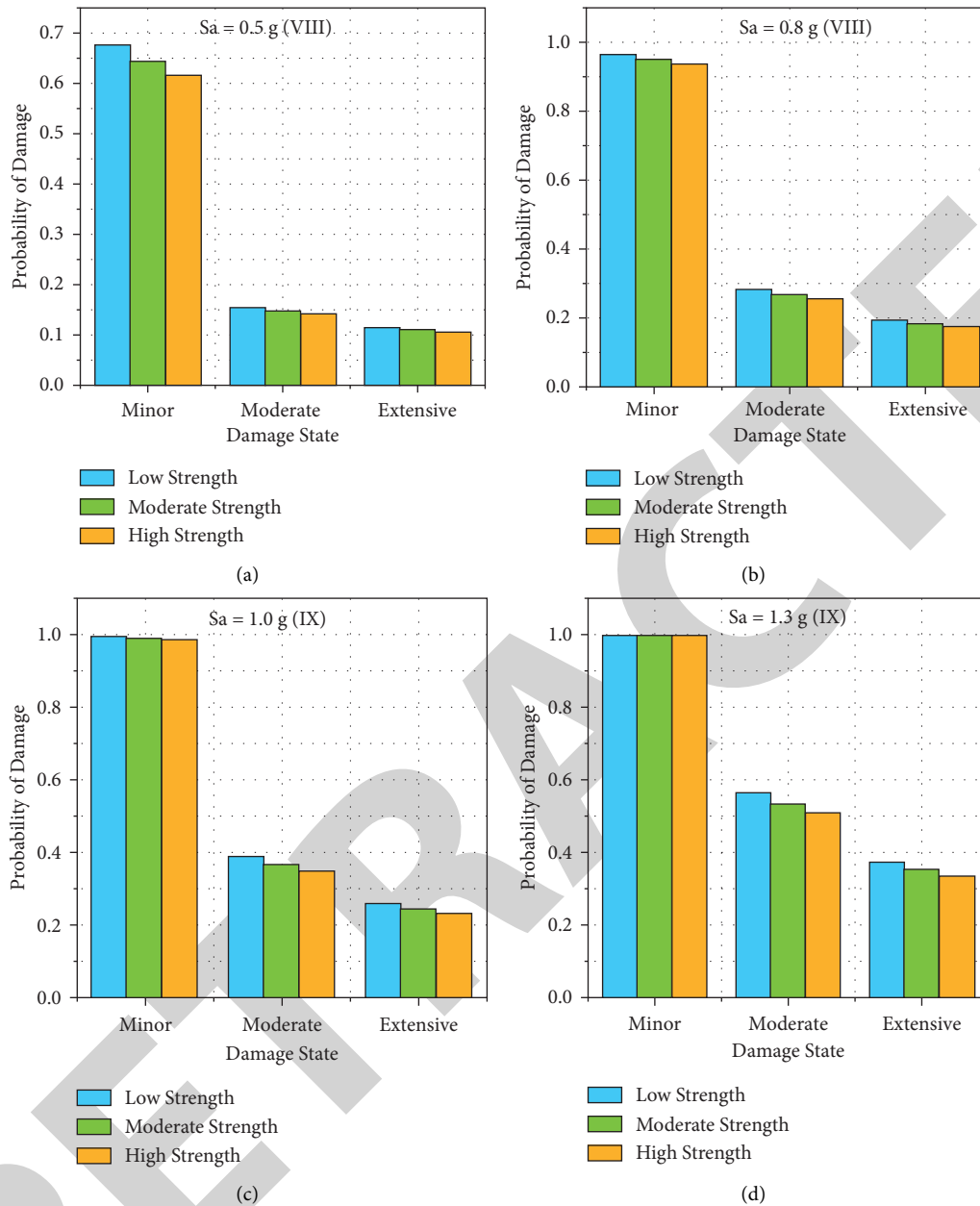


FIGURE 4: Damage probability for roads with different pavement strength (P2) for various damage states and seismic intensities.

3.1.2. (P2): *Pavement Strength*. The vulnerability assessment results for the roadway assets based on the pavement strength shows a high difference of the probability of damage values at different damage states, especially when considering the minor state compared with the other two damage states. Although a similar case is shown between the minor and moderate states as demonstrated in the vulnerability assessment for the height of embankments, it is clear that the results vary slightly between moderate and extensive damage states at all seismic intensities, as shown in Figures 4(a) and 4(b). A high variation in the probability of damage is clearly represented with a difference higher than 0.6 (60%) when comparing the results between minor and moderate states at all intensities, where it can be seen slightly higher at 1.0 g (IX) and 1.3 g (IX) as shown in

Figures 4(c) and 4(d). On the contrary, the variation in the probability of damage between the moderate and extensive states is considered low with a difference less than 0.2.

This is due to the fact that the pavement strength is influencing the roadway vulnerability slightly, since this comparison is clearly indicating that the pavement strength effect is considered critical at minor damage state. However, this effect is considered low for moderate and extensive damage states, where, only at high seismic intensities, the probability of damage can be considered more effective for moderate and extensive states as shown in Figure 4(d). Hence, roadways with lower pavement strength are showing higher vulnerability rates in comparison with roadways with higher pavement strength.

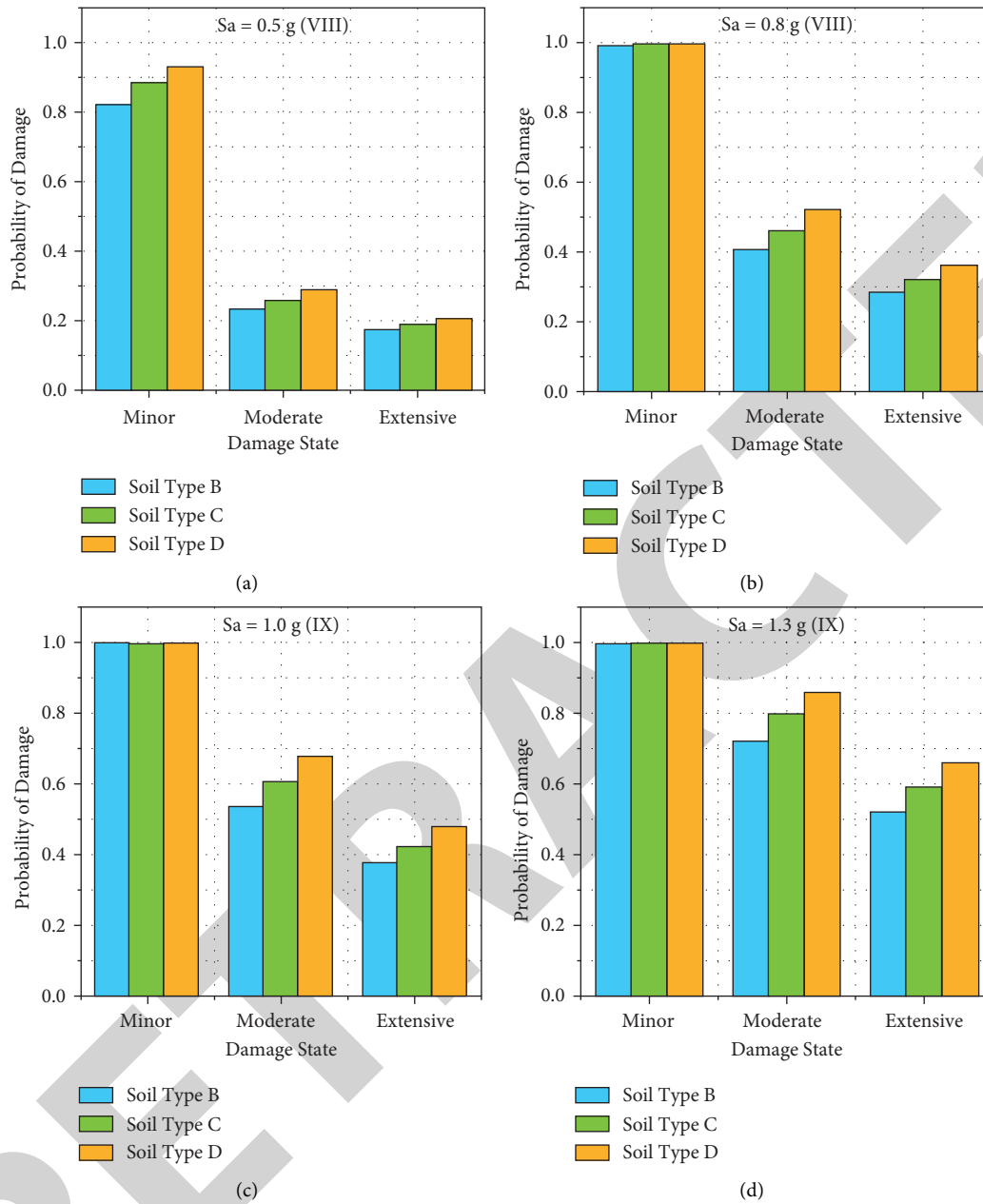


FIGURE 5: Damage probability for roads with different soil type (P3) for various damage states and seismic intensities.

3.1.3. (P3): Soil Type. The results of the vulnerability assessment of roadway and its assets based on the soil type beneath the roadway system for different seismic intensities at different damage states are showing a high variation with a difference value ranging between 0.5(50%) and 0.7(70%), when comparing the probability of damage at the minor state with moderate and extensive states at intensities of 0.5 g (VIII) and 0.8 g (VIII) as shown in Figures 5(a) and 5(b). Nevertheless, the results are also illustrating a small variation between the probabilities of damages, with a difference value ranging between 0.3 (30%) and 0.4 (40%) as shown in Figures 5(c) and 5(d).

These results clearly show that the soil type is more significant at minor damage states, but it can also moderately

affect moderate and extensive damage state occurrences. The probability of damage value distribution at different damage states is fluctuating gradually between different classes (soil types B, C, and D). This indicates that the soil type is considered a moderately effective parameter for the vulnerability of roadway systems.

3.1.4. (P4): Number of Lanes. The assessment of roadway and its assets based on the variation in the number of lanes is showing a great difference in the extracted results, where the difference can be seen clearly high with values ranging between 0.5(50%) and 0.7(70%), when comparing the results at the minor state with the moderate and extensive states

especially at 0.5 g (VIII), 0.8 g (VIII), and 1.0 g (IX) intensities as shown in Figures 6(a)–6(c). However, Figure 6(d) at 1.3 g (IX) is illustrating a sharp increase in the probability of damage at moderate and extensive states in comparison with the results of lower intensities that are shown in Figures 6(a)–6(c). This is due to the fact that the number of lanes can have a higher effect on the roadway system at higher seismic intensities when compared to lower intensities. In addition, the results have shown a small variation when assessing different roadway systems with various number of lanes classes (<2 lanes, = 2 lanes, >2 lanes) at different seismic intensities as represented in Figures 6(a)–6(d).

Subsequently, the road width parameter is being more effective when high seismic intensities are considered, while the variation of classes are gradually affecting the probability of damage for roadway system. All these results indicate that the number of lanes is considered with low effectiveness when compared with the soil type and height of embankment parameters, but still considered slightly more effective when compared to the pavement strength parameter.

**3.2. Calculation of the Intrinsic Seismic Vulnerability Index (ISVI) Scores.** The Intrinsic Seismic Vulnerability Index (ISVI) scores will be calculated based on the weighting of parameters that is concluded from the comparative analysis for the most influential parameters as described in Section 3.1. After the parameters are prioritized from the most influential one to the least, the weight of each parameter is determined based on the analytical hierarchy process (AHP) method [34] and the scoring pattern done in previous studies [16]. The weights are calculated using a specific matrix model by raising this matrix model to large powers and summing each row and dividing each by the total sum of all the rows. The main calculated weights are 0.50, 0.21, 0.18, and 0.11, and 0.65, 0.21, 0.1, and 0.04 for embankment height, number of lanes, soil type, and pavement strength at the intensity of VIII and IX, respectively. On the other hand, the scores for each parameter are categorized based on their importance as described in previous studies and the number of parameters and their categories that are investigated in this research [16].

Subsequently, the ISVI scores are calculated on the basis of the calculated weights  $WP_{a_i}$  and scores  $S_i$  for two different seismic intensities and classified as minor damage (0.0–0.4), moderate damage (0.4–0.7), and extensive damage (0.7–1.0) by using Equation (6) and are represented in Figures 7(a) and 7(b)

$$ISVI_j = \sum_{i=1}^n S_i \times WP_{a_i}, \quad (6)$$

where  $ISVI_j$  represents the Intrinsic Seismic Vulnerability Index of the  $j$ -th alternative for the road;  $S_i$  represents the main scores for each parameter;  $WP_{a_i}$  is the  $i$ -th of the four weighted parameter; and  $n$  is the number of parameters.

Figures 7(a) and 7(b) are clearly showing that the ISVI scores are considered higher at seismic intensity IX when compared to seismic intensity VIII as shown in case of most of the investigated streets; however, when looking at street numbers 3, 6, 9, and 15, the results are decreasing at higher seismic intensity, and this is due to the high weighting rate for the embankment height; thus, when the score of this parameter is decreasing sharply, the ISVI score is decreasing at higher seismic intensities. This variation in the weighting factors is giving the height embankment high effectiveness at seismic intensity IX where the other parameters are negligibly changing the ISVI score especially when considering soil type and pavement strength.

#### 4. Calculated Eccentric Seismic Vulnerability Index (ESVI) Scores for Road Networks Based on the Possibility of Blockage

The values of the Eccentric Seismic Vulnerability Index (ESVI) scores are calculated using (5), where the percentage of blockage is determined. Various scores are obtained based on the effect of debris width that resulted from the collapse of surrounding buildings. All the ESVI scores of the 16 investigated roads are calculated for collapse types 1 and 2, where they are introduced in Figures 8(a) and 8(b).

The ESVI values for the main three investigated zones of roads that are presented in Figures 9–11 are reflecting the results concluded based on ESVI scores, where, based on these ESVI scores, the accessibility rates are considered higher when assessing collapse type 1 in comparison with collapse type 2 at both seismic intensities. Nevertheless, when comparing the ESVI values for collapse types 1 and 2, the higher values are presented in the higher seismic intensity scenario (IX) when it is compared with the (VIII) seismic intensity.

**4.1. Representative Figures for the Blocked Zones of Investigated Roads.** Representative figures are conducted based on the main values of the extended debris that are extracted from the ESVI values for both types of collapses at different seismic intensities (VIII and IX). Figures 9–11 represent the three chosen samples for the investigated roads from all the 16 investigated roads.

The figures are illustrating the main zones that are considered accessible during earthquakes for emergency vehicles. For instance, in Figure 9, it is clear that zones 2 and 3 for street number 1 will be fully accessible for emergency vehicles, since there is no extended debris from surrounding buildings in these zones. However, when studying the impact of surrounding buildings on zone 1, it is showing an extended debris from buildings MRB-16 and MRB-17 from the left side only. Hence, the results are showing accessible areas for normal emergency vehicles (NEVs) and emergency service vehicles (ESVs) with accessibility distance values of 4.93 m and 3.96 m for collapse types 1 and 2 at the seismic intensity of VIII. On the other hand, when investigating the same zone at higher seismic intensity IX for collapse types 1 and 2, the road is not accessible for both types of emergency vehicles with values less than 2.5 m.

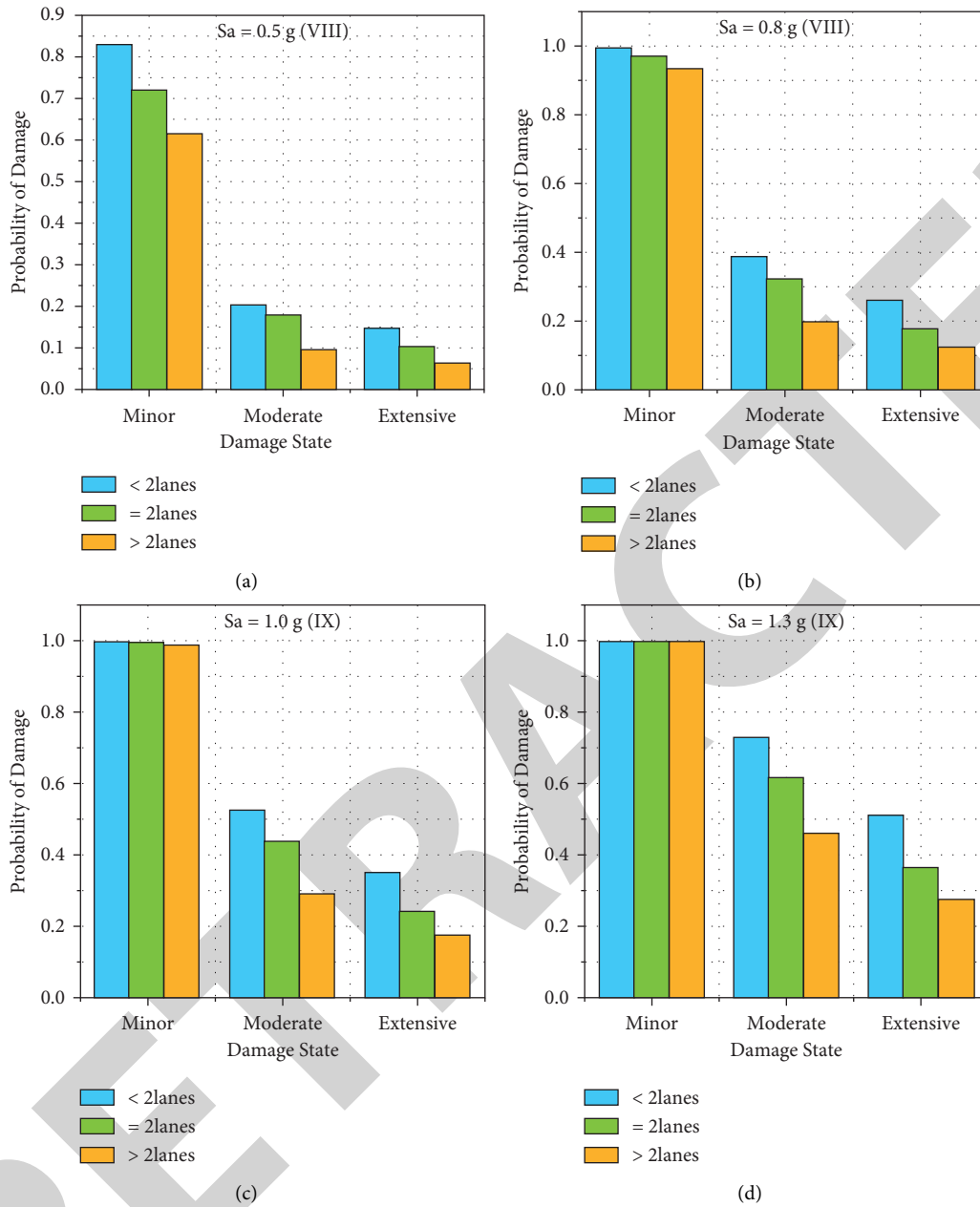


FIGURE 6: Damage probability for roads with different number of lanes (P4) for various damage states and seismic intensities.

Moreover, in Figure 10, another case for extended debris can be noted, where the debris is represented at both sides of the road for all three zones for street number 4, where in case of collapse type 1 at seismic intensity VIII, the accessible areas are considered efficient for manoeuvring of NEV and ESV at the three zones with accessibility distances ranging between 4.46 m and 4.61 m. On the contrary, collapse type 1 at the seismic intensity of IX and collapse type 2 at the seismic intensity of VIII are showing a smaller accessibility distance at the three investigated zone values ranging between 2.78 m and 3.02 m that considered efficient for manoeuvring of ESV only. Subsequently, for collapse type 2 at the seismic intensity of IX, the accessibility distance becomes very small with entire zones

blocked for both types of emergency vehicles. This case is repeated, but with fully collapsed zones as shown in Figure 11.

4.2. Percentage of Variation between Eccentric Seismic Vulnerability Index (ESVI) Values for Collapse Type 1 at Different Seismic Intensities. The percentage of variation is conducted by comparing the Eccentric Seismic Vulnerability Index (ESVI) values for collapse type 1 at two different seismic intensity scenarios (VIII) and (IX), these percentage of variation values are represented in Figure 12 for all the investigated streets. The values are showing a fluctuation between the percentages of variation when comparing the

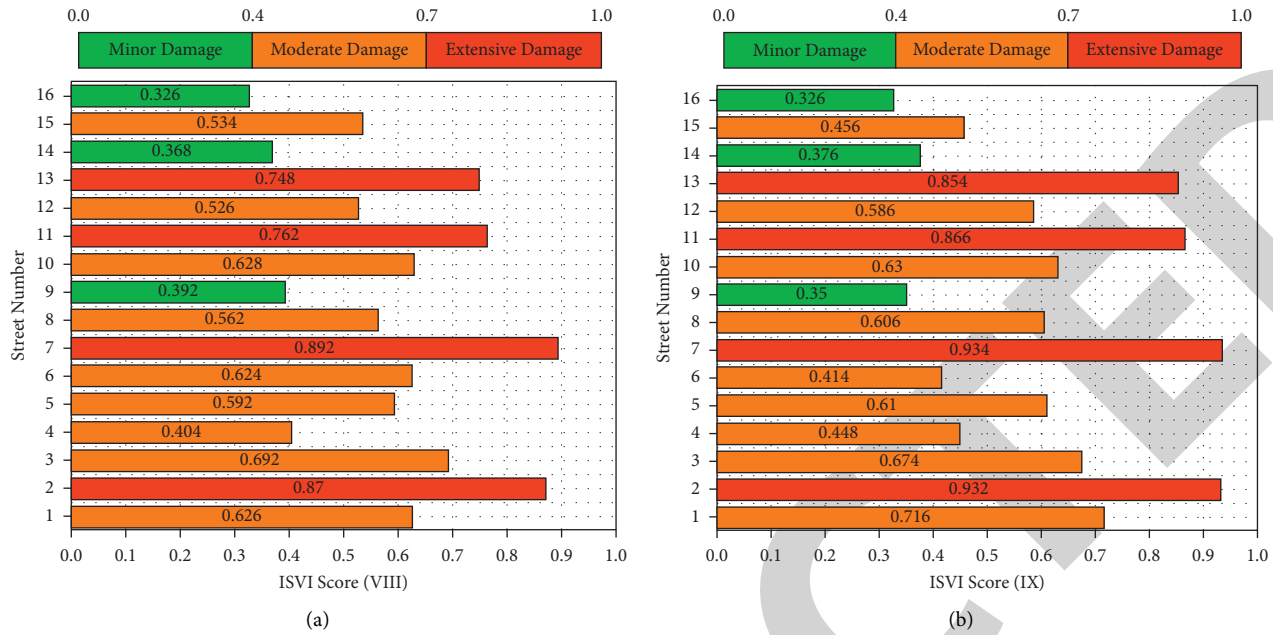


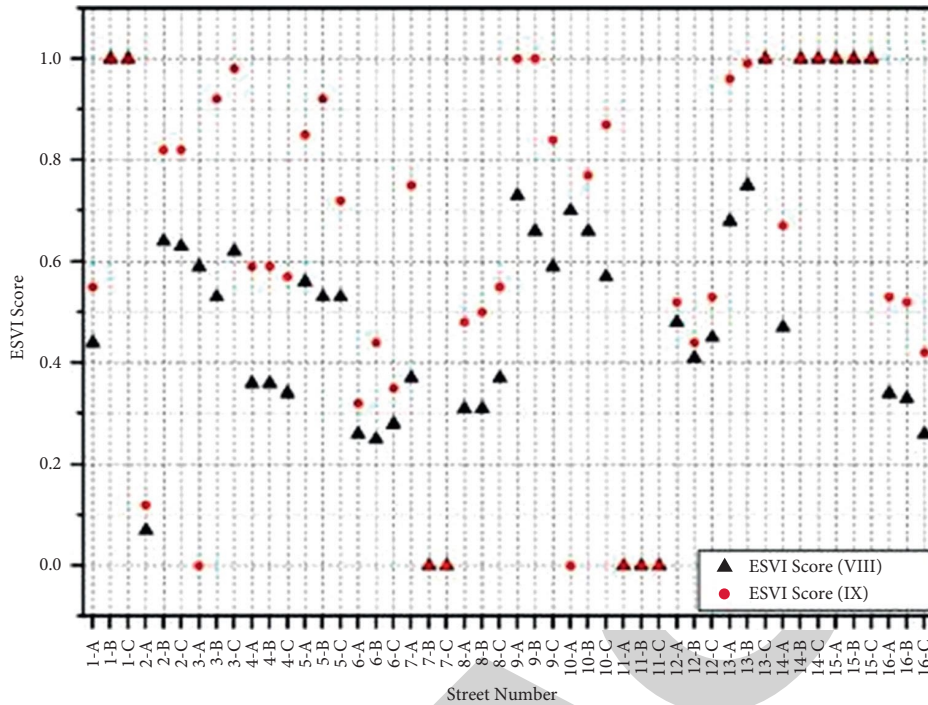
FIGURE 7: (a) ISVI scores for the investigated streets at seismic intensity (VIII). (b) ISVI scores for the investigated streets at seismic intensity (IX).

investigated roads and their zones, but it is clearly illustrating higher variations for street number 3, 4, and 16 at all three different zones with values ranging between 56% and 73%, this is due to the fact that the buildings surrounding these roads are with high collapse rates, by which they are varying highly between the changing seismic intensity scenarios. On the contrary, some of the values for investigated roads are giving low percentage of variation that in some cases, the values are giving 0%, because the surrounding buildings are not damaged or the ESVI values of these roads are still the same for both seismic intensities.

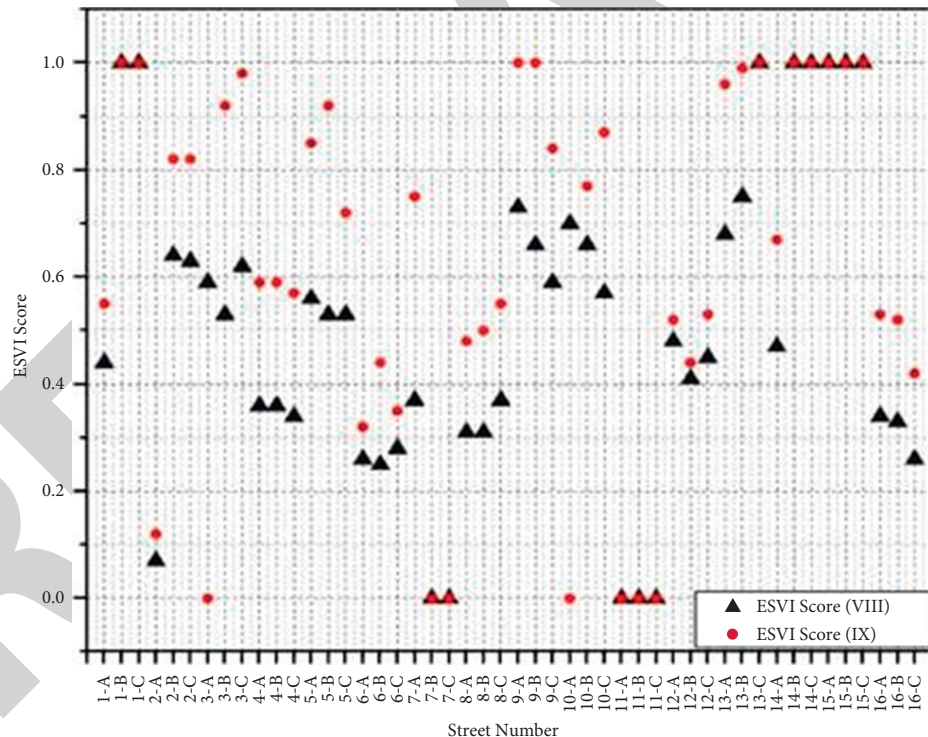
**4.3. Percentage of Variation between Eccentric Seismic Vulnerability Index (ESVI) Values for Collapse Type 2 at Different Seismic Intensities.** Figure 13 shows the percentage of variation between the Eccentric Seismic Vulnerability Index (ESVI) values for collapse type 2 based on two seismic intensity measures (VIII and IX). When comparing the results of Figure 12 with Figure 13, it is clear that the variations are considered smaller for collapse type 2, where different cases are giving 0% variation as shown in street numbers 7, 9, 11, 14, and 15. Although it is considered a critical collapse type, the ESVI values are considered small, since collapse type 2 is reaching high upper limit levels at both seismic intensities. Nevertheless, the results are showing some cases with high variation percentage values that are equal to 80% and 56% as presented in street number 6 at the second zone and 13 at the first zone, respectively. Mainly, the variation in percentages is showing a moderate fluctuation with higher values by changing the seismic intensity scenarios when compared to the assessment approach that is considering the variation of collapse types as shown in Figures 14 and 15.

**4.4. Percentage of Variation between Eccentric Seismic Vulnerability Index (ESVI) Values of Seismic Intensity (VIII) for Different Collapse Types.** The percentage of variation is calculated by comparing the Eccentric Seismic Vulnerability Index (ESVI) values of a specific seismic intensity (VIII) for the two collapse type scenarios. Figure 14 is showing a small fluctuation of these values when compared to the assessment procedure of the types of collapse at the same seismic intensity. For instance, street numbers 4, 6, and 8 are giving a constant value that is equal to 40% and most of the values are ranging between 23% and 48%. However, the values of variation are considered low when compared to Figures 12 and 13 that focus on assessing the variation percentage for different seismic intensity scenarios. All these described values are reflecting the main results that show a higher effectiveness when changing the seismic intensities in the calculation of the  $W_{eff}$  values.

**4.5. Percentage of Variation between Eccentric Seismic Vulnerability Index (ESVI) Values of Seismic Intensity (IX) for Different Collapse Types.** The percentage of variation values at the specific seismic intensity (IX) based on the difference between collapses type are illustrating the same trend as in Section 4.3, where Figure 15 is illustrating a small fluctuation for these values. For example, street numbers 4, 6, and 8 are giving constant values that are equal to 40% at the three different zones. Moreover, the variation percentages are considered small when compared to the results of Figures 12 and 13, but the values are considered slightly lower than the values that are extracted from Figure 14. This is due to the fact that the variation values at higher seismic intensities are reaching high upper limit levels for both types of collapse.



(a)



(b)

FIGURE 8: (a) ESVI scores for collapse type 1 at two different seismic intensity scenarios (IX) and (VIII). (b) ESVI scores for collapse type 2 at two different seismic intensity scenarios (IX) and (VIII): A for zone 1, B for zone 2, and C for zone 3.

4.6. *Integrated Accessibility Heat Map between Seismic Vulnerability Indices and Resistance Design of the Road.* The generated damage maps based on the Intrinsic Seismic Vulnerability Index (ISVI), Eccentric Seismic Vulnerability Index (ESVI), and the integrated seismic vulnerability index

maps have shown that it is considered important to reflect the correlation between the intrinsic and eccentric factors, because the generated integrated damage maps are showing less accessibility with high closure probability compared to the singly assessed ESVI and ISVI damage maps. This

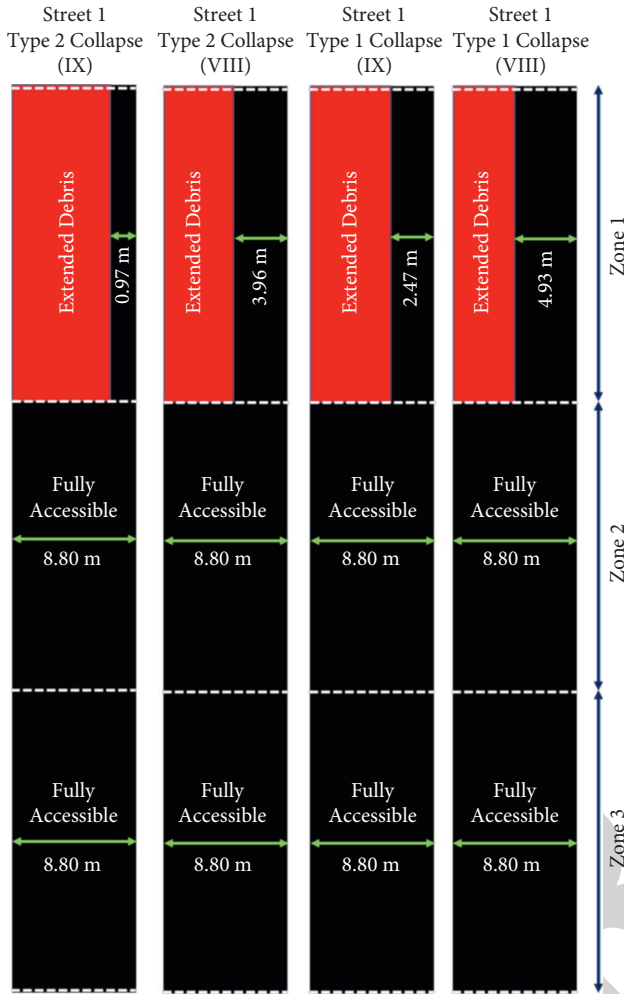


FIGURE 9: Representative figure for the obstructed zones of street number 1.

correlation can be achieved by developing the integrated accessibility heat maps that are developed in the following sections.

4.6.1. *Integrated Accessibility Heat Map Based on the Correlation between Intrinsic Seismic Vulnerability Index (ISVI) and Resistance Design of the Road.* The integrated accessibility heat map for Intrinsic Seismic Vulnerability Index (ISVI) is studied based on the correlation with the resistance design of the road, where all the four investigated parameters (embankment heights (P1), pavement strength (P2), the soil type (P3), and number of lanes (P4)) that are studied in Sections 3.1 and 3.2 are taken into consideration, by which the results indicate that the most effective parameter is considered the embankment heights (P1), followed by the number of lanes (P4), while the pavement strength (P2) and soil type (P3) are considered with lower effectiveness rates with a slightly better performance for the soil type.

Figure 16 is illustrating this correlation, by which the results are showing that the Accessibility Index (AI) is gradually decreasing as the ISVI is increasing. However, when analyzing the integrated accessibility heat map, the correlation



FIGURE 10: Representative figure for the obstructed zones of street number 4.

between both the ISVI and resistance design should be considered. For instance, when investigating the low resistance case, it can be seen that the roads are considered fully accessible when the ISVI is ranging from 0 to 0.1, while when the road system is considered with high resistance design, the road is fully accessible for ISVI ranges between 0 and 0.3. Moreover, the road is considered closed in case of low resistance design when the ISVI is ranging between 0.7 and 1.0. On the other hand, the road is considered closed at higher values of the ISVI for moderate and high resistance design, which are 0.8 and 0.9, respectively. The relation between ISVI and AI is considered inversely proportional, since as the ISVI is increasing, the AI is decreasing. However, this relation is being affected differently based on the situation of the resistance design, where at higher resistance design, the AI is being affected slightly when compared to low and moderate resistance design scenarios.

4.6.2. *Integrated Accessibility Heat Map Based on the Correlation between Eccentric Seismic Vulnerability Index (ESVI) and Road Width.* Figure 17 illustrates the integrated accessibility heat map through studying the relation between the Eccentric Seismic Vulnerability Index (ESVI) values and



FIGURE 11: Representative figure for the obstructed zones of street number 10.

number of lanes for the road. This heat map is conducted in case of normal emergency vehicles (NEVs) that are considered with a low manoeuvring limit (2.5 m) than the fast response emergency small vehicles (ESVs) (3.5 m), which is considered in the following section.

The results are showing a high variation between roads with less than two lanes and roads that are with two lanes and above, where the roads with a smaller number of lanes are showing less accessibility. For example, when assessing roads with less than two lanes, the road is considered closed for ESVI values that are ranging between 0.1 and 1.0. However, the roads with two lanes and above are showing higher accessibility, by which the road is considered closed at ESVI values ranging between 0.6 and 1.0 and 0.9 and 1.0 for roads with two lanes and above, respectively. Furthermore, the AI values are considered similar for roads with two lanes and above for ESVI ranges between 0.0 and 0.6, but a slight difference is shown for ESVI values that are ranging between 0.6 and 1.0. It is clear that the wider the road is, the smaller the effect the ESVI is having on the accessibility rates.

On the other hand, when creating the integrated accessibility heat map by studying the relation between ESVI and the number of lanes for ESV, the manoeuvring limit is increased to 3.5 m. Hence, the results and the accessibility rates

are varying compared with the heat maps that are created for NEV scenarios as shown in Figure 18. For instance, the roads with less than two lanes are considered closed at the ESVI value equal to 0.3 as shown in ESV heat maps, while for the NEV heat maps, the roads are being closed at a lower ESVI value equal to 0.1. This variation is only represented for road with less than two lanes, but for road with two lanes and above, the AI values are considered the same when comparing the heat maps of NEV and ESV scenarios. Moreover, the same trend is repeated as they created heat maps for NEV, where the results again show that the roads with a smaller number of lanes have lower accessibility rates than those with a higher number of lanes.

4.6.3. Accessibility Heat Maps Based on the Correlation between Integrated Road Characteristics and Integrated SEISMIC Vulnerability Index (SVI). The accessibility heat map is generated by investigating the relation between integrated road characteristics and the integrated seismic vulnerability index that is extracted from the correlation between the ESVI and the ISVI as shown in Figure 19. These are developed for the normal emergency vehicles (NEVs) manoeuvring scenario by studying the integration between the different road characteristics, where the road resistance and the manoeuvring limit is considered during the development of this heat map. The results shown in Figure 19 when compared to Figure 17 are illustrating some variations in the case of a road with two lanes or more, especially when comparing the ESVI and integrated vulnerability index that are ranging between 0.2 and 0.6. This variation is mainly resulting from the followed assessment procedure by which it takes into consideration the integration between the ESVI and ISVI, as well as the integration between different road characteristics.

Figure 20 describes the developed accessibility heat maps by finding the relation between integrated road characteristics and Integrated Seismic Vulnerability Index in the case of the ESV manoeuvring limit scenario. The results are showing a gradual decrease in AI values, where it is giving higher accessibility rates for wider roads with two lanes or more when compared to roads with less than two lanes. However, the results are gradually decreasing and not sharply decreasing as shown in Figure 19. For example, the roadway system with a low resilient design and with less than two lanes is showing a gradual variation for AI with respect to the integrated seismic vulnerability index values, which are ranging between 0.0 and 0.3. Moreover, the roads are closing at higher values when compared to the NEV scenario. Subsequently, the created heat maps that take into consideration the integration between the ESVI and ISVI from one side and the integrated road characteristics from the other side are considered the most efficient maps in the assessment procedure for road networks. This is due to the fact that the integrated maps are focus on all the factors that could affect road network vulnerability and accessibility.

The main findings of this research are achieved by developing an integrated model for road network, by which this research is divided into two parts: the seismic



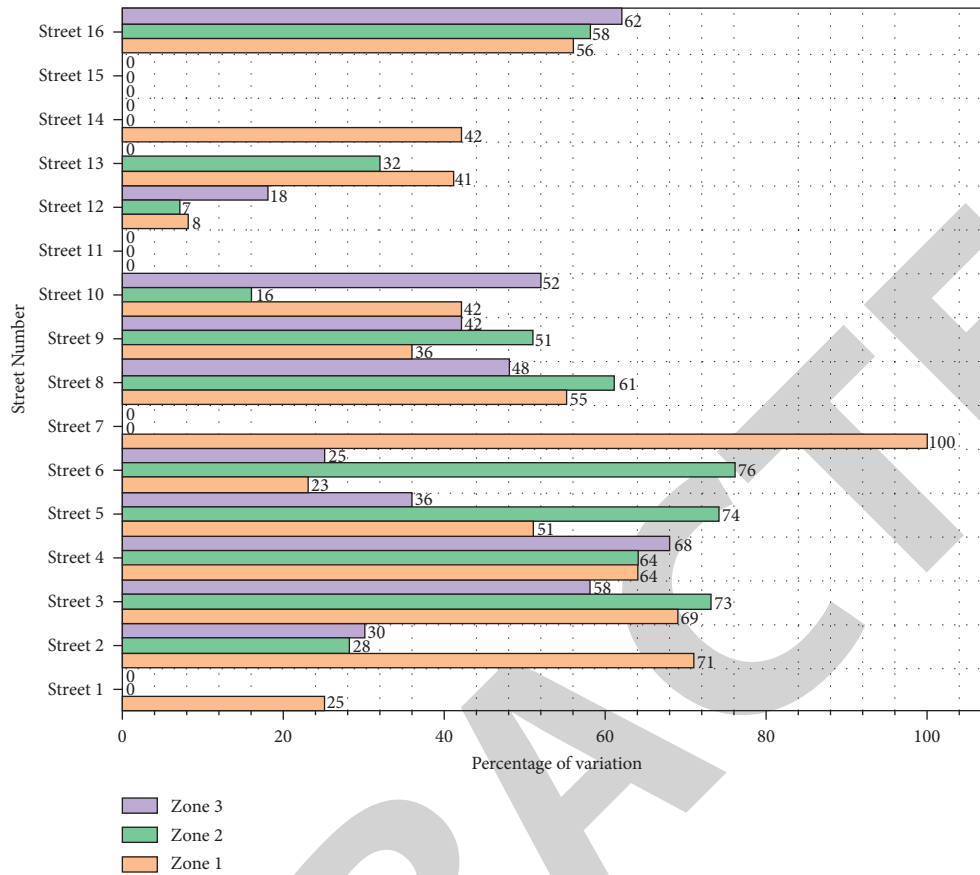


FIGURE 12: Percentage of variation between ESVI values for collapse type 1 at different seismic intensities.

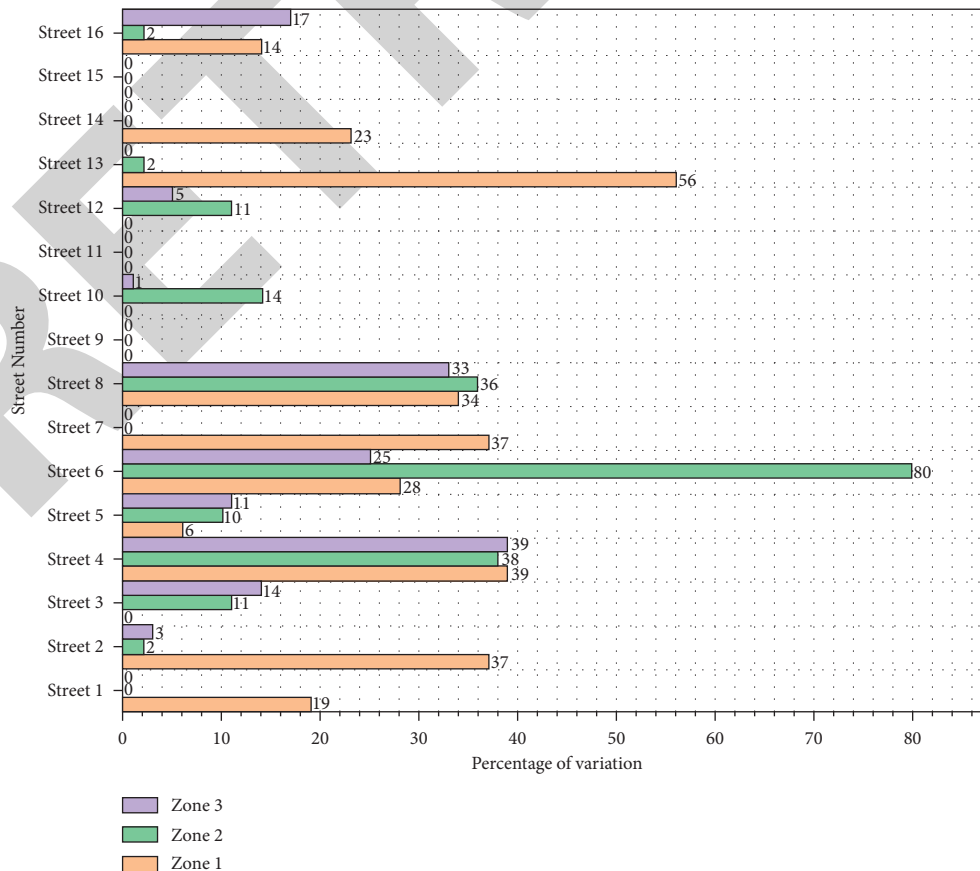


FIGURE 13: Percentage of variation between effective width ESVI values for collapse type 2 for investigated roads at different seismic intensities.

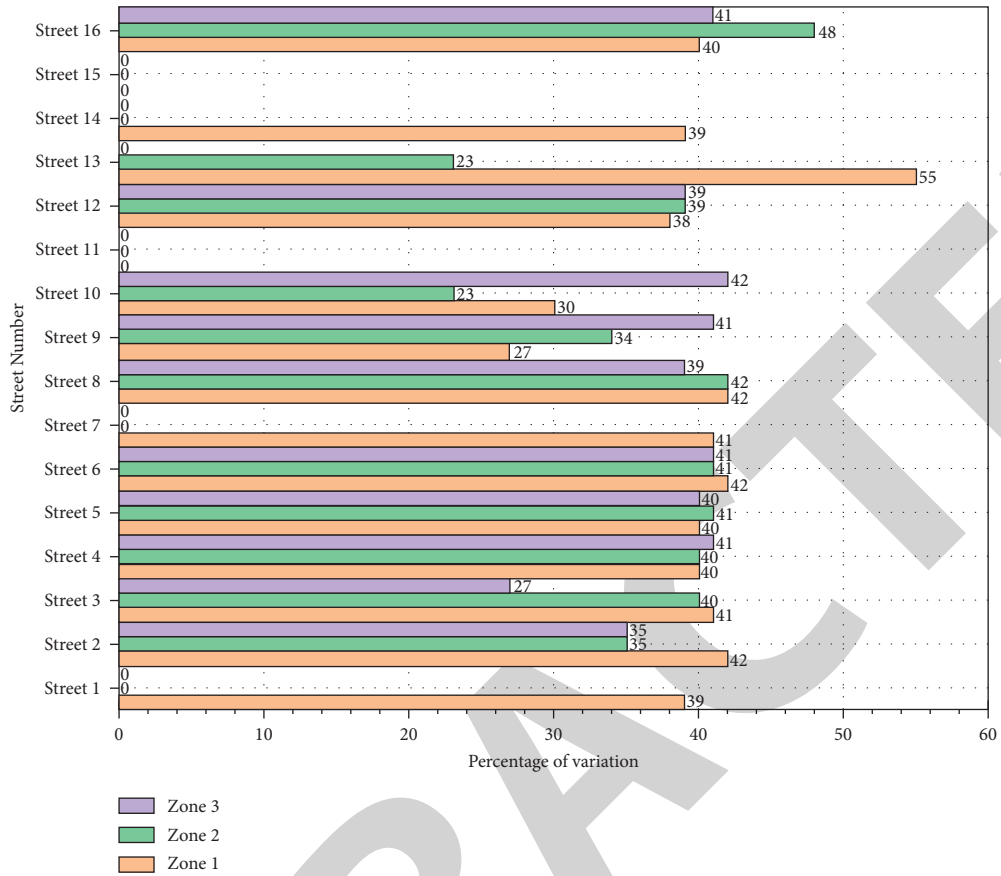


FIGURE 14: Percentage of variation between effective width ESVI values for collapse type 2 for investigated roads at different seismic intensities.

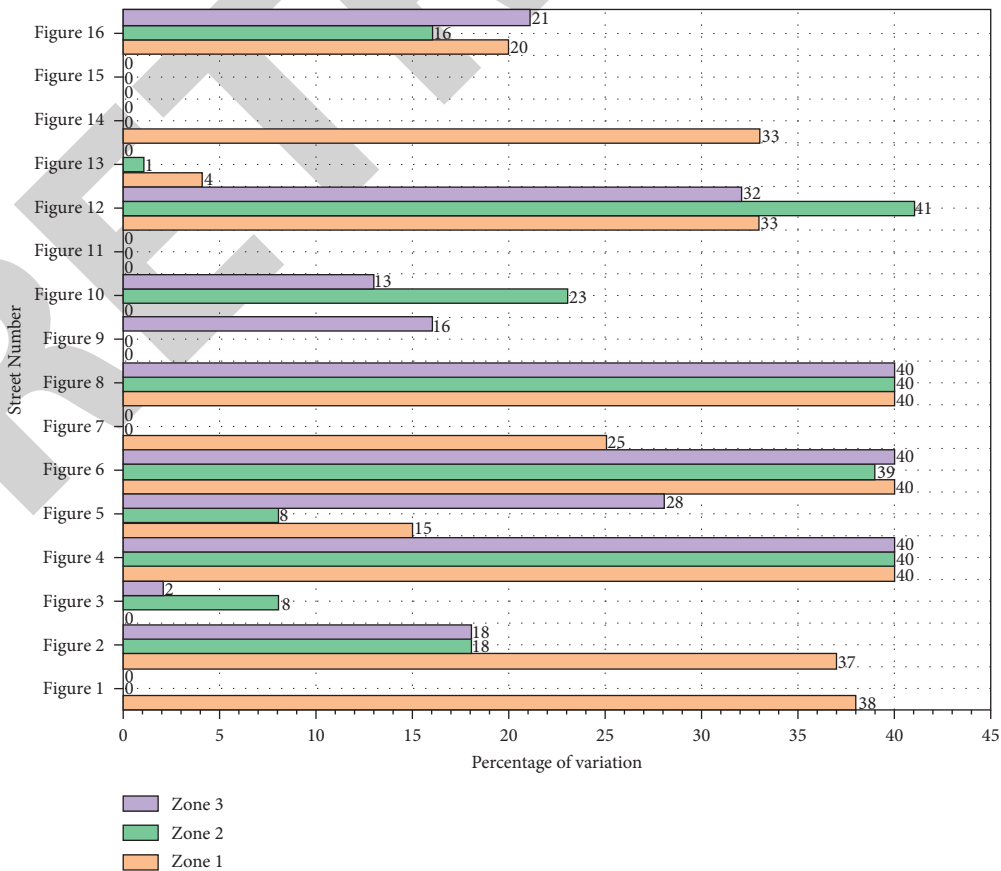


FIGURE 15: Percentage of variation between ESVI values of seismic intensity IX based on different collapse types.

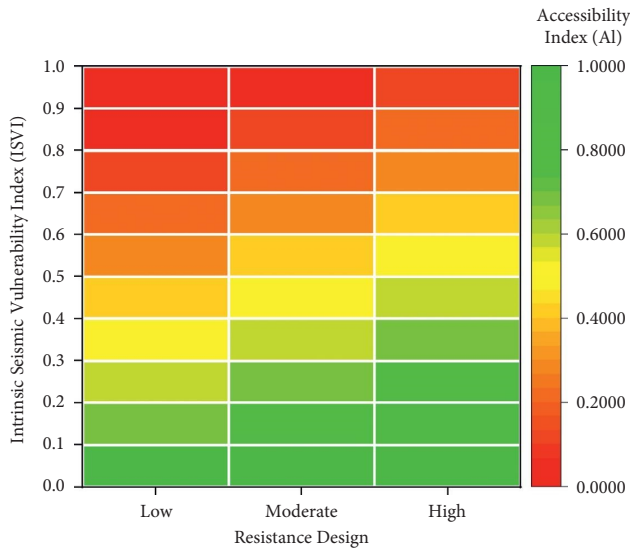


FIGURE 16: Integrated accessibility heat map between ISVI and resistance design of the road.

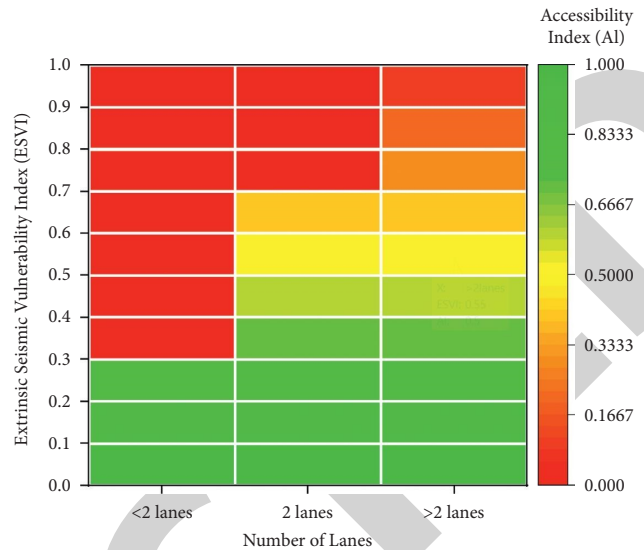


FIGURE 18: Integrated accessibility heat map between the ESVI and road width of the road for the assessment of ESV.

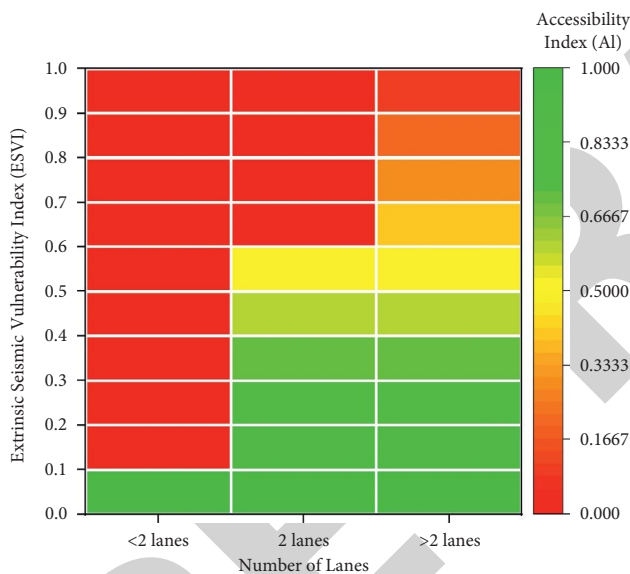


FIGURE 17: Integrated accessibility heat map between ESVI and road width of the road for the assessment of NEV.

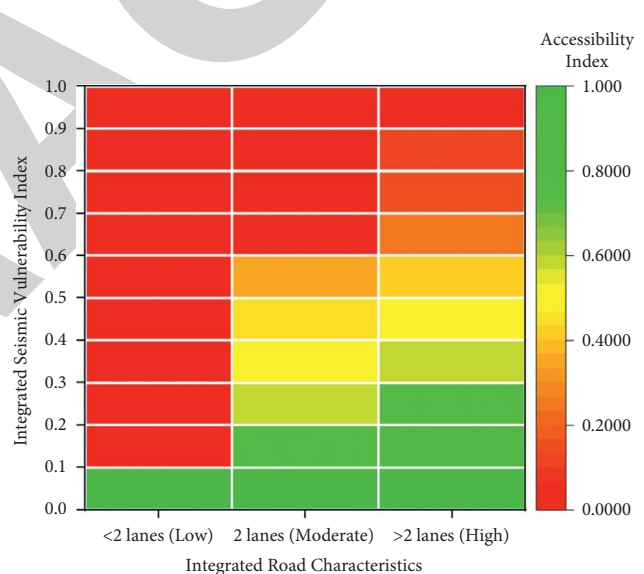


FIGURE 19: Generated accessibility heat map between integrated road characteristics and integrated seismic vulnerability index for NEVs.

vulnerability indices and the road network accessibility. First of all, this integration model utilized analytical work, which indicated that the number of lanes is considered more efficient when compared to the soil type and height of embankment parameters, but yet deemed more efficient when compared to the pavement strength parameter. This is followed by using the analytical hierarchy process (AHP) method for weighting the values of each parameter that are determined based on the prioritized parameters based on the probability of damage, which in turn develops the Intrinsic Seismic Vulnerability Index (ISVI). However, earthquake debris or road closures can have an impact on roadways as well as the surrounding environment. It is

possible to derive a second index, the Eccentric Seismic Vulnerability Index (ESVI), by comparing the width of the debris for two different kinds of collapse. Eventually, an accessibility heat map based on the correlation between integrated road characteristics and the integrated Seismic Vulnerability Index (SVI) is developed.

The aforementioned approach integrates engineering judgment with numerical methods aiming at a comprehensive assessment of the road network accessibility, toward a more efficient emergency planning and improved mitigation strategies for the communities that live in disaster-prone areas.

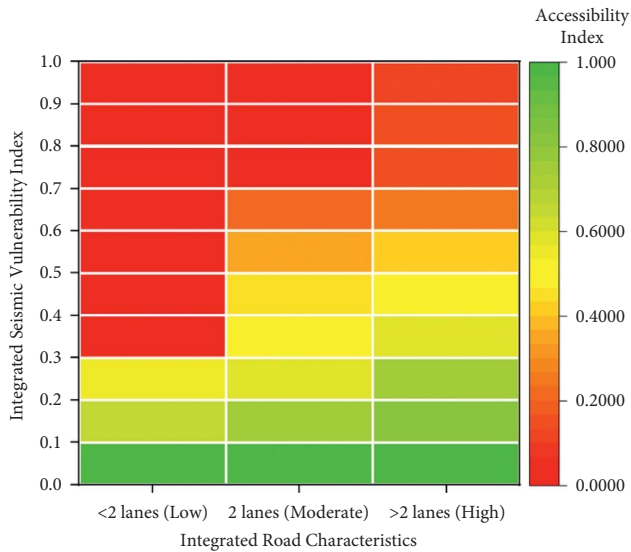


FIGURE 20: Generated accessibility heat map between integrated road characteristics and integrated seismic vulnerability index for ESV.

## 5. Conclusion

Through integrating the assessment of intrinsic and eccentric properties, this study assessed the seismic vulnerability of the road network and its interaction with the surrounding buildings. The approach emphasizes the need to combine methodologies to get more exact outcomes, which can help decision-makers lower their exposure to hazardous risk. Furthermore, the significance of this study is in determining the influence of the Intrinsic Seismic Vulnerability Index (ISVI) and Eccentric Seismic Vulnerability Index (ESVI) on road network accessibility when they are investigated separately or as a combined system that is developed in different heat maps. The following are some of the study's findings:

- (1) A model that compares the probability of damage (POD) for various collapse states to measure the efficiency of a parameter for assessing the ISVI for road networks and associated assets. The findings demonstrate that the height of the embankment is the most significant parameter, followed by the number of lanes, while the soil type and pavement strength have lower efficiency rates, with soil type having a small superiority.
- (2) The effective width ( $W_{eff}$ ) is retrieved from the data based on the ( $W_d$ ) assessment, and the  $W_d$  values are determined with regard to two different forms of collapse. When compared to standard emergency vehicles, the results show that fast emergency vehicles (ESVs) have higher manoeuvring efficiency and improved functioning levels (NEVs).
- (3) Since the resulting integrated damage heat maps reveal less accessibility with a greater closure probability than the singly assessed ESVI and ISVI damage maps, it is crucial to highlight the association between the intrinsic and eccentric properties.

In conclusion, the integrated model can be a powerful tool to increase the disaster preparedness of communities in real-life situations. However, this tool will be more impactful if the multihazard scenarios are considered in the development of this integrated model. Indeed, developing the intrinsic and eccentric vulnerability indices using analytical techniques can reduce or limit the role of the rapid visual screening methods that were used in previous studies based on expert opinion decisions, which depends on observations of damages caused by earthquakes. This can be a useful guide and criterion as an integrated model between traffic accessibility and physical vulnerability to develop a large-scale mapping prior to the earthquake event. Nevertheless, the integrated model is recognized as an innovative tool that can be effective in practical life and in the development of emergency disaster management plans, to avoid fatalities and economic losses following natural hazard occurrences.

Subsequently, future research should focus on the interdependencies of various infrastructures, such as electric power, fuel, transit, airport, or water facilities, as well as the interaction rate between transportation networks and other systems. In this regard, new emerging and digital technologies, as well as resilience analytics, should be enabled in order to develop advanced models.

## Data Availability

All the relevant data have been included in the article.

## Conflicts of Interest

The authors declare that they have no conflicts of interest.

## Acknowledgments

This research was supported by the Ministry of Higher Education Malaysia for Fundamental Research Grant Scheme with project code: FRGS/1/2020/TK02/USM/02/1.

## References

- [1] A. P. S. Golla, S. P. Bhattacharya, and S. Gupta, "Assessing the discrete and systemic response of the Built Environment to an earthquake," *Sustainable Cities and Society*, vol. 76, Article ID 103406, 2022.
- [2] W. R. McClure and T. J. Bartuska, *The Built Environment: A Collaborative Inquiry into Design and Planning*. John Wiley & Sons, Hoboken, NJ, U.S.A., 2011.
- [3] W. Miller, "What does built environment research have to do with risk mitigation, resilience and disaster recovery?" *Sustainable Cities and Society*, vol. 19, pp. 91–97, 2015.
- [4] G. Andreotti and C. G. Lai, "Use of fragility curves to assess the seismic vulnerability in the risk analysis of mountain tunnels," *Tunnelling and Underground Space Technology*, vol. 91, Article ID 103008, 2019.
- [5] S. P. Stefanidou and A. J. Kappos, "Methodology for the development of bridge-specific fragility curves," *Earthquake Engineering & Structural Dynamics*, vol. 46, no. 1, pp. 73–93, 2017.

## Research Article

# Understanding the Slow Motion of the Wangjiashan Landslide in the Baihetan Reservoir Area (China) from Space-Borne Radar Observations

Mingtang Wu,<sup>1</sup> Xiaoyu Yi ,<sup>2</sup> Jiawei Dun,<sup>2</sup> Jianyuan Yang,<sup>1</sup> Wei Cai,<sup>1</sup> and Guoqiang Zhang<sup>2</sup>

<sup>1</sup>Zhejiang Huadong Construction Engineering CO. LTD, Hangzhou 310014, China

<sup>2</sup>State Key Laboratory of Geohazard Prevention and Geoenvironment Protection, Chengdu University of Technology, Chengdu 610059, China

Correspondence should be addressed to Xiaoyu Yi; [xiaou@stu.cdut.edu.cn](mailto:xiaou@stu.cdut.edu.cn)

Received 14 February 2022; Revised 14 April 2022; Accepted 15 April 2022; Published 10 May 2022

Academic Editor: Fadzli Mohamed Nazri

Copyright © 2022 Mingtang Wu et al. This is an open access article distributed under the Creative Commons Attribution License, which permits unrestricted use, distribution, and reproduction in any medium, provided the original work is properly cited.

The analysis of landslide evolution using archived optical remote-sensing images is common, but it is often limited by the acquisition frequency, cloud cover, and resolution. With the development of space-borne radar observation technology, small baseline subset interferometric synthetic aperture radar (SAR) technology provides a new technical approach for detecting landslide deformation before disasters. The Sentinel-1A SAR datasets (20170219–20210330) were used to study the time-series deformation characteristics of the Wangjiashan landslide in the Baihetan Reservoir area before its impoundment. The time-series results show that the Wangjiashan landslide was in an initial deformation state in the prior four years, and the deformation first occurred in the middle part and then expanded to the landslide toe and crown retrogressive movement characteristics. Combined with an analysis of field deformation signs, these findings suggest that the upper landslide mass formed a local sliding surface, which caused serious deformation of the road. An analysis of historical rainfall data revealed that the Wangjiashan landslide is sensitive to rainfall, and the deformation is not only significantly correlated with cumulative rainfall but also influenced by concentrated heavy rainfall. The research in this study provides a basis for the monitoring, early warning, and risk management of the Wangjiashan landslide during the impoundment period. This work also provides a useful reference for investigations using space-borne SAR Earth observations in geological disaster prevention and control.

## 1. Introduction

The experience from the construction and impoundment of many large hydropower plants has shown that reservoir impoundment induces a large number of nascent landslide hazards while leading to increasing deformation of ancient landslides, resulting in many casualties and property losses [1–4]. Therefore, it is particularly important to understand the historical deformation of ancient landslides in reservoir inundation areas and then evaluate their stability. Due to the lack of monitoring equipment, the analyses of the deformation of landslides have mainly been performed using archived optical remote-sensing images [5, 6]. Optical remote sensing is characterized by wide coverage and a large spectral range but a long acquisition time interval; moreover,

the images are affected by clouds and fog, and the spatial resolution is inadequate.

In recent years, with the development of Earth observation technology, interferometric synthetic aperture radar (InSAR) technology has provided a new technical way to study the historical deformation of landslides. The InSAR technique uses two or more synthetic aperture radar (SAR) images from the same area and the same orbit to perform interferometric differential processing to remove residual terrain errors, atmospheric effects, and other related errors to obtain high-precision three-dimensional information on the terrain and surface deformations. Compared with traditional ground measurement technology and space-borne optical remote sensing, InSAR technology has the characteristics of less weather influence, large-scale coverage, and

high measurement accuracy. It has played an important role in landslide deformation monitoring [7–14] and large-scale landslide detection [15–18]. With the continuous improvement of hardware and software of space-borne radar Earth observation technology, InSAR technology will play an even more important role in the future [19–22]. However, due to the variability of signal propagation and scattering characteristics, the measurement results of conventional differential InSAR (DInSAR) methods are mainly affected by systematic and random errors, i.e., satellite orbit errors, atmospheric delays, elevation errors, and surface scatterer variations. These may lead to temporal and spatial dis-correlation and reduce the deformation monitoring accuracy [23–25]. In addition, these phenomena may also lead to the inability to extract surface deformation information in low-coherence regions. In contrast, the time-series InSAR technique can well compensate for the shortcomings of the traditional DInSAR technique, i.e., it uses a certain error reduction method to process multiple SAR images of long time series and then extracts the surface deformation information with high accuracy. Among the many time-series InSAR methods, the small baseline subset-InSAR (SBAS-InSAR) method has the advantage of obtaining small deformation information and long time series of slow surface deformation [18, 26, 27] and is therefore the most widely used in landslide monitoring.

Based on the above background, the SBAS-InSAR method is used to obtain the deformation rates of the Wangjiashan ancient landslide in the radar line-of-sight (LOS) and slope aspect directions based on Sentinel-1A radar images and to extract historical time-series deformation information of this landslide. Furthermore, the landslide deformation characteristics and influencing factors are analyzed in conjunction with a field investigation. On this basis, the evolution trend of the Wangjiashan landslide in the impoundment period is discussed. The research in this study provides a basis for the monitoring, early warning, and risk management of the Wangjiashan landslide during the impoundment period. This work also provides a useful reference for investigations using space-borne SAR Earth observations in geological disaster prevention and control.

## 2. Wangjiashan Landslide

Due to increasing demands for clean energy and the unique geographical conditions of Southwest China, several hydro-power stations, including the Baihetan Hydropower Station, have been built in the lower reaches of the Jinsha River in this region. Within the Baihetan Reservoir area is the Wangjiashan landslide, which is located on the right bank of the Xiaojiang River and is only 1.3 km from the Xiangbiling resettlement area (Figure 1). This valley is characterized by a subtropical dry and warm climate with an average annual temperature ranging from 12 C to 20 C. The annual precipitation in the study area is approximately 600–800 mm, with precipitation falling more frequently from May to October, and this period accounts for 90% of the annual rainfall; in contrast, from November to April of the following year, the weather is sunny and dry with sparse rainfall.

The Wangjiashan landslide is 800 m long and 90–500 m wide and covers approximately  $23.5 \times 10^4 \text{ m}^2$  (Figure 2). The elevation of the landslide toe on the right bank of the Xiaojiang River is approximately 765 m, while the crown is at an elevation of 1125 m, resulting in an elevation difference of 360 m between the landslide crown and toe. Gullies bound the left and right sides of the landslide, and these two gullies extended upward, ultimately intersecting at the landslide crown. The 870–950 m elevation section of the landslide features flat-topped hills and landslide depressions, and the terrain slope is 15–20°, whereas from an elevation of 870 m to the toe of the landslide, the terrain slope is 35–40°, and the local slope ranges from 45–50°.

The longitudinal profile of the landslide taken from the borehole data (see Figure 2, for borehole location) of the Power China Huadong Engineering Corporation (EHEC) is shown in Figure 3. The deposits on the upper landslide are mainly gravel soil that is gray-yellow, loose, and 14.0–49.9 m thick, whereas the lower landslide deposits are silty gravel that is also gray-yellow to dark gray in color, dense, and 3.04–13.30 m thick. The soil in the sliding zone comprises gray-black to gray-brown gravel clay distributed in inter-layers with silty gravel in the lower part of the landslide. The landslide bed is bedrock composed of Ordovician, Devonian, and Carboniferous limestone, dolomite, and quartz sandstone intercalated with siltstone, mudstone, and shale. The strata are oriented N0–10 W and dip NE $\angle$ 40–46°, and the strata are affected by the tectonic effect; moreover, the joint network is dense, and the rock mass is broken and highly weathered. According to drilling data, the landslide deposit is 14.0–87.6 m thick, with a total volume of approximately  $611 \times 10^4 \text{ m}^3$ . The landslide has long exhibited creep deformation, and thus, the stability and disaster risk of the Wangjiashan landslide after the impoundment of the Baihetan Reservoir has aroused concern among hydropower station authorities. Now, it is urgent to understand the deformation characteristics of the Wangjiashan landslide before impoundment to reduce or eliminate the risk of geological disasters during impoundment.

## 3. Data and Methods

*3.1. Data.* Because the ancient Wangjiashan landslide tends to move toward the SW, the terrain slope is smaller than the complementary angle of the central incident angle (36.8°) of the Sentinel-1A descending track [28]. Hence, Sentinel-1A descending track data are conducive to analyzing the deformation of the landslide. The coverage of the Sentinel-1A descending track data is shown in Figure 1. In this study, 77 scenes from the descending track of Sentinel-1A are used to investigate the historical deformation of the Wangjiashan landslide before impoundment from February 19, 2017, to March 30, 2021, with a time interval of 12 days. To eliminate the influence of terrain relief on the InSAR results, the Advanced Land Observing Satellite (ALOS) World 3D (AW3D30) digital elevation model (DEM) with a spatial resolution of 12.5 m is used as the external DEM data to simulate the terrain phase.

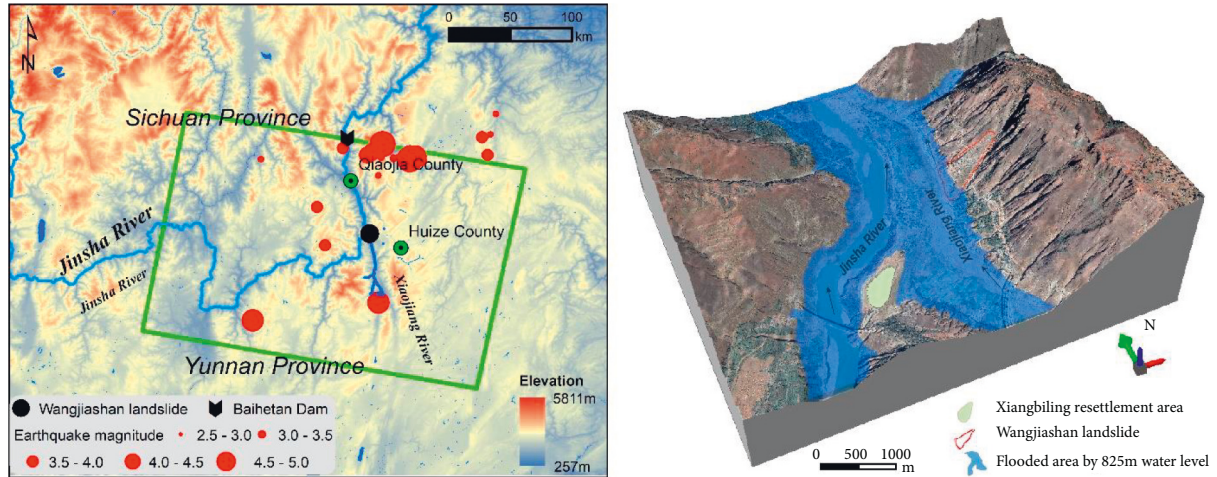


FIGURE 1: The location of the Baihetan Dam and Wangjiashan landslide, and the coverage of Sentinel-1A descending track data is superimposed in the green polygon. In addition, the epicenter and magnitude of earthquakes within 100 km of the Wangjiashan landslide from 2017 to 2020 are marked.

Moreover, to reduce the phase error caused by the orbit error, before processing the Sentinel-1A data, we download precise orbit data at the corresponding time and import the relevant data to correct the orbit information. In addition, monthly precipitation data and seismic data for the study area from January 2017 to March 2021 are acquired from the China Meteorological Data Service Center and the China Earthquake Networks Center, respectively. Finally, the engineering geological information of the Wangjiashan landslide is obtained from the geotechnical investigation report of the EHEC.

**3.2. SBAS-InSAR Method.** The SBAS-InSAR approach was first proposed by Italian scholars Berardino et al. [29]. SBAS-InSAR technology overcomes the decoherence phenomenon caused by an excessively long spatiotemporal baseline and alleviates atmospheric effects and terrain influences on the interferometric difference [29, 30]. The SBAS-InSAR technique obtains time series of surface deformation by the least-squares method while using singular value decomposition (SVD) to fit the deformation in both time and space; the InSAR surface deformation monitoring accuracy reaches the millimeter level, and thus, this technique exhibits a high measurement accuracy in landslide deformation monitoring research [31].

$N + 1$  scenes of SAR images are acquired in the same area and arranged in chronological order; then, one scene is chosen as the main image for registration, while the other SAR images are registered to the main image by setting appropriate temporal and spatial baseline thresholds. Ultimately,  $M$  scene interferograms are obtained. Assuming that  $t$  is the image acquisition time, after removing the flat terrain effect, terrain phase, and atmospheric phase error, the interference phase  $\delta_\varphi(x, r)$  at pixel point  $(x, r)$  ( $x$  is the azimuth coordinate and  $r$  is the range coordinate) can be obtained from the phases  $\varphi(t_A, x, r)$  and  $\varphi(t_B, x, r)$  in the images generated at times  $t_A$  and  $t_B$ , respectively [29, 32, 33].

During SBAS-InSAR data processing,  $M$  interferograms are generated.  $\varphi(x, r)$  is adopted to represent the matrix composed of the image deformation phases at point  $(x, r)$  at  $N$  times; then, the matrix composed of  $M$  interferometric pair phase values is  $\delta_\varphi(t_A, x, r) = \mathbf{A}\varphi(x, r)$ , where  $\mathbf{A}$  is an  $M \times N$  matrix. When  $M \geq N$ , the deformation time series can be obtained by the least-squares method. When  $M < N$ , the result obtained by the least-squares method is not unique, SVD is implemented to jointly solve multiple small baselines, and the phase velocities obtained for each period are integrated into the time domain to obtain the deformation time series of the entire observation period.

In this study, ENVI SARscape software is used to analyze the historical deformation of the Wangjiashan landslide. The temporal baseline threshold is set to 72 days, and the critical baseline percentage is 2%. The 20201025 SAR image is used as the main image, while images from other periods are used as auxiliary images for interferometric pairing, and 213 sets of interferometric pairs are generated. The relationship between the specific acquisition dates of the descending track data and the spatiotemporal baseline is shown in Figure 4. Synthetic interferogram inversion, geocoding, and raster vector conversion are performed to generate the mean LOS deformation rate, and finally, the time-series deformation results are obtained.

**3.3. Slope Aspect Velocity Fields.** The sliding direction of a landslide is generally downward along the slope. In the process of radar interferometry, the obtained deformation is usually the deformation value along the radar LOS direction, which often cannot accurately reflect the true deformation of the slope surface [34, 35]. According to the geometric relationship among the radar LOS direction, the slope aspect, and the vertical settlement direction, the deformation in the radar LOS direction ( $V_{LOS}$ ) is transformed into slope aspect deformation ( $V_{Slope}$ ) [36, 37]. The specific conversion formula is as follows:

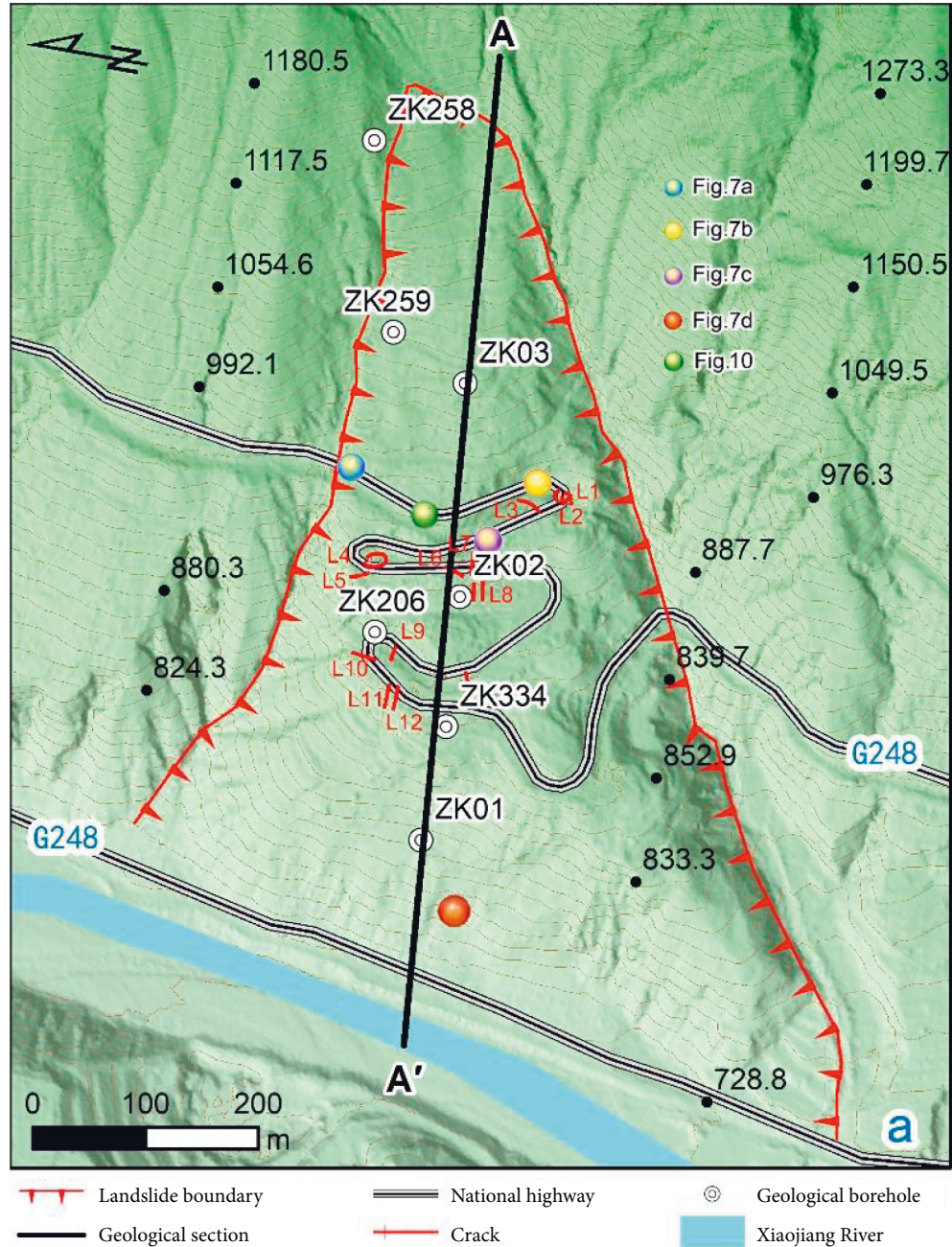


FIGURE 2: Geological map of the Wangjiashan landslide.

$$V_{\text{slope}} = \frac{V_{\text{LOS}}}{\text{Index}}, \quad (1)$$

$$\text{Index} = n_{\text{LOS}} \times n_{\text{slope}}, \quad (2)$$

$$n_{\text{LOS}} = (-\sin \theta \cos \theta, \sin \theta \sin \alpha, \cos \theta), \quad (3)$$

$$n_{\text{slope}} = (-\sin \beta \cos \varphi, -\cos \beta \sin \varphi, \sin \varphi). \quad (4)$$

In the above equations,  $\theta$  represents the incident angle of the radar,  $\alpha$  is the satellite flight direction angle,  $\beta$  is the slope direction, and  $\varphi$  is the slope. Among them,  $\beta$  and  $\varphi$  can be calculated from the DEM.

(1) demonstrates that if the value of Index is close to 0,  $V_{\text{slope}}$  will tend toward infinity, but the ground unit at this time is completely decoherent. To correct this anomaly, according to the study of Herrera et al. [38],  $|\text{Index}| = 0.3$  can be set as a threshold so that the acceptable projected velocity value can be distinguished from the data with unreliable projection values. That is, when  $-0.3 < \text{Index} < 0$ ,  $\text{Index} = -0.3$ , and when  $0 < \text{Index} < 0.3$ ,  $\text{Index} = 0.3$ . In addition, when  $V_{\text{slope}} > 0$ , the landslide mass moves upward along the slope. Even if expansion causes a bulge on the front edge of the landslide or the landslide mass accumulates at the foot of the slope, the displacement vector in the horizontal direction remains oriented in the downward direction of the



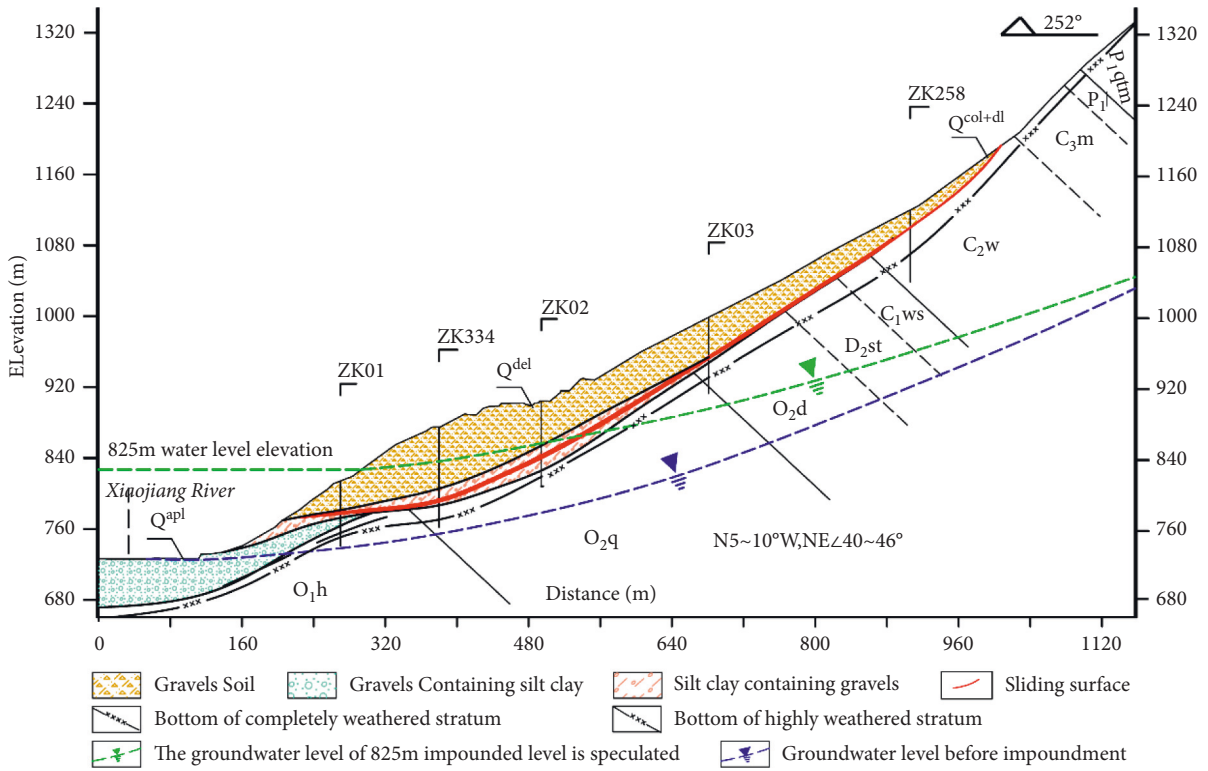


FIGURE 3: Longitudinal profile A-A' of the Wangjiashan landslide in Figure 6.

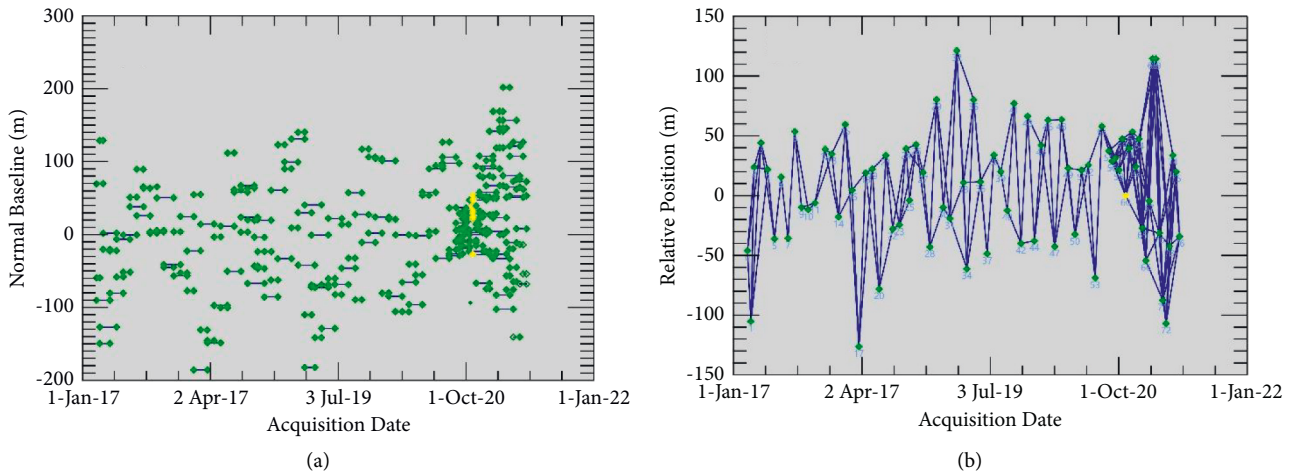


FIGURE 4: Spatial and temporal baselines of SAR datasets used in this study: (a) time-baseline plot of interferometric pairs of SAR images; (b) time-position plot of SAR image.

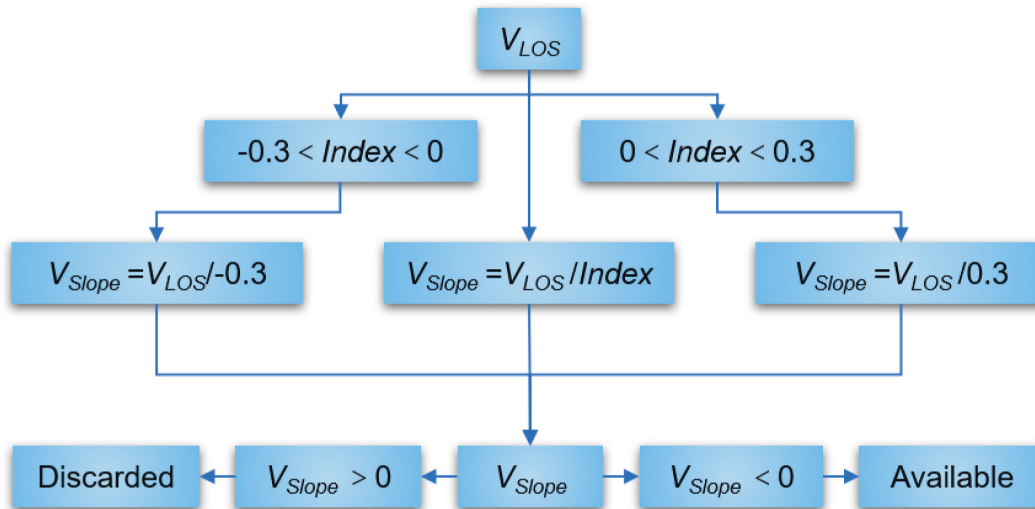


FIGURE 5: Flowchart of calculating slope aspect velocity fields from LOS direction velocity fields.

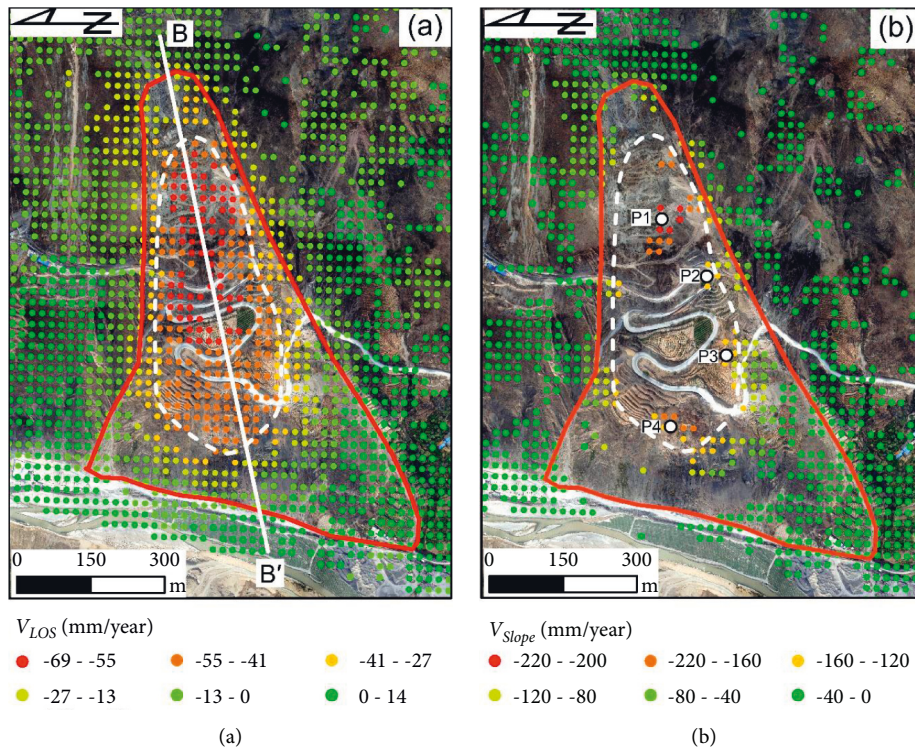


FIGURE 6: The mean deformation velocity of the Wangjiashan landslide (201702–202103): (a) LOS directional deformation rate; (b) slope aspect deformation rate.

slope surface. These deformation points with  $V_{Slope} > 0$  need to be eliminated consistently. In this way, the average deformation rate of the surface displacement along the slope direction in the study area can be obtained (Figure 5).

#### 4. Results

4.1. Mean Deformation Velocities. In this study, the SBAS-InSAR method is utilized to analyze the mean deformation

rate of the Wangjiashan landslide in the radar LOS and slope aspect directions. As shown in Figure 6, the mean deformation rate of the Wangjiashan landslide in the LOS direction ranges from  $-69$  to  $-14$  mm/year, while the mean deformation rate in the slope aspect direction reaches  $-220$  mm/year. The landslide deformation is concentrated in the white dashed circle in the middle with a longitudinal length of approximately 600-700 m. The mean  $V_{LOS}$  ranges from  $-41$  to  $-69$  mm/year, and the mean  $V_{Slope}$  ranges from

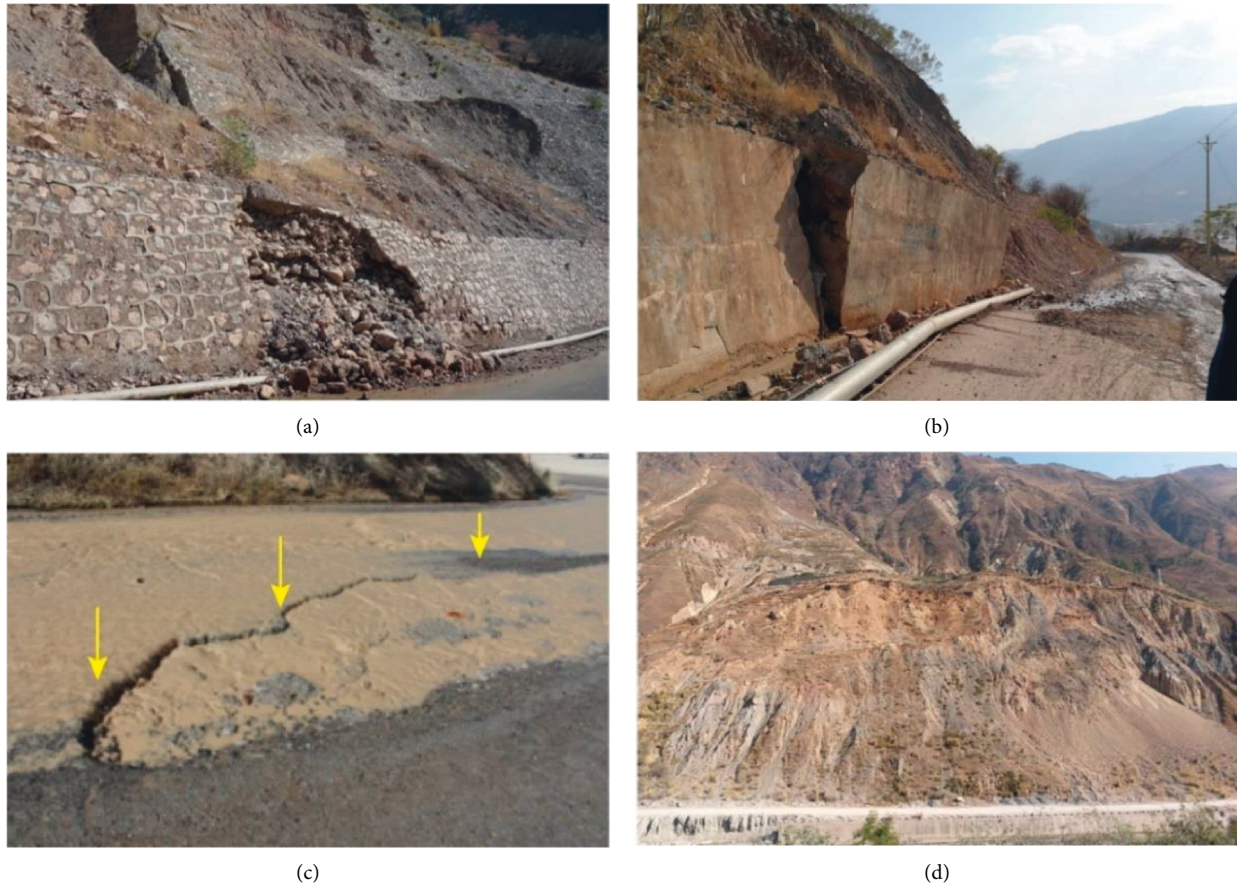


FIGURE 7: Photographs of deformation signs of Wangjiashan landslide: (a) broken retaining wall; (b) toppling of retaining wall; (c) tension cracks in road surface; (d) landslide deformation on the front edge of the landslide.

–120 to –220 mm/year. The field investigation revealed deformation phenomena such as fracturing (Figure 7(a)) and toppling of the retaining wall (Figure 7(b)) in the area of the white dashed circle. Furthermore, as many as 12 cracks are found in the slope (Figure 2); the longest crack is approximately 17 m long, and the tensile crack with the maximum width is 30 cm wide (Figure 7(c)). These cracks are mostly located around the road and are dominated by tension cracks, which may be the result of landslide deformation caused by road excavation. Some deformation phenomena, such as local collapse in front of the landslide, are also observed (Figure 7(d)).

**4.2. Time-Series Cumulative Deformation.** Based on SBAS-InSAR technology, nine time-series cumulative deformation graphs of the Wangjiashan landslide are obtained (Figure 8). It should be noted that all accumulated deformation is referenced to the first image on February 19, 2017. In 2018, the deformation area of the landslide was in the middle of the landslide area (red part). In 2019, the landslide deformation expanded to the front and rear edges. Over time, the deformation of the Wangjiashan landslide gradually increased, and the maximum cumulative deformation in the LOS direction reached 294 mm. As shown in Figure 9, the deformation of the Wangjiashan landslide exhibits obvious

spatial heterogeneity, with the largest deformation in the middle of the landslide, followed by the landslide toe, and the smallest deformation at the landslide crown. According to the field investigation, the cracks are mainly developed in the middle of the landslide (Figure 2 and Table 1), consistent with the area with the largest cumulative deformation.

## 5. Interpretation of Landslide Motion

**5.1. Kinematic Behavior.** To further understand and analyze the temporal and spatial characteristics of landslide deformation, the mean LOS deformation rate curve along section B–B' in Figure 6(a) and the LOS cumulative deformation curve along section B–B' in Figure 9 are superimposed onto the geological profile, and the result is shown in Figure 5. A comparison of the data revealed the following:

- (i) The largest deformation of the Wangjiashan landslide is in zones B and C. The average LOS cumulative deformation is 220 mm, and the maximum LOS cumulative deformation is 289 mm. The deformation of area A is relatively low; the average LOS cumulative deformation in zone A is 90 mm, and the maximum LOS cumulative deformation is 120 mm. Likewise, the deformation in area E is very weak; the average LOS deformation rate is only eight mm/year.

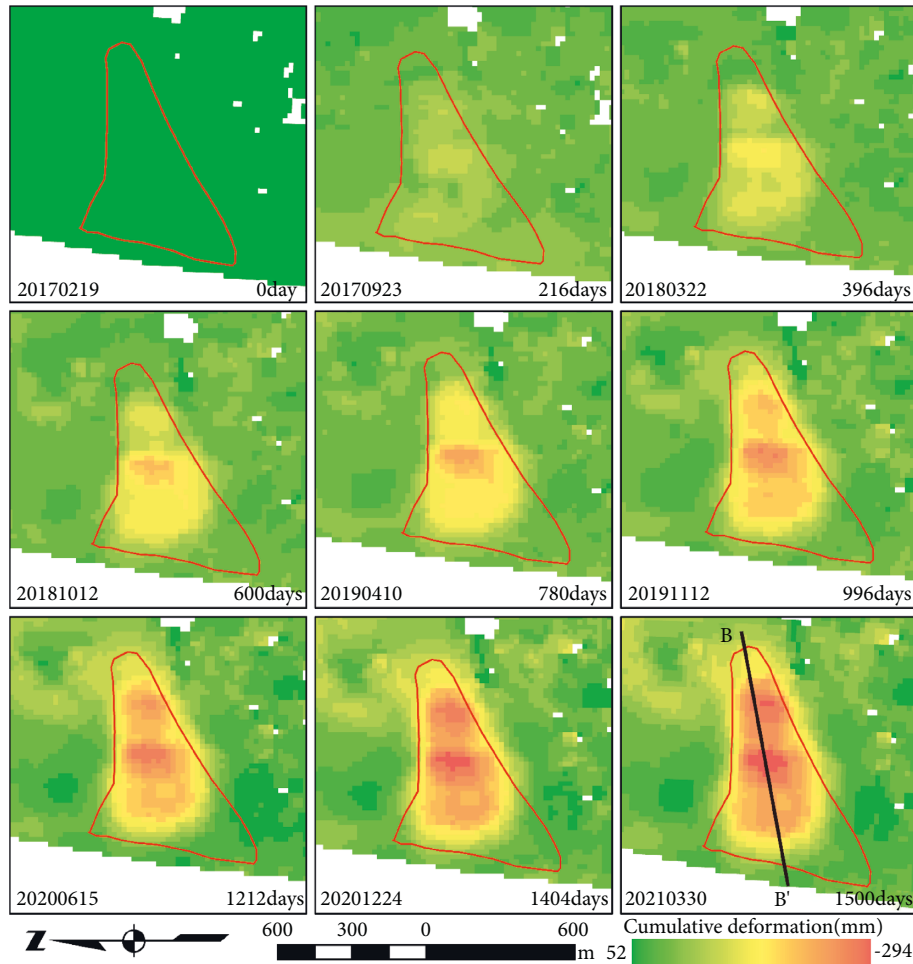


FIGURE 8: The time-series cumulative deformation maps along the LOS from February 19, 2017, to March 30, 2021, with a reference SAR acquisition date of 20170219.

The cumulative deformation and LOS deformation rate in zone *D* increase along the profile. The deformation rate at the crown of the Wangjiashan landslide is the smallest, while the deformation rates of the central zone (zone *C*) and the toe (zone *B*) are larger. As shown in Figure 5, the middle of the landslide deformed first and then expanded to the front and rear edges. The landslide exhibits the deformation characteristics of a retrogressive landslide [39].

- (ii) The data of zone *F* show a decreasing deformation rate but increasing cumulative deformation. A field investigation revealed that the retaining wall on the side of the road in this area is broken (Figure 7(b)), and the road surface was bulging (Figure 10) and cracked (Figure 7(c)). These observations indicate that the sliding force of the landslide mass exceeded the slip resistance of the retaining wall, resulting in damage to both the retaining wall and the ground. Considering the deformation rate in conjunction with the topographic characteristics [40, 41], due to excavation of the road, the upper landslide seems to

have formed a local sliding surface, leading to serious road deformation. Of course, the final determination of this local sliding surface requires further detailed research.

### 5.2. Influencing Factors and Evolution Trend.

Gravity-driven retrogressive sliding is the main deformation mechanism of the Wangjiashan landslide. However, other factors, such as changes in the groundwater level, heavy rainfall, and earthquakes, can accelerate deformation [42]. Nevertheless, no groundwater was discovered in the boreholes in the Wangjiashan landslide, which indicates that the groundwater level within the landslide is much lower than the sliding surface (Figure 3). Therefore, groundwater is not the main factor affecting landslide deformation. To understand the response relationship between deformation and rainfall, four monitoring points (P1, P2, P3, and P4 in Figure 6(b)) with different elevations are selected from the slope deformation rate map to further analyze the correlation between the slope time-series deformation and the precipitation observed by adjacent meteorological stations.

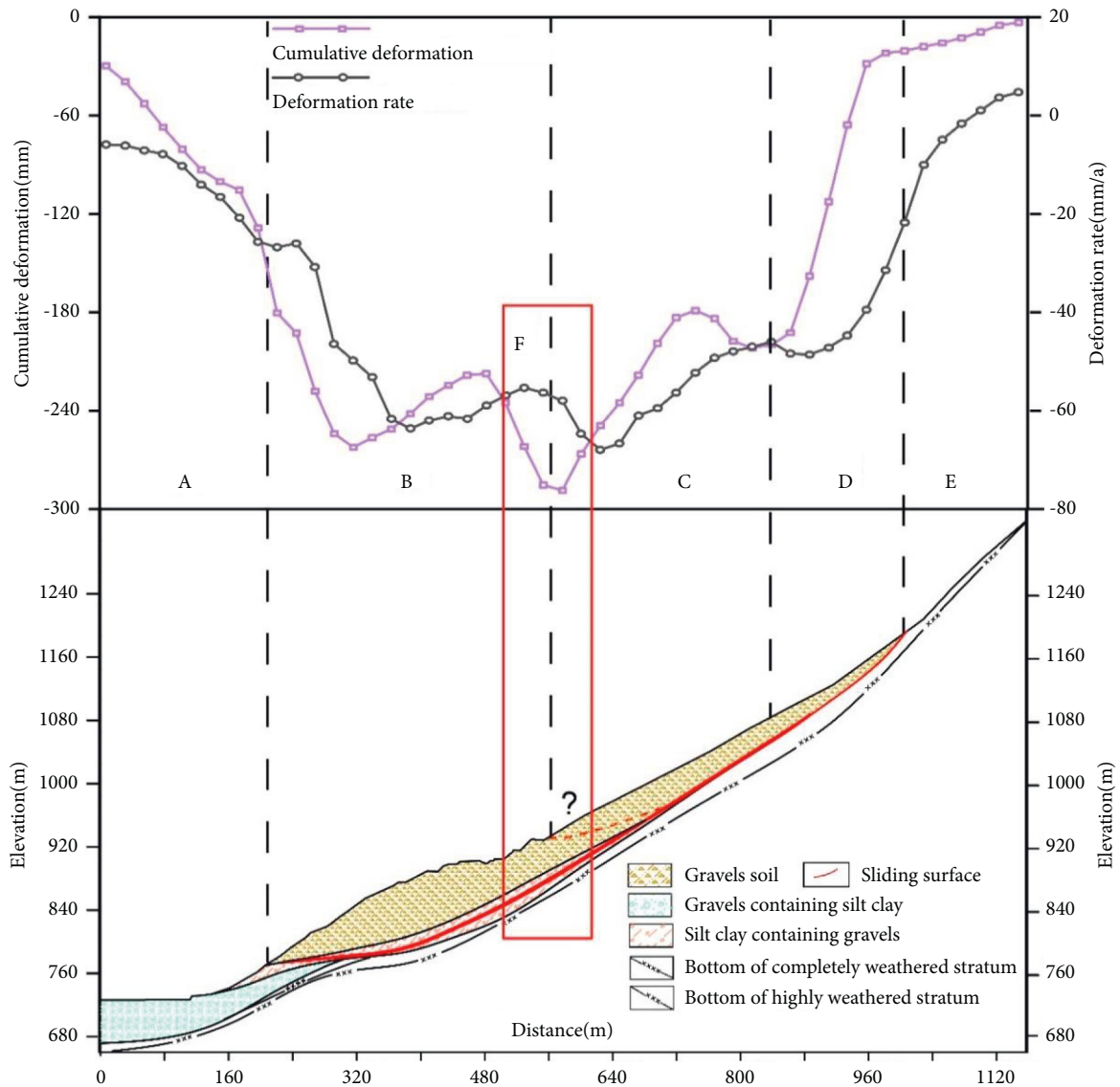


FIGURE 9: Landslide LOS deformation rate curve and cumulative deformation curve along profile B-B' calculated by the SBAS-InSAR technique.

TABLE 1: Characteristics of tensile cracks in Figure 2.

Crack number	Altitude (m)	Strike angle (°)	Extension length (m)	Width (cm)
L1	945	EW	10	20-30
L2	945	N20°W	17	1-2
L3	943	N60°E	7	3-5
L4	914	EW	10	5-10
L5	912	N20°E	12	0.5-1
L6	916	N20°W	10	1-2
L7	898	N60°E	10	0.5-1
L8	887	N66°E	10	1-10
L9	885	N85°E	10	1-5
L10	880	EW	8	2-5
L11	879	N10°W	15	5-15
L12	874	EW	9	2-3



FIGURE 10: Cracks in the retaining wall and bulging deformation of the road.

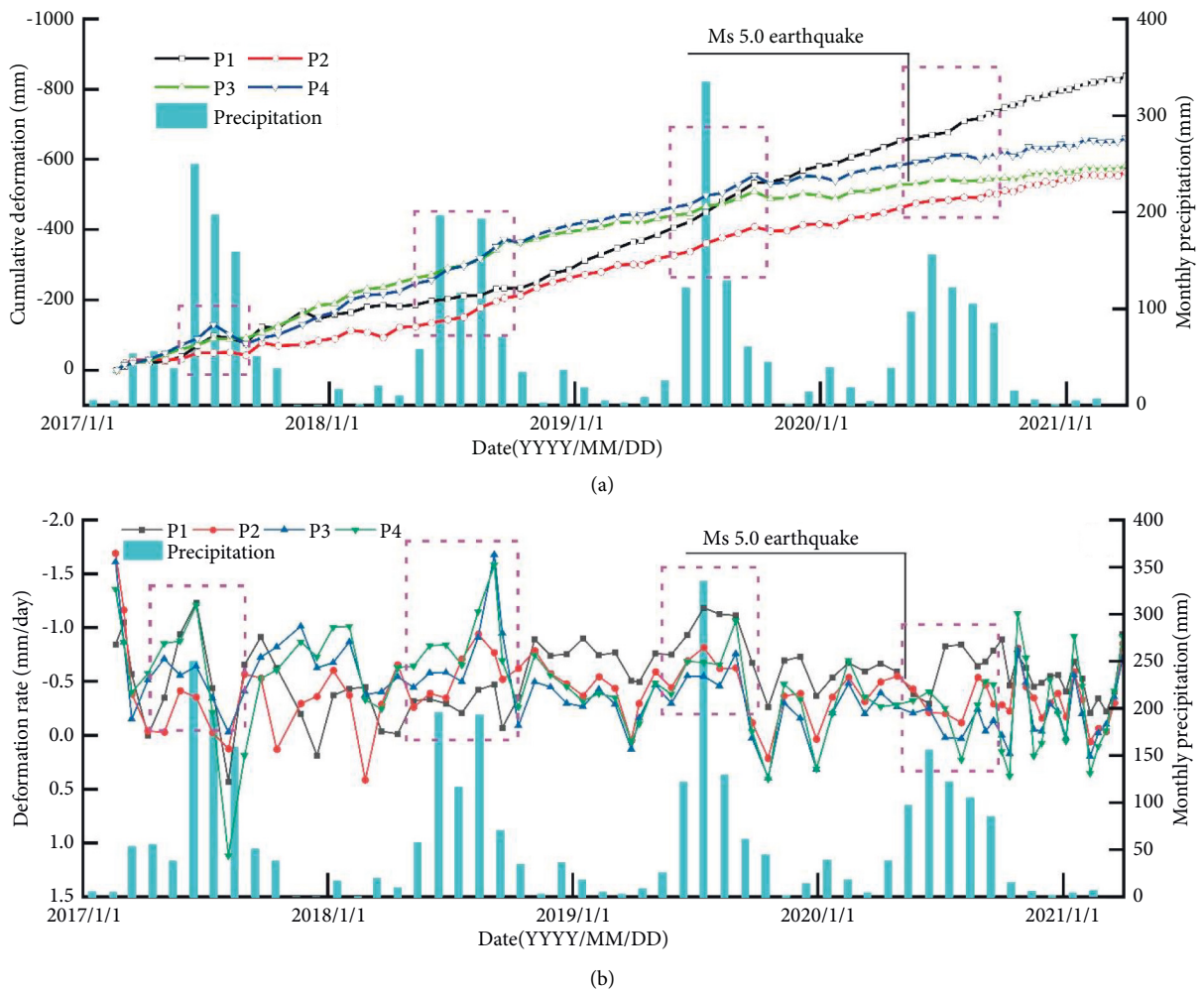


FIGURE 11: Correlation between the Wangjiashan landslide slope aspect deformation and rainfall. P1, P2, P3, and P4 are located at different elevations of the Wangjiashan landslide (Figure 6(b)): (a) cumulative deformation; (b) deformation rate.

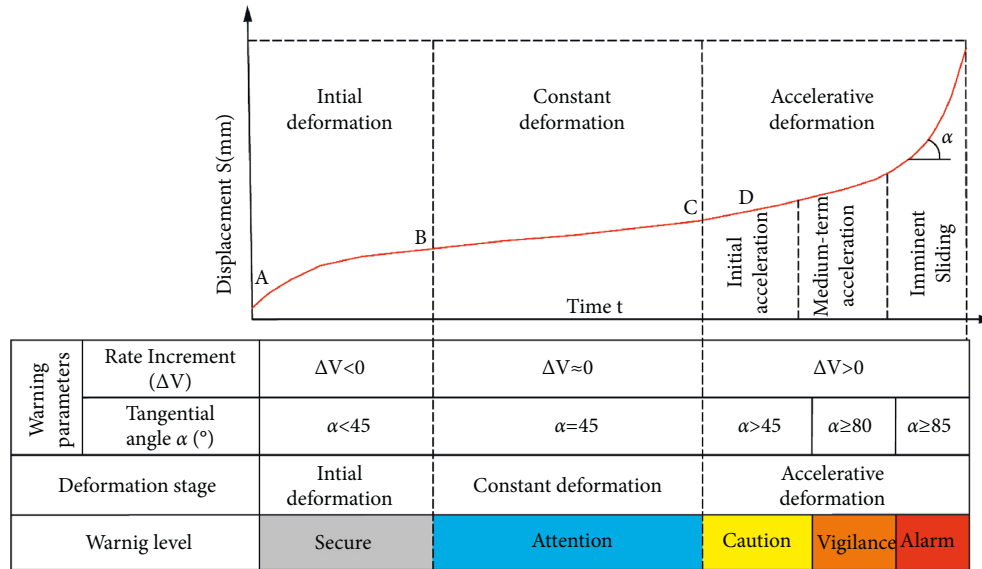


FIGURE 12: Early warning criteria for creep failure of a slope [46].

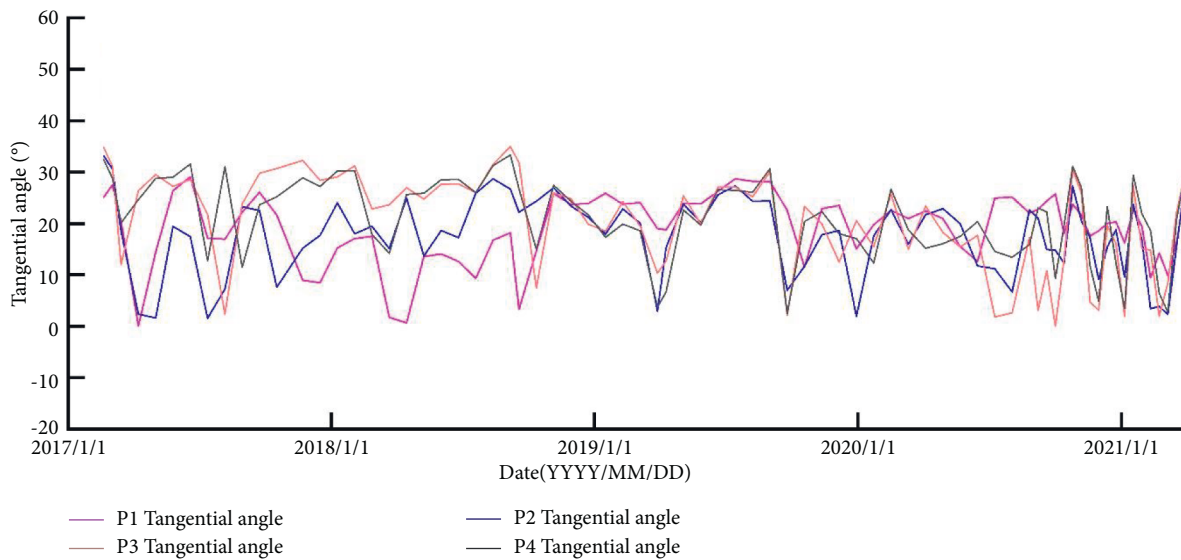


FIGURE 13: Time history of tangential angle  $\alpha$  of P1~P4 in Figure 11.

Figure 11 shows the slope aspect time-series cumulative deformation and deformation rate of the Sentinel-1A data from February 2017 to March 2021 at the four observation points P1, P2, P3, and P4. The deformations at P1, P2, P3, and P4 increase linearly, and the deformations increase obviously during the rainy season. In the rainy season of 2017, the deformations at the four observation points increased. However, in the 2018 rainy season, only the deformations at P2, P3, and P4 changed significantly with seasonal precipitation. In July 2019, the monthly precipitation reached 334.5 mm, and the cumulative displacements at the four observation points increased significantly. Through the deformation rate curve of the landslide time series, we can see that the displacement rate of landslides in the rainy season is increased compared with that in the dry season. This shows that heavy rainfall will accelerate the

deformation of a landslide. Because the Wangjiashan landslide is a reactivated ancient landslide, there is also deformation in the dry season, but the deformation rate is less than that in the rainy season. These findings indicate that rainfall is one of the main reasons for the reactivation and deformation of the Wangjiashan landslide.

In contrast, during the rainy season of 2020, the deformations at the four observation points did not increase significantly because the rainfall was low. In addition, the cumulative rainfall from June to August in the study area during 2019 and 2018 was 504.5 mm and 584.5 mm, respectively, and the cumulative deformation at point P2 was 61.86 mm and 50.38 mm, respectively. The above phenomenon indicates that concentrated heavy rainfall is more likely to cause large deformation of the landslide [43, 44]. The above data analysis shows that the

deformation of the Wangjiashan landslide in the rainy season is related to the accumulation of rainfall and concentrated heavy rainfall.

In addition, seismic data within a 100 km radius of the Wangjiashan landslide from 2017 to 2020 were downloaded from the China Earthquake Networks Center (<http://www.ceic.ac.cn/>) (Figure 2). Based on its epicentral location, focal depth, magnitude, and intensity, the Ms5.0 earthquake at 21:47 on May 18, 2020, caused many houses to collapse and damaged several roads in Qiaojia County. The epicenter of the earthquake was 74 km from the Wangjiashan landslide, and the focal depth was 8 km. However, comparative data show that the earthquake did not accelerate the deformation of the Wangjiashan landslide (Figure 11).

## 6. Discussion

According to the theory of creep deformation [45], before a landslide occurs, it usually undergoes an initial deformation stage, a constant deformation stage, and an accelerated deformation stage (which in turn is divided into three substages: an initial acceleration stage, a moderate acceleration stage, and an imminent sliding stage). As shown in Figure 12, Xu et al. [47, 48] proposed using the tangential angle ( $\alpha$ ) as the basis for dividing these three stages. When the tangent angle is much less than  $45^\circ$ , the landslide is considered to be in its initial deformation stage; when the tangent angle is approximately equal to  $45^\circ$ , the landslide is assumed to undergo constant velocity deformation; when the tangent angle greatly exceeds  $45^\circ$ , the landslide is believed to be in its accelerated deformation stage (with  $80^\circ$  and  $85^\circ$  representing the boundaries between the first and second substages and the second and third substages, respectively). The gravity landslide warning model shown in Figure 12 has been widely used to monitor and warn landslides in Northwest and Southwest China [46, 49–53].

The long-term displacement curve in Figure 11 shows that the Wangjiashan landslide has exhibited a stable deformation rate in the past four years, except for a briefly accelerated rate during the rainfall period and average tangential angle  $\alpha$  between  $23^\circ$  and  $32^\circ$ , which is less than  $45^\circ$  (Figure 13). Therefore, from the perspective of its evolution, the Wangjiashan landslide was in the initial deformation stage before impoundment and maintained slow deformation without strong interference from external factors.

The signs of deformation during the impoundment period of the Wangjiashan landslide and studies on areas such as the Three Gorges Reservoir have shown that fluctuations in the water level of large reservoirs may lead to the reactivation of ancient landslides, resulting in considerable losses [3, 4, 54, 55]. Given the rainfall concentration characteristics of the study area and the sensitivity of the deformation of the Wangjiashan landslide to rainfall, its future development deserves further attention. Therefore, it is urgent to systematically identify and analyze potential landslides in the Baihetan Reservoir area and establish a monitoring and early warning system to reduce the losses of life and property.

## 7. Conclusions

Sentinel-1A SAR data were used to study the time-series deformation characteristics of the Wangjiashan landslide in the Baihetan Reservoir area before its impoundment. We found that the Wangjiashan landslide has been in an initial deformation state in recent years. Deformation first occurred in the middle of the landslide and then expanded to the landslide toe and crown, thereby demonstrating the characteristics of retrogressive movement. Combined with an analysis of field deformation evidence, the upper landslide mass seems to have formed a local sliding surface, which has caused serious deformation of the road. An analysis of historical rainfall data revealed that the Wangjiashan landslide is sensitive to rainfall, and the deformation is not only significantly correlated with cumulative rainfall but also influenced by concentrated heavy rainfall. Considering the sensitivity of the Wangjiashan landslide to rainfall, coupled with the environmental changes caused by impoundment, establishing a landslide monitoring and early warning system in this area is particularly important.

## Data Availability

The precipitation data and historical earthquake data were provided by China Meteorological Data Service Center (<http://data.cma.cn/>) and China Seismic Network Center (<http://www.ceic.ac.cn/>), respectively. Sentinel-1 A/B images were from the European Space Agency (ESA) project, and these data were downloaded from the Sentinel-1 Scientific Data Hub. DEM data were provided by the Japan Aerospace Exploration Agency (JAXA).

## Conflicts of Interest

The authors declare that they have no conflicts of interest.

## Acknowledgments

This research was funded by the National Key R&D Plan (Grant no. 2018YFC1505503), the State Key Laboratory of Geohazard Prevention and Geoenvironment Protection Independent Research Project (Grant no. SKLGP2020Z001), and the Zhejiang Huadong Construction Engineering Co., Ltd Research Project (KY2020-HDJS-19).

## References

- [1] D. Huang and D. M. Gu, "Influence of filling-drawdown cycles of the Three Gorges reservoir on deformation and failure behaviors of anaclinal rock slopes in the Wu Gorge," *Geomorphology*, vol. 295, pp. 489–506, 2017.
- [2] B. Huang, Y. Yin, G. Liu, S. Wang, X. Chen, and Z. Huo, "Analysis of waves generated by Gongjiafang landslide in Wu Gorge, three Gorges reservoir, on November 23, 2008," *Landslides*, vol. 9, no. 3, pp. 395–405, 2012.
- [3] H. Tang, J. Wasowski, and C. H. Juang, "Geohazards in the three Gorges reservoir area, China - lessons learned from decades of research," *Engineering Geology*, vol. 261, p. 105267, 2019.



- [4] Y.-p. Yin, B. Huang, X. Chen, G. Liu, and S. Wang, "Numerical analysis on wave generated by the qianjiangping landslide in three Gorges reservoir, China," *Landslides*, vol. 12, no. 2, pp. 355–364, 2015.
- [5] R. Behling, S. Roessner, D. Golovko, and B. Kleinschmit, "Derivation of long-term spatiotemporal landslide activity-A multi-sensor time series approach," *Remote Sensing of Environment*, vol. 186, pp. 88–104, 2016.
- [6] C. Wu, X. Li, W. Chen, and X. Li, "A review of geological applications of high-spatial-resolution remote sensing data," *Journal of Circuits, Systems, and Computers*, vol. 29, no. 6, Article ID 2030006, 2020.
- [7] P. Liu, Z. Li, T. Hoey et al., "Using advanced InSAR time series techniques to monitor landslide movements in Badong of the Three Gorges region, China," *International Journal of Applied Earth Observation and Geoinformation*, vol. 21, pp. 253–264, 2013.
- [8] K. Dai, Z. Li, R. Tomás et al., "Monitoring activity at the Daguangbao mega-landslide (China) using Sentinel-1 TOPS time series interferometry," *Remote Sensing of Environment*, vol. 186, pp. 501–513, 2016.
- [9] R. Tomás, Z. Li, J. M. Lopez-Sanchez, P. Liu, and A. Singleton, "Using wavelet tools to analyse seasonal variations from InSAR time-series data: a case study of the Huangtupo landslide," *Landslides*, vol. 13, no. 3, pp. 437–450, 2016.
- [10] X. Hu, R. Bürgmann, W. H. Schulz, and E. J. Fielding, "Four-dimensional surface motions of the Slumgullion landslide and quantification of hydrometeorological forcing," *Nature Communications*, vol. 11, no. 1, 2020.
- [11] I. N. S. Parwata, S. Nakashima, N. Shimizu, and T. Osawa, "Effect of digital elevation models on monitoring slope displacements in open-pit mine by differential interferometry synthetic aperture radar," *Journal of Rock Mechanics and Geotechnical Engineering*, vol. 12, no. 5, pp. 1001–1013, 2020.
- [12] Q. Meng, W. Li, F. Raspini et al., "Time-series analysis of the evolution of large-scale loess landslides using InSAR and UAV photogrammetry techniques: a case study in Hongheyan, Gansu Province, Northwest China," *Landslides*, vol. 18, no. 1, pp. 251–265, 2021.
- [13] C. Zhou, Y. Cao, K. Yin et al., "Landslide characterization applying sentinel-1 images and InSAR technique: the muyubao landslide in the three Gorges reservoir area, China," *Remote Sensing*, vol. 12, no. 20, p. 3385, 2020.
- [14] C. Zhou, Y. Cao, X. Hu, K. Yin, Y. Wang, and F. Catani, "Enhanced dynamic landslide hazard mapping using MT-InSAR method in the Three Gorges Reservoir Area," *Landslides*, 2022.
- [15] R. Guo, S. Li, Y. n. Chen, X. Li, and L. Yuan, "Identification and monitoring landslides in Longitudinal Range-Gorge Region with InSAR fusion integrated visibility analysis," *Landslides*, vol. 18, no. 2, pp. 551–568, 2020.
- [16] X. Liu, C. Zhao, Q. Zhang et al., "Integration of Sentinel-1 and ALOS/PALSAR-2 SAR datasets for mapping active landslides along the Jinsha River corridor, China," *Engineering Geology*, vol. 284, p. 106033, 2021.
- [17] Y. Zhang, X. Meng, G. Chen, L. Qiao, R. Zeng, and J. Chang, "Detection of geohazards in the Bailong River Basin using synthetic aperture radar interferometry," *Landslides*, vol. 13, no. 5, pp. 1273–1284, 2016.
- [18] J. Dun, W. Feng, X. Yi, G. Zhang, and M. Wu, "Detection and mapping of active landslides before impoundment in the baihetan reservoir area (China) based on the time-series InSAR method," *Remote Sensing*, vol. 13, no. 16, p. 3213, 2021.
- [19] A. C. Mondini, F. Guzzetti, K.-T. Chang, O. Monserrat, T. R. Martha, and A. Manconi, "Landslide failures detection and mapping using Synthetic Aperture Radar: past, present and future," *Earth-Science Reviews*, vol. 216, p. 103574, 2021.
- [20] Z. Yang, Z. Li, J. Zhu, Y. Wang, and L. Wu, "Use of SAR/InSAR in mining deformation monitoring, parameter inversion, and forward predictions: a review," *IEEE Geoscience and Remote Sensing Magazine*, vol. 8, no. 1, pp. 71–90, 2020.
- [21] E. Bayramov, M. Buchroithner, and M. Kada, "Radar remote sensing to supplement pipeline surveillance programs through measurements of surface deformations and identification of geohazard risks," *Remote Sensing*, vol. 12, no. 23, p. 3934, 2020.
- [22] J. Galve, J. Pérez-Peña, J. Azañón et al., "Evaluation of the SBAS InSAR Service of the European space agency's geohazard exploitation platform (GEP)," *Remote Sensing*, vol. 9, no. 12, p. 1291, 2017.
- [23] L. Li, X. Yao, J. Yao, Z. Zhou, X. Feng, and X. Liu, "Analysis of deformation characteristics for a reservoir landslide before and after impoundment by multiple D-InSAR observations at Jinshajiang River, China," *Natural Hazards*, vol. 98, no. 2, pp. 719–733, 2019.
- [24] N. Richter and J.-L. Froger, "The role of interferometric synthetic aperture radar in detecting, mapping, monitoring, and modelling the volcanic activity of piton de la Fournaise, La réunion: a review," *Remote Sensing*, vol. 12, no. 6, p. 1019, 2020.
- [25] L. Solari, M. Del Soldato, F. Raspini et al., "Review of satellite interferometry for landslide detection in Italy," *Remote Sensing*, vol. 12, no. 8, p. 1351, 2020.
- [26] B. Osmanoglu, F. Sunar, S. Wdowski, and E. Cabral-Cano, "Time series analysis of InSAR data: methods and trends," *ISPRS Journal of Photogrammetry and Remote Sensing*, vol. 115, pp. 90–102, 2016.
- [27] L. Zhang, K. Dai, J. Deng et al., "Identifying potential landslides by stacking-InSAR in southwestern China and its performance comparison with SBAS-InSAR," *Remote Sensing*, vol. 13, no. 18, p. 3662, 2021.
- [28] J. Wasowski and F. Bovenga, "Investigating landslides and unstable slopes with satellite Multi Temporal Interferometry: current issues and future perspectives," *Engineering Geology*, vol. 174, pp. 103–138, 2014, <https://doi.org/10.1016/j.enggeo.2014.03.003>.
- [29] P. Berardino, G. Fornaro, R. Lanari, and E. Sansosti, "A new algorithm for surface deformation monitoring based on small baseline differential SAR interferograms," *IEEE Transactions on Geoscience and Remote Sensing*, vol. 40, no. 11, pp. 2375–2383, 2002.
- [30] S. Usai, "A least squares database approach for SAR interferometric data," *IEEE Transactions on Geoscience and Remote Sensing*, vol. 41, no. 4, pp. 753–760, 2003.
- [31] R. Lanari, F. Casu, M. Manzo et al., "An overview of the small Baseline subset algorithm: a DInSAR technique for surface deformation analysis," *Pure and Applied Geophysics*, vol. 164, no. 4, pp. 637–661, 2007.
- [32] A. Ferretti, C. Prati, and F. Rocca, "Nonlinear subsidence rate estimation using permanent scatterers in differential SAR interferometry," *IEEE Transactions on Geoscience and Remote Sensing*, vol. 38, no. 5, pp. 2202–2212, 2000.
- [33] R. Lanari, O. Mora, M. Manunta, J. J. Mallorqui, P. Berardino, and E. Sansosti, "A small-baseline approach for investigating deformations on full-resolution differential SAR interferograms," *IEEE Transactions on Geoscience and Remote Sensing*, vol. 42, no. 7, pp. 1377–1386, 2004.

- [34] X. Shi, L. Zhang, C. Zhou, M. Li, and M. Liao, "Retrieval of time series three-dimensional landslide surface displacements from multi-angular SAR observations," *Landslides*, vol. 15, no. 5, pp. 1015–1027, 2018.
- [35] S. Samsonov, A. Dille, O. Dewitte, F. Kervyn, and N. D'Oreye, "Satellite interferometry for mapping surface deformation time series in one, two and three dimensions: a new method illustrated on a slow-moving landslide," *Engineering Geology*, vol. 266, p. 105471, 2020.
- [36] C. Colesanti and J. Wasowski, "Investigating landslides with space-borne synthetic aperture radar (SAR) interferometry," *Engineering Geology*, vol. 88, no. 3-4, pp. 173–199, 2006.
- [37] L. Cascini, G. Fornaro, and D. Peduto, "Advanced low- and full-resolution DInSAR map generation for slow-moving landslide analysis at different scales," *Engineering Geology*, vol. 112, no. 1-4, pp. 29–42, 2010.
- [38] G. Herrera, F. Gutiérrez, J. C. García-Davalillo et al., "Multi-sensor advanced DInSAR monitoring of very slow landslides: the Tena Valley case study (Central Spanish Pyrenees)," *Remote Sensing of Environment*, vol. 128, pp. 31–43, 2013.
- [39] O. Hungr, S. Leroueil, and L. Picarelli, "The Varnes classification of landslide types, an update," *Landslides*, vol. 11, no. 2, pp. 167–194, 2014.
- [40] R. Schlögel, C. Doubre, J.-P. Malet, and F. Masson, "Landslide deformation monitoring with ALOS/PALSAR imagery: a D-InSAR geomorphological interpretation method," *Geomorphology*, vol. 231, pp. 314–330, 2015.
- [41] R. Schlögel, J.-P. Malet, C. Doubre, and T. Lebourg, "Structural control on the kinematics of the deep-seated La Clapière landslide revealed by L-band InSAR observations," *Landslides*, vol. 13, no. 5, pp. 1005–1018, 2016.
- [42] X. Yi, W. Feng, H. Bai, H. Shen, and H. Li, "Catastrophic landslide triggered by persistent rainfall in Sichuan, China: August 21, 2020, Zhonghaicun landslide," *Landslides*, vol. 18, no. 8, pp. 2907–2921, 2021.
- [43] H. Bai, W. Feng, X. Yi et al., "Group-occurring landslides and debris flows caused by the continuous heavy rainfall in June 2019 in mibei village, longchuan county, guangdong province, China," *Natural Hazards*, vol. 108, no. 3, pp. 3181–3201, 2021.
- [44] B. Bayer, A. Simoni, M. Mulas, A. Corsini, and D. Schmidt, "Deformation responses of slow moving landslides to seasonal rainfall in the Northern Apennines, measured by InSAR," *Geomorphology*, vol. 308, pp. 293–306, 2018.
- [45] M. Saito, "Forecasting time of slope failure by tertiary creep," *Proceedings of the 7th International Conference on Soil Mechanics and Foundation Engineering*, vol. 2, pp. 677–683, 1969.
- [46] N. Ju, J. Huang, C. He et al., "Landslide early warning, case studies from Southwest China," *Engineering Geology*, vol. 279, p. 105917, 2020.
- [47] Q. Xu, Y. P. Zeng, J. P. Qian, C. J. Wang, and C. J. He, "Study on a improved tangential angle and the corresponding landslide pre-warning criteria," *Geological Bulletin of China*, vol. 28, pp. 501–505, 2009.
- [48] Q. Xu, Y. Yuan, Y. Zeng, and R. Hack, "Some new pre-warning criteria for creep slope failure," *Science China Technological Sciences*, vol. 54, no. S1, pp. 210–220, 2011.
- [49] X. Fan, Q. Xu, J. Liu et al., "Successful early warning and emergency response of a disastrous rockslide in Guizhou province, China," *Landslides*, vol. 16, no. 12, pp. 2445–2457, 2019.
- [50] R. Huang, J. Huang, N. Ju, C. He, and W. Li, "WebGIS-based information management system for landslides triggered by Wenchuan earthquake," *Natural Hazards*, vol. 65, no. 3, pp. 1507–1517, 2013.
- [51] Q. Xu, D. Peng, S. Zhang et al., "Successful implementations of a real-time and intelligent early warning system for loess landslides on the Heifangtai terrace, China," *Engineering Geology*, vol. 278, p. 105817, 2020.
- [52] N.-p. Ju, J. Huang, R.-q. Huang, C.-y. He, and Y.-r. Li, "A Real-time monitoring and early warning system for landslides in Southwest China," *Journal of Mountain Science*, vol. 12, no. 5, pp. 1219–1228, 2015.
- [53] J. Huang, R. Huang, N. Ju, Q. Xu, and C. He, "3D WebGIS-based platform for debris flow early warning: a case study," *Engineering Geology*, vol. 197, pp. 57–66, 2015.
- [54] Z. Li, C. Song, and Y. Chen, "Application of satellite radar remote sensing to landslide detection and monitoring: challenges and solutions geomatics and," *Information Science of Wuhan University*, vol. 44, no. 7, pp. 967–979, 2019.
- [55] F. Ji, C. Liu, Y. Shi, W. Feng, and D. Wang, "Characteristics and parameters of bank collapse in coarse-grained-material reservoirs based on back analysis and long sequence monitoring," *Geomorphology*, vol. 333, pp. 92–104, 2019.

## Review Article

# Comprehensive Review of Community Seismic Resilience: Concept, Frameworks, and Case Studies

H'ng Chee Yin, Moustafa Moufid Kassem , and Fadzli Mohamed Nazri 

*School of Civil Engineering, Engineering Campus, Universiti Sains Malaysia, 14300 Nibong Tebal, Penang, Malaysia*

Correspondence should be addressed to Fadzli Mohamed Nazri; [cefmn@usm.my](mailto:cefmn@usm.my)

Received 6 January 2022; Revised 21 February 2022; Accepted 21 March 2022; Published 11 April 2022

Academic Editor: Alessandro Rasulo

Copyright © 2022 H'ng Chee Yin et al. This is an open access article distributed under the Creative Commons Attribution License, which permits unrestricted use, distribution, and reproduction in any medium, provided the original work is properly cited.

Seismic resilience is a concept to evaluate the postearthquake functionality of structures that significantly play a critical role in postearthquake rescue and recovery. Indeed, the community is made up of more than just buildings; it is also made up of other subsystems such as hospital and school facilities as well as roads, drainage systems, sewer systems, and electrical power transmission networks. In recent years, the concept of community resilience as a tool for disaster risk management has attracted substantial attention from all parties, such as governments, designers, decision-makers, and stakeholders. Community resilience can be assessed more effectively by using a multi-disciplinary approach that takes into account the community's uncertainties, as opposed to a single-criteria approach. The global community resilience model must be long-term validated and dependent on the most vulnerable and low-resilience portions of the community, according to a prior study. According to the review of the seismic resiliency studies performed in the recent decades, the frameworks for the quantification assessment of the community resilience are explained. Moreover, several case studies for community resilience and the application of different subsystems are reviewed and elaborated in this paper. Based on these resilience studies, the main challenges on the effectiveness of the resilience assessment are the availability and accessibility of the data, the financial resources, and the cooperation from all the parties.

## 1. Introduction

In the past centuries, many earthquakes that happened around the world were recorded in history. Recent major earthquakes such as the Sumatra Earthquake with a magnitude of 8.6 (also called as Indian Ocean earthquakes) which occurred in 2012 had reported 10 deaths and 12 injuries; Tōhoku Earthquake with a magnitude of 9.1 which occurred in 2011 had destroyed over one hundred thousand buildings in Japan, caused nuclear accidents and over ten thousand deaths were reported; Maule Earthquake with a magnitude of 8.8 (also known as Chile earthquake) which occurred in 2010 had damaged the port at Talcahuano and collapsed several buildings in many cities; and Valdivia Earthquake with a magnitude of 9.5 which occurred in 1960 was the most powerful earthquake ever recorded in the history. From the Earth's history, an earthquake will cause a lot of impacts to the communities such as the collapse of structures, casualties, economic loss, and other tragedies.

In the aspects of sustainable development of the society and communities, structural systems such as buildings, water supply plants, and power supply plants play key roles to achieve sustainability. Due to the difficulties and challenges of recovery and reconstruction of structural systems of the communities in postseismic events, the seismic performance, and the structural properties of the systems such as resiliency, redundancy, and robustness have raised the significant interests of the stakeholders, government, and designers.

Seismic resilience is a concept to evaluate the post-earthquake functionality of structures that significantly play a critical role in postearthquake rescue and recovery [1]. In the event of an earthquake, seismic resilience is the ability of a building to continue operating normally after the initial damage has been repaired [2]. Aside from that, seismic resilience is considered as an alternate method of dealing with the issue of functionality, which has been disregarded in earlier or existing seismic code developments [3]. Previous

seismic design codes such as British Standard have not taken the consideration of the seismic effects in the structure design process, thus, this may lead to the increase in the risk of the structures designed using the design codes without consideration of seismic effects when subjected to the earthquake events.

Multiple frameworks have been proposed and used in recent years to assess the seismic resilience of structures that have been built over the past century [4–7]. Some of the frameworks proposed by Cimellaro et al. [8] include a quantitative definition of resilience based on an analytical function that can be used to both technical and organizational concerns. Cimellaro et al. [9] has been created a complete model for quantifying the catastrophe resilience of a hospital system that incorporates both loss estimating and recovery models that can be used to critical facilities. Verucci et al. [10] proposed an evaluation of multi-disciplinary indicators for the seismic resilience of metropolitan areas that would be comparative and disaggregated. Besides, the transportation system, and the electric power supply system functionality is considered one of the most important critical infrastructures to have a seismic resilience in the community. Zhao and Sun [11] examined the impact of looped interdependences among Critical Infrastructure Systems (CISs) on their seismic resilience, by proposing an agent-based modeling (ABM) framework. In such a framework, the coupled Transportation System (TS) and Electric Power Supply System (EPSS) have been included. The developed framework is able to delineate the postshock recovery of the coupled TS-EPSS-Community. Similarly, for the functionality of road networks, water systems, electric power, and the resilience of the affected bridge damages and restoration, surrounded by urban areas [12–15].

Moreover, a framework for assessing the seismic resilience of urban hospitals based on fault tree analysis has been developed and tested (FTA) by Yu et al. [3]. Shang et al. [16] proposed a quantitative framework to assess the seismic resilience of the hospital systems which consists of four stages: the seismic hazard analysis, the fragility analysis, the seismic risk analysis, and lastly the calculation of the seismic resilience. Nevertheless, simple resilience evaluation metrics for the quantification and appraisal of resilience have been proposed by Yarveisy et al. [17] which are based on the concepts of dependability and maintainability, as well as the system modeling methodology, and are easy to implement. Moreover, measuring community resilience is an essential work for municipal policy makers towards a unified approach [18]. He et al. [19] conducted a comprehensive assessment on community resilience adapted to the fire following earthquakes (FFE) scenarios. Yet, in terms of computational approaches, these frameworks still need to adequately address community interdependencies and consider the impact of decision-making in modeling. Melendez et al. [20], Koliou et al. [21], and Marasco et al. [22] provided studies and reviews in terms of computational methods to model community resilience, progress and challenges to have a resilience community, and an integration platform to assess seismic resilience in communities by focusing on the last few decades.

In this study, several methods and framework for assessing and quantifying the seismic resilience index of structures are described in this review paper. The assessment of building structures is examined by utilizing the functional curves, and obtaining the direct and indirect loss functions, as well as the time recovery functions. However, a community not only consists of buildings but also consists of other subsystems such as bridges, road and drainage systems, sewerage systems, power transmission systems, and other fundamental subsystems. Therefore, the applications of the seismic resilience index approach in a community system which had been performed by previous studies are also introduced.

## 2. Concept of Seismic Resilience Index in Post Seismic Event

*2.1. Community Resilience in Disaster Situation.* The perception of community resilience has gained extraordinary attention in recent decades since the community is very first responder toward any disaster. The researcher that first introduced the term “resilience” in ecology has defined it as “a measure of the persistence of systems and of their ability to absorb change and disturbance and still maintain the same relationship between the population or state variable” [23]. However, the term “resilience” is now more specifically defined as “the contribution in the establishment of the capacity or ability to rebuild back effectively after a tragedy” [24]. Natural catastrophes such as earthquakes, floods, fires, landslides, and Hurricane winds have resulted in both social and physical consequences, with civilian deaths and damage to buildings and infrastructures being among the most severe.

There are four levels of achievement proposed for the community resilience which is illustrated in Figure 1, namely (1) Better bounce back refers to a community that can absorb disturbances and function better than before the crisis; (2) The ability to bounce back refers to a community’s ability to return to predisaster state, (3) It is tough to recover but worse than before, referring to the community’s reduced ability to recover, and (4) collapse which refers to the community that incapable to function after faced the disaster [25–27].

*2.2. Community Resilience Framework.* In the early decades, the resilience of the communities is proposed and evaluated qualitatively and conceptually which has less real and effective. The community resilience index can be acted as a baseline in monitoring the changes of the community over time through a set of indicators in several aspects such as socio-demographic, economic, environmental, organizational, infrastructures, and cultural [28]. Furthermore, the concept of the resiliency of the communities is seldom used as a tool in seismic risk management and mitigation due to the limited political and specific planning activities [29]. Consequently, a reconstruction process is deficient and economically ineffective due to the lack of accurate and appropriate mitigation strategies.

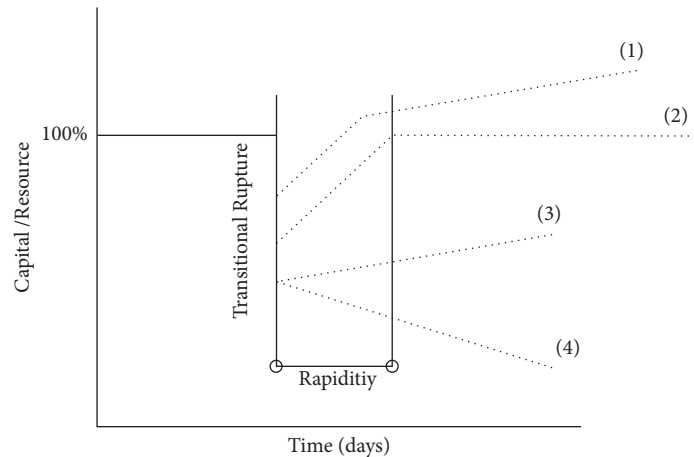


FIGURE 1: Resilience concept in the schematic.

Recently, several classic frameworks which effective and useful for single systems of the whole community have been introduced to assess the resilience of communities. For example, a framework that links community resilience to the seismic performance of buildings had been proposed by You et al. [30]. The framework is schematized as Figure 2.

The probabilistic seismic performance assessment (PSPA) in this framework is targeted to investigate the correlated seismic performance of buildings. The seismic performance is depicted in terms of the collapse capacity curve, the recovery time function, and also the cumulative distribution function of the repair cost. These seismic performance characteristics are used as inputs to the framework's network-based recovery model. Refers to Figure 2, by adapting the seismic performance parameters, the estimated community loss due to the seismic excitation can be evaluated through the network-based recovery simulation. Thus, the resilience index of the community can be calculated by performing the postseismic simulations. However, the existing frameworks require modification and improvements to predict the whole community while accounting for the influence of the interaction between the subsystems of the communities.

Didier et al. [31] developed an innovative compositional demand catastrophe resilience assessment framework for critical facilities in civil infrastructure systems, which was designated Re-CoDeS (Resilience-Compositional Demand/Supply). The framework is comprised of three major components, namely, the demand layers, the supply layers, and the manage system service model. In the framework, the resiliency of the civil infrastructure system was evaluated through two major dimensions: the resilience at a component level which represents the amount of supply of the particular components, and the resilience at a system level which occurs when the service demand exceeds the available supply at any component of a system. Moreover, the resilience time of the components and the systems were assessed. The authors highlighted that the framework was able to be used for variety of recovery priorities as well as the evaluation of recovery rates in a variety of community system configurations. However, the examination of the

consequences of interconnection and dependency of the investigated civil infrastructure system with other systems is one of the most difficult challenging tasks for the frameworks.

Maroufi and Borhani [28] proposed a framework to evaluate the community seismic resilience in subcity districts of Mashhad, Iran. The framework consists of six resilience dimensions and each of the dimensions employed a set of measurable indicators. The resilience dimensions defined in the framework include the economic dimension, the socio-demographic dimension, the environmental features, the organizational dimension, the physical or infrastructure dimensions, and the cultural or community competence dimension. A total of 23 indicators were selected for the framework as summarized in Table 1. The authors highlighted that a more comprehensive assessment of the seismic resilience for a community could be achieved by taking into consideration of these fundamental dimensions of a community into the framework. However, one of the limitations of this framework was the availability of the data required for the indicators.

Furthermore, Svetina et al. [32] had performed an analysis of pandemic risk management within a resilience framework on the two 2020 Zagreb earthquakes and the COVID-19 pandemic. The occurrence of the pandemic was considered into the concept of seismic resilience of the community in the framework. In the study, the testing intensity after the earthquake was observed to present the seismic resiliency of the community within an ongoing pandemic. As the earthquake destroyed the hospital systems, the natural responses of hospitals to the seismic excitations subsequently influenced the disease transmission rate due to the increased socializing of citizens after the seismic events. The results of the study indirectly highlight the importance of the improvement of the resiliency of a community, especially during a pandemic.

Using a hybrid information fusion framework, Chen and Zhang [33] proposed a method for evaluating the earthquake resilience of regional areas at an early stage. The framework was proposed based on the basic probability assignments (BPAs) and the Dempster-Shafer (D-S) evidence theory

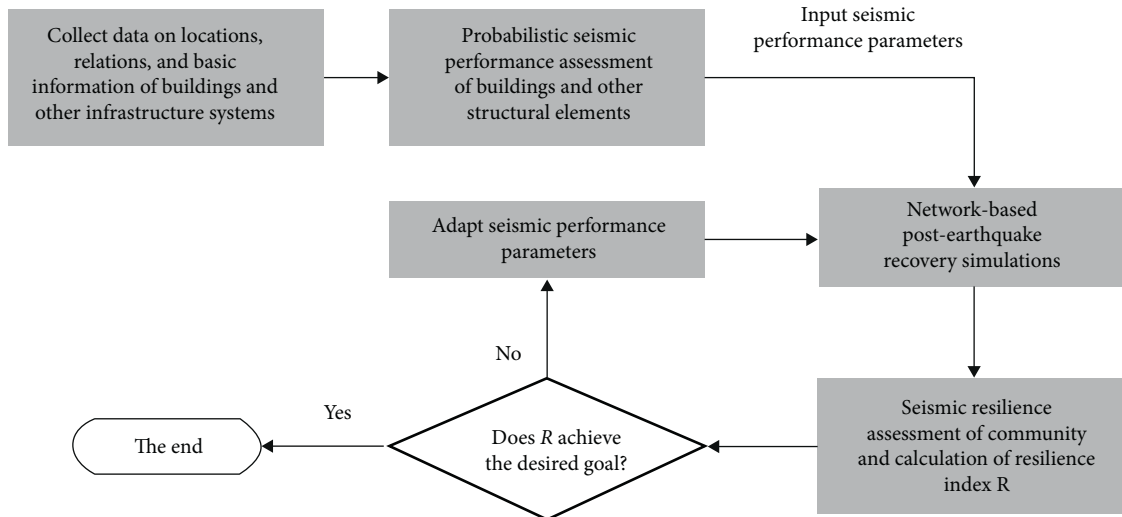


FIGURE 2: The flowchart of the framework [30].

TABLE 1: Summary of community seismic resilience indicators for each dimension and the main attributes of the dimensions. [28].

Category/dimension	Indicators
Economic (occupation, housing capital, financial capital, economic diversity)	(1) Percentage of employed population (2) Percentage of home ownership (3) Number of construction licenses issued by the district municipality in the last fiscal year (4) Ratio of large to small business
Socio-demographic (population exposure to hazard, education level, age, special needs)	(1) Number of populations per 1,000 square meters (2) Percentage of the population within high-risk zones (3) Percentage of people with higher education level (4) Percentage of populations aged between 6 and 65 (5) Percentage of people with physical or mental disability
Environmental (exposure, vegetation, vulnerability of place, land slope)	(1) Percentage of the areas with a slope of more than 4% in the neighborhood (2) Natural or green areas per capita
Organization/Managerial (managerial resources, managerial process, managerial qualifications)	(1) Municipal budget line of each district for crisis management and prevention (2) Number of emergency management maneuvers (3) Number of neighborhood emergency response volunteers per 1,000 people
Physical/Infrastructures (physical capital, infrastructural capital, physical exposure to hazard)	(1) Percentage of the deteriorated urban fabric (2) Number of healthcare centres per 1,000 residents (3) Number of emergency shelters per 1,000 people (4) Percentage of critical infrastructures located inside high-risk areas
Cultural/Community competence (social trust, religious ties, cultural features, community participation, public satisfaction)	(1) Inhabitants' perception of social trust (2) Number of mosques and other religious-based per 1,000 residents (3) Number of phone calls to public relation centre of each subcity district per 1,000 residents (4) Inhabitants' satisfaction toward life (5) Percentage of satisfaction from local councils

which is capable of integrating evidence from various sources with epistemic uncertainty. The proposed framework was employed in the regional areas of Nepal with the consideration of three dimensions, namely geological dimension, building dimension, and social dimension. Table 2

summarize the indicators of each dimension adopted in the framework. The authors highlighted that the proposed framework can be applied to other earthquake-prone areas and suggested involving infrastructures in the framework to achieve a holistic digital twin framework. Other than the

TABLE 2: Summarizing the indicators for each dimension [33].

Dimensions	Indicators
Geological	(1) Acceleration with a likelihood of reaching 10 percent in 50 years is predicted to occur (2) Distance to nearby active faults (3) Shear-wave velocity down to a depth of 30 m
Building	(1) Type of foundation for a building (2) Type of internal wall of a building (3) Building roof type
Social	(1) Density of the inhabitants (2) The proportion of the population aged between 15 and 64 (3) The proportion of people over the age of 25 who have high school or a higher degree

aforementioned frameworks, Table 3 summarizes the frameworks proposed and introduced in previous studies. Those frameworks applied the quantitative data to measure the seismic resiliency of the communities at different geographical scales.

**2.3. Seismic Resilience Improvement in Communities.** Due to the ineffective and weakness of the conceptual framework in assessing the resilience of a community, a new seismic communities resilience model is introduced to improve and quantify the resilience of the communities probabilistically. This new model which was proposed by Vona et al. [29] is aimed to define the mitigation strategies based on the prioritization of the retrofit interventions to increase the resiliency of the communities and to address the economic resources on the low seismically resilient areas and building types. In the way of explanation, the resiliency of a community is considered all the essential independent systems of the community, for instance, residential, transportation, urban systems, utility systems, and other systems. The main roles of these systems in emergency management and the prioritization of the functionality strategies shall be identified to recover the functionality of the community in the essential dimensions such as socio-economic, managerial, and technical. However, the functionality of the residential buildings is still depleted when other systems are ready to provide services.

Therefore, in the new model, the relationship between community resilience and the residential building's performance is emphasized and defined. Subsequently, the new probabilistic methodology was proposed by the authors for the housing system based on the seismic reconstruction process data which will provide a more accurate numerical analysis. The new methodology considered the vulnerability of the building types, the economic resources, and the damage levels which influenced the recovery time in the analysis. Figure 3 illustrated the new proposed qualitative trend of a community's functionality function in postseismic events.

The conceptual model emphasizes the reliance of the overall resilience on the residential system as a source of information. Following the explanation provided by Vona et al. [29], with reference to Figure 3, the grey regions represent the fundamental subsystems of the community such as hospitals and highways as well as water, sewerage

and electric power supply, whose functionality should be prioritized. The blue area, on the other hand, corresponds to the residential system. The authors distinguish three major components of the new model: a rapid return to functionality in the short term; a pseudohorizontal step that is linked to the planning and mitigation of preliminary activities for the reconstruction process; and an increasing branch that is based on the distribution of financial funding and the corresponding repair activities. In this sense, the resiliency of a community may be expressed as the ability of a community to maintain a specific level of performance while also restoring the state that existed prior to the seismic event.

Consequently, Vona et al. [29] mentioned that the total control time and the final functionality level of the whole community including the housing systems are not only influenced by the seismic effect and also by the decision phase and implementation phase of the reconstruction process and the availability of the financial resources from the parties and based on the damage levels which refer as the L'Aquila reconstruction process.

### 3. Seismic Resilience Index Approach

**3.1. Functionality Curve.** The fundamental purpose of resilience is to evaluate the functionality of structures after an earthquake event. Based on the damage level and the functionality of a structure postseismic event, the recovery period for a structure to rehabilitate its structure purpose or function which safe for end-users can also be evaluated. The functionality of a structure is commonly defined and expressed in the terms of direct and indirect economic losses due to earthquakes, direct and indirect casualties losses, structure recovery time, and business or function interruption time. Moreover, the level of functionality of the structures is defined depending on the types of structures. For instance, the level of functionality of a hospital or a health care centre is basically defined based on whether the hospital or health care centre is able and safe to provide the emergency medical services whereas the level of functionality of residential buildings can be defined based on whether the buildings are safe for residents to occupied for a particular serving period.

The functionality curves are developed and utilized for evaluating the seismic resilience of the structures. Generally, the functionality curves can be evaluated with the use of

TABLE 3: Summarization of community seismic resilience frameworks.

Author	Framework	Main dimensions	Methodology of framework development
Sauti et al. [34]	Vulnerability index	Exposure module, resilience module, capacity module	Literature review, theoretical assumptions
Peacock et al. [35]	Community disaster resilience index (CDRI)	Social, economic, physical, human capital	Literature review
Bastaminia et al. [36]	Disaster resilience	Social, institutional, environmental and physical, economic	Literature review
Rus et al. [37]	Disaster resilience	Building, infrastructure, community, open space	Literature review
Alshehri et al. [38]	Framework of community resilience to disaster	Social, economic, physical, and environmental issues, governance, health and well-being, and information and communication technologies are all covered in this research.	Three-round delphi study
Alshehri et al. [39]	Community resilience disaster framework (CRDSA)	Social, physical and environmental, economic, health and wellbeing, governance, information and communication	Delphi expert survey and analytic hierarchy process (AHP)
Asadzadeh et al. [40]	Disaster resilience index	Urban land usage and dependent population, socio-cultural capability, life quality, open space, social capital, emergency infrastructure, economic structure	Literature review, factor analysis (FA), analytic network process (ANP)
Cutter et al. [41]	Community resilience	Social, housing or infrastructural, community capital, economic, institutional, environmental	Literature review
Ainuddin et al. [42]	Community resilience index (CRI)	Physical, social, economic, institutional	Literature review
Burton [43]	Disaster resilience	Social, economic, institutional, infrastructure, community, and environmental systems resilience.	Literature review, factor analysis (FA), reliability/item analysis (Cronbach's alpha), multidimensional scaling (MDS), multivariate analysis procedure
Verrucci et al. [10]	Multi-disciplinary framework for seismic resilience	Planning with land-use, built-in resilience, continued functioning or redundancy of critical service and infrastructure, distribution of resources, social cohesion	Literature review, system diagram
Sherrieb et al. [44]	Community resilience index	Economic development, social capital	Literature review
Cutter et al. [45]	Disaster resilience of place (DROP) model	Ecological, social, economic, institutional, infrastructure, community competence	Literature review

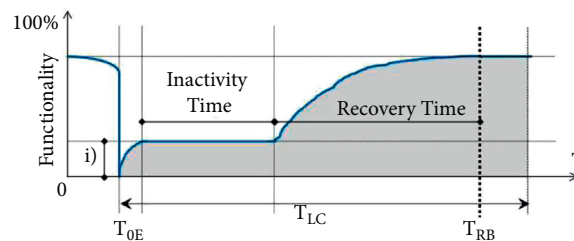


FIGURE 3: Conceptual seismic resilience measurement of whole communities [29].

fragility curves or vulnerability curves. The functionality curve which also known as the resilience curve defines the functionality of a structure in percentage over the control time. The functionality curve is developed by using the functionality function which is a nondimensional quality system function. The functionality of a structure can be evaluated using several indicators such as direct loss, indirect loss, and recovery time. Figure 4 shows the schematic of the functionality curve which is commonly used by previous studies [3, 8, 16, 46, 47].

The functionality function was first introduced by Cimellaro et al. [8]. The functionality function is also a nonstationary stochastic process and it is usually indicated as  $Q(t)$ . According to Cimellaro et al. [8] and by referring to the schematic of the functionality curves shown in Figure 4, the seismic resilience functionality function is expressed as in (1). The values of the quantities in the function are less than 1 since the desired full functionality is 100% functionality which is indicated as 1.0 in the function.



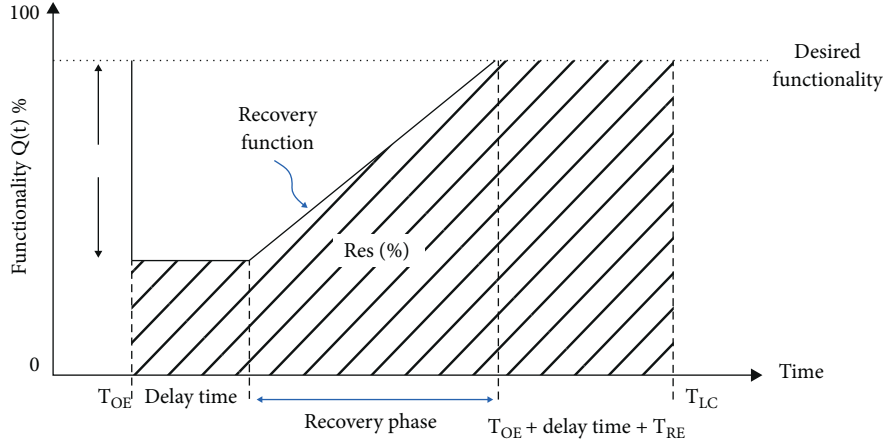


FIGURE 4: Schematic of functionality curve that commonly adopted [8].

$$Q(t) = [1 - L(I, T_{RE})] \cdot \{H(t - t_{OE}) - H(t - [T_{OE} + T_{RE}])\} \cdot f_{REC}(t, T_{OE}, T_{RE}), \quad (1)$$

where,  $L(I, T_{RE})$  is the loss function,  $f_{REC}(t, T_{OE}, T_{RE})$  is the recovery function,  $T_{RE}$  is the recovery time after an event,  $T_{OE}$  is the time occurred event with intensity, and  $H(t)$  is the Heaviside step function.

**3.2. Loss Function: Direct and Indirect Losses.** In general, the loss function is the combination of direct loss and indirect loss and is expressed as (2) [8]:

$$L(I, T_{RE}) = L_D + (\alpha_1 \cdot L_I), \quad (2)$$

where  $L_D$  and  $L_I$  represent the direct losses and indirect losses, respectively, whereas  $\alpha_1$  is the weight factor that depends on the significance of the structures for the society and the influence of the structure on the other system.

Direct losses due to earthquakes refer directly into quantifiable losses which occur instantly during a disaster, for instance, the number of fatalities or injuries and replacement or repair cost of damaged structures. Moreover, for a building, the direct economic losses also refer to the physical structure, and nonstructural impact caused by the disaster or seismic event. Thus, the direct economic losses are defined as the ratio of building repairing costs to the replacement costs. As mentioned previously, the functionality curves can be developed using fragility curves or vulnerability curves. By using the fragility curves to develop the functionality curves, the direct loss of the structural or nonstructural member  $k$  is calculated using (3) [8]:

$$L_{DE,K} = \sum_{j=1}^n \left[ \frac{C_{S,j}}{I_s} \prod_{i=1}^{t_i} \frac{1 + \delta_i}{1 + r_i} \right] \cdot P_j \{U_{i=1}^n (R_i \geq r_{lim,i}) | I\}, \quad (3)$$

where,  $P_j$  is the conditional probability of exceeding a performance limit state  $j$ , when an extreme event of intensity  $I$  occurs,  $C_{S,j}$  is the building repairing costs related to a  $j$  damage state,  $I_s$  is the replacement building costs related to a  $j$  damage state,  $r_i$  is the annual discount rate applied for the

time interval in years between initial investment and the extreme event, and  $\delta_i$  is the annual depreciation rates.

Thus, the direct economic losses for a structure are computed using the weight average expression as shown in (4) [48]:

$$L_{DE}(I) = \frac{\sum_{k=1}^n W_k \cdot L_{DE,K}}{N}, \quad (4)$$

where  $W_k$  is the weight factor representing the importance of each structural and nonstructural element in a structure or building and  $N$  is the total number of structural and nonstructural elements in a structure or building. Furthermore, the term  $\sum_{j=1}^n P_j \{U_{i=1}^n (R_i \geq r_{lim,i}) | I\}$  in (4) is derived from the fragility analysis.

Direct casualties losses are defined as the ratio of the number of people injured inside the building to the total number of occupants inside the building. The direct casualties losses are calculated using (5) [48]:

$$L_{DC}(I) = \frac{N_{in}}{N_{tot}}, \quad (5)$$

where  $N_{in}$  is the number of people injured in the fatal and nonfatal manner depends on several factors such as the time of the day of the seismic event, the age of the population, and the number of available hospitals. Meanwhile,  $N_{tot}$  is the total number of occupants in the building.

Other than fragility curves, the vulnerability curves can also be used to assess the loss function by using the modified expression as shown in (6) [8]:

$$L_{DE,K} = \left[ \frac{C_S}{I_s} \cdot \prod_{i=1}^{t_i} \frac{1 + \delta_i}{1 + r_i} \right] \cdot \text{Damage}(\%), \quad (6)$$

where  $C_S$  is the building repair costs,  $I_s$  is the replacement building costs,  $\delta_i$  is the annual depreciations rate,  $r_i$  is the annual discount rate applied for the time interval in years between initial investment and the extreme event, the

Damage (%) is the percentage obtained from the vulnerability curve.

Both the fragility curves and vulnerability curves can be used to assess the loss function. However, the loss function can be calculated quickly by using vulnerability curves which are sufficient to calculate the percentage of estimated damage of a structure. Moreover, throughout the study performed by Samadian et al. [46] the authors concluded that the results of resiliency extracted from the vulnerability curves are more ideal than those extracted from the fragility curves. Whereas Kassem et al. [49] provided the basic steps that's involved in developing the seismic resilience index for a particular building from vulnerability and fragility curves as shown in Figure 5.

Indeed, the depreciation of a building is the process of methodically deducting the documented cost of the building from its current value until it hits zero or is no longer worth salvaging the building [51]. The annual rate of depreciation varies depending on the type of building being depreciated. The annual rate of depreciation for various types of buildings is summarized in Table 4. Furthermore, the yearly rate of depreciation can be calculated as the reciprocal of the asset's useful life.

In the construction industry, the discount rate is defined as the percentage rate required to calculate the present value of a future cash flow, moreover, it is also a factor reflecting the time value of money that is used to convert the cash flows occurring at different times to a common time base [52]. In the other words, a discount rate is used for bringing future costs to a comparable time base. The annual discount rate can be calculated using (7) where is the number of years [51].

$$\text{Annual discount rate, } r = \left( \frac{\text{future cash flow}}{\text{present value of asset}} \right). \quad (7)$$

Indirect losses due to the seismic excitation refer to the subsequent results of the initial destruction such as the business interruption losses and revenue. Similar to direct losses, the indirect losses also involved two contributions: indirect economic losses and indirect casualties losses. The indirect economic losses are time-dependent and difficult to quantify due to different expression forms. They can be expressed in the terms of business interruptions, rental income losses, or revenue expenses. Furthermore, indirect casualties losses are defined as the ratio of the number of injured people outside the building to the total population of the area. Thus, the indirect casualties losses can be calculated using (8) [48]:

$$L_{IC}(I) = \frac{N_{in}}{N_{tot}}, \quad (8)$$

where  $N_{in}$  is the number of people injured outside the building and  $N_{tot}$  is the total population of the affected area.

Finally, as suggested by Cimellaro et al. the total direct losses computed by direct economic losses and direct casualties losses can be calculated by using :

$$L_D = (L_{DE})^{\alpha_{DE}} \cdot (1 + \alpha_{DC} L_{DC}), \quad (9)$$

where  $\alpha_{DE}$  is the weighting factor related to the construction losses in economic terms while  $\alpha_{DC}$  is the weighting factor related to the nature of occupancy. Next, the total indirect losses which are computed by indirect economic losses and indirect casualties losses can be calculated by using :

$$L_I = (L_{IE})^{\alpha_{IE}} \cdot (1 + \alpha_{IC} L_{IC}), \quad (10)$$

where  $\alpha_{IE}$  is the weighting factor related to the construction losses in business interruption while  $\alpha_{IC}$  is the weighting factor related to the nature of occupancy.

**3.3. Time Recovery Function.** The recovery time is defined as the period necessary to restore the functionality of a structure and infrastructure system to the desired level that can operate or provide a similar or better service than the initial function [53]. The time recovery function is used to express the complicated recovery process that is influenced by several variables such as time and spatial dimensions. The recovery functions that are used to establish the functionality curves are classified into three types: linear recovery function, trigonometry recovery function, and exponential recovery function. Figure 6 show the examples of linear recovery functionality curves, trigonometry recovery functionality curves, and exponential recovery functionality curves.

Different kind of recovery functions is adopted depending on the system and the social response. Equations (11)–(13) show the linear recovery function, trigonometry recover function, and exponential recovery function, respectively.

$$f_{REC}(t, T_{OE}, T_{REC}) = 1 - \left( \frac{1 - T_{OE}}{T_{REC}} \right), \quad (11)$$

$$f_{REC}(t) = 0.5 \cdot \left\{ 1 + \cos \left[ \frac{\pi(t - t_{OE})}{T_{REC}} \right] \right\}, \quad (12)$$

$$f_{REC}(t) = \exp \left[ -(t - t_{OE}) \frac{\ln(200)}{T_{REC}} \right], \quad (13)$$

where  $T_{OE}$  is the time of occurrence event with intensity I,  $T_{REC}$  is the recovery time after an event,  $t_{OE}$  is the time of earthquake occurred.

As explained by Cimellaro et al. the linear recovery function is generally adopted when there is no information of the social response. However, the trigonometry recovery function is adopted where the society response to a drastic event is initially slow whereas the exponential recovery function is used where the society response to an extreme event is fast driven by an initial inflow of resources and thus the rapidity of the recovery process decreases.

**3.4. Resilience Index Evaluation.** As defined by the International Strategy for Disaster Reduction (2004) [54], resilience is "the ability of a system, community, or society that is potentially exposed to hazards to adapt by resisting or modifying in order to establish and sustain an adequate level

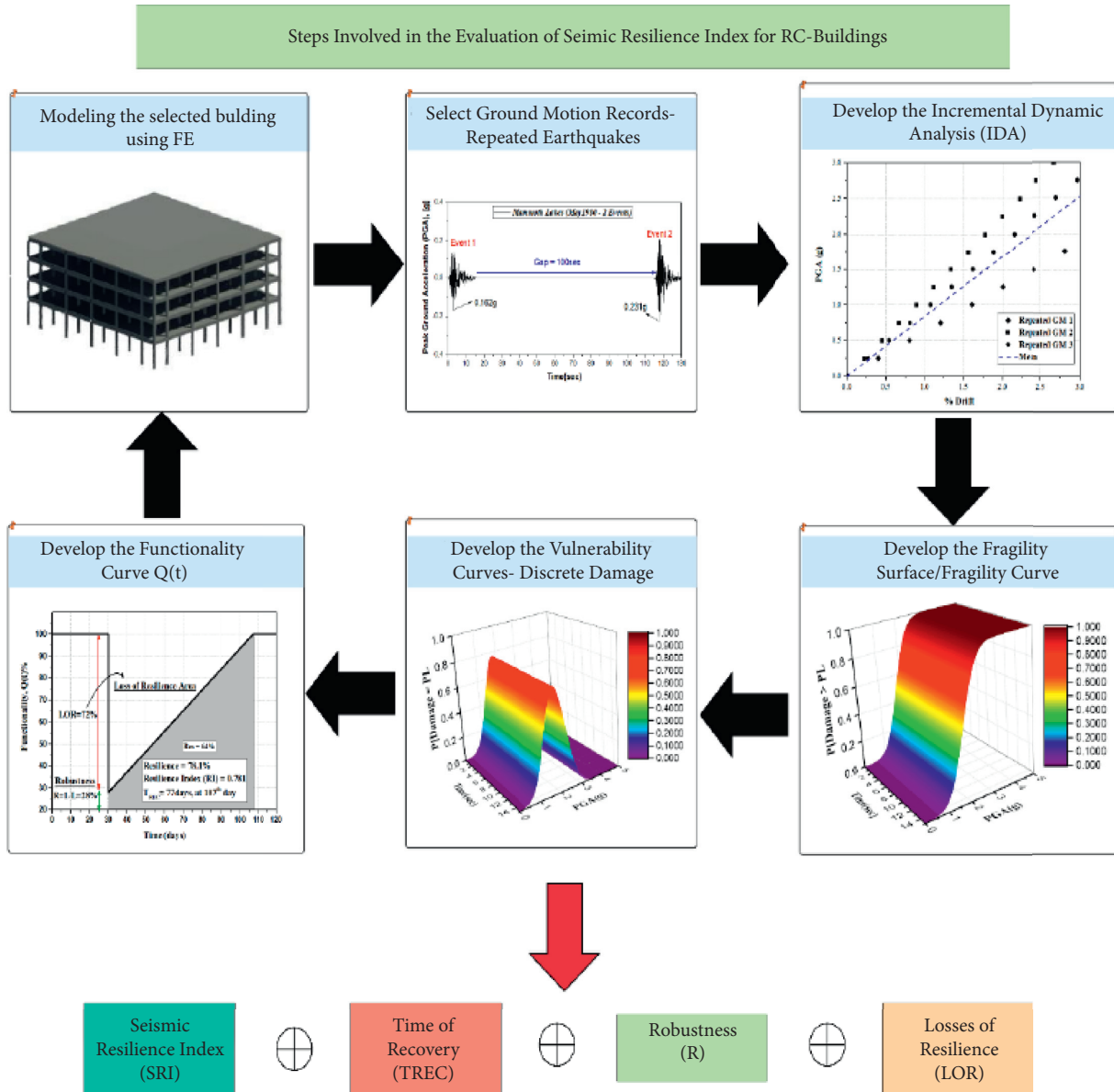


FIGURE 5: Framework steps for developing seismic resilience index (SRI) [50].

TABLE 4: Quantities or rates of depreciation for various types of buildings [51].

Rate of depreciation (%)	Type of building
5	Buildings that are utilized exclusively for residential purposes, with the exception of boarding houses and hotels, are referred to as residential premises. It is only when more than 66.66 percent of a building's built-up floor space is used for residential purposes that the structure is regarded to be used for residential purposes.
10	All other types of buildings do not belong into the category of residential buildings
100	Generally speaking, buildings are utilized for the installation of machinery and plants that are integral to the water treatment system and the water supply project. Furthermore, timber constructions and tin shelters are only intended to be temporary structures.

of reliability and functionality, which is determined by the degree to which a social system is capable of managing itself to raise this ability of lessons from previous disasters for better future preservation and to improve risk management.”

Seismic resilience assessment can be qualitative or quantitative. According to Verrucci et al. [10], the selection of indicators is one of the critical factors in evaluating seismic resilience and has shown that qualitative assessment models tend to be more comprehensive than quantitative

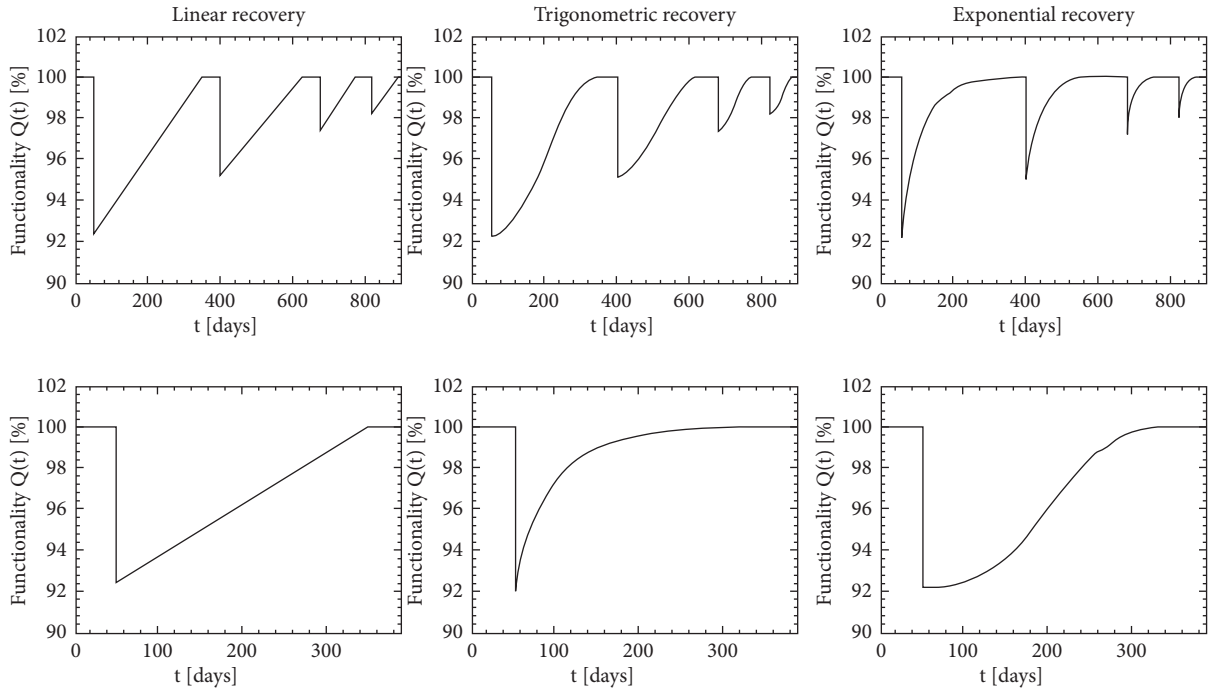


FIGURE 6: Examples of three types of functionality curves [53].

assessment models. The authors had reviewed previous models available in the literature and summarized a candidate set of indicators which categorized into five topical macro-areas. The topical macro-areas included planning and land-use, built-in resilience, continued functioning or redundancy, resources, and social cohesion.

Generally, the seismic resilience index is determined from the functionality curves with the aids of the fragility curves and/or the vulnerability curves. Although, it is important to note that, while the recovery progress is dependent on a variety of resources such as manpower and materials, the approach for quantifying the seismic resilience index is commonly written as (14) [8]:

$$R = \frac{1}{T_{LC}} \int_{t_{OE}}^{t_{OE}+T_{LC}} Q(t) dt, \quad (14)$$

where,  $Q(t)$  is the dimensionless percentile which is defined from the functional curve,  $T_{LC}$  is the control time interested which is the investigated time interval after an earthquake (usually considered to be 50 years for residential buildings) or the longest recovery time under the considered seismic intensities, and  $R$  is the resilience index.

### 3.5. Resilience Quantification Methods for Single Building.

The concept of resilience is being implemented and defined according to several different perspectives which essentially explains the capability of a structure or a system to recover its functionality after an unexpected natural disaster such as earthquake, flood, fire, and landslides. From an engineering perspective, resilience is typically characterized as the ability of human societies to endure external disasters and to recover from such disasters [55]. In recent decades, several

studies proposed frameworks that focused on the quantitative measures of disaster resilience after the different types of natural disasters. Engineering-related facilities and social-economic resilience were among the categories of catastrophe resilience that had gotten the most attention, particularly when it came to seismic resilience of structures. From in civil engineering perspective, the quantification of resilience consists of four parts: first, the assessment of resilience for an urban system which consists of physical elements (individual buildings, transportation systems, piping system, and other urban lifeline facilities) and non-physical elements (social, economic, and ecosystems); second, the quantifiable indicators of the resilience in infrastructures and disturbed networks; third, measures of building sub-system resiliency; and forth is the analysis of resilience limit state [56].

The resilience of a single building is described as the capacity of the building to endure shocks from external threats while also having the ability to recover its functionality after being damaged or destroyed. Bruneau et al. [57] studied structural resilience by identifying four primary characteristics. These characteristics are known as the 4R attributes: robustness, redundancy, rapidity, and resourcefulness. According to Lu et al. [56] there are two main existing methodologies for evaluating the resilience of single buildings: risk and resistance analysis of structures; and rating of structural resilience.

The first existing methodology is the risk and resistance analysis of a building by taking into account various hazards. The design phase and information for a hazard, such as the risk and design loadings, is often obtained based on the environmental conditions, the types of structural elements, the building materials, and the structure's geographic

information system (GIS) data. As a result, the design information is used to determine the structural resilience of the construction. According to this methodology, US Green Building Council had proposed the Leadership in Energy and Environmental Design (LEED) assessment and planning for resilience which a hazard assessment for the project site is a prerequisite of this assessment [58]. Besides, the Insurance Council of Australia (ICA) developed the Building Resilience Rating Tool (BRRT) based on this methodology [59]. The BRRT rates the resilience of the building by identifying the potential hazards the building is exposed to. Thus, an evaluation of the vulnerability based on the materials and the structural types of the building is performed.

The second method currently in use is the grading of structural resilience under a given hazard scenario. When a hazard is identified, the indicators relating to the 4R, as well as other properties of the structure, can be quantified, allowing the structure's resistance to be measured in terms of grades or star ratings. The Building Rating System proposed by the United States Resiliency Council (USRC) and the Resilience-Based Earthquake Design Initiative (REDi) Rating System proposed by [62] is the typical examples of this methodology. According to the USRC building rating system, the evaluation approach employed is based on either ASCE 41-06 (ASCE, 2007) or FEMA P-58; in contrast, the REDi building rating system utilized the methodology of FEMA P-58 without modification [56].

**3.6. Recent Seismic Resilience Applications.** In both civil and earthquake engineering, the assessment of seismic resilience is majorly applied to residential and commercial buildings. The types of buildings commonly chosen by the researchers have reinforced concrete buildings and steel frame structures. Moreover, masonry buildings and timber structures have also become the target of researchers in investigating the seismic performance of the buildings in the cities. The seismic resilience assessments for these major types of structures which had been performed and proposed in the earlier research are discussed in this review paper.

Asadi et al., [61] proposed a multi-criteria decision-making framework that is divided into three main modules: the System Concept and Criteria (SCC) module; the Resilience, Sustainability, and Energy Analysis (RSEA) module; and the Multi-Criteria Decision Making (MCDM) module. For the purposes of this study, the framework was applied to two different sets of archetypal reinforced concrete shear wall structures. To evaluate the seismic performance of the case studies, the following analysis was performed: incremental dynamic analysis, fragility analysis, loss estimation, recovery analysis, and resilience analysis. The authors highlighted that the key factors such as repair or construction cost, recovery time, injuries, fatalities, embodied energy, and operational energy shall be integrated to achieve a holistic framework. Furthermore, the findings of the study revealed that the proposed framework was more appropriate for use in assessing various design alternatives for low-rise to midrise residential or commercial structures.

Using structural reliability approaches, Sangaki et al. [62] created a probabilistic integrated framework that contained a collection of probabilistic models. The proposed framework was applied to a standard concrete framed structure in order to determine the seismic resilience index of the structure and, as a result, to develop a resilience curve. The methodology of the framework includes non-linear response history analysis, fragility analysis, functionality analysis, recovery analysis, and resilience analysis. With the proposed framework, the consideration of the impacts of an unlimited number of doubts has revealed as the most significant benefit of the proposed framework. Furthermore, it was asserted that the proposed framework was able to supply the capability of determining the probabilistic model of the resilience index as well as the development of resilience curves, both of which may be used in the resilience-based design (RBD) approach.

Sardari et al. [47] had evaluated the seismic resilience of a steel frame school building in Iran and examined the accuracy of the seismic index results by comparing two common methodologies of resiliency assessment and the resiliency parameters. The research study concentrated on the resiliency and reliability analysis of the steel frame buildings, therefore, the analysis involved included the non-linear time history analysis, the incremental dynamic analysis, the fragility analysis, the vulnerability analysis, loss estimation, and recovery analysis. Moreover, in order to evaluate the reliability of the frame structures, the First Order Reliability Method (FORM) and sampling method were adopted. In addition, several retrofitting techniques were proposed in the study, and the analysis of the efficiency of the retrofitting techniques was performed and compared to provide an additional reference for future study. The authors point out that retrieving resiliency measures via the use of vulnerability curves produces more truthful and reasonable findings than extracting resiliency indicators through the use of resilience curves.

Hosseinzadeh and Galal [63] had performed the seismic resilience assessment of reinforced masonry shear wall buildings with masonry boundary elements. When developing a numerical model for the research project, the fiber-based modeling approach was adopted. The accuracy of the numerical model was then verified by comparing the results of experimental and numerical hysteresis loops at different drift levels. The non-linear time history analysis was done on two sets of 44 far-field and near-field ground motion records. The procedures involved in the study include the incremental dynamic analysis (IDA), fragility analysis, development of variation of interstory drift, the development of story shear response plot, and the evaluation of seismic resilience. The authors compared the results of building with and without masonry boundary elements for both far-field records and near-field records. The outcomes of the assessment show that by utilizing the masonry boundary elements, the resiliency of the reinforced masonry shear wall building had effectively reduced the structural and nonstructural losses of the buildings and resulted in improving the resiliency of the buildings.

Avila-Haro et al. [64] had conducted a probabilistic seismic assessment of a high-rise unreinforced masonry building in Spain. The methodology of the framework includes modal and pushover analysis, non-linear static analysis, and fragility analysis. Thus, the damage index of the case study was derived from the fragility curves developed. However, the study also performed a comparison of the analysis result of buildings with and without a probabilistic approach. As an outcome of the probabilistic approach, the variability in the mechanical properties of the masonry had generated significant uncertainties in the seismic response of the case study which led to unexpected damage, compared to that of the approach without consideration of probabilistic nature.

Furthermore, the previous studies which concentrated on the assessment for these four major structural types: reinforced concrete frame structures, steel frame structures, masonry structures, and timber structures in the past few years had been summarized in Table 5.

#### 4. Seismic Resilience of Community Infrastructures

In past decades, frameworks used to evaluate the seismic resiliency of other subsystems of a community such as hospitals, schools, bridges, and infrastructures have been proposed and introduced. The frameworks for the subsystems proposed and obtained in different countries in previous studies are discussed in the following section.

*4.1. Frameworks for Hospital Systems.* Hospital systems are recognized as critical systems in a community that plays an important role in disaster rescues. However, hospitals were inevitable to encounter the earthquake and lost their functionalities due to the impact of seismic events. Therefore, several studies had been conducted previously to propose an effective framework in evaluating the seismic resilience of the hospital systems. In summary, the frameworks adopted by previous studies have a major similarity in methodology except for the application of the indicators and parameters.

Hassan and Mahmoud [81] had proposed a framework for a six-stories high hospital which is assumed to be located in Memphis, Tennessee, United States. In the study, the functionality of the hospital comprised both quantity and quality portions. The quantity portion is indicated by three major components, namely space availability (including the accessibility, supportive infrastructures, and working space), personnel availability (staff and professionals), and supplies availability. The aforementioned components were the essential components that were required to ensure the hospital's operation. Meanwhile, the quality portion of the functionality of the hospital was represented by the satisfaction of the patients toward the provided medical services. Finally, the overall functionality of the hospital was evaluated by combining both the quantity and quality functionalities. Thus, the resiliency of the hospital was assessed graphically using the functionality curve plotted.

Yu et al. [3] provided a framework for assessing the seismic resilience of reinforced concrete frame urban hospitals in China that are designed in accordance with the Chinese seismic design code (GB 20011-2010). The framework is proposed by considering the importance of the critical roles of hospital systems; therefore, the seismic resiliency of the hospitals is indicated based on the damage states of the structural system, the number of casualties, the availabilities of the medical services, and also the economic losses. In the study, the fault tree analysis (FTA) is adopted to investigate the effect of the interdependencies such as damage of the nonstructural elements on the functionality of the medical equipment. The results claimed that the assessment results be more realistic with the application of fault tree analysis (FTA). There were three types of repair strategies used in the recovery phase of the study, namely parallel repair strategy, serial repair strategy, and REDi method. The results show that the recovery period required by the case study varies with the selection of repair strategy.

Shang et al. [16] also introduced a quantitative framework to assess the seismic resilience of the hospital systems in China that was designed based on the Chinese seismic design code (GB 20011-2010). The framework considered the seven essential sub-systems of the hospital, namely structural system, electrical system, mechanical system, water supply, and drainage system, medical system, egress system, and architectural system. In addition, each of the subsystems was rated and scaled depending on their importance toward the hospital systems and their contribution toward the degree of damage of the hospital systems. Throughout the framework, an idealized repair sequence for the subsystems was suggested by the authors to recover the emergency functionality of the hospital systems.

Niazi et al. [85] had performed an assessment of the seismic resilience index of the hospital in Tehran, Iran. Due to the case study itself being able to supply the water and electricity for the hospital in emergency states, therefore, the impact of the disturbances in water and power supply were neglected in the study. The major parameter indicating the functionality of the hospital was the patient waiting window which was influenced by the availability of the hospital staff and the medical services. The admission rate of patients entering the emergency department was evaluated through a demand model to represent the patient waiting time. The functionality of the hospital was expressed as the ratio of the total number of the functional emergency ward to all units that provide proper services without a reduction in performance. Thus, the resiliency of the hospital was evaluated through the functionality curve.

*4.2. Frameworks for Bridges.* Bridges are a crucial component of the transportation network in a community from decades ago. The exposure of the bridges to a natural disaster will give a significant impact on social losses and economic losses. Therefore, the seismic performance of the aging bridges has taken the attention of the communities.

Andrić and Lu [86] had evaluated the seismic resiliency of the bridge located in California, United States. The fuzzy

TABLE 5: Seismic resilience case studies applications on different building typology.

Author	Methodology	Type of structure
Bu et al. [65]	Incremental dynamic analysis, fragility analysis	Steel frames with steel slit shear walls
Chen and Bai [66]	Nonlinear static analysis, nonlinear dynamic analysis, damage index assessment	Buckling-restrained braced reinforced concrete frames
Estrella et al. [67]	Nonlinear static and dynamic analysis	Timber buildings with wood-frame shear walls
Hassan et al. [68]	Nonlinear response history analysis, incremental dynamic analysis, fragility analysis, vulnerability analysis, resilience assessment	Steel-reinforced concrete (SRC) composite column buildings
Hejazi and Jalaeefar [69]	Incremental dynamic analysis, fragility analysis, risk analysis, resilience analysis	Infilled special steel moment-resisting frames
Hosseinzadeh and Galal [70]	Nonlinear dynamic analysis, fragility analysis, loss estimation, recovery analysis, resilience analysis, Monte Carlo simulation, sensitivity analysis	Reinforced masonry shear wall system with boundary elements
Jiménez et al. [71]	Vulnerability index method (VIM)	Hybrid timber-masonry buildings
Mohammadi et al. [72]	Incremental dynamic analysis, fragility analysis	Infilled steel frame structures
Vona et al. [73]	Fragility analysis, vulnerability analysis, resilience analysis	Reinforced concrete buildings
Yun and Chao [74]	Experimental test, development of hysteresis curve and skeleton curve, residual deformation, energy dissipation, validation of earthquake resilience	Prefabricated self-centering steel frame
Zhu et al. [75]	Nonlinear static pushover analysis, fragility analysis, risk assessment	Steel moment-resisting frames with self-centering viscous-hysteretic devices
Anwar and Dong [76]	Fragility analysis, recovery analysis, functionality analysis, resilience analysis	Retrofitted reinforced concrete buildings
Anwar et al. [77]	Hazard analysis, structural analysis, damage analysis, seismic risk assessment, seismic sustainability, and resilience assessment	Reinforced concrete structures
Fang et al. [78]	Nonlinear response history analysis, vulnerability analysis, resilience analysis	Self-centering steel frames with SMA-viscoelastic hybrid braces
Giordano et al. [79]	Vulnerability analysis	Unreinforced masonry schools
Xu et al. [80]	Loss estimation, fragility analysis, functionality analysis, resilience analysis	Six-story reinforced concrete frame building

framework used in the study comprises the seismic hazard analysis, bridge fragility analysis, and seismic resilience assessment. The residual functionality of the bridge was assessed by investigating the relationship between the bridge damage and the functionality based on the data collected (expert's opinion and expert's subjective judgment of the expected level of traffic capacity). Thus, the recovery period required was calculated by mathematical expressions for the membership functions. A similar framework was also obtained by Dong and Frangopol [84] to evaluate the seismic risk and resilience of highway bridges in California.

Huang and Huang [85] had introduced a resilience framework for the reinforced concrete bridges which exposed to the earthquake. The framework comprises of physical vulnerability model, restoration model, and resilience analysis. The physical vulnerability model was used to obtain the damage probabilities of the bridge piers whereas the restoration model was used to evaluate the functionality of the aging bridges. In the study, the seismic performance of the bridge piers was evaluated by considering the impact of the corrosion of main reinforcements, the cracking of the concrete covers, and the degradation of the bond strength between reinforcements and concrete.

Sun et al. [86] had examined the seismic resiliency of the road network across the Luchon Valley, France by proposing an agent-based modeling framework. In the study, the critical bridges of the road networks were

chosen to represent the resilience of the road network under earthquake scenarios. The damage level of each of the single bridges was determined by the fragility analysis. Thus, the long-term functional recovery of the bridges was driven by three agents which have different attributes of the traveling speed and efficiency. Finally, the seismic resilience of the whole road network was indicated by the integration of the total functional bridges to the recovery time required.

*4.3. Frameworks for Water Supply Systems.* Water is one of the indispensable natural elements to all livings. The failure of water supply not only impacts the residents and critical consumers but also impacts other infrastructures and services. Therefore, the functionality of the water supply systems in the communities in the aftermath of natural disasters such as earthquakes had attracted the attention of the government and the community.

Balaei et al. [87] had examined the robustness of the water system in Pukerua Bay which is located in Wellington, New Zealand. The damage degree of the buried pipelines of the water system due to the slope failure and the fault rupture was measured. The robustness of the water system was analyzed as a ratio of the product of the robustness and the length of functional subsectors to the total length of the subsectors.

Liu et al. [88] had performed an assessment of seismic resilience for water distribution systems in Mianzhu, China. The performance levels of the water distribution systems in the daily operation state were indicated depending on the degree of satisfaction of consumers which is indicated by consumer nodes toward the water served. In the study, the satisfaction degree of the consumers was obtained through the flow analysis method which considered the time-dependent water demand. Moreover, the study was focused on the recovery of the buried pipes which play the most critical part in a water distribution system. Therefore, the study analyzed the degree of damage of the buried pipes by proposing a pipe recovery model which included three important aspects such as joint seismic reliability, pipe seismic reliability, and pipe damage number. The recovery period required evaluated by the framework can be influenced by three critical factors, namely recovery resources, recovery method, and recovery sequence.

**4.4. Frameworks for Electric Power Systems.** In the modern era, most of the infrastructures, structures, and human beings rely on the electric power distribution networks to provide and support the daily essential services to the whole community. Power distribution systems play a crucial role to generate and transmit the electrical to the consumers at various locations. Consequently, the functionality of the power distribution system to support daily services and activities had become the focus of the government and the community.

Fotouhi et al. [89] had introduced a model applied to the coupled electric power-traffic system in Minneapolis, Minnesota, United States, to quantify the resilience of the coupled system. In the study, the components considered will contribute the damage toward the whole system including the substations, the traffic signals, the roadway links, and the transmission lines. Thus, the damage levels of the aforementioned components under the scenarios were indicated in two scales: functional and damaged. During the repair phases, the recovery degree of the networks was varying with the levels of budgets and the repair options adopted. As a result, the resilience levels of the networks under restricted repair and recovery opportunities were evaluated and presented.

Cho et al. [90] had conducted an experimental study to investigate the seismic resilience of the enhancement applied for the piping system of a nuclear power plant in Fukushima, Japan. The enhancement tool used in the experiment was the steel coil damper which claimed to improve the seismic safety of the piping systems by accommodating the thermal transformation of the piping supports. The seismic resiliency of the enhanced piping systems was assessed throughout the dynamic response analysis.

Cardoni et al. [91] proposed a methodology to evaluate the resilience of the power distribution networks in Italy. The Similarities Design Method and the Density Design Method are the two most important components of this technique. The resiliency of the power distribution networks was expressed as a ratio of the return period of the seismic event

to the number of consumers with no power supply. In the study, a new indicator called the Power Resilience Index (PRI) was established, which was defined as the integration of transformer restoration rate, network robustness, and the presence of alternate functional lines. According to the scientists and the authors, PRI was capable of measuring the early resilience conditions of the networks. Meanwhile, the recovery time for the substations of the networks was determined by either taking into account solely the transformers' recovery time or by using data that was readily available.

**4.5. Compilation of Infrastructure Resilience Framework Applications.** Other than the aforementioned frameworks for those sub-systems, there are still many frameworks being proposed and introduced for the sub-systems of a community in the past centuries in different countries. Table 6 summarizes the recent frameworks proposed.

## 5. Summary

Earthquake excitation is considered as a complex loading to a structure. Fundamentally, the seismic performance of the structures can be evaluated by the seismic resilience index, the damage index, and the seismic vulnerability index. Each of the assessments has its advantages and drawbacks. Some may be time-consuming with precise results, and some may be simple and speed with limitations in the interpretation of results. It is essential to select the appropriate assessment by considering the availability of the collection of the data required by each assessment and the availability of the equipment required if any.

One of the essential goals of the evaluation of the seismic resilience index of the structures is to introduce or propose the repair strategy or the retrofitting techniques. With the aids of the functionality curves, the repair strategy or the retrofitting techniques can be proposed or introduced effectively based on the recovery time and the resilience assessment results. Apart from the implementation of the design codes which consider the seismic effect in the design such as Eurocode 8, various novel building damage evaluation techniques and retrofitting tactics offer a variety of options that can be employed to improve or accelerate the recovery process's functionality. Compared to constructing a new building with a similar purpose or service, retrofitting a damaged structure is often more cost-effective. Retrofitting process is a general term that consists of various treatments such as preservation, rehabilitation, restoration, and reconstruction [110].

Retrofitting process with respect to seismic consideration is usually applied on the existing buildings which potentially subjected to the seismic excitation to extend their serviceability, to improve the sustainability of the buildings, and to maintain or improve the seismic safety of the building. Hence, selecting the appropriate retrofitting method must be determined depending on the project or structure objectives. Commonly, the decision-makers, designers, or stakeholders prefer to choose the retrofitting



TABLE 6: Seismic resilience frameworks for sub-systems of the community.

Author	Framework	Methodology	System	Location
Ferrario et al. [92]	Seismic risk and resilience	Seismic hazard analysis, functionality analysis, recovery analysis, analysis of topological measures	Electrical power networks	Chile
Iannacone et al. [93]	Seismic resilience	Reliability analysis, functionality analysis, recovery analysis, resilience analysis	Potable water infrastructure	USA
Ahmadi et al. [94]	Resilience index	Adaptability analysis, absorbability analysis, recovery analysis	Energy systems	—
Cardoni et al. [95]	Seismic vulnerability and resilience	Seismic analysis, damage assessment, vulnerability analysis, resilience assessment	Urban telecommunication network	—
ChienKuo et al. [96]	Seismic resilience	Reliability analysis, resilience analysis	Bridge (retrofitted through reinforced concrete jacking)	Taiwan
Katayama et al. [49]	Seismic diversity and robustness	Fault tree analysis (FTA), inter-period correlation	Nuclear power plants	Japan
Ramezani et al. [97]	Damage index and seismic resilience	Ductility analysis, damage analysis, resilience analysis	Stabilized or un-stabilized rammed earth walls	—
Xiao et al. [98]	Seismic resilience	Fragility analysis, Monte Carlo simulation, recovery analysis	Power-natural gas lifeline networks	—
Zhai et al. [99]	Physical-organizational method for functionality assessment	Structural analysis, damage analysis, availability analysis, the arrival of patients, functionality analysis	Hospital	China
Zong et al. [100]	Seismic resilience index	Three-stages resilience enhancement (pre-earthquake network enhancement, postearthquake pipeline pressure tests, postearthquake pipeline repairs), resilience analysis	Gas distribution networks	China
Capacci and Biondini [101]	Seismic resilience index	Fragility analysis, functionality analysis, recovery analysis	Bridge networks	—
Chen and Li [102]	Seismic response	Seismic analysis (shear deformation, drift, displacement, and overturning Stability)	Tall pier bridges (retrofitted with lead rubber bearings and rocking foundation)	China
Eghbali et al. [103]	Seismic resilience index	Retrofitting operations monitoring, functionality analysis, recovery analysis	Schools	Iran
Koc et al. [104]	Comprehensive resilience assessment (CRAFT)	Hazard characterization, damage assessment, transportation system analysis	Transportation systems	Loss angeles
Li et al. [105]	Seismic resilience index	Fragility analysis, functionality analysis, recovery analysis	Electrical substation system	China
Rezaei Ranjbar and Naderpour [106]	Seismic resilience index	IDA, fragility analysis, vulnerability analysis, loss estimation, functionality analysis, resilience analysis	Hospital	Loss angeles
Kilani et al. [107]	Seismic risk and resilience	Seismic hazard analysis, fragility analysis, recovery analysis	Roadway networks	—
Tong et al. [108]	Seismic resilience	Experimental analysis, numerical modeling	Prestressed precast segmental bridge piers reinforced with high-strength bar	—
Hassan et al. [68]	Interdependent functionality reduction framework	Fragility analysis, direct losses, functionality analysis	Hospital	USA
Nan and Sansavini [109]	Resilience of interdependent infrastructures	Development of an integrated resilience metric, multi-layer hybrid modeling approach (screening analysis, individual model development, model interaction)	Infrastructures (electronic performance support systems)	Switzerland
Cimellaro et al. [9]	Disaster resilience	Loss function, simplified recovery function models, mechanical analogy, fragility analysis	Hospital	Southern California

strategy with the maximum resiliency and the minimum cost required. To investigate the effectiveness and also the appropriate degree of the selected retrofitting technique, it is suggested to perform the seismic resilience assessment by modeling the retrofitted structures. In order to preserve economic activities, the retrofitting plan must achieve three primary objectives: reduction of seismic damage, reduction of recovery time, and reduction or annulment of downtime or disruption of business operations [73]. As a result, the best and most appropriate retrofitting strategy has the lowest possibility of causing a complete collapse damage condition and the highest possibility of causing a fully operational state.

Other than the resiliency of a single structure or building, the concept of community resilience can be adopted as a useful tool for decision-makers in disaster or risk management and mitigation strategies planning. In order to improve the effectiveness of the evaluation of the resilience of communities, the resiliency of each subsystem of a community with consideration of their uncertainty is defined and considered in multi-disciplinary and multi-criteria methodologies. In addition, Vona et al. [29] highlighted that a global community resilience model must be long-term validated and contingent on the most vulnerable and low resilient parts of the community. Furthermore, compared to previously existing approaches that evaluate resilience based on both the technical and economical characteristics, the new resilience model also evaluated the community resilience based on the organizational and social aspects.

Based on the considerations taken in the development of the new resilience model, the repair time and final functionality level are influenced by the entire seismic damages and losses. Not only that, but the reconstruction procedure as well as the accessible economic ability are also taken into consideration. In addition, the approval process for funding and financial support applications takes a significant amount of time. Thus, considering the period for approval of financial supports into the reconstruction process will improve the accuracy and the resiliency of the community. [108].

## Conflicts of Interest

The authors declare that they have no conflicts of interest.

## References

- [1] G. Tsionis, "Seismic resilience: concept, metrics and integration with other hazards," *Joint Research Centre, Publications Office of the European Union, Luxembourg*, vol. 10, Article ID 713724, 2014.
- [2] Z. Shamsoddini Motlagh, M. Raissi Dehkordi, M. Eghbali, and D. Samadian, "Evaluation of seismic resilience index for typical RC school buildings considering carbonate corrosion effects," *International Journal of Disaster Risk Reduction*, vol. 46, Article ID 101511, 2020.
- [3] P. Yu, W. Wen, D. Ji, C. Zhai, and L. Xie, "A framework to assess the seismic resilience of urban hospitals," *Advances in Civil Engineering*, vol. 2019, pp. 1–11, 2019.
- [4] O. Kammouh, P. Gardoni, and G. P. Cimellaro, "Probabilistic framework to evaluate the resilience of engineering systems using Bayesian and dynamic Bayesian networks," *Reliability Engineering & System Safety*, vol. 198, Article ID 106813, 2020.
- [5] R. Guidotti, P. Gardoni, and N. Rosenheim, "Integration of physical infrastructure and social systems in communities' reliability and resilience analysis," *Reliability Engineering & System Safety*, vol. 185, pp. 476–492, 2019.
- [6] L. Sun, B. Stojadinovic, and G. Sansavini, "Resilience Evaluation Framework for Integrated Civil Infrastructure-Community Systems under Seismic Hazard," *Journal of Infrastructure Systems*, vol. 25, no. 2, Article ID 04019016, 2019.
- [7] E. J. Sutley, J. W. van de Lindt, and L. Peek, "Community-level framework for seismic resilience. I: coupling socio-economic characteristics and engineering building systems," *Natural Hazards Review*, vol. 18, no. 3, Article ID 04016014, 2017.
- [8] G. P. Cimellaro, A. M. Reinhorn, and M. Bruneau, "Framework for analytical quantification of disaster resilience," *Engineering Structures*, vol. 32, no. 11, pp. 3639–3649, 2010.
- [9] G. P. Cimellaro, A. M. Reinhorn, and M. Bruneau, "Seismic resilience of a hospital system," *Structure and Infrastructure Engineering*, vol. 6, no. 1-2, pp. 127–144, 2010.
- [10] E. Verrucci, T. Rossetto, J. Twigg, and B. Adams, "Multi-disciplinary indicators for evaluating the seismic resilience of urban areas," in *Proceedings of the 15th World Conference Earthquake Engineering*, Verrucci, Enrica, 2012.
- [11] T. Zhao and L. Sun, "Seismic resilience assessment of critical infrastructure-community systems considering looped interdependences," *International Journal of Disaster Risk Reduction*, vol. 59, Article ID 102246, 2021.
- [12] A. Rasulo, A. Pelle, B. Briseghella, and C. Nuti, "A resilience-based model for the seismic assessment of the functionality of road networks affected by bridge damage and restoration," *Infrastructures*, vol. 6, no. 8, p. 112, 2021.
- [13] C. Chen, L. Xu, D. Zhao, T. Xu, and P. Lei, "A new model for describing the urban resilience considering adaptability, resistance and recovery," *Safety Science*, vol. 128, Article ID 104756, 2020.
- [14] C. Nuti, A. Rasulo, and I. Vanzi, "Seismic safety of network structures and infrastructures," *Structure and Infrastructure Engineering*, vol. 6, no. 1-2, pp. 95–110, 2010.
- [15] B. Liu, S. Han, H. Gong, Z. Zhou, and D. Zhang, "Disaster resilience assessment based on the spatial and temporal aggregation effects of earthquake-induced hazards," *Environmental Science and Pollution Research*, vol. 27, no. 23, pp. 29055–29067, 2020.
- [16] Q. Shang, T. Wang, and J. Li, "A quantitative framework to evaluate the seismic resilience of hospital systems," *Journal of Earthquake Engineering*, pp. 1–25, 2020.
- [17] R. Yarveisy, C. Gao, and F. Khan, "A simple yet robust resilience assessment metrics," *Reliability Engineering & System Safety*, vol. 197, Article ID 106810, 2020.
- [18] P. Bocchini, D. M. Frangopol, T. Ummenhofer, and T. Zinke, "Resilience and sustainability of civil infrastructure: toward a unified approach," *Journal of Infrastructure Systems*, vol. 20, no. 2, Article ID 04014004, 2014.
- [19] Z. He, H. Chen, H. Yan, Y. Yin, Q. Qiu, and T. Wang, "Scenario-based comprehensive assessment for community resilience adapted to fire following an earthquake, implementing the analytic network process and preference

- ranking organization method for enriched evaluation II techniques,” *Buildings*, vol. 11, no. 11, p. 523, 2021.
- [20] A. Melendez, D. Caballero-Russi, M. Gutierrez Soto, and L. F. Giraldo, “Computational models of community resilience,” *Natural Hazards*, vol. 111, no. 2, pp. 1–32, 2021.
- [21] M. Koliou, J. W. van de Lindt, T. P. McAllister, B. R. Ellingwood, M. Dillard, and H. Cutler, “State of the research in community resilience: progress and challenges,” *Sustainable and resilient infrastructure*, vol. 5, no. 3, pp. 131–151, 2020.
- [22] S. Marasco, A. Cardoni, A. Zamani Noori, O. Kammouh, M. Domaneschi, and G. P. Cimellaro, “Integrated platform to assess seismic resilience at the community level,” *Sustainable Cities and Society*, vol. 64, Article ID 102506, 2021.
- [23] C. S. Holling, “Resilience and Stability of Ecological Systems,” *Annual Review of Ecology and Systematics*, vol. 4, no. 1, pp. 1–23, 1973.
- [24] N. O. Chong, K. H. Kamarudin, and S. N. Abd Wahid, “Framework considerations for community resilient towards disaster in Malaysia,” *Procedia Engineering*, vol. 212, pp. 165–172, 2018.
- [25] G. Wilson, *Community Resilience and Environmental Transitions*, Routledge, London, 2012.
- [26] F. Berkes and H. Ross, “Community resilience: toward an integrated approach,” *Society & Natural Resources*, vol. 26, no. 1, pp. 5–20, 2013.
- [27] H. Boon, “Investigation rural community communication for flood and bushfire preparedness,” *Australian Journal of Emergency Management*, vol. 29, no. 4, pp. 17–25, 2014.
- [28] H. Maroufi and M. Borhani, “A measurement of community seismic resilience in sub-city districts of Mashhad, Iran,” *Journal of Environmental Planning and Management*, vol. 65, no. 4, pp. 675–702, 2021.
- [29] M. Vona, M. Mastroberti, L. Mitidieri, and S. Tataranna, “New resilience model of communities based on numerical evaluation and observed post seismic reconstruction process,” *International Journal of Disaster Risk Reduction*, vol. 28, pp. 602–609, 2018.
- [30] T. You, W. Wang, and Y. Chen, “A framework to link community long-term resilience goals to seismic performance of individual buildings using network-based recovery modeling method,” *Soil Dynamics and Earthquake Engineering*, vol. 147, Article ID 106788, 2021.
- [31] M. Didier, M. Broccardo, S. Esposito, and B. Stojadinovic, “A compositional demand/supply framework to quantify the resilience of civil infrastructure systems (Re-CoDeS),” *Sustainable and Resilient Infrastructure*, vol. 3, no. 2, pp. 86–102, 2018.
- [32] L. Svetina, A. Kosec, M. Curkovic, and A. Nola Iskra, “A case study of complex disasters within the resilience framework in Zagreb, Croatia: two earthquakes in one pandemic,” *Environmental Research*, vol. 204, Article ID 112079, 2022.
- [33] W. Chen and L. Zhang, “Resilience assessment of regional areas against earthquakes using multi-source information fusion,” *Reliability Engineering & System Safety*, vol. 215, Article ID 107833, 2021.
- [34] N. S. Sauti, M. E. Daud, M. Kaamin, and S. Sahat, “GIS spatial modelling for seismic risk assessment based on exposure, resilience, and capacity indicators to seismic hazard: a case study of Pahang, Malaysia,” *Geomatics, Natural Hazards and Risk*, vol. 12, no. 1, pp. 1948–1972, 2021.
- [35] W. G. Peacock, S. D. Brody, W. A. Seitz, W. J. Merrell, A. Vedlitz, and S. Zahran, “Advancing resilience of coastal localities: developing, implementing, and sustaining the use of coastal resilience indicators: a final report,” *Hazard Reduction and Recovery Center*, pp. 1–148, 2010.
- [36] A. Bastaminia, M. Safaeepour, Y. Tazesh, M. R. Rezaei, M. H. Saraei, and M. Dastoorpoor, “Assessing the capabilities of resilience against earthquake in the city of Yasuj, Iran,” *Environmental Hazards*, vol. 17, no. 4, pp. 310–330, 2018.
- [37] K. Rus, V. Kilar, and D. Koren, “Resilience assessment of complex urban systems to natural disasters: a new literature review,” *International Journal of Disaster Risk Reduction*, vol. 31, pp. 311–330, 2018.
- [38] S. A. Alshehri, Y. Rezgui, and H. Li, “Delphi-based consensus study into a framework of community resilience to disaster,” *Natural Hazards*, vol. 75, no. 3, pp. 2221–2245, 2015.
- [39] S. A. Alshehri, Y. Rezgui, and H. Li, “Disaster community resilience assessment method: a consensus-based Delphi and AHP approach,” *Natural Hazards*, vol. 78, no. 1, pp. 395–416, 2015.
- [40] A. Asadzadeh, T. Kötter, and E. Zebardast, “An augmented approach for measurement of disaster resilience using connective factor analysis and analytic network process (F’ANP) model,” *International Journal of Disaster Risk Reduction*, vol. 14, pp. 504–518, 2015.
- [41] S. L. Cutter, K. D. Ash, and C. T. Emrich, “The geographies of community disaster resilience,” *Global Environmental Change*, vol. 29, pp. 65–77, 2014.
- [42] S. Ainuddin and J. K. Routray, “Community resilience framework for an earthquake prone area in Baluchistan,” *International Journal of Disaster Risk Reduction*, vol. 2, pp. 25–36, 2012.
- [43] C. G. Burton, *The Development of Metrics for Community Resilience to Natural Disasters*, 2012.
- [44] K. Sherrieb, F. H. Norris, and S. Galea, “Measuring capacities for community resilience,” *Social Indicators Research*, vol. 99, no. 2, pp. 227–247, 2010.
- [45] S. L. Cutter, L. Barnes, M. Berry et al., “A place-based model for understanding community resilience to natural disasters,” *Global Environmental Change*, vol. 18, no. 4, pp. 598–606, 2008.
- [46] D. Samadian, M. Ghafory-Ashtiany, H. Naderpour, and M. Eghbali, “Seismic resilience evaluation based on vulnerability curves for existing and retrofitted typical RC school buildings,” *Soil Dynamics and Earthquake Engineering*, vol. 127, Article ID 105844, 2019.
- [47] F. Sardari, M. Raissi Dehkordi, M. Eghbali, and D. Samadian, “Practical seismic retrofit strategy based on reliability and resiliency analysis for typical existing steel school buildings in Iran,” *International Journal of Disaster Risk Reduction*, vol. 51, Article ID 101890, 2020.
- [48] G. P. Cimellaro, A. Reinhorn, and M. Bruneau, “Seismic resilience of a health care facility,” in *Proceedings of the 2005 ANCEP Annual Meeting, Session III, November 10–13, Jeju, Korea, November 2005*.
- [49] Y. Katayama, Y. Ohtori, T. Sakai, H. Muta, and T. Annaka, “Evaluating the seismic diversity and robustness of nuclear power plants,” *Journal of Nuclear Science and Technology*, vol. 58, no. 9, pp. 970–983, 2021.
- [50] M. M. Kassem, F. Mohamed Nazri, and A. M. El-Maissi, “Evaluation of Seismic Resilience of RC-buildings Subjected to Repeated Earthquake Using Resilient Index and Fragility Surface Functions,” in *Proceedings of the 8th International Conference on Computational Methods in Structural Dynamics and Earthquake Engineering (COMPdyn 2015)*, Athens, Greece, June 2021.

- [51] M. Thakur, *Depreciation of Building*, <https://www.wallstreetmojo.com/depreciation-of-building/>, 2020.
- [52] *inDiscount Rate in the Construction Industry*, [https://www.designingbuildings.co.uk/wiki/Discount\\_rate\\_in\\_the\\_construction\\_industry](https://www.designingbuildings.co.uk/wiki/Discount_rate_in_the_construction_industry), 2021.
- [53] A. Caverzan and G. Solomos, *Review on Resilience in Literature and Standards for Critical Built-Infrastructure*, EC JRC, Ispra, Italy, 2014.
- [54] D. R. C. Asian, *Living with Risk. A Global Review of Disaster Reduction initiatives. Preliminary Version*, United Nations, Geneva, Switzerland, 2002, <https://www.undrr.org/publication/living-risk-global-review-disaster-reduction-initiatives>.
- [55] A. Bozza, D. Asprone, and F. Fabbrocino, "Urban resilience: a civil engineering perspective," *Sustainability*, vol. 9, no. 1, p. 103, 2017.
- [56] X. Lu, W. Liao, D. Fang et al., "Quantification of disaster resilience in civil engineering: a review," *Journal of Safety Science and Resilience*, vol. 1, no. 1, pp. 19–30, 2020.
- [57] M. Bruneau, S. E. Chang, R. T. Eguchi et al., "A Framework to Quantitatively Assess and Enhance the Seismic Resilience of Communities," *Earthquake Spectra*, vol. 19, no. 4, pp. 733–752, 2003.
- [58] U. S. Green Building Council, "Assessment and Planning for Resilience. From US Green Building," 2021, <https://www.usgbc.org/credits/assessmentresilience?view=language>.
- [59] "Insurance Council of Australia. Building Resilience Rating Tool (BRRT)," 2021, <https://insurancecouncil.com.au/resource/building-resilience-rating-tool-brrt>.
- [60] I. Almufti, *REDi WM. Rating System: Resilience-Based Earthquake Design Initiative for the Next Generation of Buildings*, ARUP, San Francisco, 2013.
- [61] E. Asadi, Z. Shen, H. Zhou, A. Salman, and Y. Li, "Risk-informed multi-criteria decision framework for resilience, sustainability and energy analysis of reinforced concrete buildings," *Journal of Building Performance Simulation*, vol. 13, no. 6, pp. 804–823, 2020.
- [62] A. H. Sangaki, F. R. Rofooei, and H. Vafai, "Probabilistic integrated framework and models compatible with the reliability methods for seismic resilience assessment of structures," *Structures*, vol. 34, pp. 4086–4099, 2021.
- [63] S. Hosseinzadeh and K. Galal, "System-level seismic resilience assessment of reinforced masonry shear wall buildings with masonry boundary elements," *Structures*, vol. 26, pp. 686–702, 2020.
- [64] J. A. Avila-Haro, R. Gonzalez-Drigo, Y. F. Vargas-Alzate, L. Pujades, and A. Barbat, "Probabilistic seismic assessment of a high-rise URM building," *Journal of Building Engineering*, vol. 45, Article ID 103344, 2022.
- [65] H. Bu, L. He, and H. Jiang, "Seismic fragility assessment of steel frame structures equipped with steel slit shear walls," *Engineering Structures*, vol. 249, Article ID 113328, 2021.
- [66] H. Chen and J. Bai, "Seismic performance evaluation of buckling-restrained braced RC frames considering stiffness and strength requirements and low-cycle fatigue behaviors," *Engineering Structures*, vol. 239, Article ID 112359, 2021.
- [67] X. Estrella, P. Guindos, J. L. Almazán et al., "Seismic performance factors for timber buildings with woodframe shear walls," *Engineering Structures*, vol. 248, Article ID 113185, 2021.
- [68] W. M. Hassan, J. C. Reyes, C. González, F. J. Pallarés, and J. S. Spinel, "Seismic vulnerability and resilience of steel-reinforced concrete (SRC) composite column buildings with non-seismic details," *Engineering Structures*, vol. 244, Article ID 112810, 2021.
- [69] M. Hejazi and A. Jalaeefer, "Effect of infills on seismic resilience of special steel moment resisting frames," *Structures*, vol. 33, pp. 2771–2791, 2021.
- [70] S. Hosseinzadeh and K. Galal, "Probabilistic seismic resilience quantification of a reinforced masonry shear wall system with boundary elements under bi-directional horizontal excitations," *Engineering Structures*, vol. 247, Article ID 113023, 2021.
- [71] B. Jiménez, S. Saloustros, and L. Pelà, "Seismic vulnerability index method for hybrid timber-masonry structures. Numerical calibration and application to the city of Valparaíso, Chile," *Journal of Building Engineering*, vol. 44, Article ID 103185, 2021.
- [72] M. Mohammadi, M. Mirzaei, and M. R. Pashaie, "Seismic Performance and Fragility Analysis of Infilled Steel Frame Structures Using a New Multi-Strut Model," *Structures Elsevier*, vol. 34, 2021.
- [73] M. Vona, A. Flora, E. Carlucci, and E. Foscolo, "Seismic retrofitting resilience-based for strategic RC buildings," *Buildings*, vol. 11, no. 3, p. 111, 2021.
- [74] C. Yun and C. Chao, "Study on seismic performance of prefabricated self-centering steel frame," *Journal of Constructional Steel Research*, vol. 182, Article ID 106684, 2021.
- [75] R. Zhu, T. Guo, and S. Tesfamariam, "Seismic performance assessment of steel moment-resisting frames with self-centering viscous-hysteretic devices," *Journal of Constructional Steel Research*, vol. 187, Article ID 106987, 2021.
- [76] G. A. Anwar and Y. Dong, "Seismic resilience of retrofitted RC buildings," *Earthquake Engineering and Engineering Vibration*, vol. 19, no. 3, pp. 561–571, 2020.
- [77] G. A. Anwar, Y. Dong, and C. Zhai, "Performance-based probabilistic framework for seismic risk, resilience, and sustainability assessment of reinforced concrete structures," *Advances in Structural Engineering*, vol. 23, no. 7, pp. 1454–1472, 2020.
- [78] C. Fang, Y. Ping, Y. Chen, M. C. H. Yam, J. Chen, and W. Wang, "Seismic performance of self-centering steel frames with SMA-viscoelastic hybrid braces," *Journal of Earthquake Engineering*, vol. 1, pp. 1–28, 2020.
- [79] N. Giordano, F. De Luca, and A. Sextos, "Out-of-plane closed-form solution for the seismic assessment of unreinforced masonry schools in Nepal," *Engineering Structures*, vol. 203, Article ID 109548, 2020.
- [80] J.-G. Xu, G. Wu, and D.-C. Feng, "Near fault ground motion effects on seismic resilience of frame structures damaged in Wenchuan earthquake," *Structure and Infrastructure Engineering*, vol. 16, no. 10, pp. 1347–1363, 2020.
- [81] E. M. Hassan and H. Mahmoud, "Full functionality and recovery assessment framework for a hospital subjected to a scenario earthquake event," *Engineering Structures*, vol. 188, pp. 165–177, 2019.
- [82] M. Niazi, M. Raissi Dehkordi, M. Eghbali, and D. Samadian, "Seismic resilience index evaluation for healthcare facilities: a case study of hospital in Tehran," *International Journal of Disaster Risk Reduction*, vol. 65, Article ID 102639, 2021.
- [83] J. M. Andrić and D.-G. Lu, "Fuzzy methods for prediction of seismic resilience of bridges," *International Journal of Disaster Risk Reduction*, vol. 22, pp. 458–468, 2017.
- [84] Y. Dong and D. M. Frangopol, "Risk and resilience assessment of bridges under mainshock and aftershocks incorporating uncertainties," *Engineering Structures*, vol. 83, pp. 198–208, 2015.

- [85] C. Huang and S. Huang, "Seismic resilience assessment of aging bridges with different failure modes," *Structures*, vol. 33, pp. 3682–3690, 2021.
- [86] L. Sun, D. D'Ayala, R. Fayjaloun, and P. Gehl, "Agent-based model on resilience-oriented rapid responses of road networks under seismic hazard," *Reliability Engineering & System Safety*, vol. 216, Article ID 108030, 2021.
- [87] B. Balaei, S. Wilkinson, R. Potangaroa, and P. McFarlane, "Investigating the technical dimension of water supply resilience to disasters," *Sustainable Cities and Society*, vol. 56, Article ID 102077, 2020.
- [88] W. Liu, Z. Song, M. Ouyang, and J. Li, "Recovery-based seismic resilience enhancement strategies of water distribution networks," *Reliability Engineering & System Safety*, vol. 203, Article ID 107088, 2020.
- [89] H. Fotouhi, S. Moryadee, and E. Miller-Hooks, "Quantifying the resilience of an urban traffic-electric power coupled system," *Reliability Engineering & System Safety*, vol. 163, pp. 79–94, 2017.
- [90] S. G. Cho, O. Furuya, and H. Kurabayashi, "Enhancement of seismic resilience of piping systems in nuclear power plants using steel coil damper," *Nuclear Engineering and Design*, vol. 350, pp. 147–157, 2019.
- [91] A. Cardoni, G. P. Cimellaro, M. Domaneschi, S. Sordo, and A. Mazza, "Modeling the interdependency between buildings and the electrical distribution system for seismic resilience assessment," *International Journal of Disaster Risk Reduction*, vol. 42, Article ID 101315, 2020.
- [92] E. Ferrario, A. Poulos, S. Castro, J. C. de la Llera, and A. Lorca, "Predictive capacity of topological measures in evaluating seismic risk and resilience of electric power networks," *Reliability Engineering & System Safety*, vol. 217, Article ID 108040, 2022.
- [93] L. Iannacone, N. Sharma, A. Tabandeh, and P. Gardoni, "Modeling time-varying reliability and resilience of deteriorating infrastructure," *Reliability Engineering & System Safety*, vol. 217, Article ID 108074, 2022.
- [94] S. Ahmadi, Y. Saboohi, and A. Vakili, "Frameworks, quantitative indicators, characters, and modeling approaches to analysis of energy system resilience: a review," *Renewable and Sustainable Energy Reviews*, vol. 144, Article ID 110988, 2021.
- [95] A. Cardoni, S. L. Borlera, F. Malandrino, and G. P. Cimellaro, "Seismic vulnerability and resilience assessment of urban telecommunication networks," *Sustainable Cities and Society*, vol. 77, Article ID 103540, 2022.
- [96] C. ChienKuo, Y. Eiki, and D. Santoso, "Seismic resilience analysis of a retrofit-required bridge considering moment-based system reliability," *Structure and Infrastructure Engineering*, vol. 17, no. 6, pp. 757–778, 2021.
- [97] M. Ramezanpour, A. Eslami, and H. Ronagh, "Seismic performance of stabilised/unstabilised rammed earth walls," *Engineering Structures*, vol. 245, Article ID 112982, 2021.
- [98] Y. Xiao, X. Zhao, Y. Wu et al., "Seismic resilience assessment of urban interdependent lifeline networks," *Reliability Engineering & System Safety*, vol. 218, Article ID 108164, 2022.
- [99] C. Zhai, P. Yu, and W. Wen, "A physical-organizational method for the functionality assessment of A hospital subjected to earthquakes," *Journal of Earthquake Engineering*, vol. 1, pp. 1–21, 2021.
- [100] C. Zong, K. Ji, R. Wen, X. Bi, Y. Ren, and X. Zhang, "Seismic resilient three-stage enhancement for gas distribution network using computational optimization algorithms," *Soil Dynamics and Earthquake Engineering*, vol. 152, Article ID 107057, 2022.
- [101] L. Capacci and F. Biondini, "Probabilistic life-cycle seismic resilience assessment of aging bridge networks considering infrastructure upgrading," *Structure and Infrastructure Engineering*, vol. 16, no. 4, pp. 659–675, 2020.
- [102] X. Chen and C. Li, "Seismic performance of tall pier bridges retrofitted with lead rubber bearings and rocking foundation," *Engineering Structures*, vol. 212, Article ID 110529, 2020.
- [103] M. Eghbali, D. Samadian, M. Ghafory-Ashtiani, and M. Raissi Dehkordi, "Recovery and reconstruction of schools after M 7.3 Ezgeleh-Sarpole-Zahab earthquake; part II: recovery process and resiliency calculation," *Soil Dynamics and Earthquake Engineering*, vol. 139, Article ID 106327, 2020.
- [104] E. Koc, B. Cetiner, A. Rose, L. Soibelman, E. Taciroglu, and D. Wei, "CRAFT: comprehensive resilience assessment framework for transportation systems in urban areas," *Advanced Engineering Informatics*, vol. 46, Article ID 101159, 2020.
- [105] J. Li, T. Wang, and Q. Shang, "Probability-based seismic resilience assessment method for substation systems," *Structure and Infrastructure Engineering*, vol. 18, no. 1, pp. 71–83, 2020.
- [106] P. Rezaei Ranjbar and H. Naderpour, "Probabilistic evaluation of seismic resilience for typical vital buildings in terms of vulnerability curves," *Structures*, vol. 23, pp. 314–323, 2020.
- [107] I. Kilanitis and A. Sextos, "Integrated seismic risk and resilience assessment of roadway networks in earthquake prone areas," *Bulletin of Earthquake Engineering*, vol. 17, no. 1, pp. 181–210, 2019.
- [108] T. Tong, W. Zhuo, X. Jiang, H. Lei, and Z. Liu, "Research on seismic resilience of prestressed precast segmental bridge piers reinforced with high-strength bars through experimental testing and numerical modelling," *Engineering Structures*, vol. 197, Article ID 109335, 2019.
- [109] C. Nan and G. Sansavini, "A quantitative method for assessing resilience of interdependent infrastructures," *Reliability Engineering & System Safety*, vol. 157, pp. 35–53, 2017.
- [110] Ba, "Study on various methods and techniques of retrofitting," *International Journal of Engineering Research and Technology*, vol. 2, no. 9, 2013.